DEPARTMENT OF ONCOLOGY
Medical Sciences Division

Towards the synthesis and delivery of a halogenated MCT1 substrate

Irini Skaripa-Koukelli

St Cross College

Michaelmas, 2019

Supervisors:

Professor Katherine A. Vallis

Professor Robert C. Carlisle

A thesis submitted to the University of Oxford in partial fulfilment of the requirement for the degree of Doctor of Philosophy

To my grandma,
who will never read it,
but who has been looking forward to it all the way
and will be happy to know it is done.

Declaration

I declare that this thesis has been written solely by myself, and that it has not been submitted, in whole or in part, in any previous application for a degree. Except where stated otherwise by reference or acknowledgment, the work presented is a true and honest account of my own research, which was conducted ethically, and the results obtained are genuine.

Irini Skaripa-Koukelli

Acknowledgements

I would like to thank my supervisors, Professors Kate Vallis and Robert Carlisle for their guidance and support throughout this project and for allowing me to develop my own ideas.

These four years would not have been the same without everyone in the lab and previous lab members. As is presumably the case in all theses from the Vallis group, the first person to thank is our lab manager, Sarah, who has been there for my emergency ordering and all the random questions I have in the day. To my 'desk mate' Elliot – thank you for always being/looking happy and optimistic. Eloise, currently back in France, thank you for all the long days we spent together, your help and your magical organisational skills (which I clearly don't have). Javian… I'm not sure that you can be grouped with 'lab people', but you make a big difference when you are in the lab. Abirami and Martin, thank you for being so helpful, smart and there to discuss. Ole, thank you for the chemistry ideas and help. Nadia, Richard, Sree, Rachel, Bas and Boon – thank you for all your help and for being there. Anne-Marie, thank you for dealing with all the emergencies so efficiently. And thanks to people I'm sure I have missed!

BUBBL lab is another big group of nice and helpful people. Josh, thank you for your enthusiasm, humour and willingness to try new things. Mike and Christophoros, thanks for being so reliable and dealing with my basic ultrasound questions.

Christina, I would literally not submit a thesis without you. Thank you for being a great friend. Miles, thank you for being so patient and supportive during this difficult time.

Above all, I want to thank my family for their continuous support for all these years, during and before the DPhil. Thanks for waking me up every morning, dealing with my grumpiness, and sending me treats.

Abstract

The monocarboxylate transporter 1 (MCT1) has received special attention as a potential therapeutic target in cancer thanks to its role in lactate shuttling. In breast cancer (BC), high MCT1 expression has been correlated with basal-like phenotype and a 'triple-negative' status, an aggressive subgroup of tumours with no identified molecular targets.

In this thesis, MCT1 was targeted with a brominated pyruvate derivative, 3-bromobyruvate (3BP). 3BP is an alkylating agent known to inhibit glycolysis. Here, it was shown that 3BP is selectively toxic to cells expressing MCT1. Metabolomics, used to investigate metabolic effects, is a high-throughput, unbiased approach that requires no assumptions on possible targets. Inhibition of glyceraldehyde phosphate dehydrogenase (GADPH), an established 3BP target, was confirmed. Accumulation of pentose phosphate pathway (PPP) intermediates, inhibition of nucleotide synthesis, ATP and thiol-based antioxidant depletion were found to be profound in MCT1-expressing cells.

The reactivity of 3BP towards thiols necessitates the use of a delivery system. 3BP was encapsulated in cavitation-sensitive liposomes and co-administered with lipid microbubbles (MBs) as ultrasound contrast agents (UCAs). Ultrasound locally triggers the release of the therapeutic, which was confirmed using an *in vitro* apparatus developed in house.

With radiotherapy being one of the main modalities used in BC treatment, the next question was whether a radio-labelled therapeutic agent could be delivered via MCT1. A radio-iodinated lactate derivative ('^{123}I-HPLA') was synthesised and tested for selectivity towards MCT1-expressing cells with positive outcomes.

Finally, Poly(lactic-co-glycolic acid) (PLGA) MBs were investigated for the development of a novel delivery system. Clinically relevant ultrasound pressures resulted in persistent cavitation, fragmentation and accelerated monomer release from PLGA MBs.

The findings of this study support the use of small halogenated carboxylic acids to selectively target MCT1 and addresses the delivery challenges associated with such compounds.

Publications

Owen, J., Thomas, E., Menon, J., Gray, M., **Skaripa-Koukelli, I.**, Gill, M., Wallington, S., Miller, R., Vallis, K., Carlisle, R. Indium-111 after-loading of preformed HEGF-containing liposomes for molecularly targeted radionuclide delivery via ultrasound-induced cavitation. *Journal of Controlled Release*, **319**, 222-233 (2020)

Thomas, E., Menon, J., Owen J., **Skaripa-Koukelli, I.**, Wallington, S., Gray, M., Mannaris C., Kersemans, V., Allen, D., Kinchesh, P., Smart, S., Carlisle, R., Vallis, K. Ultrasound-mediated cavitation enhances the delivery of an EGFR-targeting liposomal formulation designed for chemo-radionuclide therapy. *Theranostics*, **9 (19)** 5595-5609 (2019).

Gill, M., Menon, J., Jarmanm P., Owen, J., **Skaripa-Koukelli, I**., Able, S., Thomas, J., Carlisle, R., Vallis, K. ^{111}In-labelled polymeric nanoparticles incorporating a ruthenium-based radiosensitizer for EGFR-targeted combination therapy in oesophageal cancer cells. *Nanoscale*, **10**, 10596-10608 (2018).

Conference contributions

I. Skaripa-Koukelli, E. Thomas, D. Hauton, J. Owen, J. Walsby-Tickle, S. Wallington, M. Gray, R. Carlisle, K. Vallis. 'Towards the synthesis and delivery of halogenated MCT1 substrates', *OxCD3 Oncological Conference*, September 2019, Oxford, UK. **Poster and mini presentation**.

I. Skaripa-Koukelli, J. Walsby-Tickle, J. Owen, E. Thomas, J. McCullagh, R. Carlisle, K. Vallis. 'Towards the synthesis and delivery of a radio-labelled MCT1 substrate', *CRUK Oxford Centre Symposium*, June 2019, Oxford, UK. **Poster**.

I. Skaripa-Koukelli, J. Walsby-Tickle, J. Owen, E.Thomas, J.McCullagh, R. Carlisle, K. Vallis . 'Towards the synthesis and delivery of a radio-labelled MCT1 substrate', *Keystone Symposia on Tumour Metabolism*, February 2019, Keystone Colorado, USA. **Poster**.

I. Skaripa-Koukelli, J. Owen, O. Tietz, R. Carlisle, K. Vallis. 'Ultrasound-triggered delivery of halogenated pyruvate analogues to breast cancer cells', *EACR25 congress*, June 2018, Amsterdam, Netherlands. **Poster**.

I. Skaripa-Koukelli, O. Tietz, C. Mannaris, J. Brown, J. Owen, R. Carlisle, K. Vallis. 'Ultrasound-responsive lactic acid based agents for the selective delivery of targeted radiotherapy to solid tumours', *NCRI conference*, November 2017, Liverpool, UK. **Poster**.

I. Skaripa-Koukelli, O. Tietz, C. Mannaris, J. Brown, J. Owen, R. Carlisle, K. Vallis. 'Ultrasound-responsive polymeric agents for the selective delivery of a radiolabelled lactate mimetic to cancer cells', *CRUK/MRC Oxford Institute for Radiation Oncology Symposium*, September 2017, Oxford, UK. **Poster**.

I. Skaripa-Koukelli, J. Menon, J. Owen, R. Carlisle, K. Vallis. 'Poly(lactic acid)-based cavitation agents for the delivery of a radionuclide to a solid tumour', *CRUK Oxford Centre Symposium*, June 2016, Oxford, UK. **Poster.**

I. Skaripa-Koukelli, J. Menon, J. Owen, R. Carlisle, K. Vallis. 'Poly(lactic acid)-based cavitation agents for the delivery of a radionuclide to a solid tumour', *MEIBioEng*, September 2016, Oxford, UK. **Oral presentation**.

Contents

1 INTRODUCTION 31

1.1 Targeting cancer metabolism 31

1.1.1 Monocarboxylic acid transport 33

1.1.2 MCT1 in human cancers 36

1.1.3 MCT1 as a therapeutic target 41

1.2 Stimulus-responsive drug delivery systems 44

1.2.1 Path to the target 44

1.2.2 Externally applied stimuli to improve delivery 45

1.3 Concept 49

1.4 References 52

2 MATERIALS AND METHODS 64

2.1 *In vitro* studies 64

2.1.1 Cell culture 64

2.1.2 Measurement of protein content in cell lysates 65

2.1.3 Western blot analysis 65

2.1.4 Metabolic activity assay 67

2.1.5 MCT1 siRNA knockdown 68

2.1.6 Statistical analysis 68

2.2 *In vivo* studies 69

2.2.1 Tumour model 69

2.2.2 Contrast-enhanced imaging for the assessment of tumour vascularity 70

3 PERTURBATION OF METABOLISM OF BREAST CANCER CELLS BY 3-BROMOPYRUVATE 71

3.1 Abstract 71

3.2 Introduction 72

3.2.1 Triple negative breast cancer (TNBC) 72

3.2.2 Using 3-bromopyruvate for cancer treatment 74

3.3 Aims 77

3.4 Materials & methods 77

3.4.1 Toxicity of 3BP 77

3.4.2 Metabolic studies 78

***3.4.2.1 Metabolomics* 78**

3.5 Results 85

3.5.1 Toxicity of 3BP 85

3.5.2 Bromide uptake 87

3.5.3 Comparing metabolites between different TNBC cell lines 89

3.5.4 Comparing metabolites within a single TNBC cell line 96

3.5.5 Bioenergetics 104

3.6 Discussion 105

3.6.1 Transporter expression 106
3.6.2 3BP is selectively toxic to cells strongly expressing MCT1 107
3.6.3 3BP is taken up selectively by MCT1-expressing cells 108
3.6.4 3BP has multiple metabolic targets 109
3.6.5 Effects on glycolysis, TCA and PPP 111
3.6.6 Effects on antioxidants 115
3.6.7 Nucleotide synthesis is selectively inhibited in MCT1-expressing cells 117
3.6.8 Oxidative or glycolytic? 120

3.7 Conclusions & future directions 121

3.8 References 122

4 LIPOSOMAL 3BP 130

4.1 Abstract 130

4.2 Introduction 130

4.3 Aims 132

4.4 Materials & Methods 132

4.4.1 Liposome synthesis 132
4.4.2 Liposome characterisation 134
4.4.3 Quantification of 3BP 135
4.4.4 *In vitro* ultrasound exposure 136
4.4.5 *In vivo* biodistribution 139

4.5 Results 140

4.5.1 Synthesis and characterisation of liposomes 140
4.5.2 Encapsulation of 3BP 142
4.5.3 *In vitro* ultrasound exposure 142
4.5.4 *In vivo* biodistribution in tumour-free mice 145

4.6 Discussion 149
4.6.1 The approach 149
4.6.2 The formulation 150
4.6.3 The treatment 155

4.7 Conclusions & future directions 157

4.8 References 158

5 A RADIOLABELLED LACTATE MIMETIC: ^{123}I-HPLA 163

5.1 Abstract 163

5.2 Introduction 163
5.2.1 Targeted radionuclide therapy (TRT) 163
5.2.2 Delivery considerations for TRT 165
5.2.3 A radiolabelled compound to target MCT1 167

5.3 Aims 169

5.4 Materials & Methods 169
5.4.1 Synthesis of I-HPLA 169
5.4.2 Analysis and purification of I-HPLA 170
5.4.3 Radiochemical stability of I-HPLA 171

5.4.4 Optimisation of the reaction time 171
5.4.5 Cellular uptake of I-HPLA 172
5.4.6 *In vivo* tumour growth 173
5.4.7 *In vivo* biodistribution and pharmacokinetic studies 173
5.4.8 Encapsulation of I-HPLA in cavitation-sensitive liposomes 174

5.5 Results 174
5.5.1 Synthesis of I-HPLA: reaction analysis 174
5.5.2 Radiochemical stability of I-HPLA 178
5.5.3 Uptake studies 179
5.5.4 *In vivo* tumour growth 180
5.5.5 *In vivo* pharmacokinetic and biodistribution studies 181
5.5.6 Encapsulation of I-HPLA in cavitation-sensitive liposomes 184

5.6 Discussion 185
5.6.1 Iodination reaction 185
5.6.2 Cell studies 188
5.6.3 *In vivo* study 189

5.7 Conclusion & future directions 191

5.8 References 192

6 POLYMERIC MICROBUBBLES: AN ALTERNATIVE DELIVERY SYSTEM

6.1 Abstract 197

6.2 Introduction 197

6.2.1 Degradation of lactate-based constructs 199

6.2.2 Ultrasound contrast agents 202

6.3 Aims 203

6.4 Materials & methods 204

6.4.1 Synthesis of polymeric particles 204

6.4.2 Characterisation of polymeric particles 205

6.4.3 Degradation of polymeric particles 208

6.5 Results 209

6.5.1 Low molecular weight PLA particles 209

6.5.2 PLGA particles 211

6.6 Discussion 218

6.7 Concluding remarks & future directions 227

6.8 References 228

7 General Discussion 234

7.1 Inhibition or 'Trojan horse'? 234

7.2 Need for companion diagnostics 237

7.3 Potential delivery strategies 238

7.4 TRT for metabolic liabilities 239

7.5 Concluding remarks 240

7.6 References 241

8 APPENDIX 245

8.1 Standard curve for 3BP 245

8.2 Cell viability after 2 h treatment with 3BP 246

8.3 BT20 tumour growth and vascularity study 247

Figures

FIGURE 1 (a) Common physiological substrates of MCT1: lactic acid, pyruvic acid and the ketone bodies acetoacetic and β-hydroxybutyric acid. (b) cartoon illustrating the proposed mechanised of lactic acid transport by MCT1. The first step is the protonation of a lysine residue (k38), which causes the channel to open. Then, lactate moves into the extracellular pore and forms an ion pair with K38. Proton transfer from K38 to the normally negatively charged aspartate-302 (D302) neutralises the side chain of D302. This causes lactate to move through the pore and form an ion pair with arginine-306 (R306). Finally, K38 returns to its deprotonated state, the transporter relaxes back to its closed state and lactate is released into the cytosol. The cartoon is adapted from Halestrap, 2013 (reference 15). 35

FIGURE 2 Timeline of milestones in MCT1-related cancer research. 41

FIGURE 3 Chemical structures of commonly used competitive inhibitors of MCT1. 43

FIGURE 4 Chemical structure of the investigational MCT1 substrate 3-bromopyruvic acid (3BP), which is the focus of Chapter 3. 43

FIGURE 5 Mechanical effects of cavitation. Non-inertial cavitation can induce microstreaming, resulting in a local mixing effect, and generate radiation forces, which cause shear stress to the vessel walls and propels therapeutics into the tumour. Shear stress can also trigger the release of compounds encapsulated in co-administered nanocarriers. Inertial cavitation, which results in violent implosion of the bubble, can result in radiation forces, shock waves and micro-jets. Bubble fragments, if small enough, can enter the tumour tissue. 48

FIGURE 6 Diagrammatic presentation of the thesis concept 51

FIGURE 7 Mechanism of action of 3-bromopyruvate (3BP). 3BP reacts with nucleophiles, mainly thions (-SH) found on protein and peptides, resulting in their 'pyruvylation'. 75

FIGURE 8 Number of publications per year involving 3-bromopyruvate (3BP), as obtained by pubmed search for the term '3-bromopyruvate' without chronological filtering (as per October 2019)..... 76

FIGURE 9 Timeline of Seahorse XF96 experiment. Cells were seeded in 6-well plates 3 days prior to the experiment. They were transfected with sirna against mct1 2 days before the experiment and then treated with 20 μm 3BP the day before. The sensor cartridge was hydrated overnight. For measurement, treatment media was replaced with unbuffered serum-free assay media, the instrument was calibrated as per manufacturer's instructions and 5 measurements were taken over the course of 1 h (n=4). For full details, see methods. The results were analysed using Prism7 software (GraphPad, CA, USA)..... 84

FIGURE 10 MCT expression. Expression of monocarboxylate transporter (MCT) isoforms 1 and 4 by the selected triple negative breast cancer (TNBC) cell lines, BT20 and MDA-MB-231. Lysates were incubated with reducing lamelli buffer for 10 min at 70°C before loading onto a 4-12 % SDS PAGE, subsequent electrophoretic transfer onto nitrocellulose was followed by probing with an anti-MCT1 (Santa Cruz, sc-365501) or anti MCT4 (Santa Cruz, sc-50329) primary antibody and an anti-mous or anti-rabbit HRP secondary antibody (Invitrogen, 61-6520 and 32460) for MCT1 and MCT4 respectively. Magicmark™ XP (Thermo, lc5602) was used as a molecular weight marker. See methods for full details..... 85

FIGURE 11 Profiling the differential toxicity of 3bp (a) BT20 and MDA-MB-231 cells were tested for different sensitivity to 3BP treatment (n=3). Cells were treated with a concentration series of 3BP and cell viability was measured with an mtt assay (see methods). (b) the impact of CHC, an MCT1 inhibitor, was investigated by inclusion in studies exposing BT20 or MDA-MB-231 cells 3BP. Data were normalised to untreated control. Error bars represent SD, ***, ** and * represent $p<0.05$, 0.01 and 0.001 respectively as assessed using multiple t tests analysis on Prism 7 (GraphPad, ca, usa). 86

FIGURE 12 MCT1-dependent 3BP toxicity. (a) Transfection efficiency was assessed by Western blot analysis on separate wells which were processed at the start of the 3BP treatment or the following day (end of treatment), and (b) the corresponding quantification of band intensity analysed on ImageJ (FIJI, CA, USA). (c) BT20 cells, BT20 cells transfected with untargeted siRNA (sc-BT20) and BT20 cells transfected with siRNA targeted against MCT1 (siMCT1-BT20) were treated with 3BP for 24 hours and their viability is shown in the graph, n = 4, error bars represent SD, ** and * represent $p<0.05$ and 0.01 respectively as determined by multiple t-tests on Prism 7 (GraphPad, CA, USA). 87

FIGURE 13 Differential bromide uptake. (a) Intensity of bromide peak (^{78}Br and ^{80}Br) normalised to control measured by LC-MS in MDA-MB-231 and BT20 cell lysates, and (b) in BT20, sc-BT20 and siMCT1-BT20 cells (n=6). Sc-BT20 are BT20 cells transfected with scrambled siRNA and siMCT1-BT20 cells are BT20 cells transfected with siRNA against MCT1 (see methods). Error bars represent SD, *$p<0.05$, **$p<0.01$, ***$p<0.001$. Statistical analysis was performed by Prism 7 (GraphPad, CA, USA). 89

FIGURE 14 Changes in glycolysis, tricarboxylic acid (TCA) cycle and pentose phosphate pathway (PPP). MDA-MB-231 cells (a) and BT20 cells (b) were treated with 100 μM 3BP for 60 min, then the metabolites were extracted and analysed by liquid chromatography coupled with mass spectrometry (LC-MS/MS). Results are presented as fold changes normalised to untreated control for each cell line. Data were analysed using microsoft excel and Metaboanalyst online software. Error bars represent SD, n=6, *$p<0.05$, **$p<0.01$, ***$p<0.001$. 92

FIGURE 15 3BP effects on glutathione and NADH. (a) glutathione abundance in untreated controls. (b) changes in glutathione levels in response to treatment with 100 μM 3BP, expressed as $\log_2$(fold change).(c) NADH abundance in untreated controls (no statistically significant difference). (d) change in NADH levels in response to treatment with 100 μM 3BP, expressed as

log_2(fold change). Statistical analysis was performed on Prism 7 (GraphPad, CA, USA), n=6, SD shown. *p<0.05, **p<0.01, ***p<0.001. 93

FIGURE 16 Changes in the levels of nucleotides in response to treatment with 3-bromopyruvate (3BP). (a) Change expressed as log_2 (fold change) in the level of individual nucleotides after 60 min treatment of BT20 and MDA-MB-231 cells with 100 μM 3BP (n=6). (b) cumulative change in purines and pyrimidines after 60 min treatment of BT20 and MDA-MB-231 cells with 100 μM 3BP (n=6). Error bars represent the standard deviation. *p<0.05, **p<0.01, ***p<0.001. Data were analysed with Prism 7 (GraphPad, CA, USA)..... 95

FIGURE 17 Changes in glycolysis, tricarboxylic acid (TCA) and pentose phosphate pathway (PPP) in response to 3BP treatment. (a) and (b) present the changes in glycolysis following treatment with 100 μM 3BP for 30 and 60 min respectively (n=6), (c) and (d) present changes in the tca cycle following treatment with 100 μM 3BP for 30 and 60 min respectively (n=6), and (e) and (f) present changes in the PPP following treatment with 100 μM 3BP for 30 and 60 min respectively (n=6). Metabolites were extracted from treated cell lysates and analysed by LC-MS/MS (see methods for full details). Error bars represent the standard deviation. Data were analysed using Prism 7 (GraphPad, CA, USA), n=6, *p<0.05, **p<0.01, ***p<0.001. 99

FIGURE 18 Abundance of glutamine (a) and glutamate (b). Cells were treated with 100 μM 3BP for up to 60 min (n=6) and the metabolites were extracted and analysed with LC-MS/MS (see methods for full details). Error bars represent the standard deviation. Data were analysed using Prism 7 (GraphPad, CA, USA)..... 100

FIGURE 19 3BP effects on antioxidant levels following 30 min (a) or 60 min (b) treatment. Cells were treated with 100 μM 3BP for up to 60 min (n=6) and the metabolites were extracted and analysed with LC-MS/MS (see methods for full details). Error bars represent the standard deviation. Data were analysed using Prism 7 (GraphPad, CA, USA). *p<0.05, ****p<0.0001. 101

FIGURE 20 Changes in levels of nucleotides in response to 3BP treatment. Effect of 60 min treatment with 100 μM 3BP on BT20, sc-BT20 and siMCT1-BT20 cells (n=6). Sc-BT20 refers to BT20 cells transfected with scrambled siRNA. siMCT1-BT20 refers to cells transfected with sirna against siMCT1. Cells were treated with 100 μM 3BP for up to 60 min (n=6) and the metabolites were extracted and analysed with LC-MS/MS (see methods for full details). Error bars represent the standard deviation. Data were analysed using Prism 7 (GraphPad, CA, USA). *p<0.05, ****p<0.0001..... 103

FIGURE 21 Oxygen consumption and acidification rate changes in response to low concentration 3BP. (a), (b) and (c) Extracellular acidification rate (ECAR), oxygen consumption rate (OCR) and their ratio (OCR/ECAR) respectively, in BT20, MDA-MB-231 and BT20 cells transfected with sirna against MCT1 (siMCT1-BT20), treated with 20 μM 3BP overnight (d) OCR plotted against ECAR as a metric of the metabolising state of the cells (n=4). OCR and ecar were measured using a Seahorse XF96 analyser and OCR/ECAR and bioenergetic profile were calculated from these values (see methods for full details). Error bars represent the standard deviation. Data were analysed with Prism 7 (GraphPad, CA, USA)..... 104

FIGURE 22 Structure and role of nucleotides. Nucleotides consist of a pentose sugar (ribose or deoxyribose), a nitrogenous base (purine or pyrimidine) and 1-3 phosphate groups. Nucleotides are the immediate precursors of nucleic acids, they act as energy sources and participate in signal transduction. A: adenine, c: cytosine, g: guanosine, t: thymine and u: urasil. 117

FIGURE 23 Synthesis of purine and pyrimidine base. Figure adapted from Pavlova N. and Thompson C., 2016..... 119

FIGURE 24 Graphical representation of the active loading technique. 3BP, an organic acid (pKa 1.84) is ionised in strongly acidic conditions (HCl 0.1 m). In an unionised form, it can cross

the lipid bilayer of pre-formed liposomes. The liposomal core is mildly alkaline ($NaHCO_3$ 0.84%w/v) which results in ionisation and therefore entrapment of 3BP. 134

FIGURE 25 Main parts of SAT2, the device used for *in vitro* ultrasound exposures. The SAT2 is composed of a cylindrical water chamber at the bottom of which focused ultrasound (US) transducer is fitted. The sample, in an inverted 35 mm cell culture dish sealed with an ultrasound transparent lid ('sonolid') is placed in a holder 32 cm above the transducer. A passive cavitation detector (PCD) receives the acoustic emissions from the sample and feeds them to a computer equipped with TiePie software (TiePie Engineering, Netherlands) for processing. ... 138

FIGURE 26 Physicochemical properties of liposomes. (a) Size distribution by intensity measured by dynamic light scattering (DLS) of freshly prepared empty ('blank') or 3BP-containing liposomes, (b) average size, polydispersity index (PDI) and zeta potential of freshly prepared empty ('blank') or 3BP-containing ('3BP') liposomes, (c) and (d) liposome average size and PDI change respectively after incubation in phosphate-buffered saline (PBS) at different temperature 4°c, 25°C ('RT') or 37°C. N=3 for all studies. The results were analysed using Prism 7 software (GraphPad, CA, USA). Error bars represent the standard deviation. 141

FIGURE 27 Evaluation of blank liposome toxicity. Toxicity of blank liposomes and SonoVue microbubbles (SV) tested on MDA-MB-231 and BT20 cells, at a concentration range that includes the concentrations used for further experiments..... 142

FIGURE 28 Experimental Design 1 for *in vitro* treatment of cells with liposomal 3-bromopyruvate (3BP) and ultrasound (US). (a) Graphical representation of the experimental procedure. Cells are seeded in 33 mm μ-cell culture dishes the day prior to the experiment. Growth medium supplemented with liposomes and SonoVue (SV, 0.25 mg/mL) replaces the normal growth medium and the dish is treated with ultrasound in the SAT2 device. Cells are then incubated for 24 h and their viability is measured with an MTT assay. For full details see

methods. (b) % cell viability 24 h post-exposure normalised to 'no ultrasound' control for each cell group. 143

FIGURE 29 Experimental Design 2 for *in vitro* treatment of cells with 3-bromopyruvate (3BP) and ultrasound (US). (a) Graphical representation of the experimental procedure. Briefly, cells are seeded in a 6-well plate the day prior to the experiment. The following day, growth medium supplemented with liposomes and SonoVue (SV, 0.25 mg/mL) is treated in a cell-free 35 mm μ-cell culture dish in the SAT2. The treated solution is then distributed into the cells. Cells are incubated for 24 h and their viability is assessed with an MTT assay. (b) representative passive cavitation detection (PCD) spectrum of SV (20 s exposure, 1.1 MHz, 0.3 MPa, 3,000 cycles). (c) Western blot analysis for the evaluation of siRNA-mediated silencing efficiency in BT20 cells and (d) quantification of optical density as a ratio to β-actin. (e) % metabolic activity as a measure of cell viability 24 h post-exposure normalised to blank liposome control for each cell group (n=3). Error bars represent the standard deviation. *$p<0.05$, ** $p<0.01$. Western blotting (d) and metabolic activity (e) data were analysed using Prism 7 software (GraphPad, CA, USA). MatLab software (MathWorks, MA, USA) was used to plot PCD spectra (b). For full details, please refer to methods. 145

FIGURE 30 Liposome biodistribution. Imaging 60 min (a) and 24 h (b) of mice injected with sulfo-Cy5 loaded liposomes using the IVIS spectrum system (Perkin Elmer, MA, USA) operating at the FLIT mode for 3D imaging and using 640/680 excitation emission filters for acquisition. Female nude mouse and organs (liver, spleen and kidneys) phantom added artificially upon analysis to facilitate the localisation of the signal. Images were analysed by the living image software (Perkin Elmer, MA, USA). 148

FIGURE 31 Cavitation triggered released of a peptide from liposomes. Enhanced release of [111In]In-hEGF from liposomes upon exposure to ultrasound using the same conditions as

used in this work. Unpublished data reproduced with the permission of Dr J. Owen, who is the first author of this manuscript. 153

FIGURE 32 Chemical structures of the starting material, p-hydroxyphenyllactic acid (HPLA) and the mono- and di-iodination products (I-HPLA and I_2-HPLA, respectively). 170

FIGURE 33 Chromatographic trace showing starting materials and products involved in I-HPLA synthesis. Crude reaction mix (20 μL) in PBS was analysed by reversed phase-high performance liquid chromatography (RP-HPLC) and the eluting compounds were detected by an ultraviolet detector set at 230 nm. Each trace corresponds to an independently run sample. From front to back: in blue, sodium iodide (NaI 1 mg/mL in PBS), in yellow, p-hydroxyphenyllactic acid (HPLA 1 mg/mL in PBS) and in pink, crude reaction mix after 60 min incubation. HPLC was operated with a C18 column, 1-99% water-acetonitrile gradient acidified with trifluoroacetic acid, 1 ml/min, 20 min. For full details, see methods. 175

FIGURE 34 optimisation of I-HPLA reaction yield. (a) area under the curve (AUC) of chromatographic peaks of reagents (sodium iodine, NaI, and p-hydroxyphenyllactic acid, HPLA) and products 1 and 2 over time. (b) % change in AUC of reagents and products from 5 min reaction time, which is the recommended time for radio-iodination. 176

FIGURE 35 Purification of ^{123}I-HPLA. Chromatographic separation of unreacted starting materials and products of HPLA reaction with ^{123}I-NaI in PBS using hplc equipped with a C18 column. Blue trace corresponds to the UV detector (280 nm) and red trace corresponds to the radioactivity detector of the radio-HPLC system. The graph was plotted using Prism 7 software (GraphPad, CA, USA). For full details, please refer to methods. 177

FIGURE 36 Radio-chemical purity of ^{123}I-HPLA. Reversed phase – high performance liquid chromatography (RP-HPLC) traces are shown. Ultraviolet (UV) signal at 280 nm is shown in grey outline and radioactivity signal is shown in red outline. Starting from the front: purified

non-radioactive I-HPLA (pure 'cold' in grey), prurified ^{123}I-HPLA (pure 'hot' in yellow) and co-injection of both solutions in cyan. HPLC was operated using a C18 column with 1-99% water-acetonitrile gradient acidified with formic acid, 1 ml/min flow rate. For full details, see methods. The graph was plotted using Microsoft Excel (Microsoft Corporation, Washington, USA). 178

FIGURE 37 Radiochemical stability of ^{123}I-HPLA at 4°C, room temperature and 37°C. Freshly synthesised and purified ^{123}I-HPLA was incubated for 24 h at 4°C, room temperature or 37°C and then analysed by reversed phase-high performance liquid chromatography (RP-HPLC). The radioactivity trace for each sample (peaks in counts per minute, CPM) is presented. Blue, green and orange trace correspond to 4°C, room temperature and 37°C incubation for 24 h. HPLC was operated using a C18 column with 1-99% water-acetonitrile gradient acidified with formic acid, 1 ml/min flow rate. For full details, see methods. Graph was plotted using Prism 7 software (GraphPad, CA, USA) 179

FIGURE 38 Uptake of ^{123}I-HPLA by breast cancer cell lines. BT20 (red) and MDA-MB-231 cells (white), which present high and low mct1 expression respectively, were incubated with increasing concentration of ^{123}I-HPLA (0.5, 1.0 and 1.5 MBq/ml) for (a) 2 h or (b) 24 h (n=3). At the end of the incubation time, the cells were washed three times with PBS, lysed and the radioactivity in the lysate was measured using an automated gamma counter (Wizard counter, Perkin Elmer, MA, USA). Results are presented as ratios of normalised activity (counts per minute/ μg of protein) in BT20 lysates over MDA-MB-231 lysates. Statistical analysis was performed using Prism 7 (GraphPad software, CA, USA). *p<0.05, **p<0.01, ***p<0.001, n=3. 180

FIGURE 39 *In vivo* characterisation of ^{123}I-HPLA. (a) biodistribution of ^{123}I-HPLA (5 MBq in PBS, pH 5) at 1.5 hours post-injection in female nude mice. (b) ratios of 'tumour to blood' and 'tumour to muscle', (c)^{123}I-HPLA blood clearance measured by single photon emission computed tomography (SPECT) imaging focused on the heart area. (d) representative

autoradiography showing the distribution of ^{123}I-HPLA in a slice at the centre of the tumour 1.5 h post-injection. (e) representative full body spect/ct image (lateral view) acquired 1 h post injection of ^{123}I-HPLA. A pressure balloon was used to monitor the breathing of the animal during imaging. Statistical analysis was performed using Prism 7 software (GraphPad software, CA, USA), n=3, error bars represent standard deviation. 183

FIGURE 40 Purification of ^{123}I-HPLA loaded liposomes. Size exclusion chromatography traces of crude liposome mix (yellow), free ^{123}I-HPLA (cyan) and purified ^{123}I-HPLA containing liposome suspension (pink). Each fraction collected was 100 μL, except the first one which was 200 μL. Sephadex G25 column was used as the stationary phase and pbs was used as the mobile phase. Graph was plotted using Microsoft Excel (Microsoft Corporation, Washington, USA). 184

FIGURE 41 Chemical structures of poly(lactic acid) (PLA) and poly(D,L-lactic-*co*-glycolic acid) (PLGA). PLA (a) is composed from lactic acid building blocks, and PLGA (b) is composed of lactic and glycolic acid building blocks linked together with ester bonds. 199

FIGURE 42 Acoustic characterisation setup. Schematic diagram showing the experimental setup used for the acoustic characterisation of microbubbles (MBs). The ultrasound apparatus is placed in the tank filled with degassed water (omitted for clarity). It consists of the focussed ultrasound (FUS) transducer, passive cavitation detection (PCD) transducer, tissue-mimicking agarose phantom and diagnostic ultrasound imaging device. The signal received by the PCD is high-pass filtered, amplified and recorded and processed on MatLab (MathWorks, MA, USA). The FUS and PCD transducers are controlled via custom-made software using a graphical programming language (Lab-View, National Instruments, Austin, TX, USA)..... 207

FIGURE 43 PLA particle characterisation. (a) Size distribution by single particle optical sizing (SPOS). For measurement, 100 μL of 1 mg/mL particle suspension was diluted in the measurement vessel with 30 mL water. (b) Optical microscopy image at 40x magnification. For imaging, 10 μL 1 mg/mL suspension was placed into each side of the hemocytometer. (c)

scanning electron microscopy (SEM) imaging of lyophilised PLA formulation (2.5 kV). (d) low-vacuum sem imaging of lyophilised PLA formulation (3 kV, 30 Pa)..... 210

FIGURE 44 Characterisation of poly(lactic-*co*-glycolic acid) particles. (a) and (b) size distribution of 'high' MW (38-54 kDa) and 'intermediate' MW (24-38 kDa) PLGA particles measured by single particle optical sizing (SPOS). For measurement, 100 μL 1 mg/mL particle suspension was diluted in the measurement vessel of the accusizer instrument which is filled with 30 mL water. (c) optical microscopy image (40x magnification) of 10 μL 1 mg/ml 'high' MW (HMW) particle suspension in water placed into each side of the hemocytometer. (d) low vacuum SEM image of HMW PLGA particles, (e) low vacuum SEM image of sonicated HMW particle suspension and (f) B-mode ultrasound imaging of HMW particles in a 1 mm channel across an agarose phantom. (g)-(j) equivalent images of the 'intermediate' MW (24-38 kda) PLGA particles..... 213

FIGURE 45 Acoustic characterisation of intermediate molecular weight microbubbles (IMW MBs). (a) and (b) cavitation spectrum at 'low' (0.18 MPa) and 'high' (0.77 MPa) pressure of different concentrations (0.1, 0.01 and 0.001 mg/mL) of MBs under 0.5 mL/min flow in a 1 mm diameter channel across a 1.5% agarose tissue-mimmicking phantom. (c) and (d) cavitation activity of IMW MBS as a function of time (in seconds) at 'low' and 'high' ultrasound pressures. Plga is poly-(lactic-*co*-glycolic acid) 24-38 kda. Ultrasound parameters used were 1.1 MHz driving frequency, 0.18 ms pulse length, 200 cycles at 0.18 or 0.77 MPa pressure. These graphs were plotted using MatLab software (MathWorks, MA, USA)..... 214

FIGURE 46 Ultrasound-induced degradation of polymeric microbubbles (MBs). (a) and (b) cavitation activity of poly(lactic-*co*-glycolic acid) (PLGA) MBs at 0.2 and 0.5 MPa respectively. (c) lactate release from PLGA MBs treated with ultrasound (0.2 MPa, 0.5 MPa or probe sonicator) and from untreated control. *$p<0.05$, where red and orange symbol correspond to the statistical significance of the difference between 0.5 and 0.2 MPa respectively. MatLab software

(MathWorks, MA, USA) was used to plot graphs a and b. Prism 7 software (GraphPad, CA, USA) was used to analyse the lactate release data (n=3) and to plot graph c. Error bars represent the standard deviation. 216

FIGURE 47 Lactate release from polymeric microbubbles (MBs) following 8 min sonication. (a) Cavitation activity of poly-(lactic-*co*-glycolic acid) (PLGA) MBs 2.5 mg/mL exposed to 0.5 MPa ultrasound (US) pressure for 8 min in the SAT2 device (please see methods in chapter 4 for full details of the device).(b) lactate release from PLGA bubbles after 8 min ultrasound exposure in the SAT2 device (0.5 MPa, 2.5 mg/mL, n=3). Lactate was measured with a colorimetric assay kit (mak064-1kt, Sigma Aldrich). PLGA was 24-38 KDa MW. MatLab software (MathWorks, MA, USA) was used to plot graphs a and b. Prism 7 software (GraphPad, CA, USA) was used to analyse the lactate release data (n=3) and to plot graph c. Error bars represent the standard deviation. 217

Tables

TABLE 1 Monocarboxylate transporter 1 (MCT1) expression in human cancers. 37

TABLE 2 Time events in the Seahorse XF96 run. 83

TABLE 3 Chemical structure of phospholipids used for liposome synthesis. 133

TABLE 4 Summary of treatments used in the pilot biodistribution study. 147

TABLE 5 Iodine isotopes and their properties. 168

1 Introduction

1.1 Targeting cancer metabolism

The reprogramming of energy metabolism, which is necessary to support the growth of rapidly dividing cancer cells, has been recognised as an emerging hallmark of cancer[1]. Otto Warburg was the first to observe the unusual energy metabolism in cancer, characterised by the upregulation of glycolysis even when oxygen is available, a phenomenon termed 'aerobic glycolysis' or simply 'Warburg effect'[2]. That seemed like a paradox. Oxidative phosphorylation (OXPHOS) produces about 18-fold more energy, in the form of ATP, compared to glycolysis. Why would a rapidly dividing cell switch to a much less efficient mechanism of energy production when oxygen is present? Warburg attributed this to the inability of cancer cells to perform OXPHOS due to dysfunctional mitochondria. Today, the 'Warburg effect' forms the basis of ^{18}F-fluorodeoxy-glucose positron emission tomography (^{18}F-FDG-PET) scan, an indispensable tool for cancer diagnosis, staging and monitoring[3]. However, we now know that most cancer cells have functional mitochondria and are capable of performing OXPHOS[3], which, in fact, they do[4]. The voracity with which many cancer cells consume glucose combined with the upregulation of several components of the glycolytic pathway has led to the misconception that cancer cells 'switch off' OXPHOS and produce most of the energy they need by glycolysis. More updated analyses of intact human tumours reveals that cancer cells upregulate both glycolysis and OXPHOS simultaneously, compared to surrounding normal tissue[4].

Targeting metabolic differences between cancer and healthy cells is a viable approach to cancer treatment which has already provided established therapeutics. For example, therapeutics can exploit particular traits of specific cancers so that a systemically administered compound is selectively toxic to cancer cells. A prime exemplar of this is the inability of acute lymphoblastic

leukemia (ALL) cells to synthesise asparagine, a non-essential amino-acid. Systemic administration of asparaginase, an enzyme that catabolises asparagine to aspartic acid and ammonia, can selectively kill ALL cells[5].

Aside from these very particular traits of specific cancer types, it seems that metabolic alterations in cancers converge to a set of pathways which allows tumours to acquire abundant nutrients and use them to produce ATP, generate biosynthetic precursors and macromolecules, and tolerate tumour-associated stresses (e.g. redox and hypoxia)[4]. A feature that makes metabolism a particularly attractive target is that these alterations, especially with regards to nutrient uptake and excretion of metabolic by-products, manifest with the upregulation of the corresponding transporters. This generic feature means that, first, targeting with small molecules is possible and second, these transporters are frequently on the cell membrane, circumventing the need for intracellular targeting.

GLUT1, the main glucose transporter isoform, has been an obvious target thanks to the 'Warburg effect'. GLUT1 upregulation is the reason why ^{18}F-FDG-PET imaging works. Attempts to target aerobic glycolysis via GLUT1 have explored glucose analogues that can be transported but not metabolised further, such as 2-deoxyglucose (2DG), small molecule inhibitors[6,7], and even non-pharmacological approaches such as the ketogenic diet[8–11]. Another transporter-dependent feature is glutamine addiction, which is present in certain cancers, including 'hard-to-treat' pancreatic carcinomas. The *SLC1A5* gene product, ASCT2, is responsible for the transport of neutral amino-acids, including glutamine[12]. ASCT2 has been targeted with glutamine analogues, which showed activity in the clinic but were discontinued due to neurotoxicity[13], and inhibitors to suppress glutamine uptake[13,14].

Finally, interest regarding the lactate/pyruvate transporters, mainly MCT1 and MCT4, has been invigorated over the last decade with the change in perception of lactate from being the

'waste product of glycolysis' to a legitimate nutrient for cancer cells and a key metabolic modulator[1].

1.1.1 Monocarboxylic acid transport

Monocarboxylic acids are dissociated in physiological conditions. The most abundant monocaroxylates are lactate and pyruvate, which are involved in sugar, amino-acid and lipid metabolism. Other important monocarboxylates involved in several metabolic pathways include: ketone bodies (e.g. acetoacetate and β-hydroxybutyrate), short-chain fatty acids (acetate, propionate, butyrate), transamination products of amino-acids, e.g. phenylpyruvate (from phenylalanine) and α-keto-β-methylvalerate (from isoleucine). In the majority of cases, these anions are transported across cell or organelle membranes through a carrier-mediated process[15]. Monocarboxylate transporters (MCTs) catalyse the net transport of a monocarboxylate anion and a proton down their concentration gradient[16]and are responsible for the majority of monocarboxylate transport. In the gastrointestinal tract and kidneys, sodium-coupled monocarboxylate transporters (SMCTs) are also important contributors. The mitochondrial pyruvate carrier (MPC) is a distinct proton-linked carrier which mediates the transport of pyruvate and other monocarboxylates across the mitochondrial membrane[15].

The MCT family of transporters consists of 14 members, encoded by the *SLC16* gene family. Only MCT1-4 have been confirmed to passively transport monocarboxylates, including lactate, pyruvate and ketone bodies. The first member of the MCT family, MCT1, is expressed by most tissues[17]. It transports L-lactate (K_m=3-5 mM) and pyruvate (K_m=0.7 mM) with high affinity, which makes it suitable for the inward and outward movement of these metabolites. MCT4 is associated with highly glycolytic tissues, such as white skeletal muscle fibres, astrocytes and white blood cells. It has lower affinity for L-lactate (K_m=28 mM) and pyruvate (K_m=150 mM) but higher turnover rate, features that make it most suitable for the outward movement of these metabolites[15]. The

high affinity isoform MCT2 (K_m=0.74 mM for L-lactate, 0.08 mM for pyruvate) is 60% identical in sequence to MCT1 and mostly expressed in tissues that use lactate for energy production such as the neurons and hepatocytes. MCT3 is most similar to MCT4 (68% sequence similarity) and its expression is limited to the retinal pigment epithelium[18]. Other characterised transporters for the *SLC16* family are isoforms MCT8, with high affinity for the thyroid hormone, and MCT10 (also known as TAT1) which is an aromatic amino-acid transporter[18].

MCT family members share a similar overall structure consisting of 12 transmembrane helices and intracellular N- and C-termini. The helices are organised into two distinct N- and C-terminus domains, each comprising 6 helices, which are connected by a large cytosolic loop between helix 6 and 7. The hydrophobic pocket at the bottom of the substrate-binding channel in the 'outside open' conformation of MCT1, the lysine-38 (K38) residue is considered essential for transport. The hydrophobic environment favours this lysine remaining uncharged (not protonated) but by accepting a proton (H^+), it provides a binding site for a monocarboxylate (e.g. lactate). MCT1 then undergoes domain rearrangement, during which the lactate and proton pass through the channel to an intracellular substrate binding site where aspartate and arginine residues (D302 and R306) form an ion pair and are essential for the transporter activity. The monocarboxylate and proton bound to K38 are transferred to D302-R306 and the transporter is thought to relax back to the 'inside open' state with deprotonation of K38 and exposure of D302-R306 to the cytosol. At this point, the monocarboxylate and proton can be released. These three amino acids (K38, D302 and R306) are conserved in isoforms MCT2, MCT3 and MCT4, and are required for the translocation cycle taking place during the transport of monocarboxylates to either side of the cell membrane[15]. The chemical structures of common MCT1 substrates (lactic acid, pyruvic acid and the ketone bodies acetoacetic and β-hydroxybutic acid) and the proposed mechanism of monocarboxylate transport through MCT1 are presented in **Figure 1A** and **B** respectively.

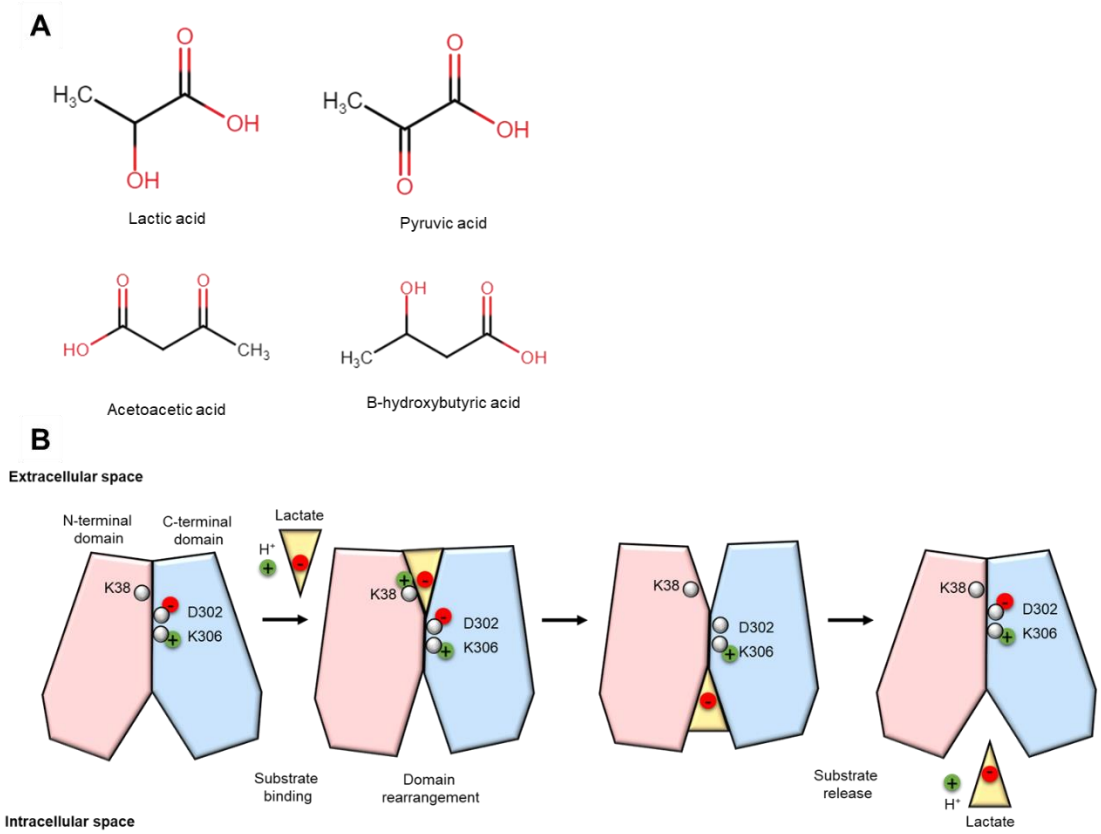

Figure 1 (A) Common physiological substrates of MCT1: lactic acid, pyruvic acid and the ketone bodies acetoacetic and β-hydroxybutyric acid. (B) Cartoon illustrating the proposed mechanised of lactic acid transport by MCT1. The first step is the protonation of a lysine residue (K38), which causes the channel to open. Then, lactate moves into the extracellular pore and forms an ion pair with K38. Proton transfer from K38 to the normally negatively charged aspartate-302 (D302) neutralises the side chain of D302. This causes lactate to move through the pore and form an ion pair with arginine-306 (R306). Finally, K38 returns to its deprotonated state, the transporter relaxes back to its closed state and lactate is released into the cytosol. The cartoon is adapted from Halestrap, 2013 (Reference 15).

The physiological role of MCTs in different tissues was thoroughly reviewed by Halestrap and Meredith[16]. Most mammalian tissues rely mainly on OXPHOS for energy metabolism under normal conditions but may become glycolytic under hypoxic conditions. MCT1, one of the high affinity MCT isoforms can in the latter case rapidly excrete lactate to prevent cytosolic acidification. However, tissues that are normally glycolytic express MCT4 as the main MCT isoform. Its low affinity for pyruvate ensures that pyruvate can be reduced to lactate, thus regenerating NAD^+ and allowing glycolysis to continue. However, the rationale for its low affinity for lactate has been more

challenging to explain. It has been suggested that lactate accumulation in the working muscle, which causes a fall in pH, is responsible for fatigue which prevents further exercise, in turn preventing systemic acidosis.

In the liver and kidney, high affinity isoforms MCT1 and 2 are responsible for lactate uptake, where lactate is used for gluconeogenesis and lipogenesis. In other tissues, like the heart, skeletal muscle and brain, lactate and ketone bodies are used as a fuel for oxidative metabolism. In skeletal muscle and heart, MCT1 fulfils that role while in the brain both MCT1 and MCT2 are expressed[16].

More than one isoform can be expressed in the same tissue, often a high and low affinity isoform, resulting in metabolic compartmentalisation. One such physiological example is the skeletal muscle. Glycolytic white muscle fibres have few mitochondria and express MCT4, thus excreting lactate, which is taken up by MCT1-expressing red muscle fibres, where lactate can enter the tricarboxylic acid (TCA) cycle[19]. Importantly, glycolysis in the muscle is related with the onset of heavy exercise and not usually with lack of oxygen[19] . Another example is the lactate shuttling between glial cells and neurons in the brain. Glial cells export lactate via MCT1 and MCT4, which is taken up by the neurons through MCT1 and MCT2 for oxidative metabolism. Physiological MCT-mediated lactate shuttling between distant tissues is also observed: the lactate produced by the working muscle can be taken up by the liver in a process described as the Cori cycle[19,20].

1.1.2 MCT1 in human cancers

MCT1 is overexpressed in various cancers, as summarised in **Table 1**. However, its role with regards to metabolism in these tumours remains unclear from the literature. Researchers have provided compelling evidence that this transporter is associated with oxidative metabolism, and in fact, metabolic compartmentalisation of solid tumours where MCT4 expressing cells produce lactate and MCT1 expressing cells take up and metabolise lactate[21,22]. On the other hand, highly glycolytic tumours such as neuroblastomas[23] and gliomas[24] were also found to overexpress the

transporter presumably to sustain glycolysis, while MCT1 inhibition has been shown to increase mitochondrial metabolism[25].

The latest findings on cancer metabolism and the involvement of MCTs, mainly MCT1, suggest that high ^{18}F-FDG uptake, linked to upregulated glycolysis, does not necessarily exclude the possibility of lactate uptake and use in oxidative metabolism. For instance, in lung tumours, DeBerardinis' group provided evidence that, strikingly, lactate's contribution to TCA cycle is higher than that of glucose, despite the high ^{18}F-FDG uptake[26]. The authors confirmed lactate uptake was MCT1-dependent. Rabinowitz's group provided evidence that this phenomenon is generalised, not exclusive to lung cancer[27]. Earlier studies had suggested a symbiotic model, where well oxygenated cells oxidise lactate, while hypoxic cells excrete it[22]. These new findings suggest that it is also possible that the two processes occur in parallel in the same cell. MCT1 expression has also been correlated with poorer prognosis in certain tumours such as endometrial[28] and breast[29] carcinomas.

Overall, the role of MCT1-4 is well characterised in several healthy tissues. However, their role in tumour pathophysiology is not fully understood. They are legitimate therapeutic targets with promising compounds in pre-clinical development and one inhibitor (AZD3965) in clinical trials (NCT01791595). It seems like their role might be context-dependent and generalisations are risky with the current body of evidence. Important developments in MCT1-related research are summarised in **Figure 2**.

Table 1 Monocarboxylate transporter 1 (MCT1) expression in human cancers.

Tumour site	MCT1 expression	Comments
Colon	↑ In cancer cells (glycolytic) and in CAFs (oxidative), (Koukourakis et al., 2006[30])	Patient samples. Metabolic collaboration between cancer and stromal cells.

	↓ In cancer cells associated with the glycolytic switch (Lambert et al., 2002[31])	Patient samples. Preference for glucose and upregulation of GLUT1, rather than butyrate.
	↑ MCT1 expression in colorectal cancer cells, compared to adjacent normal tissue (Pinheiro et al., 2008[32,33])	Patient samples. Associations with chaperone proteins (CD147, CD44) and MCT4.
	Nuclear factor E2-related factor-2 (Nrf2) promotes reverse-Warburg effect with ↑ MCT1 in a subset of cancer cells. Symbiosis with MCT4 overexpressing cancer cells, (Diehl et al.[34])	Patient samples and in vitro data. Suggested metabolic compartmentalisation in colon carcinoma.
Nervous system	↑ MCT1 expression correlated with higher grade tumours, (Froberg et al., 2001[35])	
	↑ MCT1 and 2 in glioblastoma multiforme (GBM) tissue samples, (Mathupala et al., 2004[36])	Overall shift toward higher affinity transporters (MCT1 and MCT2) to support glycolytic metabolism. MCT3 main isoform in normal brain. Silencing of MCT1 and 2 induces cell death in GBM cell lines.
	↑ MCT1, MCT4 and CD147 in glioblastomas, compared to normal brain tissue or diffuse astrocytomas, (Martinho et al., 2013[37])	Glioma samples, in vitro and in vivo data. Characterisation of MCT1, MCT4 and CD147 expression.
	↑ MCT1 in neuroblastoma associated with MYCN expression, high risk disease and >1 year old upon diagnosis, (Fang et al., 2006)	Patient samples and in vitro data.
	↑ MCT1 in glioblastoma cancer stem cells (Takada et al., 2016[38])	In vitro data.
	Glioblastoma cells induce ↑ MCT1 and oxidative metabolism in endothelial cells when co-cultured, (Miranda-Goncalves et al, 2017[39])	In vitro data.
Breast	↓ MCT1 due to epigenetic hypermethylation in breast cancer (Asada et al, 2003[40])	
	↑ MCT1 overall, compared to normal tissue, and associated with basal-like phenotype and high grade tumour, (Pinheiro et al., 2010[41])	Patient samples.
	Strong expression of MCT1 in basal-like cell lines (MDA-MB-468, BT20,	In vitro data.

	Hs578T), except MDA-MB-231 which has high MCT4 expression. HER2-positive SkBr3 express MCT4 only. Authors suggest mutually exclusive expression of the MCT1 and 4 isoforms, (Morais-Santos et al., 2014[42])	
	↑ MCT1 is a marker of lactate uptake, associated with triple negative breast cancer (TNBC), high grade tumours and poor prognosis[29] .	
Gynaecologic tract	↑ MCT1, ↑ CD147 and ↑ MDR protein in epithelial ovarian cancer cells but not in healthy tissue, (Chen et al., 2010[43])	Patient samples from primary and metastatic sites and in vitro data.
	↑ MCT1 and ↑ MCT4 associated with high grade, invasive cervical carcinoma, (Pinheiro et al., 2008[44])	Patient samples from pre-cancerous and cancerous lesions.
	↑ MCT1 expression correlates with poor prognosis in endometrial cancer.	Patient samples.
Lung	↑ invasiveness with MCT1 expression (Izumi *et al*[45]).	
	MCT1 expression determines lactate uptake, which is the preferred fuel for oxidative metabolism (DeBerardinis *et al*[26,46]).	In vivo and live human tumours.
	MCT1 involved in metabolic collaboration (Koukourakis *et al*[47])	
Bone	Metabolic relationship between osteosarcoma cell lines and mesenchymal cells, with oxidative metabolism – high MCT1 in cancer cells, and glycolytic metabolism – high MCT4 in mesenchymal cells(Bonuccelli, G. *et al* [48]).	
	↑ MCT1 expression associated with shorter survival, MCT1 expression correlated with tumour invasiveness and growth (Zhao *et al*[49]).	
Pancreas	Variable expression of MCT1 and 4 in pancreatic ductal adenocarcinoma (PDAC)(Kong, 2016[50]).	

	Effective delivery of microencapsulated 3BP to (Chapiro *et al*[51]).	
Prostate	Correlation between expression of multidrug resistance protein (MDR1) and ancillary protein CD147 and MCT1. High tumour grade correlates with high MCT1 and 4 expression (Hao *et al*[52])	
Stomach	MCT1 and its ancillary protein basigin/CD147 co-expressed in gastric carcinoma with no difference in expression as the disease progresses (Pinheiro *et al*[53])	
	Toxicity of 3BP has been demonstrated in an in vivo study on gastric cancer, which indirectly confirms expression of MCT1 (Xian, S.-L *et al*[54])	
Head and neck	Metabolic compartmentalisation with high MCT1 expression correlated with OXPHOS, high MCT4 expression with glycolysis. High grade carcinomas uniformly express MCT1(Curry, J. M. *et al*[21]*).*	
Blood	High expression of MCT1 in promyelocytic (HL60) and monocytic (THP1) cell lines, further upregulated by exposure to vascular endothelial growth factor (VEGF) and lactate. 3BP toxicity proportional to MCT1 exposure (Lopes-Coelho *et al.*[55])	

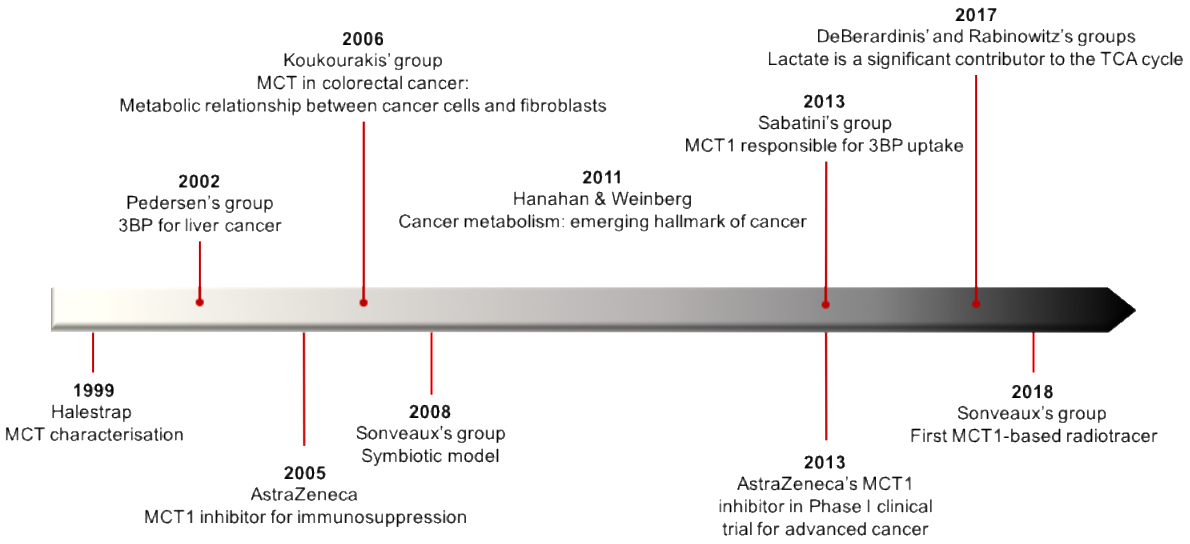

Figure 2 Timeline of milestones in MCT1-related cancer research.

1.1.3 MCT1 as a therapeutic target

The increasing awareness of the importance of lactic acid shuttles by MCT1 has led to the investigation of the transporter's potential as a therapeutic target. As for other nutrient transporters, two main strategies are being explored, namely inhibition of the transporter or using it for the transport of a toxic derivative of lactate/pyruvate, in a 'Trojan horse'-like manner. Importantly, in both cases, small molecules can be used, which can avoid the high production cost of biological treatments and circumvent some of the delivery challenges.

MCT1 inhibition has been used as a means to dampen glycolysis and, in the case of oxidative cells, it has been shown to disrupt the metabolic collaboration ('symbiosis') between different cell populations within a tumour.

Competitive inhibitors of MCT1 have been used in the discovery of MCTs. These are molecules that have affinity for the transporter and bind at the same site as the physiological substrates, but are not transported[15]. A commonly used such compound is α-cyano-4-hydroxycinnamic acid (CHC) with K_i value 250-500 μmol/L under physiological conditions[15].

Although CHC has been used in metabolic studies[24,56,57] involving MCT1, this is not always appropriate as this compound also inhibits other MCT isoforms and the mitochondrial pyruvate carrier (MPC) 2-fold more potently than it inhibits MCT1. Stilbene disulfonates, such as DIDS and DBDS, have also been used as MCT1 inhibitors with K_i values between 2-500 μmol/L[15]. Inhibition by CHC and stilbene disulfonates is reversible and pH dependent. Other non-specific, reversible inhibitors used in research are phloretin and quercetin. The chemical structures of these inhibitors are shown in **Figure 3**. More selective inhibitors with high affinity for MCT1 have recently been developed by AstraZeneca (K_i values in the nmol/L range) and one of these compounds, AZD3865 has entered clinical trials for various advanced cancers[58,59]. Interestingly, initial development of this compound was intended for immunosuppression, rather than cancer treatment[58].

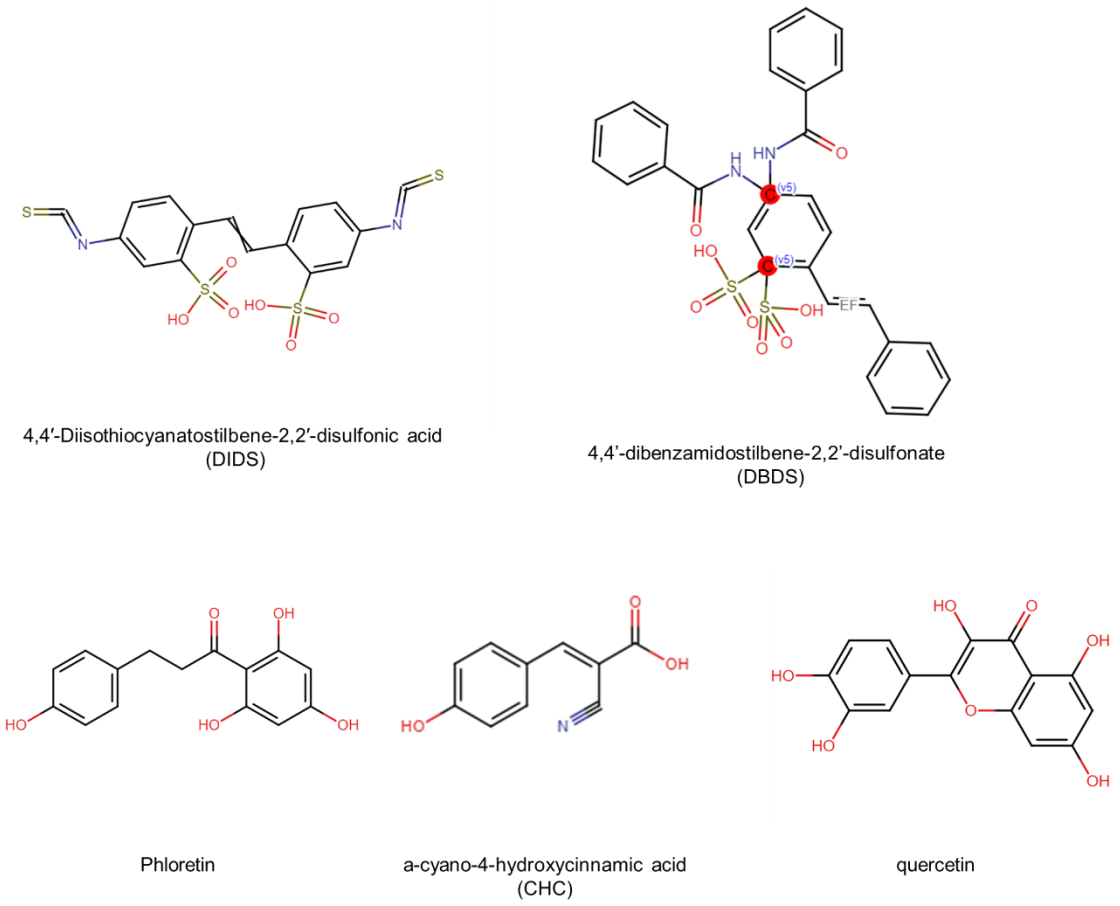

Figure 3 Chemical structures of commonly used competitive inhibitors of MCT1.

The alternative, 'Trojan horse' approach is the topic of this thesis. The main investigational compound in this category is 3-bromopyruvate (3BP), a brominated lactate/pyruvate derivative that acts as an alkylating agent once in the cytoplasm (**Figure 4**). The uptake and effects of 3BP are the focus of **Chapter 3**.

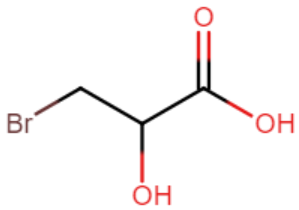

Figure 4 Chemical structure of the investigational MCT1 substrate 3-bromopyruvic acid (3BP), which is the focus of Chapter 3.

1.2 Stimulus-responsive drug delivery systems

Research on the resistance of tumours to treatment has long been focused on the molecular mechanisms of resistance to chemotherapy, whereas the importance of limited drug distribution within tumours only started to attract considerable attention over the last 15 years[60]. In normal tissues, most cells lie within a few cell diameters from the blood vessels, which gives them access to oxygen, nutrients and, when needed, administered therapeutics[60,61]. In contrast, solid tumours present reduced vascular density and significant cell populations lie further away from the blood vessels (>100 μm), which limits their access to nutrients, but most importantly in the context of medicine, to therapeutic agents[60]. Another challenge with cancer therapy in particular is that most chemotherapeutic agents are highly toxic and with poor biodistribution and pharmacokinetic profile, thus causing off-target unwanted effects. The rush to develop drug delivery systems, mainly nanocarriers (NC), was driven by the need for better distribution of cancer therapeutics around the body and within the tumour.

In this part, the physical barriers that cancer therapeutics need to overcome to reach their target are explained and the ways in which stimulus-responsive drug carriers could help are described, with a focus on externally applied stimuli and ultrasound in particular.

1.2.1 Path to the target

Although targeted therapies are often described as 'tumour seeking', it should be clarified that molecules cannot actively seek the disease[62]. They rely on their physicochemical properties to circulate in the blood stream and distribute around the body. Small molecule cancer chemotherapeutics tend to have large volumes of distribution and distribute non-selectively in the body. Peptide-based therapies are rapidly cleared by the kidneys[63]. Enclosing therapeutics in NCs can prolong their circulation time, enabling them to accumulate into the tumour, exploiting the

enhanced permeability and retention (EPR) effect[64,65]. Additionally, a biological probe, e.g. an antibody against a cell surface transporter or receptor, can target the carrier to a specific cell[62].

For solid tumours, the therapeutic must overcome additional biophysical barriers posed by the tumour pathophysiology[66,67]. Therapeutics need to cross the vessel wall and navigate into the tumour mass to find their target cells[68].

The pore size of the tumour vasculature is highly variable, generally between 100 nm to 2 μm[69]. NCs up to a few hundred nm in diameter can cross the capillary wall selectively at the tumour site. Even so, a recent analysis demonstrated that on average only 0.7% of the injected dose accumulates in the tumour[70]. Moreover, NCs tend to remain stationary in perivascular regions rather than penetrating deeper into the tumour[71]. Of the physical barriers, dense extracellular matrix (ECM) and high interstitial fluid pressure (IFP) are the major factors which negatively impact on drug delivery to solid tumours[68], slowing down or completely inhibiting diffusion and convection, respectively. Most of the new targeted vectors are macromolecules, which are most severely affected by such barriers[71,72]. Pharmacological approaches to 'normalise' the tumour microenvironment and blood vessels have been suggested as a means to improve delivery[73]. Although 'normalisation' has shown some promise, tumour heterogeneity, response variability and difficulties in non-invasive monitoring can limit its success[72].

1.2.2 Externally applied stimuli to improve delivery

Physical stimuli can act to direct the therapeutic construct to the tumour site and/or to trigger the release of a therapeutic from its carrier. Physical stimuli can be grouped as endogenous (pH, oxidative state, enzymes) or exogenous (magnetic field, ultrasound, light, hyperthermia)[74–80]. Although certainly promising, endogenous stimuli are subject to the heterogeneity among different patients and tumours, as well as within a single tumour. In contrast, exogenous stimuli are by

definition applied by an external source and therefore, they allow for better control and less reliance on the pathophysiology of the specific tumour[81].

1.2.2.1 Magnetic fields

Magnetically responsive drug carriers, in combination with an extracorporeal static or alternating magnetic field, have found exciting applications in oncological drug delivery. Iron oxides (Fe_3O_4, γ-Fe_2O_3, α-Fe_2O_3) commonly make up the core of superparamagnetic iron oxide nanoparticles (SPIONs). SPIONs can be either directly modified with targeting probes or therapeutics and coated with protective polymers, or can be incorporated in larger NCs, e.g. liposomes[82].

For drug delivery applications, SPIONs can be used in combination with a static magnetic field for physical targeting of a NC to the tumour. Small molecules[79,80,83] and macromolecules[84–86] directly bound to the SPION or incorporated into liposomes or nanoparticles have all been successfully manufactured and tested. Magnetic particles have been employed in combination with other physical stimuli such as ultrasound[87] and electric fields[79]. Alternating magnetic field can trigger drug release from a carrier containing magnetic nanoparticles[88].

1.2.2.2 Light

Photo-activatable systems that can release their payload in response to ultraviolet, visible and/or near infrared (NIR) illumination[89] have been engineered over the last decade. Their function relies on the photo-chemistry of certain chemical groups e.g. isomerisation of azo-benzene group[90], cleavability of *o*-nitro-benzene, light-to-heat conversion of gold nanoparticles[81] and ROS generation of porphyrins[91]. The main criticism of light-responsive systems is that they are restricted by the penetration depth of light, especially for UV-visible light (10 mm tissue penetration)[81], which makes them applicable only to superficial malignancies. Alternatively, *in situ*

generated Cherenkov irradiation from targeted radionuclides can trigger payload release of photosensitive carriers at the target site[92–94], which is also particularly relevant to disseminated disease.

1.2.2.3 Hyperthermia

Hyperthermia for triggered drug release was the first external stimulus used for this purpose, dating back in 1978[95]. Whole body[96] and local mild hyperthermia[97] have both been used to improve drug delivery. Temperature rise can be induced directly by externally heating the tumour area, an approach which has been clinically evaluated with high intensity focussed ultrasound (HIFU) and ThermoDox®[97,98]. Other hyperthermia-sensitive liposomal formulations, with incorporation of polymers, lysolipids or other mechanisms of sensitisation have been designed since[99,100]. Alternatively, alternating magnetic fields in combination with magnetic nanoparticles[88], or ultrasound-induced cavitation of microbubbles (MBs) can also generate local mild hyperthermia, an approach which has reached clinical trials with promising outcomes[97].

1.2.2.4 Ultrasound

Ultrasound (US) can enhance extravasation and penetration of therapeutic agents or trigger the release of a therapeutic from its carrier, with or without causing heating. Focused ultrasound in combination with US-responsive MBs can generate cavitation, which, in turn, leads to mechanical effects (**Figure 5**) or hyperthermia, all of which can be exploited for drug delivery[101]. Oscillating bubbles essentially act as a pump, pushing molecules away from the bubble surface and towards the wall of the blood vessel[72,102]. Unlike hyperthermia, which is clinically evaluated[97], the mechanical effects of cavitation remain at a more pre-clinical stage.

Locally applied pulsed high intensity focused ultrasound (HIFU) has been shown to increase the uptake of small molecules, antibodies and stable liposomes by increasing vessel permeability

[103–106]. Alternatively, its pumping effect can enhance the convective flow, and hence, extravasation of modified and unmodified viral particles, dextrans and NPs [102,107–109]. This effect could act to counteract the increased interstitial fluid pressure (IFP) in the tumours.

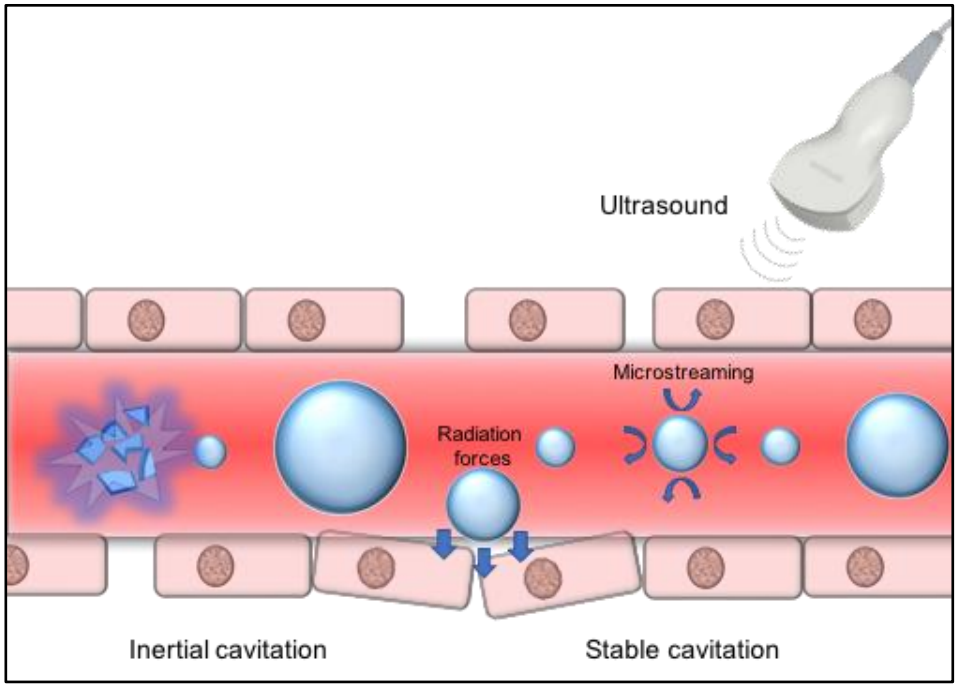

Figure 5 Mechanical effects of cavitation. Non-inertial cavitation can induce microstreaming, resulting in a local mixing effect, and generate radiation forces, which cause shear stress to the vessel walls and propels therapeutics into the tumour. Shear stress can also trigger the release of compounds encapsulated in co-administered nanocarriers. Inertial cavitation, which results in violent implosion of the bubble, can result in radiation forces, shock waves and micro-jets. Bubble fragments, if small enough, can enter the tumour tissue.

Recent developments in the field include NC - or antibody-MB hybrids, where NC or antibody is physically attached on the MB shell[110,111] and the construction of nano-sized cavitation agents, such as nanocups[112] (SonoTran®, Oxsonics) and nanodroplets[113], which have the benefit of being able to extravasate and therefore sustain their pumping effect within the tumour interstitium.

US can also trigger payload release via thermal or mechanical effects from US-labile liposomes[114], which is the focus of **Chapter 4** of this thesis. A two-stage approach could be envisaged, in which US is employed first to enhance penetration and then to rupture the liposomes within the tumour tissue. US-induced hyperthermia can trigger payload release from thermosensitive liposomes, as in the case of TARDOX[97].

Therapeutics can be entrapped in the thick shell of polymeric MBs, so the MB has a dual role both as a contrast agent and as a delivery system[111,115]. Poly(lactic acid) (PLA) MBs encapsulating paclitaxel or doxorubicin have been fabricated[116,117]. In response to US exposure the polymeric shell was shown to collapse. This design combines the ability of US to enhance the transport of particles with the *in situ* generation of 'nanoshards', acting analogously to traditional nanoparticles. **Chapter 6** of this thesis focuses on this approach.

1.3 Concept

The field of cancer metabolism has seen an explosion of interest over the past decade, exiting the era where cancer metabolism was synonymous with the 'Warburg effect' and starting to unveil its complex re-wiring. The lactate transporter MCT1 is important for maintaining glycolysis and supporting OXPHOS, which in summary qualifies it as an important player in metabolic flexibility that is the signature feature of cancer metabolism. Basal-like triple negative breast cancer (TNBC) is a subgroup of BC with dismal prognosis due to its aggressiveness and lack of specific molecular targets. However, according to recent research[29,41,118], MCT1 expression correlates not only with the basal-like phenotype, but also with the poor prognosis that accompanies it.

In this thesis, MCT1 is used as the mediator of an experimental treatment, rather than as the target of the therapeutic *per se*. Exploiting the quite low substrate specificity of the transporter, a 'Trojan horse' strategy was adopted, in which a therapeutic analogue of the natural substrates would be taken up selectively by the cells over-expressing MCT1.

This thesis starts with the investigation of a simple halogenated derivative of pyruvate, 3-bromopyruvate (3BP), which has been suggested to be taken up selectively by MCT1-expressing cells (**Chapter 3**). In this part, the relative sensitivity of two cell lines with markedly different level of MCT1 expression was assessed. Several intracellular targets of 3BP have been suggested especially in the glycolytic pathway. This led to the selection of untargeted metabolomics as an unbiased, high-throughput approach to elucidate the metabolic effects of 3BP.

3BP, although locally selective for MCT1 expressing cells, is a generic alkylating agent that could react with non-targeted proteins and, either be neutralised or cause toxicity. Picking up from **Chapter 3**, in **Chapter 4** a delivery strategy for the local release of 3BP in the tumour is developed. 3BP was enclosed in liposomes to protect it from degradation and protect healthy tissues from unwanted effects. To trigger local release of 3BP, ultrasound was selected as a non-invasive, easily adjustable and cost-effective extracorporeal stimulus.

In addition to targeted therapies, systemic treatment with radionuclides presents particular interest. Radiotherapy, along with surgery and chemotherapy, constitute one of the main pillars in cancer treatment. Radiotherapy is of particular importance in basal-like TNBC treatment, since it lacks specific molecular targets. The question asked in **Chapter 5** is whether MCT1 can transport a radio-iodinated lactate derivative intended for targeted radionuclide therapy (TRT).

To this end, the radio-iodinated compound (^{123}I-HPLA) was synthesised, purified and its selectivity for MCT1-expressing cells was assessed. This was followed up by a pilot *in vivo* study to explore the behaviour of ^{123}I-HPLA in mice. ^{123}I-HPLA was also shown to be appropriate for the same delivery strategy applied for 3BP, as it was successfully loaded in liposomes.

Finally, in **Chapter 6**, the first steps were taken towards the development of a novel delivery system, based on the same idea that was elaborated throughout the project. The ultimate goal was to take an 'all-in-one' approach. The current approach comprises a carrier (liposome), a cavitation agent (bubble) and a therapeutic lactate/pyruvate analogue. Coincidentally, lactic acid is the

building block for some of the most widely used polymers in drug delivery. Would it be possible to make an echogenic carrier with some of the 'bricks' in its structure being the therapeutic lactate/pyruvate analogue? If so, the result would be a micron-sized imaging agent and drug carrier, which would collapse into sub-micron fragments at the tumour site. These fragments may then become implanted and gradually degrade and release the therapeutic within the tumour. There are a lot of questions on the way to assessing the feasibility of this approach. To address the basic ones, commercially available, non-modified polymers were chosen. After making echogenic particles out of these polymers, the fundamental questions to assess were: First, does ultrasound break these particles into sufficiently small fragments and, second, can ultrasound treatment result in higher release of the monomer?

The rationale of this thesis is summarised in **Figure 6**.

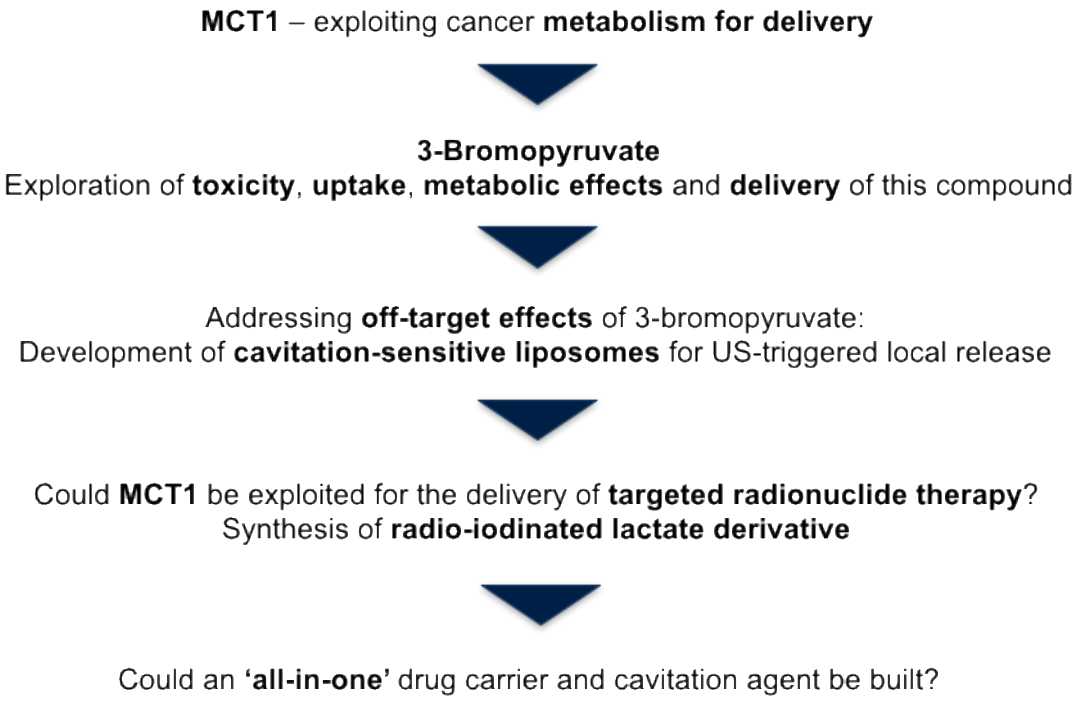

Figure 6 Diagrammatic presentation of the thesis concept

1.4 References

1. Hanahan, D. & Weinberg, R. A. Hallmarks of cancer: The next generation. *Cell* **144**, 646–674 (2011).
2. Warburg, O. On respiratory impairment in cancer cells. *Science (80-.).* **124**, 269–270 (1956).
3. Pinheiro, C. *et al.* Role of monocarboxylate transporters in human cancers: State of the art. *J. Bioenerg. Biomembr.* **44**, 127–139 (2012).
4. DeBerardinis, R. J. & Chandel, N. S. Fundamentals of cancer metabolism. *Sci. Adv.* **2**, e1600200 (2016).
5. Pavlova, N. N. & Thompson, C. B. The Emerging Hallmarks of Cancer Metabolism. *Cell Metab.* **23**, 27–47 (2016).
6. Chan, D. A. *et al.* Targeting GLUT1 and the Warburg effect in renal cell carcinoma by chemical synthetic lethality. *Sci. Transl. Med.* **3**, 94ra70 (2011).
7. Shibuya, K. *et al.* Targeting the facilitative glucose transporter GLUT1 inhibits the self-renewal and tumor-initiating capacity of cancer stem cells. *Oncotarget* **6**, 651–61 (2015).
8. İyikesici, M. S. *et al.* Efficacy of Metabolically Supported Chemotherapy Combined with Ketogenic Diet, Hyperthermia, and Hyperbaric Oxygen Therapy for Stage IV Triple-Negative Breast Cancer. *Cureus* **9**, e1445 (2017).
9. Poff, A. *et al.* Targeting the Warburg effect for cancer treatment: Ketogenic diets for management of glioma. *Semin. Cancer Biol.* **56**, 135–148 (2019).
10. Schwartz, K. A., Noel, M., Nikolai, M. & Chang, H. T. Investigating the Ketogenic Diet As Treatment for Primary Aggressive Brain Cancer: Challenges and Lessons Learned. *Front. Nutr.* **5**, 11 (2018).
11. Allen, B. G. *et al.* Ketogenic diets as an adjuvant cancer therapy: History and potential mechanism. *Redox Biol.* **2**, 963–970 (2014).
12. Bhutia, Y. D. & Ganapathy, V. Glutamine transporters in mammalian cells and their

functions in physiology and cancer. *Biochim. Biophys. Acta - Mol. Cell Res.* **1863**, 2531–2539 (2016).

13. Wise, D. R. & Thompson, C. B. Glutamine addiction: a new therapeutic target in cancer. *Trends Biochem. Sci.* **35**, 427–433 (2010).

14. Vanhove, K. *et al.* Glutamine Addiction and Therapeutic Strategies in Lung Cancer. *Int. J. Mol. Sci.* **20**, 252 (2019).

15. Halestrap, A. P. Monocarboxylic Acid Transport. *Compr. Physiol.* **3**, 1611–1643 (2013).

16. Halestrap, A. P. & Meredith, D. The SLC16 gene family—from monocarboxylate transporters (MCTs) to aromatic amino acid transporters and beyond. *Pflugers Arch -Eur J Physiol* **447**, 619–628 (2004).

17. Uhlen, M. *et al.* Tissue-based map of the human proteome. *Science (80-.).* **347**, 1260419–1260419 (2015).

18. Iwanaga, T. & Kishimoto, A. Cellular distributions of monocarboxylate transporters: a review. *Biomed. Res.* **36**, 279–301 (2015).

19. Halestrap, A. P. & Price, N. T. The proton-linked monocarboxylate transporter (MCT) family : structure, function and regulation. *Biochem. J* **343**, 281–299 (1999).

20. Garcia, C. K., Goldstein, J. L., Pathak, R. K., Anderson, R. G. W. & Brown, M. S. Molecular characterization of a membrane transporter for lactate, pyruvate, and other monocarboxylates: Implications for the Cori cycle. *Cell* **76**, 865–873 (1994).

21. Curry, J. M. *et al.* MCT1 and MCT4 are functional biomarkers of metabolic symbiosis in head and neck cancer Cancer metabolism , stemness and tumor recurrence. 1371–1384 (2013).

22. Sonveaux, P. *et al.* Targeting lactate-fueled respiration selectively kills hypoxic tumor cells in mice. *J. Clin. Invest.* (2008) doi:10.1172/JCI36843.however.

23. Fang, J. *et al.* The H+-Linked Monocarboxylate Transporter (MCT1 / SLC16A1): A

Potential Therapeutic Target for High-Risk Neuroblastoma. **70**, 2108–2115 (2006).

24. Miranda-Gonçalves, V. *et al.* Monocarboxylate transporters (MCTs) in gliomas: expression and exploitation as therapeutic targets. *Neuro. Oncol.* **15**, 172–88 (2013).

25. Beloueche-Babari, M. *et al.* MCT1 Inhibitor AZD3965 Increases Mitochondrial Metabolism, Facilitating Combination Therapy and Noninvasive Magnetic Resonance Spectroscopy. *Cancer Res.* **77**, 5913–5924 (2017).

26. Faubert, B. *et al.* Lactate Metabolism in Human Lung Tumors Human non-small cell lung cancer preferentially utilizes lactate over glucose to fuel TCA cycle and sustain tumor metabolism in vivo. Lactate Metabolism in Human Lung Tumors. *Cell* **171**, 358–371 (2017).

27. Hui, S. *et al.* Glucose feeds the TCA cycle via circulating lactate. *Nat. Publ. Gr.* **551**, (2017).

28. Latif, A. *et al.* Monocarboxylate Transporter 1 (MCT1) is an independent prognostic biomarker in endometrial cancer. doi:10.1186/s12907-017-0067-7.

29. Johnson, J. M. *et al.* MCT1 in Invasive Ductal Carcinoma: Monocarboxylate Metabolism and Aggressive Breast Cancer. *Front. Cell Dev. Biol.* **5**, 1–8 (2017).

30. Koukourakis, M. I., Giatromanolaki, A., Harris, A. L. & Sivridis, E. Comparison of metabolic pathways between cancer cells and stromal cells in colorectal carcinomas: a metabolic survival role for tumor-associated stroma. *Cancer Res.* **66**, 632–7 (2006).

31. Lambert, D., Wood, I., Ellis, A. & Shirazi-Beechey, S. Molecular changes in the expression of human colonic nutrient transporters during the transition from normality to malignancy. *Br. J. Cancer* **86**, 1262–1269 (2002).

32. Pinheiro, C. *et al.* Increased expression of monocarboxylate transporters 1, 2, and 4 in colorectal carcinomas. (2008) doi:10.1007/s00428-007-0558-5.

33. Pinheiro, C. *et al.* Expression of Monocarboxylate Transporters 1, 2, and 4 in Human Tumours and Their Association with CD147 and CD44. *J. Biomed. Biotechnol.* **2010**, (4276).

34. Diehl, K. *et al.* Nuclear factor E2-related factor-2 has a differential impact on MCT1 and

MCT4 lactate carrier expression in colonic epithelial cells: a condition favoring metabolic symbiosis between colorectal cancer and stromal cells. *Oncogene* **37**, 39–51 (2018).

35. Froberg, M. K. *et al.* Expression of monocarboxylate transporter MCT1 in normal and neoplastic human CNS tissues. *Neuroreport* **12**, 761–765 (2001).

36. Mathupala, S. P., Parajuli, P. & Sloan, A. E. Silencing of monocarboxylate transporters via small interfering ribonucleic acid inhibits glycolysis and induces cell death in malignant glioma: An in vitro study. *Neurosurgery* **55**, 1410–1419 (2004).

37. Martinho, O. *et al.* Monocarboxylate transporters (MCTs) in gliomas: expression and exploitation as therapeutic targets. **15**, 172–188 (2013).

38. Takada, T., Takata, K. & Ashihara, E. Inhibition of monocarboxylate transporter 1 suppresses the proliferation of glioblastoma stem cells. *J. Physiol. Sci.* **66**, 387–396 (2016).

39. Miranda-Gonçalves, V. *et al.* Monocarboxylate transporter 1 is a key player in glioma-endothelial cell crosstalk. *Mol. Carcinog.* **56**, 2630–2642 (2017).

40. Asada, K. *et al.* Reduced Expression of GNA1and Silencing of MCT1 in Human Breast Cancers. *Oncology* **64**, 380–388 (2003).

41. Pinheiro, C. *et al.* Monocarboxylate transporter 1 is up-regulated in basal-like breast carcinoma. *Histopathology* **56**, 860–7 (2010).

42. Morais-Santos, F. *et al.* Differential sensitivities to lactate transport inhibitors of breast cancer cell lines. *Endocr. Relat. Cancer* **21**, 27–38 (2014).

43. Chen, H. *et al.* Co-expression of CD147/EMMPRIN with monocarboxylate transporters and multiple drug resistance proteins is associated with epithelial ovarian cancer progression. doi:10.1007/s10585-010-9345-9.

44. Pinheiro, C. *et al.* Increasing expression of monocarboxylate transporters 1 and 4 along progression to invasive cervical carcinoma. *Int. J. Gynecol. Pathol.* **27**, 568–574 (2008).

45. Izumi, H. *et al.* Monocarboxylate transporters 1 and 4 are involved in the invasion activity

of human lung cancer cells. *Cancer Sci.* **102**, 1007–1013 (2011).

46. Hensley, C. T. *et al.* Metabolic Heterogeneity in Human Lung Tumors. *Cell* **164**, 681–694 (2016).

47. Koukourakis, M. I., Giatromanolaki, A., Bougioukas, G. & Sivridis, E. Lung cancer: An organized cellular and metabolic domain Lung Cancer A Comparative Study of Metabolism Related Protein Expression in Cancer Cells and Tumor Associated Stroma. *Cancer Biol. Ther.* **6**, 1476–1479 (2007).

48. Bonuccelli, G. *et al.* Role of mesenchymal stem cells in osteosarcoma and metabolic reprogramming of tumor cells. *Oncotarget* **5**, (2014).

49. Zhao, Z. *et al.* Downregulation of MCT1 inhibits tumor growth, metastasis and enhances chemotherapeutic efficacy in osteosarcoma through regulation of the NF-jB pathway. (2014) doi:10.1016/j.canlet.2013.08.042.

50. Kong, S. C. *et al.* Monocarboxylate Transporters MCT1 and MCT4 Regulate Migration and Invasion of Pancreatic Ductal Adenocarcinoma Cells. *Pancreas* **45**, 1036–1047 (2016).

51. Chapiro, J. *et al.* Systemic Delivery of Microencapsulated 3-Bromopyruvate for the Therapy of Pancreatic Cancer. *Clin Cancer Res. Clin Cancer Res* **20**, 6406–6417 (2014).

52. Hao, J. *et al.* Co-expression of CD147 (EMMPRIN), CD44v3-10, MDR1 and monocarboxylate transporters is associated with prostate cancer drug resistance and progression. *Br. J. Cancer* **103**, 1008–1018 (2010).

53. Pinheiro, C. *et al.* The prognostic value of CD147/EMMPRIN is associated with monocarboxylate transporter 1 co-expression in gastric cancer. (2009) doi:10.1016/j.ejca.2009.06.018.

54. Xian, S.-L., Cao, W., Zhang, X.-D. & Lu, Y.-F. Inhibitory effects of 3-bromopyruvate on human gastric cancer implant tumors in nude mice. *Asian Pac. J. Cancer Prev.* **15**, 3175–8 (2014).

55. Lopes-Coelho, F. *et al.* Monocarboxylate transporter 1 (MCT1), a tool to stratify acute myeloid leukemia (AML) patients and a vehicle to kill cancer cells. *Oncotarget* **8**, 82803–82823 (2017).

56. Kennedy, K. M. *et al.* Catabolism of Exogenous Lactate Reveals It as a Legitimate Metabolic Substrate in Breast Cancer. *PLoS One* **8**, (2013).

57. Miranda-Gonçalves, V. *et al.* Hypoxia-mediated upregulation of MCT1 expression supports the glycolytic phenotype of glioblastomas. *Oncotarget* **7**, (2016).

58. Murray, C. M. *et al.* Monocarboxylate transporter MCT1 is a target for immunosuppression. doi:10.1038/nchembio744.

59. Ovens, M. J., Davies, A. J., Wilson, M. C., Murray, C. M. & Halestrap, A. P. AR-C155858 is a potent inhibitor of monocarboxylate transporters MCT1 and MCT2 that binds to an intracellular site involving transmembrane helices 7-10. *Biochem. J.* **425**, 523–30 (2010).

60. Minchinton, A. I. & Tannock, I. F. Drug penetration in solid tumours. *Nat. Rev. Cancer* **6**, 583–592 (2006).

61. Jain, R. K. Delivery of molecular medicine to solid tumors. *Science* **271**, 1079–1080 (1996).

62. Bae, Y. H. & Park, K. Targeted drug delivery to tumors: myths, reality and possibility. *J. Control. Release* **153**, 198–205 (2011).

63. Di, L. Strategic approaches to optimizing peptide ADME properties. *AAPS J.* **17**, 134–43 (2015).

64. Torchilin, V. P. Drug targeting. *Eur. J. Pharm. Sci.* **11 Suppl 2**, S81–S91 (2000).

65. Matsumura, Y. & Maeda2, H. A New Concept for Macromolecular Therapeutics in Cancer Chemotherapy: Mechanism of Tumoritropic Accumulation of Proteins and the Antitumor Agent Smancs1. *CANCER Res.* **46**, 6387–6392 (1986).

66. Sriraman, S. K., Aryasomayajula, B. & Torchilin, V. P. Barriers to drug delivery in solid tumors. *Tissue barriers* **2**, e29528 (2014).

67. Stylianopoulos, T., Munn, L. L. & Jain, R. K. Reengineering the Tumor Vasculature: Improving Drug Delivery and Efficacy. *Spec. Issue Phys. Sci. Oncol. Proc. Natl. Acad. Sci. U. S. A* **10**, 19059–19064 (2018).

68. Jain, R. K. & Stylianopoulos, T. Delivering nanomedicine to solid tumors. *Nat. Rev. Clin. Oncol.* **7**, 653–64 (2010).

69. Hobbs, S. K. *et al.* Regulation of transport pathways in tumor vessels: role of tumor type and microenvironment. *Proc. Natl. Acad. Sci. U. S. A.* **95**, 4607–12 (1998).

70. Wilhelm, S. *et al.* Analysis of nanoparticle delivery to tumours. *Nat. Rev. Mater.* **1**, 16014 (2016).

71. Wittrup, D. The Koch Institute Galleries: Poor Antibody Distribution in a Tumor. https://ki-galleries.mit.edu/2011/wittrup-2.

72. Carlisle, R. & Coussios, C.-C. Mechanical approaches to oncological drug delivery. *Ther. Deliv.* **4**, 1213–5 (2013).

73. Stylianopoulos, T., Munn, L. L. & Jain, R. K. Reengineering the Tumor Vasculature: Improving Drug Delivery and Efficacy. *TRENDS in CANCER* **4**, 258–259 (2018).

74. Levacheva, I. *et al.* Optimized thermosensitive liposomes for selective doxorubicin delivery: Formulation development, quality analysis and bioactivity proof. *Colloids Surfaces B Biointerfaces* **121**, 248–256 (2014).

75. Spring, B. Q. *et al.* A photoactivable multi-inhibitor nanoliposome for tumour control and simultaneous inhibition of treatment escape pathways. *Nat. Nanotechnol.* **11**, 378–387 (2016).

76. Ranjan, A. *et al.* Image-guided drug delivery with magnetic resonance guided high intensity focused ultrasound and temperature sensitive liposomes in a rabbit Vx2 tumor model. *J. Control. Release* **158**, 487–94 (2012).

77. Nahire, R. *et al.* Ultrasound enhanced matrix metalloproteinase-9 triggered release of contents from echogenic liposomes. *Mol. Pharm.* **9**, 2554–64 (2012).

78. Sedlacek, O. *et al.* Multistage-targeted pH-responsive polymer conjugate of Auger electron emitter: Optimized design and in vivo activity. *Eur. J. Pharm. Sci.* **63**, 216–225 (2014).

79. Rodzinski, A. *et al.* Targeted and controlled anticancer drug delivery and release with magnetoelectric nanoparticles. *Sci. Rep.* **6**, 20867 (2016).

80. Tang, Z. *et al.* Redox-responsive star-shaped magnetic micelles with active-targeted and magnetic-guided functions for cancer therapy. *Acta Biomater.* **42**, 232–246 (2016).

81. Mura, S., Nicolas, J. & Couvreur, P. Stimuli-responsive nanocarriers for drug delivery. *Nat. Publ. Gr.* **12**, (2013).

82. Torchilin, V. P. Multifunctional, stimuli-sensitive nanoparticulate systems for drug delivery. *Nat. Rev. Drug Discov.* **13**, 813–827 (2014).

83. Mahmoudi, M., Sant, S., Wang, B., Laurent, S. & Sen, T. Superparamagnetic iron oxide nanoparticles (SPIONs): Development, surface modification and applications in chemotherapy. *Adv. Drug Deliv. Rev.* **63**, 24–46 (2011).

84. Chiang, C.-S. *et al.* Combination of fucoidan-based magnetic nanoparticles and immunomodulators enhances tumour-localized immunotherapy. *Nat. Nanotechnol.* 1 (2018) doi:10.1038/s41565-018-0146-7.

85. Dowaidar, M. *et al.* Magnetic Nanoparticle Assisted Self-assembly of Cell Penetrating Peptides-Oligonucleotides Complexes for Gene Delivery. *Sci. Rep.* **7**, 9159 (2017).

86. Nagesh, P. K. B. *et al.* PSMA targeted docetaxel-loaded superparamagnetic iron oxide nanoparticles for prostate cancer. *Colloids Surf. B. Biointerfaces* **144**, 8–20 (2016).

87. Owen, J. *et al.* A versatile method for the preparation of particle-loaded microbubbles for multimodality imaging and targeted drug delivery. *Drug Deliv. Transl. Res.* **8**, 342–356 (2018).

88. Oliveira, R. R. *et al.* Triggered release of paclitaxel from magnetic solid lipid nanoparticles by magnetic hyperthermia. *Mater. Sci. Eng. C* **92**, 547–553 (2018).

89. Li, Q. *et al.* A photosensitive liposome with NIR light triggered doxorubicin release as a

combined photodynamic-chemo therapy system. *J. Control. Release* **277**, 114–125 (2018).

90. Lu, J., Choi, E., Tamanoi, F. & Zink, J. I. Light-activated nanoimpeller-controlled drug release in cancer cells. *Small* **4**, 421–6 (2008).

91. Liu, L. *et al.* Light-triggered release of drug conjugates for an efficient combination of chemotherapy and photodynamic therapy. *Biomater. Sci.* **6**, 997–1001 (2018).

92. Kamkaew, A. *et al.* Cerenkov Radiation Induced Photodynamic Therapy Using Chlorin e6-Loaded Hollow Mesoporous Silica Nanoparticles. *ACS Appl. Mater. Interfaces* **8**, 26630–26637 (2016).

93. Shaffer, T. M., Pratt, E. C. & Grimm, J. Utilizing the power of Cerenkov light with nanotechnology. *Nat. Nanotechnol.* **12**, 106–117 (2017).

94. Kotagiri, N. *et al.* Radionuclides transform chemotherapeutics into phototherapeutics for precise treatment of disseminated cancer. *Nat. Commun.* **9**, 275 (2018).

95. Yatvin B., M., Weinstein N., J., Dennnis H., W. & Blumenthal, R. Design of liposomes for enhanced local release of drugs by hyperthermia. *Science (80-.).* **202**, (1978).

96. Saga, T. *et al.* Enhancement of the therapeutic outcome of radio-immunotherapy by combination with whole-body mild hyperthermia. *Eur. J. Cancer* **37**, 1429–1434 (2001).

97. Lyon, P. C. *et al.* Safety and feasibility of ultrasound-triggered targeted drug delivery of doxorubicin from thermosensitive liposomes in liver tumours (TARDOX): a single-centre, open-label, phase 1 trial. *Lancet Oncol.* (2018) doi:10.1016/S1470-2045(18)30332-2.

98. Zagar, T. M. *et al.* Two phase I dose-escalation/pharmacokinetics studies of low temperature liposomal doxorubicin (LTLD) and mild local hyperthermia in heavily pretreated patients with local regionally recurrent breast cancer. *Int. J. Hyperth.* **30**, 285–294 (2014).

99. Boissenot, T., Bordat, A., Fattal, E. & Tsapis, N. Ultrasound-triggered drug delivery for cancer treatment using drug delivery systems: From theoretical considerations to practical

applications. *J. Control. Release* **241**, 144–163 (2016).

100. Poon, R. T. & Borys, N. Lyso-thermosensitive liposomal doxorubicin: a novel approach to enhance efficacy of thermal ablation of liver cancer. *Expert Opin. Pharmacother* **10**, 333–343 (2009).

101. Browning, R. J., Rajkumar, V., Pedley, R. B., Eckersley, R. J. & Blower, P. J. Prospects for enhancement of targeted radionuclide therapy of cancer using ultrasound. *J. Label. Compd. Radiopharm.* **57**, 279–284 (2014).

102. Paris, J. L. *et al.* Ultrasound-mediated cavitation-enhanced extravasation of mesoporous silica nanoparticles for controlled-release drug delivery. *Chem. Eng. J.* **340**, 2–8 (2018).

103. Park, M. J. *et al.* Pulsed High-Intensity Focused Ultrasound Therapy Enhances Targeted Delivery of Cetuximab to Colon Cancer Xenograft Model in Mice. *Ultrasound Med. Biol.* **39**, 292–299 (2013).

104. Larkin, J. O. *et al.* Effective Tumor Treatment Using Optimized Ultrasound-Mediated Delivery of Bleomycin. *Ultrasound Med. Biol.* **34**, 406–413 (2008).

105. Khaibullina, A. *et al.* Pulsed high-intensity focused ultrasound enhances uptake of radiolabeled monoclonal antibody to human epidermoid tumor in nude mice. *J. Nucl. Med.* **49**, 295–302 (2008).

106. Frenkel, V. *et al.* Delivery of Liposomal Doxorubicin (Doxil) in a Breast Cancer Tumor Model: Investigation of Potential Enhancement by Pulsed-High Intensity Focused Ultrasound Exposure. *Acad. Radiol.* **13**, 469–479 (2006).

107. Carlisle, R. *et al.* Enhanced tumor Uptake and Penetration of Virotherapy Using Polymer Stealthing and Focused Ultrasound. (2013) doi:10.1093/jnci/djt305.

108. Arvanitis, C. D., Bazan-Peregrino, M., Rifai, B., Seymour, L. W. & Coussios, C. C. Cavitation-Enhanced Extravasation for Drug Delivery. *Ultrasound Med. Biol.* **37**, 1838–1852 (2011).

109. Bhatnagar, S., Schiffter, H. & Coussios, C. C. Exploitation of acoustic cavitation-induced microstreaming to enhance molecular transport. *Journal of Pharmaceutical Sciences* vol. 103 1903–1912 (2014).

110. Yu, F. T. H., Chen, X., Wang, J., Qin, B. & Villanueva, F. S. Low Intensity Ultrasound Mediated Liposomal Doxorubicin Delivery Using Polymer Microbubbles. *Mol. Pharm.* **13**, 55–64 (2016).

111. Sirsi, S. R. & Borden, M. A. State-of-the-art materials for ultrasound-triggered drug delivery. *Adv. Drug Deliv. Rev.* **72**, 3–14 (2014).

112. Kwan, J. J. *et al.* Ultrasound-Propelled Nanocups for Drug Delivery. *Small* **11**, 5305–5314 (2015).

113. Lee, J. Y. *et al.* Nanoparticle-Loaded Protein-Polymer Nanodroplets for Improved Stability and Conversion Efficiency in Ultrasound Imaging and Drug Delivery. *Adv. Mater.* **27**, 5484–5492 (2015).

114. Graham, S. M. *et al.* Inertial cavitation to non-invasively trigger and monitor intratumoral release of drug from intravenously delivered liposomes. *J. Control. Release* **178**, 101–107 (2014).

115. Sirsi, S. & Borden, M. Microbubble Compositions, Properties and Biomedical Applications. *Bubble Sci Eng Technol.* **1**, 3–17 (2010).

116. Cochran, M. C., Eisenbrey, J., Ouma, R. O., Soulen, M. & Wheatley, M. A. Doxorubicin and paclitaxel loaded microbubbles for ultrasound triggered drug delivery. *Int. J. Pharm.* **414**, 161–170 (2011).

117. Eisenbrey, J. R. *et al.* Development and optimization of a doxorubicin loaded poly(lactic acid) contrast agent for ultrasound directed drug delivery. *J. Control. Release* **143**, 38–44 (2010).

118. Li, Z. *et al.* Monocarboxylate transporters in breast cancer and adipose tissue are novel

biomarkers and potential therapeutic targets. *Biochem. Biophys. Res. Commun.* **501**, 962–967 (2018).

2 Materials and Methods

This chapter outlines the materials and experimental methods employed throughout the thesis. Materials and methods that are specific to a particular chapter are described in their corresponding results chapter.

2.1 *In vitro* studies

2.1.1 Cell culture

MCT1-high/MCT4-low BT20 cells and MCT1-low/MCT4-high MDA-MB-231 cells were purchased from the American Type Culture Collection (ATCC) and cultured in Dulbecco's Modified Eagle Medium (DMEM) supplemented with 10% Fetal Bovine Serum (FBS) and 1% penicillin/streptomycin/L-glutamine. Cell lines were maintained at 37°C in a humidified, 5% CO_2 atmosphere (HeraCell™ 150 incubator, Thermo Fisher Scientific, Waltham, USA). BT20 cells were seeded in a T25 flask following recovery from a frozen stock aliquot, then maintained in T75 or T175 flasks as needed. MDA-MB-231 cells were seeded directly in T75 or T175 flasks directly following recovery from frozen stocks. For sub-culture, cells were treated with trypsin 0.05% solution, 3-4 min for MDA-MB-231 and 8-10 min for BT20, and plated at a dilution 1:2-1:4 for BT20 cells and 1:8-1:10 for MDA-MB-231 cells. Cells were checked for mycoplasma on a monthly basis and used at passage number 25 or lower, counting from the original ATCC stock. Subsequent frozen stock vials were prepared with complete DMEM containing approximately $4x10^6$ cells further supplemented with 10% v/v dimethyl sulfoxide (DMSO) and 40% FBS (final concentration 50% v/v in freezing media) in 1.5 mL cryovials. The vials were transferred into a freezing container (Mr Frosty™, Thermo Fisher Scientific, Waltham, USA) and kept at -80°C for 1-2 days, then maintained in liquid nitrogen until needed. While in use, MDA-MB-231 cells were

authenticated by ATCC (Reference STRA4990). BT20 cells we purchased for this project twice from ATCC.

2.1.2 Measurement of protein content in cell lysates

Measurement of protein content was required for Western blot analysis and for across sample normalisation (e.g. CPM/μg protein for radioactivity uptake). Protein was measured by Pierce ™ BCA assay (Thermo Fisher, MA, USA) as per manufacturer's instructions. Briefly, 10 μL of known concentrations of bovine serum albumin (BSA) and lysates (neat and diluted) were prepared in a transparent 96-well plate. A freshly prepared BCA working solution was added (100 μL per well) and the plate was incubated for 40 min at 37°C and subsequently read at 562 nm using a plate reader (Infinite 200 Pro, Tecan, Switzerland).

2.1.3 Western blot analysis

Cells were dissociated from the culture flask with trypsin as described in section 2.1.1, pelleted with centrifugation at 1200 rpm for 5 min at room temperature (Megafuge 40R centrifuge with TX-1000 swing-bucket rotor, Thermo Fisher Scientific, MA, USA), washed with cold phosphate-buffered saline (PBS) solution and lysed with RadioImmunoprecipitation Assay (RIPA) lysis buffer supplemented with protease inhibitor cocktail (10 μg/mL leupeptin, 2 μg/mL pepstatin, 50 μg/mL antipain, 2 μg/mL aprotinin, 20 μg/mL chyprostatin, 2 μg/mL benzamidine, 1 mM phenylmethanesulfonyl fluoride) as per manufacturer's instructions (Thermo Fisher Scientific, MA, USA). When 6-well or smaller plates were used for treatment, cells were washed with PBS and lysed directly in the plate without the dissociation step. Insoluble membrane impurities were removed by centrifugation (14,000 rpm for 10 min, 4°C using an Eppendorf 5417R centrifuge equipped with a F54-30-17 fixed angle rotor).

Protein content in the lysates was determined by BCA assay (Thermo Fisher Scientific, MA, USA). Samples were prepared in lithium dodecyl sulfate (LDS) loading buffer supplemented with sample reducing agent (NuPAGE™, Thermo Fisher Scientific, Waltham, USA) and heated at 70°C for 10 min.

For Western blot analysis of MCT1 and MCT4, 10-30 μg of extracted protein was loaded per well (total volume up to 25 μL) and proteins were separated on 4-12% Bis-Tris gels and MOPS running buffer supplemented with antioxidant to maintain the reduced state of the proteins (NuPAGE™, Thermo Fisher Scientific, Waltham, USA). Gel was run at 120 V for 70 min using a XCell SureLockTM Mini-cell system (Thermo Fisher Scientific, UK) at room temperature.

Protein transfer was performed using an XCell IITM blot module (Thermo Fisher Scientific, UK) on ice. Transfer buffer was prepared by diluting NuPAGE transfer buffer (Thermo Fisher Scientific, Waltham, USA) 1:20 in 20% v/v methanol in MilliQ water. A pair of blotting pads, a pair of filter papers (2.5 mm thickness, Invitrogen, USA) and membrane were pre-soaked in transfer buffer and then secured into a transfer cassette. The cassette was then placed into the transfer module, which was pre-filled with transfer buffer. Transfer was performed at 100 V for 60 min on ice.

The membrane was blocked for 1 h at room temperature with 5% w/v dry, non-fat milk reconstituted in PBS-Tween 20 0.05% v/v solution. The membrane was briefly rinsed with PBS (1-2 min). Membranes were probed with MCT1 (sc-365501, 1:200 dilution, Santa Cruz Biotechnology, CA, USA) or MCT4 (sc-50329, 1:500 dilution, Santa Cruz Biotechnology, CA, USA) antibody in 0.5% w/v milk in PBS (4°C, overnight incubation). Rabbit anti-mouse IgG (61-6520, Invitrogen, Waltham, USA) and goat anti-rabbit IgG (32460, Invitrogen, Waltham, USA) conjugated with horseradish peroxidase (HRP) were used as secondary antibodies at dilution 1:2000. Bands were visualised using Pierce ECL (Thermo Fisher Scientific, MA, USA) or WesternSure PREMIUM (LI-COR Biosciences, Nebraska, USA) chemiluminescent substrates

with X-ray film development (Fuji medical film and Optimax 2010 processor) or a digital scanner (C-Digit Blot Scanner, LI-COR Biosciences, Nebraska, USA).

β-Actin was used as a loading control for all Western blots (ab8227, Abcam, Cambridge, UK, 1:1000 dilution). Probing for β-αctin was performed on the same membrane used for MCT1/MCT4 detection. After visualisation of the MCT1/MCT4 signal, the membrane was rinsed with PBS and then incubated in neat Restore™ buffer (21059, Thermo Fisher Scientific, MA, USA) for 15 min at room temperature for stripping. The aforementioned steps from membrane blocking onwards were repeated for β-actin detection.

2.1.4 Metabolic activity assay

A colorimetric assay measuring metabolic activity, MTT, was employed to assess cell viability. MTT is based on the conversion of 3-(4,5-dimethylthiazol-2-yl)-2,5-diphenyltetrazolium bromide to insoluble, purple coloured formazan crystals by NAD(P)H-dependent cellular oxidoreductase enzymes. When comparing between cells treated under the same conditions, the colour intensity can be related to the number of viable (metabolising) cells.

Cells were seeded at appropriate density depending on the dish or plate used, e.g. $2x10^5$ cells per well in a 12-well plate or 35 mm diameter Ibidi μ-dish, and allowed to adhere overnight. This assay was employed to assess cell viability after treatment with 3BP, liposomes and/or SonoVue microbubbles (MBs) and/or ultrasound. For all studies, treatment was performed on the day after seeding. After treatment, the media was replaced with fresh serum-free media supplemented with MTT reagent (thiazolyl blue tetrazolium bromide, 0.5 mg/mL). Following 45 min incubation at 37°C, MTT medium was removed and the purple formazan crystals which had formed were dissolved with DMSO and mixed by pipetting. Samples were transferred into flat transparent 96-well plates and absorbance at 540 nm (with reference at 630 nm) was quantified using a plate reader (Infinite 200 Pro, TECAN, Switzerland). The viability of treated cells was compared to that of

control cells and expressed as % metabolic activity mean value of four replicates. Control cells were untreated, unless otherwise stated.

2.1.5 MCT1 siRNA knockdown

Cells were seeded at $4x10^5$ cells/well (approximately 80% confluency for BT20 cells) in 6-well plates. All transfection reagents were purchased from Santa Cruz Biotechnology, CA, USA. The cells were incubated overnight and transfected with siRNA against MCT1 (sc-37235) or control sequence (sc-37007) at a concentration of 100 nM. For transfection, siRNA solution was mixed with transfection reagent solution (sc-29528) in serum-free transfection medium (sc-36868), followed by 40 min incubation at room temperature. The mix was then diluted to the final siRNA concentration and 1 mL was added to each well. After 6 hours incubation, 1 mL of 20% FBS containing DMEM was added to each well. The transfection medium was replaced the following day and the transfected cells were used for experiments. Transfection efficiency was assessed by Western blot analysis, as described in **section 2.1.3**.

2.1.6 Statistical analysis

Processing of raw data was performed using Microsoft Excel (Microsoft, WA, USA) and then imported to Prism 7 (GraphPad Software, USA) for statistical analysis and graph plotting. Data were obtained at a minimum of three replicates, unless otherwise stated. Data were plotted using means and error bars representing the standard deviation. For the assessment of statistical significance, the α value was set at 0.05 and the data analysed by the Holm-Sidak method. Statistically significant results are indicated with asterisk symbols (*) where: * $P<0.05$, ** $P<0.001$, *** $P<0.0001$, and **** $P<0.0001$, while non-significant results are not indicated on the graph.

2.2 *In vivo* studies

2.2.1 Tumour model

Animal procedures were carried out in accordance with the UK Animals (Scientific Procedures) Act 1986 and with local ethical committee approval (Project Licence number P13B66CD9 issued by the Home Office). Female athymic nude mice (9-10 weeks old, 25-30 g) were purchased from Charles River, UK. All animals were housed under a 12 h light/dark cycle and supplied with food and water *ad libitum*. Mice were checked daily for health and behavioural changes throughout the experiments.

BT20 cells were used as the MCT1-positive cell line throughout the thesis, however this cell line has only infrequently been used to generate xenografts in mice due to their slow doubling time and recovery from frozen stocks. Therefore, pilot studies for the investigation of tumour growth and vascularity were conducted following both subcutaneous and mammary fat pad inoculation.

For subcutaneous injection, 5 x 10^6 cells were suspended in 200 μL 1:1 serum-free DMEM: Matrigel and injected into the right dorsal flank of female athymic nude mice. After inoculation, tumours were measured at least weekly using callipers and the mice were weighed to confirm no weight loss was occurring due to the procedure.

Orthotopic models (i.e. transplanted in the organ of origin) better recapitulate the clinical disease and are more suitable for testing the uptake and efficacy of experimental agents. The microenvironment of the organ of origin induces tumour behaviour and metabolism more similar to that of the original tumour. For orthotopic inoculation, 5 x 10^6 cells were suspended in 100 μL serum-free DMEM and injected subcutaneously into the mammary fat pad of female athymic nude mice using an insulin syringe. The animals were monitored closely for unusual behaviour or signs of distress because mammary fat pad tumours are more likely to metastasize to the lung. Although BT20 xenografts are not known to metastasize, *post mortem* histological analysis of the lungs was planned (tumours were still growing at the time of writing).

2.2.2 Contrast-enhanced imaging for the assessment of tumour vascularity

Contrast enhanced US was performed using a Vevo3100 scanner (FUJIFILM Visualsonics, Joop 266 Geesinkweg 140, 1114 AB Amsterdam, Netherlandsusing) with a MX250 probe (Centre Transmit 267 Frequency: 20 MHz, Axial Resolution: 75 μm). SonoVue (SV) (0.25 mg/mL lipid content, 50 μL, Bracco, Milano, Italy) was administered intravenously under anaesthesia. Imaging was acquired in Non-Linear Contrast mode. Vevo LAB software (VisualSonics, Fujifilm, Tokyo, Japan) was used to trace regions of interest within the tumour and quantify contrast intensity as a function of time.

3 Perturbation of metabolism of breast cancer cells by 3-bromopyruvate

3.1 Abstract

Since its introduction as an experimental agent for cancer treatment, less than 20 years ago, 3-bromopyruvate (3BP) has attracted immense research focus and lately, also significant controversy. Several publications have investigated its toxic effects in different cancers, while others have explored its molecular targets by biochemical assays. Looking at these studies as a whole, it seems that 3BP has a broad spectrum of effects, which could be more efficiently investigated with a holistic approach, such as metabolomics. To date, a metabolomics analysis on breast cancer cells treated with 3BP has not been carried out.

Due to its chemical structure, the compound has been hypothesized to enter the cells by hijacking the transport system for monocarboxylates, such as lactate and pyruvate. Evidence that 3BP is transported through the monocarboxylate transporter 1 (MCT1) has only been provided by a single, yet thorough, publication[1].

In this chapter, initial experiments showed that MCT1 expression provides sensitivity to 3BP treatment in triple negative breast cancer (TNBC) cell lines. Subsequently the metabolic effects of 3BP and their correlation with MCT1 expression by metabolomics and metabolic flux analysis, was explored. The data obtained provide compelling evidence that this is a powerful and selective small molecule that is worthy of further investigation for the treatment of TNBC, especially in combination with a 'smart' delivery system that will better target its effects.

3.2 Introduction

3.2.1 Triple negative breast cancer (TNBC)

Breast cancer (BC) is the most common cancer and the second most common cause of cancer-related mortality in women[2]. BC is a highly heterogeneous disease. Clinically, immunohistochemical classification of breast carcinomas is based on the presence or absence of oestrogen receptors (ER), progesterone receptors (PR), and human epidermal growth factor receptor-2 (HER2). While most breast carcinomas are ER-positive, around 10-20% of cases lack expression of all of these molecular targets and are classified as triple negative breast cancers (TNBC). Gene expression profiling has further categorised breast cancer into five molecular subtypes[3]. These are luminal A, luminal B, HER-2/neu over-expressing, basal-like and normal-like. Of those, basal-like lacks hormone and HER2/neu receptors and constitutes 80% of TNBC[4–6]. Basal-like phenotype is more common in younger (<50 years) and African-American women and those with *BRCA1* mutation, but the reasons for these correlations remain unclear[4,5]. It is important to note, however, that TNBC is a heterogeneous disease by itself. TNBC tumours can be molecular-apocrine, HER2-enriched or claudin-low molecular subtypes, while luminal A and B are much less common in the TNBC group[7,8].

The overall survival of breast cancer patients keeps increasing, which can be attributed to early detection and improved adjuvant therapy with targeted agents[9]. However, the management of TNBC remains challenging due to the aggressive behaviour of these tumours and the lack of molecular targets, which limits the therapeutic options. Cytotoxic chemotherapy is currently the only systemic therapeutic option for TNBC patients[4]. Therefore, the development of targeted therapeutic agents for these tumours is urgently needed.

Triple-negative tumours tend to exhibit high metabolic activity and share features with other tumours of similarly high metabolic activity. These features include high histologic grade, necrosis, frequent mitosis, aggressive behaviour and poor prognosis[7]. Kim and colleagues looked at the

metabolic profiles within a TNBC cohort of 132 patients and identified the 'Warburg type', in which malignant cells are predominantly glycolytic and stromal cells oxidative, as the most frequent metabolic phenotype. In contrast, the least frequent was the 'Reverse Warburg type', while no significant correlation was found between the molecular and the metabolic phenotypes[7]. Recent metabolomics analysis of TNBC tumours found certain unique metabolic traits in this heterogeneous BC subtype. Specifically, choline levels were found to be higher in TNBC as compared to $ER^+/PR^+/HER2^+$ tumours, which the authors related to the high proliferation rate of these tumours[10]. From a therapeutic point of view, it is interesting that TNBC tumours presented with lower concentration of glutamine and higher glutamate, which points towards a higher glutaminolysis rate. 'Glutamine addiction' is a metabolic trait of other aggressive tumours and has been suggested as a metabolic target in cancer[10]. Further, more recent work[11] has revealed glutamine dependence specifically in TNBC breast cancer cell lines *in vitro* and *in vivo*, with survival dependence on the ASCT2 transporter, which is responsible for the uptake of neutral amino-acids including glutamine.

Pinheiro *et al.*[12] were the first to show a correlation between high MCT1 expression and basal-like breast carcinoma, which constitutes the majority of TNBC cases. Shortly after, they also reported high expression of MCT1, but not MCT4, in GLUT1 and CAIX positive human breast carcinomas. As GLUT1 and CAIX are involved in glucose uptake and pH regulation respectively,this points towards an important role of MCT1 in glycolytic tumours[13]. A thorough study by Sun Hong and colleagues correlated MCT1 expression with high ^{18}F-fluorodeoxyglucose (FDG) uptake in breast cancer cell, implicating that MCT1 is involved in glycolytic metabolism. They also demonstrated that in BC cell lines that express MCT1 and 4, MCT1 determines pyruvate but not lactate export[14]. More recently, Johnson and colleagues[15] independently showed higher MCT1 expression in TNBC as compared to other immunohistological types of BC, and went on to show a correlation between high MCT1 expression and poor clinical outcomes. These authors

associated MCT1 expression with oxidative metabolism[15], which is in contrast with the results by Kim *at al.*[7] ,Pinheiro *et al.*[12] and Sun Hong *et al.*[14]. The same group has found that breast tumours in general tend to have high expression of TIGAR, which dampens glycolysis and promotes oxidative catabolism of lactate and glutamine[16]. Finally, a recent study by Li *et al.*, also correlated high MCT1 expression in breast tumours with poor prognosis (short progression-free survival), ER^- status and high proliferation (high Ki67 expression). The researchers concluded that the combination of high MCT1 expression in cancer cells and high MCT4 expression in cancer-associated adipocytes, the main stromal cell in breast cancer, constitutes an independent risk factor for poor prognosis[17]. Literature on MCT1 is ambiguous as it has been associated both with high oxidative/mitochondrial metabolism and with glycolytic/Warburg phenotype. It is likely that the metabolism depends on other factors related to the cancer cell itself – e.g. expression of other MCT isoforms – and related to the tumour as a whole e.g. metabolism of stromal cells, nutrient and oxygen availability. Arguments aside, MCT1 is undeniably recognised as a promising target for cancer therapy in particular in TNBC, where the lack of other molecular targets makes it even more attractive.

3.2.2 Using 3-bromopyruvate for cancer treatment

Given the important roles of MCTs in several solid tumours, therapeutic strategies exploiting these transporters, MCT1 isoform in particular, have started to emerge. MCT1 can be targeted by inhibitors, such as α-cyano-4-hydroxycinnamate (CHC), lonidamine and AZD3965, a potent MCT1/2 inhibitor designed by AstraZeneca. Lonidamine entered clinical trials for advanced breast cancers as a combination with epirubicin but unfortunately showed no added benefit. It has also been tested for symptomatic benign prostate hyperplasia in a phase III clinical trial in Germany[18,19]. AZD3965 is currently in phase II clinical trials for several advanced cancers[20,21].

Alternatively, MCT1 can act as a mediator of a therapeutic response, rather than being the target *per se*, in a 'Trojan horse'-like approach. The metabolism of cancer cells could be better described as a network with multiple qualitative and quantitative alterations compared to the metabolism of healthy counterparts. Consequently, a multi-targeted therapeutic strategy able to address the complexity of the metabolic alterations of cancer cells is needed. One of the most promising investigational therapeutics with such a pleiotripic action is 3BP, a brominated derivative of pyruvate. It has been hypothesized that 3BP would be taken up by MCT1 thanks to its structural similarity to the physiological substrates of the transporter, and robust evidence for the MCT1-mediated transport of 3BP was provided by Birsoy *et al.*[1].

Unlike other 'Trojan horses', e.g. 2-deoxy-glucose (2DG), which act as antimetabolites, 3BP acts mostly as a broad spectrum alkylating agent via S_N2 mechanism[22]. It binds covalently to its targets and irreversibly modifies them[22]. As this simple mechanism of action (**Figure 7**) suggests, 3BP has been shown to act on multiple targets, within the glycolytic and other pathways. Thanks to this known multifaceted reactivity toward nucleophiles[23], mainly thiols, 3BP has been used by biochemists for decades in enzymatic studies[24–26].

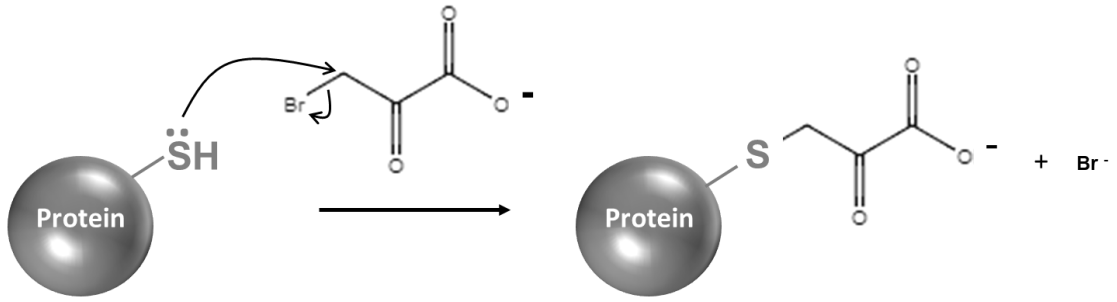

Figure 7 Mechanism of action of 3-bromopyruvate (3BP). 3BP reacts with nucleophiles, mainly thions (-SH) found on protein and peptides, resulting in their 'pyruvylation'.

Its potential as a cancer therapeutic only started to be investigated in 2001 by Ko *et al.*[27] who reported promising results of 3BP in the treatment of liver cancer. Since then, the interest in 3BP

has rapidly increased, as shown by the number of publications per year (**Figure 8**). Confirmed targets include glyceraldehyde-3-phosphate dehydrogenase (GAPDH)[28] and mitochondrially bound hexokinase II (HK-2)[29]. 3BP has also been shown to affect the redox homeostasis of the cells not only because of its enzymatic targets, but also because of direct reaction with glutathione[30].

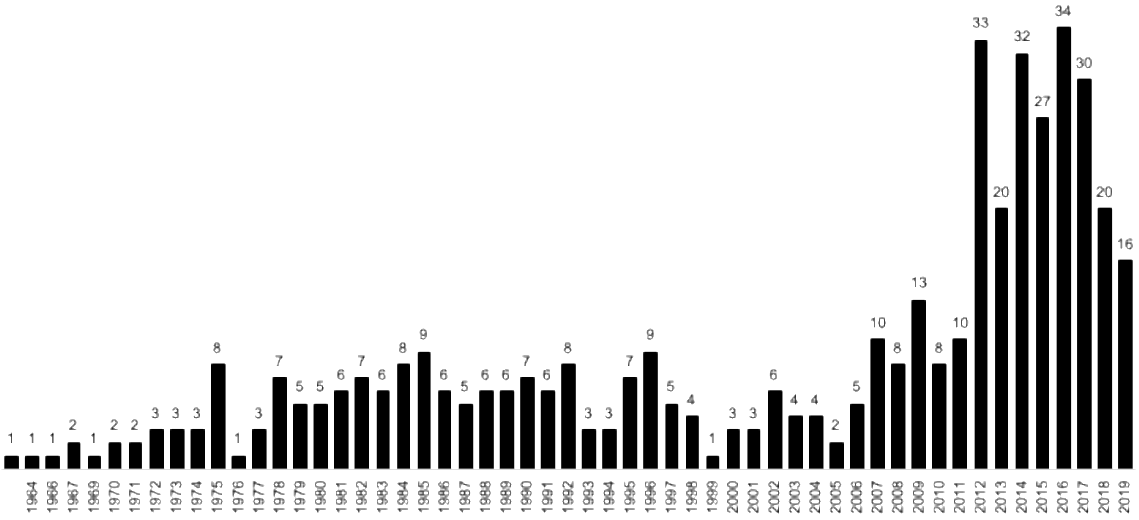

Figure 8 Number of publications per year involving 3-bromopyruvate (3BP), as obtained by PubMed search for the term '3-bromopyruvate' without chronological filtering (as per October 2019).

Faced with the broad spectrum of 3BP activity, an unbiased, holistic approach to study its effects was adopted. First, the sensitivity of MCT1-expressing or MCT1-null TNBC cell lines was tested and then untargeted metabolomics was utilised to elucidate the metabolic effects of the compound on these cells. Although various enzymes have been shown to be inhibited either in cell-free conditions or in various cell lines, limited studies have investigated the effects of 3BP on the metabolome as a whole[1,31]. The question of whether the equilibrium between mitochondrial and glycolytic metabolism shifts in response to 3BP treatment, was also addressed by measuring oxygen consumption and media acidification rate.

3.3 Aims

The aims of this part of the work were:

- To establish MCT1-positive and negative TNBC cell lines
- To confirm the MCT1-dependent toxicity of 3BP in breast cancer cell lines
- To investigate the metabolic effects of 3BP in breast cancer cell lines
- To establish an *in vivo* model for future studies

3.4 Materials & methods

Cells were grown as described in **Chapter 2, section 2.1**. Protein content and Western blot analysis are described in **Chapter 2**, **sections, 2.2** and **2.3**.

3.4.1 Toxicity of 3BP

Cells viability following 3BP treatment was assessed with an MTT assay, as described in **Chapter 2**, **section 2.4**. Cells were seeded at 5 x 10^4 cells/well density in 24-well-plates and incubated overnight to attach. 3BP stock solution (1 mM, Sigma-Aldrich, UK, product code: 16490) was freshly prepared by dissolving 3BP powder in complete growth media. Stock solution was kept on ice throughout the experiment to prevent 3BP degradation[22]. Growth media was substituted by media supplemented with a series of 3BP concentrations (0-300 μM. The cells were incubated for 24 h, when their viability was assessed.

3.4.2 Metabolic studies

3.4.2.1 Metabolomics

3.4.2.1.1 Sample preparation

Cells were grown as described in **Chapter 2, section 2.1** in T25 flasks. All samples were prepared in 6 replicates. Cells were treated when they reached approximately 80% confluence and media was changed the day before treatment. First, the effects of 3BP on the two different cells lines, BT20 (MCT1-positive) and MDA-MB-231 (MCT1-negative), were compared. All cells were treated with 100 μM 3BP in complete DMEM for 5, 15, 30 or 60 min. The results were expressed as fold-change in metabolite concentration between the untreated control group for each cell line and the treatment group. Then, the question of how the effects of 3BP in the BT20 cells change if MCT1 is silenced by siRNA was addressed. Treatment was the same for this study, however the cells were seeded in 6-well plates as per siRNA transfection protocol described in **Chapter 2, section 2.5**. This study included two control groups: non-transfected BT20 cells and BT20 cells transfected with a control (scrambled) siRNA. The control siRNA group was intended to correct for transfection-related alterations in metabolic pathways, unrelated to 3BP treatment.

Following treatment with 3BP, the treatment media were removed and the cells were washed with ice-cold PBS twice. Cells were lysed with ice-cold 80% v/v methanol (HPLC grade), scraped and transferred into 1.5 mL centrifugation tubes. Volumes of the methanol solution were kept at 250 and 500 μL for 6-well plates and T25 flasks respectively to achieve double-stranded DNA (dsDNA) concentration of at least 10 ng/μL for all samples. Lysates were centrifuged at 14,000 rpm for 30 min at 4°C. The supernatants were then collected and dsDNA concentration was measured using a Nanodrop set up for dsDNA measurements. Soluble protein and nucleic acids were removed by centrifugal filtration at 13,000 x g for 30 min at 4°C through a pre-washed 10 kDa molecular weight cut-off filter (Amicon Ultra, Millipore). Samples were normalised to

approximately 10 ng/μL dsDNA with 80% v/v methanol, transferred into total recovery HPLC vials and stored at -80ºC until the day of MS analysis.

3.4.2.1.2 Analysis of metabolite extracts with LC-MS/MS

Each sample was analysed using up to three separate LC-MS/MS methods using two different LC systems (Thermo Scientific ICS-5000+ ion chromatography system and a Thermo Ultimate 3000). Each was coupled directly to a Q-Exactive HF Hybrid Quadrupole-Orbitrap mass spectrometer with a HESI II electrospray ionisation source (Thermo Scientific, San Jose, CA).

Method 1: IC-MS/MS

Ion exchange chromatography was performed using a ICS-5000+ HPLC system incorporating an electrolytic anion generator (KOH) which was programmed to produce a OH^- gradient over 37 min. An inline electrolytic suppressor removed OH^- ions and cations from the post-column eluent stream prior to MS analysis (Thermo Scientific Dionex AERS 500). A 10 μL partial loop injection was used for all analyses and the chromatographic separation was performed using a Thermo Scientific Dionex IonPac AS11-HC 2 × 250 mm, 4 μm particle size column with a Dionex Ionpac AG11-HC 4 μm 2 x 50 guard column inline. The IC flow rate was 0.250 mL/min. The total run time was 37 min and the hydroxide ion gradient comprised as follows: 0 mins, 0mM; 1 min, 0 mM; 15 min, 60 mM; 25 min, 100 mM; 30 min, 100 mM; 30.1 min, 0mM; 37 min, 0 mM. Analysis was performed in negative ion mode using a scan-range from m/z 60-900 and resolution set to 70,000. The tune file source parameters were set as follows: Sheath gas flow 60 mL/min; Aux gas flow 20 mL/min; Spray voltage 3.6 V; Capillary temperature 320ºC; S-lens RF value 70; Heater temperature 350ºC. AGC target was set to 1e6v ions and the Max IT value was 250 ms. The column temperature was kept at 30°C throughout the experiment. Full scan data were acquired in continuum mode.

Method 2: C18 Reversed Phase (underivatised samples)

C18 reversed-phase analysis of underivatised samples was performed using a Thermo Utimate 3000 UHPLC system with a gradient elution program coupled directly to a Q-Exactive HF Hybrid Quadrupole-Orbitrap mass spectrometer. A 5 µL partial loop injection was used for all analyses with pre- and post-injection wash program. A Waters CORTECS UPLC T3 1.6µm (2.1x100mm) column was used with a flow rate of 0.4 mL/min. The total run time was 18 mins. Mobile phase A comprised milli-Q water with 0.1% formic acid and mobile phase B was 100% methanol with 0.1% formic acid. The gradient elution program was as follows: 0 mins, 5% B; 4 min, 50% B; 12 min, 99% B; 15 mins, 99% B; 15.1 min, 5% B; 18 min, 5% B. The column temperature was kept at 40°C throughout the experiment. Mass spectrometry analysis was performed in positive and negative ion mode separately using a scan-range from m/z 60-900 and resolution set to 70,000. The tune file source parameters were set as follows: Sheath gas flow 60 mL/min; Aux gas flow 20 mL/min; Spray voltage 3.6v; Capillary temperature 320°C; S-lens RF value 70; Heater temperature 350°C. Full MS setting were AGC target 5e6 ions and the Max IT value was 120ms. Full scan data were acquired in continuum mode. A data directed tandem mass spectrometry method was utilised (ddMS2) with no inclusion list. The orbitrap detector and HCD setting for ddMS2 were as follows: Microscans 2, resolution 17,500, AGC target 5e4 ions, maximum IT 80ms, loop count 10 and NCE 35.

Method 3: C18 Reversed phase (derivatised samples)

The third LC-MS method used a sample derivatisation protocol followed by analysis based on a modified version of the Waters AccQ-Tag method (Salazar et al., 2011). C18 reversed-phase analysis of derivatised samples was also performed using the Thermo Utimate 3000 UHPLC system coupled directly to a Q-Exactive HF Hybrid Quadrupole-Orbitrap mass spectrometer. A 5 µL partial loop injection was used for all analyses with pre- and post-injection wash program. A Waters AccQ-Tag column (2.1x100 mm) was used with a flow rate of 0.5 mL/min. The total run time was 9.5 min. Mobile phase A and B comprised commercially available AccQ-Tag reagents

prepared as recommended by Waters (Waters PLC, Elstree, UK). The gradient elution program was modified from the published AccQ-Tag method as follows: 0mins, 0.1%B; 0.54 min, 9.1%B; 5.74 min, 21.2%B; 7.74 min, 59.6%B; 8.04 min, 90%B; 8.05 min, 90%B; 8.64 min, 0%B; 9.5 min, 0.1% B. The column temperature was kept at 40°C throughout the experiment. Mass spectrometry analysis was performed in positive ion mode separately using a scan-range from m/z 70-1050 and resolution set to 70,000. The tune file source parameters were set as follows: Sheath gas flow 60 mL/min; Aux gas flow 20 mL/min; Spray voltage 3.6 V; Capillary temperature 320°C; S-lens RF value 70; Heater temperature 350°C. Full MS setting were AGC target 3e6 ions and the Max IT value was 200ms. Full scan data were acquired in continuum mode.

3.4.2.1.3 Data analysis

Raw data files were processed using ProgenesisQI (Waters, Elstree, UK). This process included alignment of retention times, peak picking by identification of the presence of natural abundance isotope peaks, characterising multiple adducts forms and identification of metabolites using in-house database. Retention times, accurate mass values, relative isotope abundances and fragmentation patterns were compared between authentic standards and the samples measured. Identifications were accepted only when the following criteria were met: <5 ppm differences between measured and theoretical mass (based on chemical formula), <30 s differences between authentic standard and analyte retention times, isotope peak abundance measurements for analytes were >90% matched to the theoretical value generated from the chemical formula. Where measured, fragmentation patterns were matched to at least the base peak and two additional peak matches in the MS/MS spectrum to within 12 ppm. The top 10 data directed fragmentation method was not always able to provide fragment ions for all ions measured in the MS 1 spectrum.

After peak identification, fold change was calculated within each cell group. For fold change calculation, the following formula was used: $\log_2[FC]=\log_2[final]-\log_2[control]$, where FC stands for fold change, [final] is the normalised abundance at the time point of interest and [control] is

the average abundance of the untreated control of this cell group. Where measurements from different batches were to be compared, the average abundance value of a random selection of metabolites ('QC') was compared between the two batches (QC ratio). Then, the values of interest were normalised between different batches. Where possible, all samples of the same data set were analysed together.

3.4.2.2 Bioenergetics

The bioenergetic profiles of BT20 and MDA-MB-231 cells treated with 3BP were determined using a Seahorse XF96 Extracellular Flux Analyser (Agilent, CA, USA). The day before the experiment, 20,000 cells/well were seeded in Seahorse tissue culture 96-well plates using 100 µL normal growth media per well (DMEM complemented with 1% PSG and 10% FBS). The cells were incubated at room temperature (RT) in the tissue culture cabinet for 30-60 min and then transferred into the standard 5% CO_2 incubator and allowed to adhere for at least 4 hours. Where siRNA-transfected cells were used, cells were seeded for transfection 3 days before the Seahorse analysis and transfected 2 days before. Transfected cells were trypsinised the day before the experiment and seeded in assay plates together with the other cell groups. Excess cells were kept from all groups and lysed for Western blot analysis while the Seahorse experiment was running to confirm MCT1 expression status at the time of the run. Each well was then topped up to 200 µL with media containing 3BP to reach a final concentration of 10, 20 or 40 µM per well, or 100 µL of culture media for control wells. The plate was incubated further in the 5% CO_2 incubator overnight. Simultaneously, a sensor cartridge was hydrated and calibrant solution equilibrated overnight in the CO_2-free incubator. On the day of the assay, unbuffered serum-free Seahorse DMEM (103575-100, Agilent Technologies, CA, USA) was freshly complemented with unbuffered glutamine and glucose solutions (103579-100, Agilent Technologies, CA, USA) ('assay media'). Treatment media was replaced with assay media in the cell plate and the cells were

incubated in the CO_2-free incubator for 1 h prior to the assay. In the meantime, the water was replaced with calibrant solution in the utility plate and the sensor were calibrated for 20 min in the Seahorse XF96 instrument (Agilent Technologies, CA, USA). The instrument was set to acquire 5 consecutive measurements with no injection through the injection ports. The instrument protocol is presented in **Table 2**. The timeline of the experiment is summarised in **Figure 9**.

Table 2 Time events in the Seahorse XF96 run.

Command	Time (min)
Calibrate	20.00
Equilibrate	
Mix	3.00
Measure	4.00
Mix	3.00
Measure	4.00
Mix	3.00
Measure	4.00
Mix	3.00
Measure	4.00
Mix	3.00
Measure	4.00

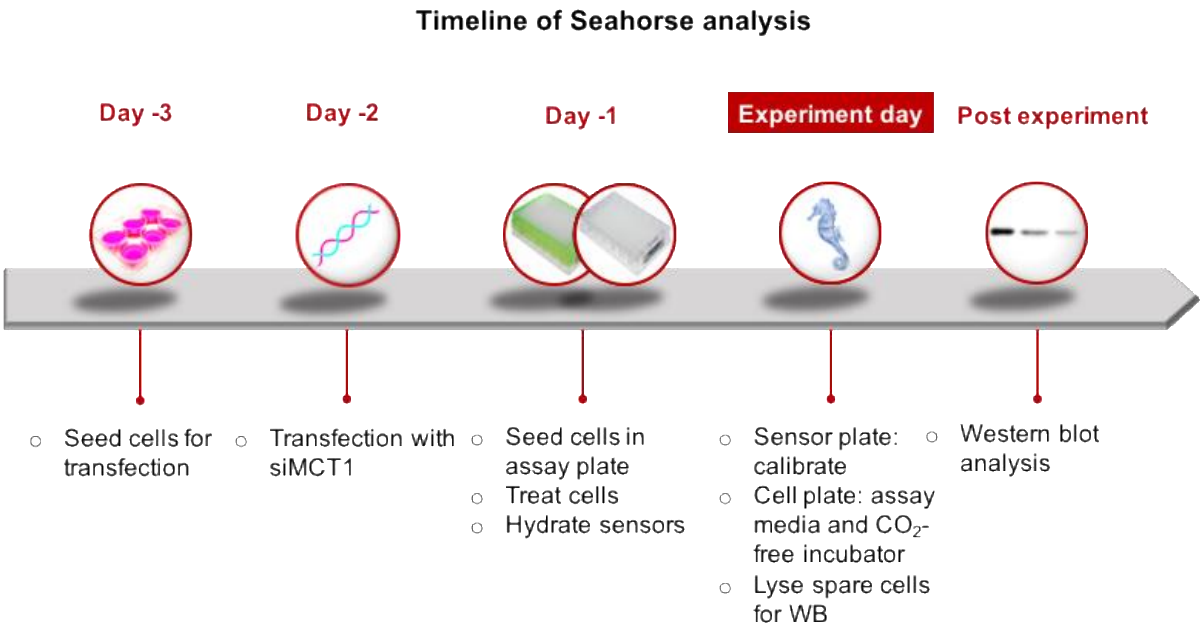

Figure 9 Timeline of Seahorse XF96 experiment. Cells were seeded in 6-well plates 3 days prior to the experiment. They were transfected with siRNA against MCT1 2 days before the experiment and then treated with 20 µM 3BP the day before. The sensor cartridge was hydrated overnight. For measurement, treatment media was replaced with unbuffered serum-free assay media, the instrument was calibrated as per manufacturer's instructions and 5 measurements were taken over the course of 1 h (n=4). For full details, see methods. The results were analysed using Prism7 software (GraphPad, CA, USA).

3.5 Results

3.5.1 Toxicity of 3BP

A literature search for TNBC cell lines suggested that BT20 and MDA-MB-231 cells could be used as a positive and negative model for MCT1 expression respectively. WB analysis of cell lysates confirmed strong expression of MCT1 (theoretical molecular weight 54 kDa) in BT20 cells while levels were undetectable in MDA-MB-231 cells (**Figure 10**). MCT1 apparent molar mass is approximately 40 kDa. MCT4 is an isoform of the transporter associated with export of lactate and hence glycolytic metabolism. It has been suggested that expression of MCT4 could, in theory confer resistant to MCT1-targeted treatments. Therefore, MCT4 expression status was also established in BT20 and MDA-MB-231 cells.

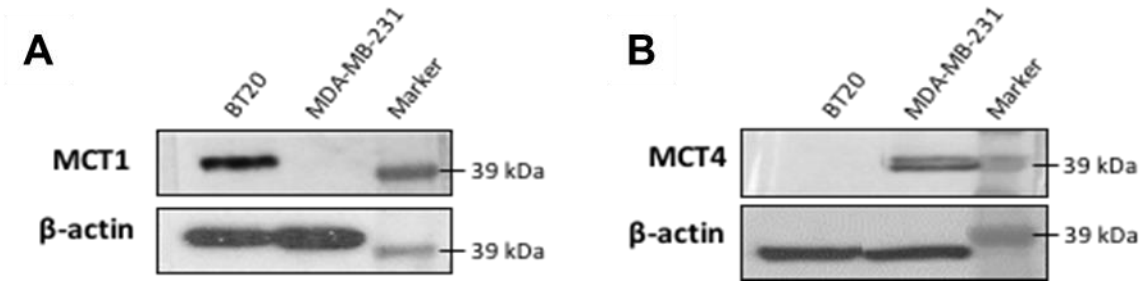

Figure 10 MCT expression. Expression of monocarboxylate transporter (MCT) isoforms 1 and 4 by the selected triple negative breast cancer (TNBC) cell lines, BT20 and MD-MB-231. Lysates were incubated with reducing Lamelli buffer for 10 min at 70ºC before loading onto a 4-12 % SDS PAGE, subsequent electrophoretic transfer onto nitrocellulose was followed by probing with an anti-MCT1 (Santa Cruz, sc-365501) or anti MCT4 (Santa Cruz, sc-50329) primary antibody and an anti-mous or anti-rabbit HRP secondary antibody (Invitrogen, 61-6520 and 32460) for MCT1 and MCT4 respectively. MagicMark™ XP (Thermo, LC5602) was used as a molecular weight marker. See methods for full details.

3BP is thought to be taken up by MCT1. If uptake is the determinant of toxicity, then BT20 cells, with high MCT1 expression, would be expected to be more sensitive to 3BP treatment than MDA-MB-231 cells. Also, inhibition of MCT1 is expected to lower cell sensitivity to 3BP provided

that the MCT1 inhibition is not cytotoxic by itself. Indeed, **Figure 11** shows the differential sensitivity between the two cell lines and the resistance conferred to the BT20 cells by treatment with CHC, a commonly used MCT inhibitor. Of note, CHC is not specific to MCT1 and it is known to inhibit other MCT isoforms and the mitochondrial pyruvate transporter (MPC).

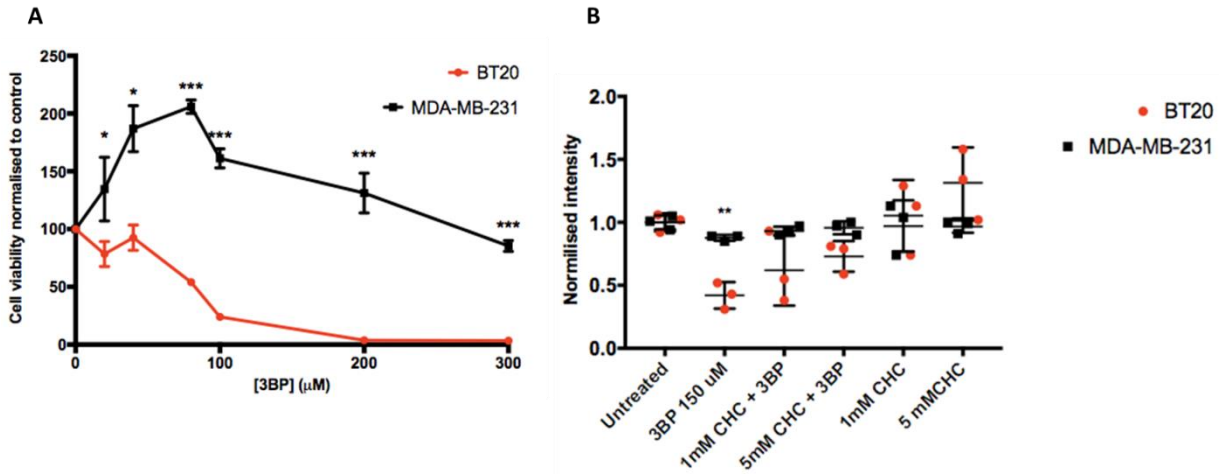

Figure 11 Profiling the differential toxicity of 3BP (A) BT20 and MDA-MB-231 cells were tested for different sensitivity to 3BP treatment (n=3). Cells were treated with a concentration series of 3BP and cell viability was measured with an MTT assay (see methods). (B) The impact of CHC, an MCT1 inhibitor, was investigated by inclusion in studies exposing BT20 or MDA-MB-231 cells 3BP. Data were normalised to untreated control. Error bars represent SD, ***, ** and * represent p<0.05, 0.01 and 0.001 respectively as assessed using multiple t tests analysis on Prism 7 (GraphPad, CA, USA).

Although MDA-MB-231 and BT20 cells are TNBC cell lines, they are from a different origin, and as such they have many other differences apart from MCT expression levels. To ensure that MCT1 expression is a major determinant of toxicity, BT20 cells were transfected with siRNA against MCT1 (siMCT1) or 'scrambled' siRNA as a transfection control (sc-siRNA) to silence MCT1 expression. The expression level of the transporter was assessed by Western blot and band optical density was normalised to that of β-actin (**Figure 12A** and **B**, respectively). Wild type BT20 cells were shown to be significantly more sensitive to 3BP than BT20 cells with silenced MCT1 expression (siMCT1-BT20) while the cells transfected with the sc-siRNA (sc-BT20) showed similar sensitivity to that of the non-transfected cells (**Figure 12C**). It is noted that cells, siMCT1-BT20 and MDA-MB-231, are more resistant but not completely immune to 3BP.

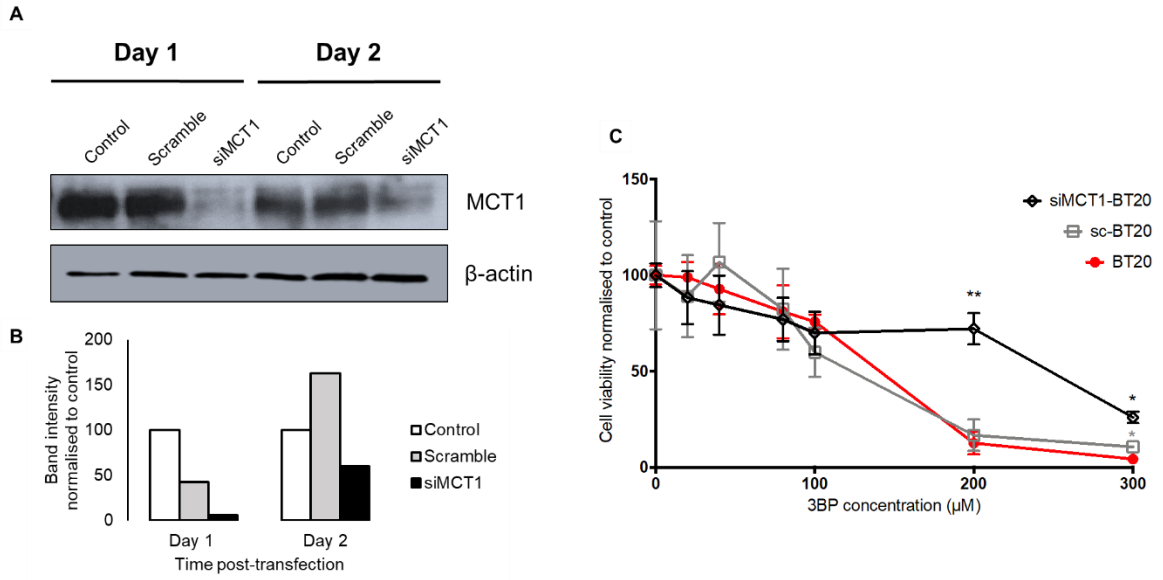

Figure 12 MCT1-dependent 3BP toxicity. (A) Transfection efficiency was assessed by Western blot analysis on separate wells which were processed at the start of the 3BP treatment or the next day (end of treatment), and (B) the corresponding quantification of band intensity analysed on ImageJ (FIJI, CA, USA). (C) BT20 cells, BT20 cells transfected with untargeted siRNA (sc-BT20) and BT20 cells transfected with siRNA targeted against MCT1 (siMCT1-BT20) were treated with 3BP for 24 hours and their viability is shown in the graph, n = 4, error bars represent SD, ** and * represent $p<0.05$ and 0.01 respectively as determined by multiple t-tests on Prism 7 (GraphPad, CA, USA).

3.5.2 Bromide uptake

Direct measurement of 3BP uptake would also confirm a role for MCT1 but this was more challenging to achieve. Commonly used approaches that enable selective and sensitive detection and quantification of compounds in cells include fluorescently labelling and radio-labelling of the compound of interest. In the case of 3BP, a 3-carbon atom molecule, association with any of the commonly used fluorophores would significantly change its size and physicochemical properties – most common fluorophores are in fact larger than 3BP. While this work was ongoing, [14C]-3BP was not accessible and *de novo* in-house radio-synthesis of the compound was out of the scope of this project.

Liquid chromatography coupled with mass spectrometry (LC-MS) was the only viable option for measuring the uptake. For these measurements were performed on the same samples used for metabolomics, following the same procedure for sample preparation and analysis. However, intact 3BP does not survive the LC-MS conditions. Bromide peak (sum of ^{78}Br and ^{80}Br) was compared between the two cell lines, and between wild type BT20 cells and transfected BT20 cells (sc-BT20 and siMCT1-BT20). According to the mechanism of action of 3BP, an alkylating agent, the organic part of the molecule covalently binds to a protein or peptide – which is 'pyruvylated' – while bromide is the leaving group. There is no overt reason why bromide would naturally be preferentially retained in either of the employed cell groups. Therefore, the data showing an increase in bromide content in MCT1-positive cells in the early time points (**Figure 13**) are in agreement with the expected preferential uptake of 3BP. Specifically, at 5 min BT20 cells show a doubling of bromide vs MDA-MB-231 cells (**Figure 13A**) and a 50% increase vs siMCT1 BT20 cells (**Figure 13B**). Data from later time points (60 min) where a reversal is evident, with both MDA-MB-231 and siMCT1 BT20 cells showing greater levels than BT20 cells, is harder to explain.

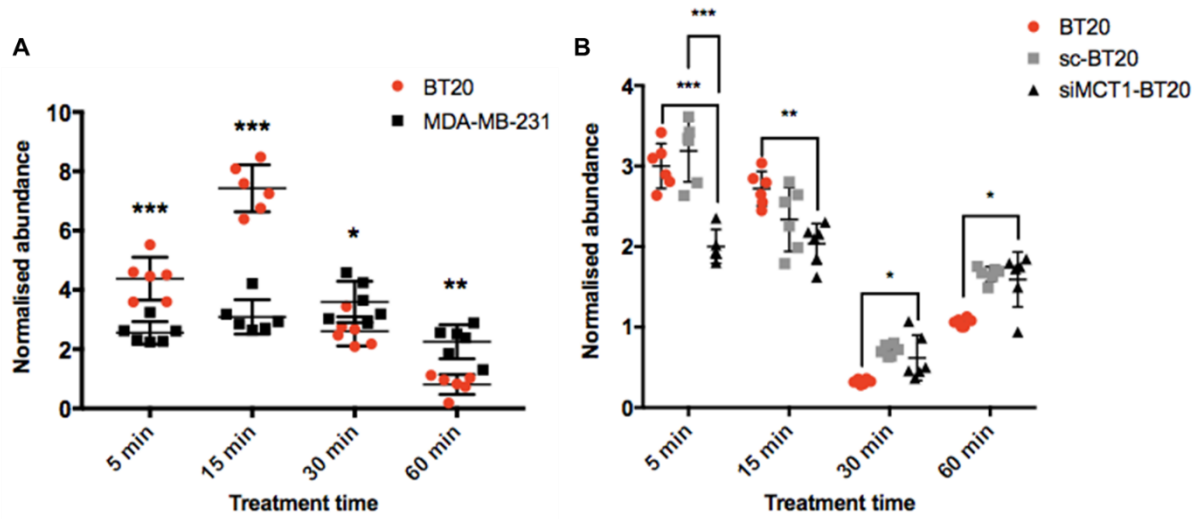

Figure 13 Differential bromide uptake. (A) Intensity of bromide peak (^{78}Br and ^{80}Br) normalised to control measured by LC-MS in MDA-MB-231 and BT20 cell lysates, and (B) in BT20, sc-BT20 and siMCT1-BT20 cells (n=6). Sc-BT20 are BT20 cells transfected with scrambled siRNA and siMCT1-BT20 cells are BT20 cells transfected with siRNA against MCT1 (see methods). Error bars represent SD, *P<0.05, **P<0.01, ***P<0.001. Statistical analysis was performed by Prism 7 (GraphPad, CA, USA).

3.5.3 Comparing metabolites between different TNBC cell lines

3.5.3.1 Energy metabolism: Glycolysis, tricarboxylic acid cycle and pentose phosphate pathway

Cell lysates were successfully analysed by LC-MS, with help from Drs David Hauton and John Walsby-Tickle. **Figure 14** summarises the changes of intracellular metabolites involved in the glycolysis, tricarboxylic acid (TCA) cycle and pentose phosphate pathway (PPP) that were detected and quantified. Green signifies a decrease in level compared to control and pink signifies increase compared to control, while colour saturation relates to the magnitude of the change. The results were expressed as fold change compared to untreated control for each cell line.

Looking at the heat maps as a whole, it is evident that the BT20 cells are overall more affected by the treatment, both in metabolites that are depleted and the ones that accumulate. Unfortunately, few metabolites in glycolysis have been identified.

Starting from the top, it is notable that glucose-1-phosphate (glucose-1P), glucose-6-phosphate (glucose-6P), fructose-1-phosphate (fructose-1P) and fructose-6-phosphate (fructose-

6P) are isomers and would not be distinguished by LC-MS. From the heat map, it is evident that glucose-6P concentration has significantly ($p<0.01$, 2-fold) decreased in BT20 cells, but not in MDA-MB-231 cells. Glucose is phosphorylated by hexokinase enzymes (glucose to glucose-6P), with simultaneous conversion of ATP to ADP (energy consuming step of glycolysis). There are four isoforms of this enzyme, of which hexokinase 2 (HK-2) is found both in the cytoplasm and the mitochondrial outer membrane, where it has direct access to ATP. HK-2 is the main isoform upregulated in cancer cells and has been identified as a target of 3BP.

A few steps down the pathway, glyceraldehyde phosphate dehydrogenase (GAPDH) is responsible for the production of 3-phosphoglycerate (3PG) from glyceraldehyde 3-phosphate. GAPDH is recognised as the main target of 3BP and some researchers have suggested that inhibition of GAPDH, and the resulting energy depletion of cells dependent on glycolysis, is the main cause of 3BP toxicity[28]. Although in this data set it is not possible to identify the direct substrate and product of this enzyme, dramatic accumulation (over 5-fold in BT20 cells) of fructose-1,6-phosphate (fructose-1,6P2) strongly suggests that this enzyme is indeed inhibited. This provides a reliable quality control for the study. Notably, a significant ($P<0.01$, 2-fold) increase in fructose-1,6P_2 in MDA-MB-231 cells is also observed. From this it could be concluded that some 3BP enters most likely by other isoforms of the transporter. Although this is a significant level of inhibition of GAPDH, this cell line is significantly more resistant to 3BP effects. Overall, in the glycolytic pathway, HK-2 inhibition cannot be confirmed, but the strong inhibition of GAPDH found here is in accordance with results reported in the literature[28,31].

Moving to the TCA cycle, (at the right bottom corner of the map), it is evident that both cell lines are affected, but not severely. As the alternative name of the TCA cycle, (the citric acid cycle), suggests, citrate is consumed and re-generated. Most of the pyruvate that is not converted to lactate, enters the mitochondria by its carrier. Pyruvate dehydrogenase (PDH) catalyses the reaction of pyruvate and co-enzyme A (CoA-SH), generating acetyl-CoA with parallel generation

of one equivalent of NADH. Acetyl-CoA enters the TCA cycle, bridging mitochondrial metabolism with glycolysis. Citrate itself can be used to generate acetyl-CoA and initiate lipid synthesis. An important metabolite in the context of cancer is 2-oxoglutarate/ketoglutarate (2KG). This is the point at which TCA can be fed by glutaminolysis rather that glycolysis. In these studies, the TCA cycle has shown significant variations depending on the time point so no robust conclusions can be drawn.

What has been consistent, however, is the accumulation of metabolites of the pentose phosphate pathway (PPP). Glucose-6P can be metabolised through glycolysis for energy production, or fed into the PPP from which the main products are ribose-5-phosphate (ribose-5P), the sugar component of nucleotides, and NADPH. Thus, PPP has a crucial role in the maintenance of redox homeostasis. Importantly, ribulose- and ribose-5-phosphate (ribose-5P) showed dramatic accumulation in BT20 cells and less so in MDA-MB-231 cells. Intriguingly however, PRPP, the activated form of ribose-5P (phosphorylated) is depleted, suggesting that the PRPP-synthase, a kinase, is inhibited. Overall, it seems that PPP is proceeding but pathways that would consume the metabolites generated by it are inhibited. It has already been noted that GAPDH is inhibited. Sedoheptulose-7-phosphate can feed glycolysis at the glucose-6P point, but this is before GAPDH. Ribose-5P is consumed for the biosynthesis of nucleotides but this is also inhibited, as discussed in section **3.6.7** (**Chapter 3, Discussion**).

Overall, this untargeted metabolomics approach shows that 3BP affects energy metabolism and biosynthetic pathways at multiple points and it seems unlikely that it is limited to GAPDH inhibition.

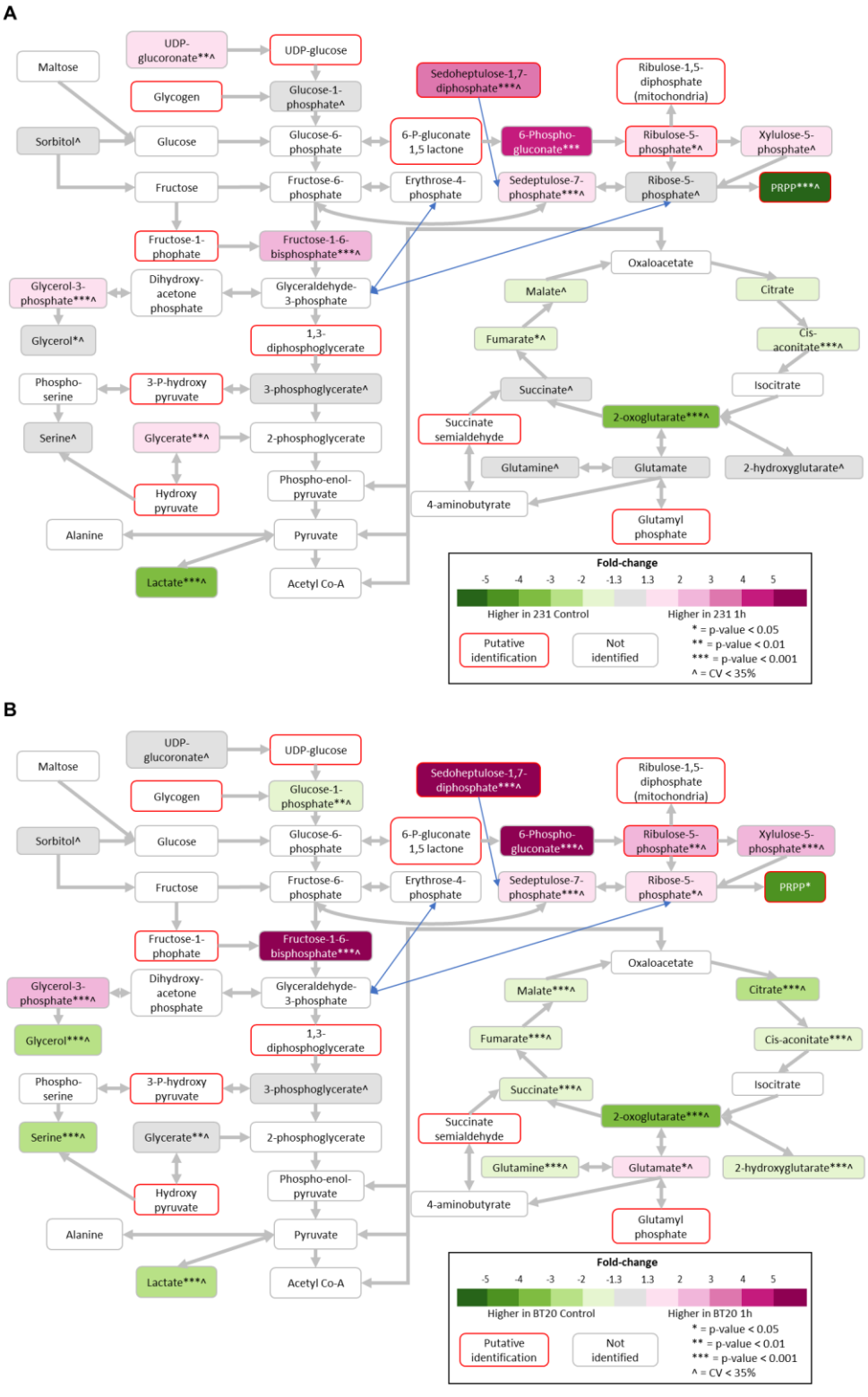

Figure 14 Changes in glycolysis, tricarboxylic acid (TCA) cycle and pentose phosphate pathway (PPP). MDA-MB-231 cells (A) and BT20 cells (B) were treated with 100 µM 3BP for 60 min, then the metabolites were extracted and analysed by liquid chromatography coupled with mass spectrometry (LC-MS/MS). Results are presented as fold changes normalised to untreated control for each cell line. Data were analysed using Microsoft Excel and Metaboanalyst online software. SD is shown, n=6, *P<0.05, **P<0.01, ***P<0.001.

3.5.3.2 Reducing capacity

The chemical structure of 3BP suggest that it would readily react with major cell antioxidants like N-acetyl-cysteine (NAC) and glutathione. Importantly, both of these compounds contain a thiol (-SH) moiety. Reduced forms nicotinamide adenine dinucleotides (NADH and NADPH) are co-factors that act primarily as hydride donors in redox and other reactions. NADPH is the main molecule contributing to the redox homeostasis, while NADH is crucial for energy (ATP) production via the mitochondrial electron transport chain (ETC).

Although NADPH cannot be detected with the use of our current protocol for LC-MS, there is indirect evidence that NADPH is generated, i.e. the fact that the oxidative part of PPP, the main biosynthetic route of NADPH, is proceeding. As was observed in the previous section, PPP metabolites, including those of the oxidative phase, are accumulating (e.g. ribulose-5P

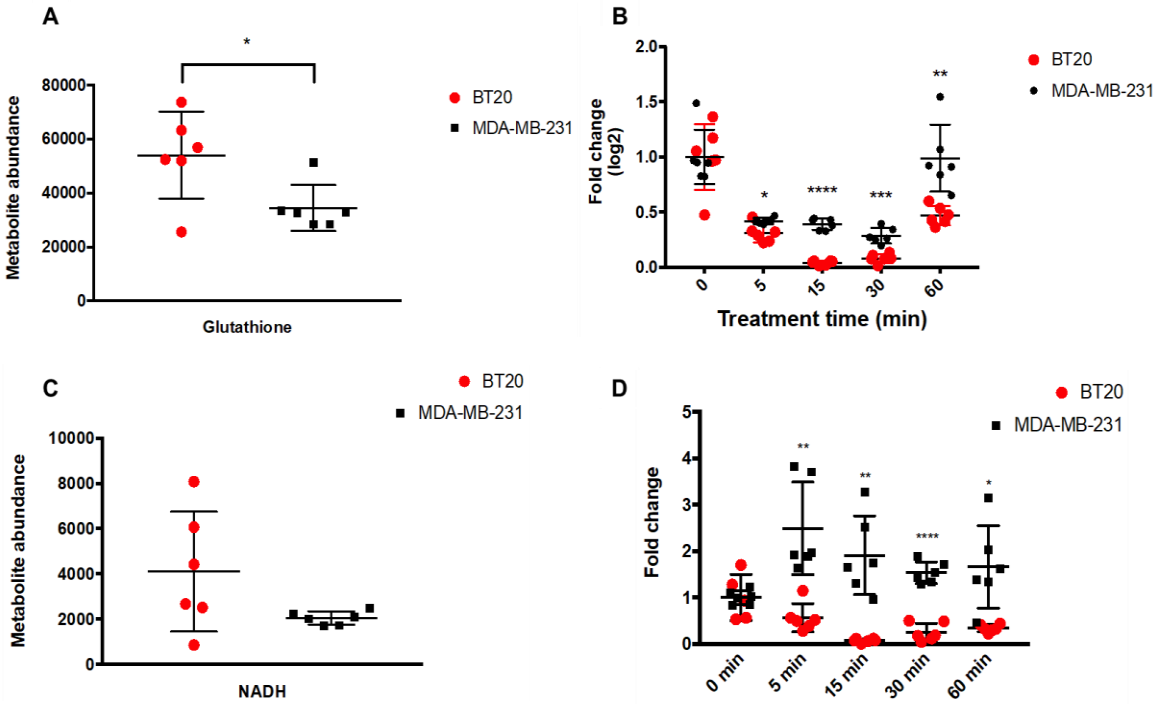

Figure 15 3BP effects on glutathione and NADH. (A) Glutathione abundance in untreated controls. (B) Changes in glutathione levels in response to treatment with 100 µM 3BP, expressed as log2(fold change).(C) NADH abundance in untreated controls (no statistically significant difference). (D) Change in NADH levels in response to treatment with 100 µM 3BP, expressed as log_2(fold change). Statistical analysis was performed on Prism 7 (GraphPad, CA, USA), n=6, SD shown. *P<0.05, **P<0.01, ***P<0.001.

increases 3-fold, P<0,01), suggesting that NADPH is produced – inhibition occurs downstream. NADH was identified and shown to be depleted.

Of the thiol-containing antioxidants, glutathione has been identified for all the groups examined. Interestingly, BT20 cell lysates were found to constitutively contain more (reduced) glutathione, which could protect them from the 3BP. To control for the different levels at baseline, change in glutathione was normalised to the untreated control for each cell line (**Figure 15A**). Glutathione was severely depleted (P<0.0001) at short time points (up to 15 min) for BT20 cells, and then partial recovery was observed at 60 min (**Figure 15B**). For MDA-MB-231 cells, levels did fall with treatment, albeit to a lesser extent and full recovery was observed at 60 min.

3.5.3.3 Nucleotide biosynthesis

Nucleotide (mono-, di- and tri-phosphates) abundance was measured using LC-MS/MS. Nucleotides are the immediate precursors for poly-nucleic acid synthesis (DNA and RNA). The general trend for all identified nucleotides was a decrease, although there was a wide deviation from the mean for several of them. Consistent with the 3BP-mediated glycolysis inhibition, ATP level decreases but not markedly ($\log_2$(FC)= -0.33 for BT20 cells and 0.49 for MDA-MB-231) (**Figure 16**). This level is in accordance with Byrne *et al.* who showed a 60% reduction in endometrial cancer cell lines at 1.5 hr after 3BP exposure[32]. However, AMP (or its cyclic isomer, cAMP), which is often used as a signifier of cellular starvation, may be expected to rise. Contrary to these expectations, on average a decrease between the samples was observed, although the deviations are large so this might not be a true decrease in AMP (**Figure 16**). Nucleotides which showed a marked (at least 2-fold) and reliable (SD <0.01) change include GTP, CDP, CMP, dCTP, UMP and uridine. dATP does not present a statistically significant difference between the cell lines, but its concentration clearly plunges in the BT20 cells (compared to baseline). What can be observed overall, is that there is less change in the MDA-MB-231 (MCT1-negative) cell line.

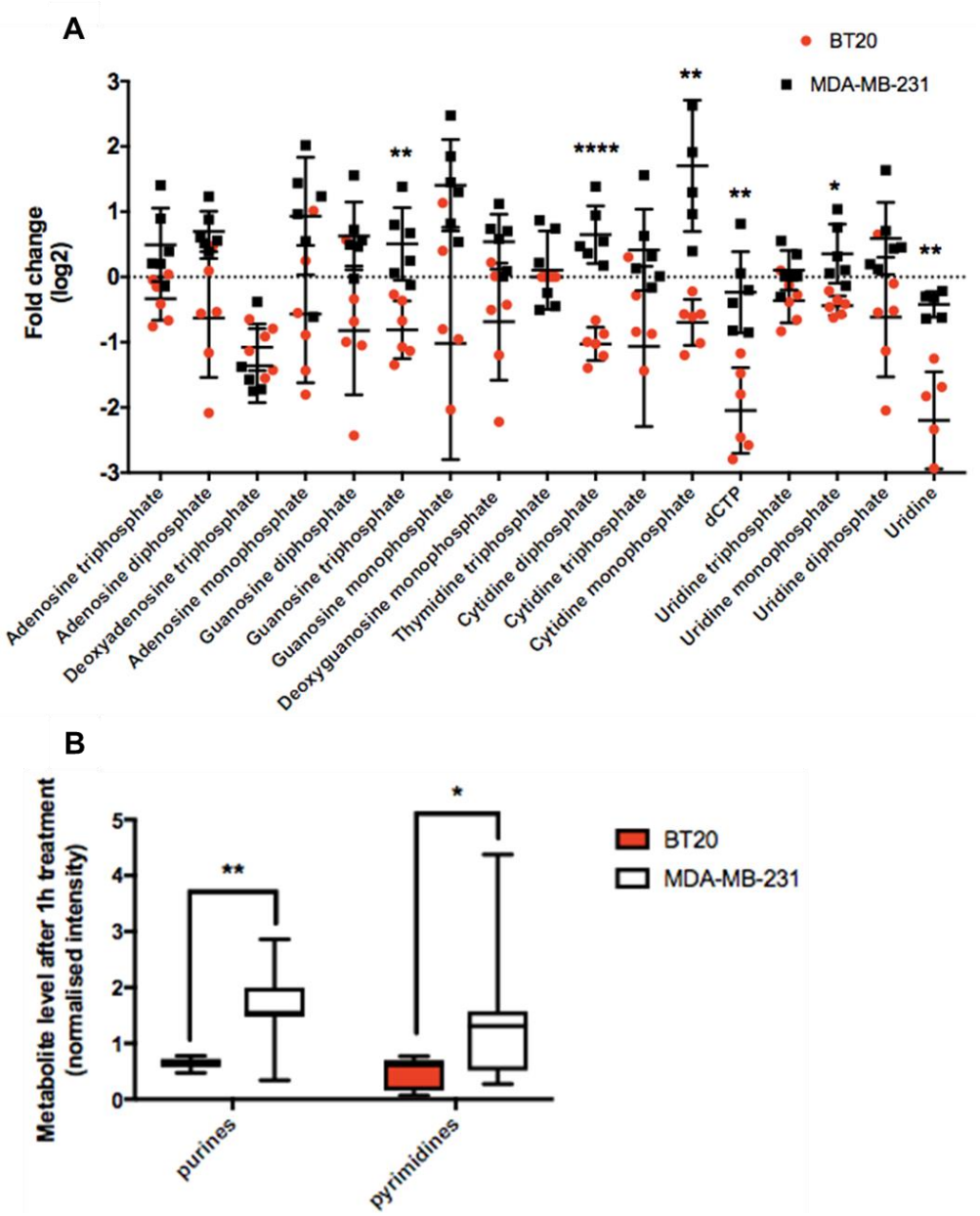

<u>Figure 16</u> Changes in the levels of nucleotides in response to treatment with 3-bromopyruvate (3BP). (A) Change expressed as $\log_2$ (fold change) in the level of individual nucleotides after 60 min treatment of BT20 and MDA-MB-231 cells with 100 μM 3BP (n=6). (B) Cumulative change in purines and pyrimidines after 60 min treatment of BT20 and MDA-MB-231 cells with 100 μM 3BP (n=6). Error bars represent the standard deviation. *P<0.05, **P<0.01, ***P<0.001. Data were analysed with Prism 7 (GraphPad, CA, USA).

3.5.4 Comparing metabolites within a single TNBC cell line

In the previous section, the basic energy metabolism, antioxidant content and synthesis of nucleic acid precursors were compared between two TNBC cell lines, one with naturally high and one with naturally low expression of MCT1. The results obtained suggest that 3BP affects more than one pathway potentially at more than a single point. Glycolysis was inhibited, while pathways interlinked with it, TCA cycle and PPP, showed interesting responses: TCA showed an overall slight decrease and the PPP showed accumulation of several metabolites. Importantly, the TCA can be fed directly by glutaminolysis at the 3KG entry point. With regards to the cell antioxidant capacity, three pieces of information were obtained. First, PPP proceeds, suggesting that NADPH is produced. Second, glutathione is depleted but partially recovers, while, third, NADH follows a similar but less pronounced trend. Nucleotide synthesis presented with an overall decrease but with wide variability, which blurred the trends for certain molecules.

One reason for the variability is the fact that these two cell lines, i.e. MDA-MB-231 and BT20, are different in multiple ways. For example, the baseline levels of glutathione are different. A way to potentially obtain more significant, MCT1-relevant results would be to use siRNA against MCT1 (siMCT1) to silence the expression of the transporter in the BT20 cells and then proceed with the same treatment and analysis that was used to compare between the 'positive' and 'negative' cell line. It is noteworthy that siRNA, although a quick and practical solution when it comes to gene silencing, does not give complete knockdown of expression and is not absolutely specific and is expected to affect the cell in other ways. This can be partially accounted for with a use of a control comprised of the same cells transfected with scrambled siRNA (sc-BT20) which shares the properties of the siRNA sequence but does not reduce expression of the target protein.

3.5.4.1 Glycolysis, tricarboxylic acid cycle and pentose phosphate pathway

Generally, MCT1-expressing cells (BT20 and sc-BT20) are expected to react similarly to 3BP treatment, while, MCT1-null cells (siMCT1-BT20) are expected to be less responsive to 3BP treatment. The viability study showed that siMCT1-cells are not completely immune to 3BP, therefore, it is expected that these cells will also exhibit a level of metabolic disturbance.

Glycolytic intermediates (glucose-1P, fructose-6P and fructose 1,6P2) showed significant build-up in BT20 cells which strongly contrasted with the 3BP effect on the same metabolites in siMCT1-BT20 cells. Changes in the sc-BT20 cells followed the same trend as for BT20 cells but the intensity of the effect appeared to be in-between the MCT1-expressing and MCT1-null cells. Since this is generally the case for most metabolites, this effect could be attributed to non-specific silencing of genes, a well-known phenomenon of siRNA-mediated silencing[33]. Hydroxypyruvate also showed a statistically significant increase ($\log_2(FC)=0.85$, $p<0.05$) in BT20 cells (**Figure 17A**). Hydroxypyruvate is a metabolite of serine which can be converted back to glycerate and contribute to gluconeogenesis. Dihydroxyacetone and its phosphorylated form are important precursors for the biosynthesis of triglycerides[34]. These results (**Figure 17A** and **B**) show a slight change in the BT20 cells, which is however significantly ($\log2(FC)= 0.18$, $p<0.05$) bigger than the change in siMCT1-BT20 cells. Dihydroacetone phosphate increases but in a similar manner across all three cell groups. 2,3-Diphosphoglycerate (glycerate-2,$3P_2$) is an intermediate between phosphoglycerate-1,$3P_2$ and glycerate-3P in the glycolytic pathway. It presented with a time-dependent statistically significant decrease in abundance upon 3BP addition, which is in agreement with inhibition of GAPDH[35].

Changes in the metabolites of the TCA cycle and related metabolites that are not themselves in the cycle are presented in **Figure 17C** and **D** (30 and 60 min of 3BP treatment respectively). The fuel for TCA is acetyl-coA, which may derive from pyruvate generated from glucose metabolism (glycolysis and gluconeogenesis), or the metabolism of fatty acids and amino acids.

Crucially, the TCA cycle can be fuelled directly from glutaminolysis at the 2-oxoglutarate (also known as α-ketoglutarate, αKG) entry point. It is worth noting that the cells have constant access to glutamine in culture conditions, which is not necessarily the case *in vivo*. Intracellular glutamine and glutamate concentrations were constant throughout the treatment (**Figure 18**), in accordance with the steady glutamine supply by the culture media. Citrate is consumed and regenerated in the TCA cycle. For regeneration, malate converts to oxaloacetate, which then combines with acetyl-CoA to give back citrate. Interestingly, it is clear that malate selectively increased in BT20 cells and, simultaneously, citrate slightly decreased, contrasting with the pattern in siMCT1-BT20 cells. Citrate is an important precursor for the biosynthesis of fatty acids.

The PPP (**Figure 17E** and **F,** for 30 and 60 min treatment respectively) is presented together with glycolysis and TCA because of the metabolic continuity between these pathways but its contribution to cellular metabolism is not energy production, rather biosynthetic intermediates and reducing equivalents. The first part of the PPP is oxidative and results in the synthesis of 2 eq NADPH and phosphorylated 5-carbon sugars (ribose-5P, xylulose-5P) which serve as building blocks for nucleotide synthesis. The second, non-oxidative part, interconverts sugars with 3, 4, 5, 6 or 7 carbon atoms and can give back glycolytic intermediates. The general trend, already from 30 min, is a selective, statistically significant build-up of PPP intermediates in both the oxidative (glucose-6P, ribulose-5P, ribose-5P) and the non-oxidative phase (sedoheptulose phosphates and fructose-6P, which is in the glycolysis graph). The latter, 7-carbon products (sedoheptulose phosphates) present with the most pronounced increase ($\log_2(FC)=4.00$, $P<0.0001$ for sedoheptulose-7P), suggesting that the pathway proceeds but the metabolites are not consumed. Importantly, sedoheptulose phosphates can feed back to glycolysis before the GAPDH point of action, hence their accumulation also supports GAPDH inhibition by 3BP.

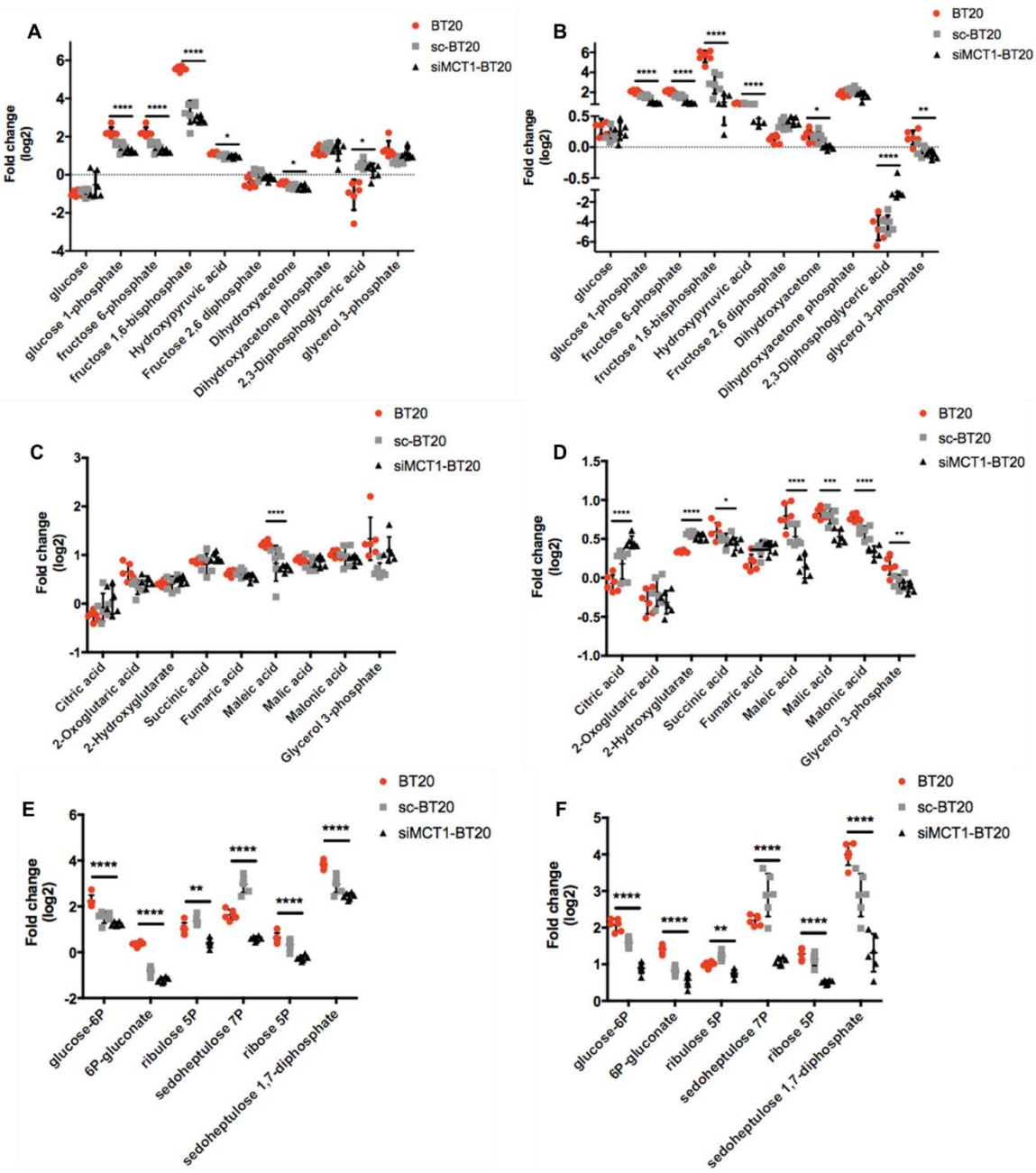

Figure 17 Changes in glycolysis, tricarboxylic acid (TCA) and pentose phosphate pathway (PPP) in response to 3BP treatment. (A) and (B) present the changes in glycolysis following treatment with 100 µM 3BP for 30 and 60 min respectively (n=6), (C) and (D) present changes in the TCA cycle following treatment with 100 µM 3BP for 30 and 60 min respectively (n=6), and (E) and (F) present changes in the PPP following treatment with 100 µM 3BP for 30 and 60 min respectively (n=6). Metabolites were extracted from treated cell lysates and analysed by LC-MS/MS (see methods for full details). Error bars represent the standard deviation. Data were analysed using Prism 7 (GraphPad, CA, USA), n=6, *P<0.05, **P<0.01, ***P<0.001.

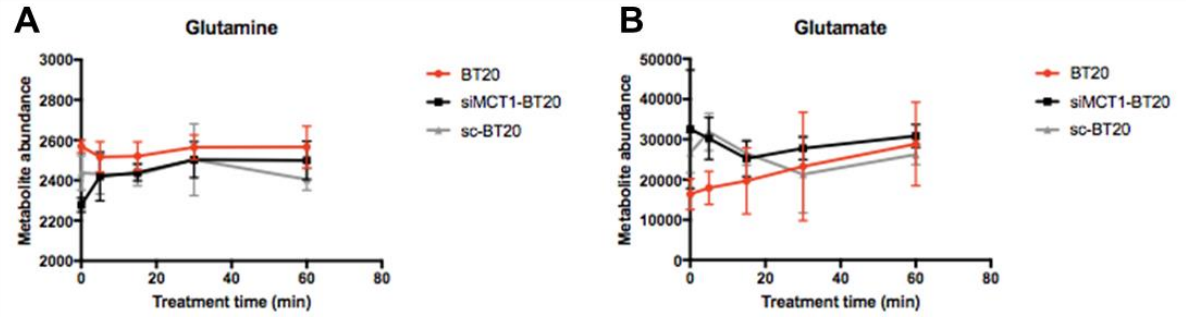

Figure 18 Abundance of glutamine (A) and glutamate (B). Cells were treated with 100 µM 3BP for up to 60 min (n=6) and the metabolites were extracted and analysed with LC-MS/MS (see methods for full details). Error bars represent the standard deviation. Data were analysed using Prism 7 (GraphPad, CA, USA).

3.5.4.2 Reducing capacity

In the context of 3BP, it is useful to divide antioxidants in thiol-based and non-thiol-based, because those containing a thiol group can react with 3BP directly. The two main thiol-containing molecules that act as scavengers for reactive oxygen species (ROS), protecting the cells from oxidative stress, are glutathione (reduced form, GSH) and N-acetyl-cysteine (NAC). Both GSH and NAC were identified. NAC abundance was found to be reduced selectively in MCT1-expressing cells at 30 min treatment. At 60 min, there is still significant difference between BT20 cells and siMCT1-BT20 cells but the difference between the sc-BT20 and siMCT1-BT20 cells is lost (**Figure 19**). This could be related to the transfection or it could be attributed to experimental error. GSH, which was also identified in the previous data set, shows a very interesting pattern. Specifically, it gets selectively depleted in MCT1-expressing cells, and then recovers, which is consistent with the pattern in the previous data set (**Figure 15**). Since the interaction between 3BP and GSH is irreversible, this could be attributed to biosynthesis of more GSH.

Nicotinamide adenine dinucleotide and its phosphate (NADH and NADPH) are ubiquitous enzyme cofactors donating high energy electrons (hydride) for redox and non-redox biosynthetic

reactions. NADH and NADPH are essential for the catabolism of glucose, amino acids, fatty acids and ketone bodies, and are required for the action of over 200 enzymes, most of which are dehydrogenases. The hydrides (reducing equivalents) of NADH are mainly used in the respiratory chain for energy production while those of NADPH are preferentially used for the biosynthesis of various metabolites. NADH was identified and the change in its abundance is shown in **Figure 19A** and **B**, for 30 and 60 min treatment, respectively. Although it appears as if there is a trend of selective decrease in MCT1-expressing cells, which would be in agreement with the previous data set, the variability is too big to produce statistically significant results. NADPH cannot be detected by the method used to produce these data. However, the major biosynthetic pathway for NADPH is the oxidative part of PPP, in which we see accumulation of all intermediates, implying that NADPH is generated. Overall, in MCT1 positive cells, there is a significant decrease in compounds serving to protect from oxidative stress, but the current data suggest that this is due to direct reaction of 3BP with the sulfhydryl group of NAC and GSH rather than an effect of ROS content.

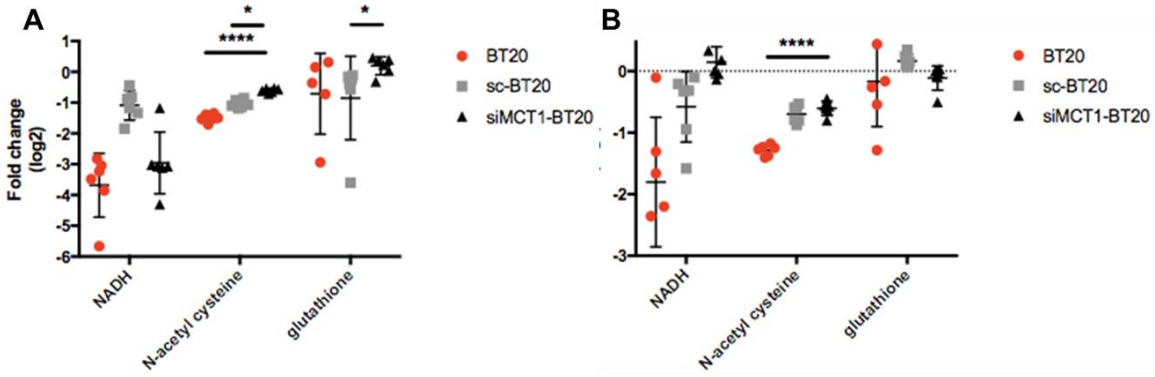

Figure 19 3BP effects on antioxidant levels following 30 min (A) or 60 min (B) treatment. Cells were treated with 100 µM 3BP for up to 60 min (n=6) and the metabolites were extracted and analysed with LC-MS/MS (see methods for full details). Error bars represent the standard deviation. Data were analysed using Prism 7 (GraphPad, CA, USA). *P<0.05, ****P<0.0001.

3.5.4.3 Nucleotide synthesis

Nucleotide synthesis was affected substantially by 3BP treatment and, crucially, siMCT1-BT20 cells seem to be significantly less affected than both other groups (**Figure 20**). While there is major difference between the BT20 control and the siMCT1-BT20 group for most metabolites on the graph, it seems that the sc-BT20 group lies in between the two groups. This could be attributed to the non-specific effects of the transfection or, more likely, to the incomplete silencing of the gene. This is not unusual – siRNA transfection is not likely to result in permanent 100% silencing. Despite this incomplete silencing, statistical analysis of the difference between the sc-BT20 group and the siMCT1-BT20 group shows that for most metabolites, there is a small but significant difference. This provides strong evidence that the metabolite changes reported here are actually induced by 3BP delivery into cells via the MCT1. With regards to energy production, we can observe that ATP is significantly ($P<0.0001$) but only moderately ($\log_2(FC)=0.89$) decreased in BT20 cells, which is consistent with the previous data set (**Figure 16**), which compared between different cell lines. The 3BP concentration used here, 100 μM, is close to the IC50 for these cells and has been shown to be toxic even at short time points (2 and 3 h MTT assays, data not shown). This could imply that energy depletion might not be substantial enough to result in cell death, so this point could be considered for further investigation.

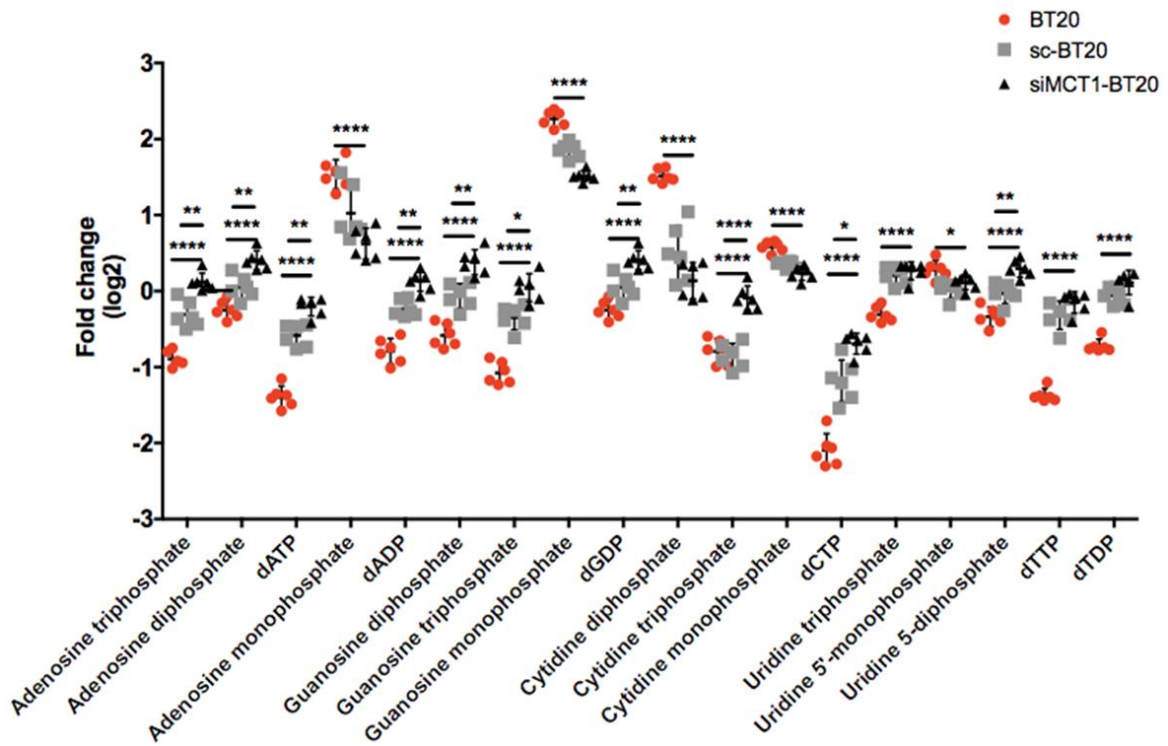

Figure 20 Changes in levels of nucleotides in response to 3BP treatment. Effect of 60 min treatment with 100 µM 3BP on BT20, sc-BT20 and siMCT1-BT20 cells (n=6). Sc-BT20 refers to BT20 cells transfected with scrambled siRNA. siMCT1-BT20 refers to cells transfected with siRNA against siMCT1. Cells were treated with 100 µM 3BP for up to 60 min (n=6) and the metabolites were extracted and analysed with LC-MS/MS (see methods for full details. Error bars represent the standard deviation. Data were analysed using Prism 7 (GraphPad, CA, USA). *P<0.05, ****P<0.0001.

3.5.5 Bioenergetics

Oxygen consumption rate (OCR) and extracellular acidification rate (ECAR) were measured using a Seahorse XF96 analyser following overnight incubation of cells with a sub-toxic concentration of 3BP (20 μM). It was hypothesized that since there is a clear inhibition of glycolysis in MCT1-expressing cells, ECAR would decrease in BT20 cells with a potential simultaneous increase in OCR. Overall, we expected the cells to be more oxidative. However, no statistically significant decrease in ECAR was observed in BT20 cells at this low concentration of 3BP. Importantly, the cells do not appear to be significantly less metabolising ('less energetic' in the bioenergetic profile graph **Figure 21D**) and the BT20 cells seem slightly more aerobic after

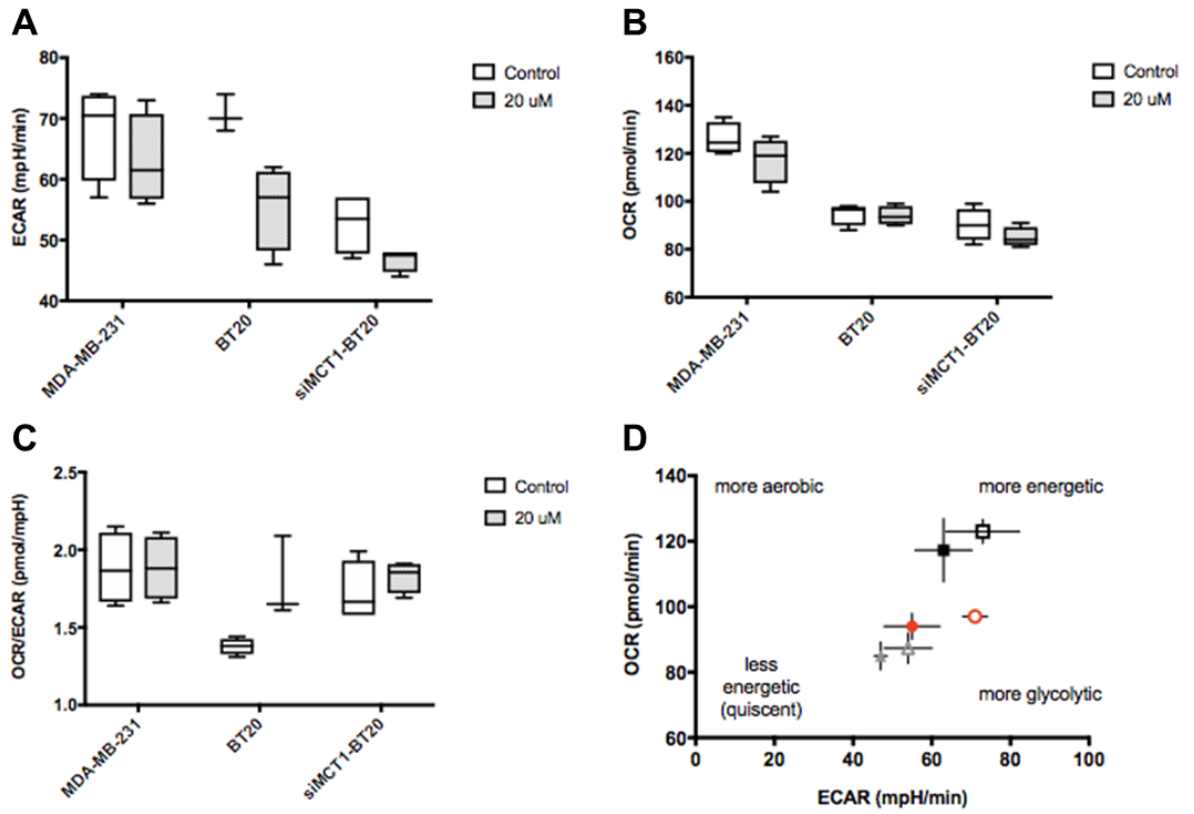

Figure 21 Oxygen consumption and acidification rate changes in response to low concentration 3BP. (A), (B) and (C) Extracellular acidification rate (ECAR), oxygen consumption rate (OCR) and their ratio (OCR/ECAR) respectively, in BT20, MDA-MB-231 and BT20 cells transfected with siRNA against MCT1 (siMCT1-BT20), treated with 20 μM 3BP overnight (D) OCR plotted against ECAR as a metric of the metabolising state of the cells (n=4). OCR and ECAR were measured using a Seahorse XF96 analyser and OCR/ECAR and bioenergetic profile were calculated from these values (see methods for full details). Error bars represent the standard deviation. Data were analysed with Prism 7 (GraphPad, CA, USA).

treatment. This result aligns with the expected direction, but needs to be further confirmed with other concentrations and incubation times. In BT20 cells, OCR is not altered at all so the change in bioenergetics is attributed to the marginal decrease in ECAR. ECAR, OCR, ECAR/OCR ratio and bioenergetic profile are presented in **Figure 21.**

3.6 Discussion

This chapter explored the effects of 3BP, a promising emerging therapeutic, on two TNBC cell lines. TNBC is defined by the lack of expression of hormone and human epidermal growth factor receptors (ER^-, PR^- and $HER2^-$) and it is an aggressive and intrinsically heterogeneous form of breast cancer with no available targeted therapies. Apart from surgery and radiotherapy, the mainstay of treatment is chemotherapy with cytotoxic agents. TNBC responds to chemotherapy and patients benefit from it, but the need for targeted, less toxic treatments is immense. Most tumours with a triple-negative histological profile belong to the basal-like molecular subgroup.

Although MCT1 presents a ubiquitous expression across the body[36–38], many tumours have been found to overexpress this isoform[37,39]. Birsoy *et al.*[1] also compared its expression in cancer cell lines and compared it to expression in their healthy counterpart, in many cases showing MCT1 overexpressed in the cell lines. In the context of BC, MCT1 has been found to be more often overexpressed in the basal-like breast carcinomas and its expression has been co-related with more aggressive disease and poorer outcomes in breast and other solid tumours[3712,15,40–42]. MCT1 and MCT4 are the isoforms of the monocarboxylate transporters that have been investigated the most in the context of cancer. MCT4 expression is correlated with glycolytic metabolism, in which it serves mainly as a lactate exporter, as seen physiologically in the white muscle fibres[36,43]. In physiological conditions, MCT1 is mostly associated with lactate uptake for mitochondrial metabolism, although it is prevalent in tissues that mainly export lactate as well e.g. glial cells[36]. Entering through MCTs, lactate can be converted to pyruvate by lactate dehydrogenase (LDH),

enter the mitochondrial matrix via its transporter and fuel the TCA cycle after conversion into acetyl-CoA. In fact, a recent publication from Rabinowitz's group has shown that circulating lactate constitutes the main fuel of the TCA cycle for most tissues, including tumours, with notable exceptions being the brain and pancreatic cancer[44]. There is also metabolic coupling between tissues with glycolytic metabolism/high MCT4 expression and those with oxidative metabolism/high MCT1 expression. In healthy physiology, this coupling has been long established e.g. between the liver and the working muscle (Cori cycle), while Sonveaux *et al.* were the first to unveil this 'metabolic symbiosis' in tumours[45].

Nonetheless, there is also compelling evidence that MCT1 is strongly expressed in cancer tissues with high rates of glycolysis, including basal-like carcinomas which, typically, are highly glycolytic[1,12,32,46,47]. It seems that the role of MCT1 might be context-related since the transporter itself is bidirectional depending on substrate concentration on either side. It would be interesting to investigate if glycolytic tumours with high MCT1 expression can metabolise lactate in normoxic conditions. In contrast to the traditional view of cancer metabolism, it is now recognised that the majority of cancer cells still produce most of their ATP by mitochondrial metabolism, upregulating both OXPHOS and glycolysis simultaneously[48,49].

3.6.1 Transporter expression

For this work, the aim was to identify a cell line in the TNBC cohort that has high expression of MCT1 and, ideally, low MCT2 and MCT4, to serve as an 'MCT1-positive' control, and one with low MCT1 to serve as an 'MCT1-negative' control. For the negative control, MCT2 would ideally be low as well because this transporter also has monocarboxylate import capacity. Most breast cancer cell lines do not express both 'high affinity' isoforms (MCT1 and MCT2) but co-expression of MCT1 and MCT4 is common[32], as seen by correlating mRNA expression for each transporter within a data set of 60 BC cell lines available from the Broad Institute Cancer Cell Line

Encyclopedia (CCLE). Although MCT4 has been considered as a potential resistance mechanism to treatments targeting MCT1, the latter has been shown to be the main regulator of pyruvate export[14] – when present – and, in the case of 3BP treatment, the main indicator of 3BP sensitivity[1]. MDA-MB-231 was selected as the MCT1-negative cell line and BT20 as the MCT1-positive. Both cell lines belong to the TNBC basal-like subgroup. Expression of MCT1 and MCT4 was confirmed with Western blot (**Figure 10**). Interestingly, MDA-MB-231 was the first TNBC cell line that was examined for MCT1 expression, erroneously leading to the conclusion that MCT1 is not expressed in TNBC[50].

3.6.2 3BP is selectively toxic to cells strongly expressing MCT1

In accordance with the expression levels of MCT1, BT20 cells were found to be significantly more sensitive to 3BP treatment than MDA-MB-231 cells. The differential sensitivity was evident even at time points as short as 2 h under normal growth conditions (**Appendix, Figure A2**). The initial apparent increase in viability of MDA-MB-231 cells at the 24 h time point could be due to the high division rate of these cells (25-40 h). Co-treatment with 3BP and CHC, a classic MCT1 inhibitor, strengthened the evidence for an MCT1 specific effect provided by previous viability measurements by partially reversing 3BP toxicity against BT20 cells, while MDA-MB-231 cells remained unaffected. CHC is routinely used for MCT1 inhibition but it is not highly specific for MCT1[51–53]. AZD3865, a newly developed specific MCT1/2 inhibitor[54], could also be used. CHC was not found to be toxic to either of the cell lines at the selected concentration (1 and 5 mM) implying that even in the BT20 cells MCT1 might not be essential for at least short-term survival. Long-term proliferation studies, e.g. clonogenic assays, would be needed to confirm whether MCT1 function affects cell viability and growth. Work by Pinheiro *et al.* has shown that cells pre-treated with siRNA against MCT1 formed smaller tumours in mice than BT20 cells with normal

MCT1 expression or transfected with scrambled siRNA, although the transporter was silenced only for the first few days after inoculation[55].

siRNA-mediated silencing of MCT1 in BT20 cells confirmed that for this cell line, MCT1 is an important determinant of sensitivity to 3BP treatment. Cells transfected with scrambled siRNA showed identical sensitivity to that of wild type BT20 cells (**Figure 12C**), confirming that the transfection itself does not compromise cell viability. Intriguingly, however, siMCT1-BT20 cells are not completely resistant to 3BP, and still more sensitive than MDA-MB-231 cells. This can be attributed to either the remaining MCT1 expression in the siMCT1-BT20 cells (although much reduced it still detectable by WB) or it could imply that there is another route of 3BP entry in addition to MCT1. The two theories are not mutually exclusive, both could be happening at the same time. MCT1 expression in MDA-MB-231 cells is below the detection limit of the WB analysis however, they are affected by 3BP to some extent. The alternative transport route could be another MCT isoform or passive diffusion. Both BT20 and MDA-MB-231 cells express MCT2[56,57], the role of which in 3BP transport has not been investigated in this work and has not received much research attention in general. Transport of 3BP via passive diffusion is unlikely to be a significant contributor to 3BP effects because 3BP is ionised in physiologic or mildly acidic tumour-associated pH (7.4 and 6-6.5 respectively) and therefore cannot efficiently cross the lipid bilayer which forms the cell membrane.

3.6.3 3BP is taken up selectively by MCT1-expressing cells

Uptake is a prerequisite for toxicity, so it can be safely concluded that 3BP is taken up by BT20 cells and its uptake is reduced when MCT1 is silenced. However, cells could take up 3BP but be otherwise resistant to its effects. Therefore, experiments at early time points were performed and showed that bromide (^{78}Br and ^{80}Br) content was higher in wild type BT20 cell lysates compared to both MDA-MB-231 and siMCT1-BT20 cell lysates. Bromide content in control sc-BT20 cells was similar to that in non-transfected BT20 cells, as expected (**Figure 13**).

There is no reason why bromide would be preferentially retained by any of these cell lines. Intact 3BP does not survive the LC-MS conditions, which is why uptake of the whole molecule cannot be profiled. Once in the cell, 3BP acts as an alkylating agent with bromide acting as a leaving group. Therefore, it would not be expected that significant differences in the organic peak (hydroxypropanedioic acid) would be observed as it would not be found as a free ion, rather the target proteins would be 'pyruvylated'.

Arguably, the most commonly used method to test uptake of a metabolite is to use a radiolabelled analogue of it, usually with ^{14}C, ^{3}H or ^{18}F. These analogues are readily available for natural metabolites e.g. glucose, lactate and pyruvate. Access to ^{14}C-3BP however was impractical, time consuming and uneconomical, while in-house synthesis was time and resource-consuming and largely out of the scope of this work. Heavy isotope labelling for detection via nuclear magnetic resonance (NMR) spectroscopy was also considered but presented similar limitations.

Taken together, the cell viability studies and differential bromide abundance in cell lysates provide strong evidence that 3BP is taken up preferentially by MCT1-expressing BT20 cells and that reduced expression of the transporter results in reduced uptake, and ultimately reduced toxicity.

3.6.4 3BP has multiple metabolic targets

Previous research on the intracellular targets of 3BP suggests the existence of multiple targets in various pathways[58]. Most studies have been based on biochemical assays looking at a single or a limited number of enzymes or metabolic endpoints. Pedersen's group, the first group that drew attention to 3BP for cancer treatment, have suggested that HK-2 inhibition, and subsequent ATP depletion is the main cause of 3BP toxicity[59]. Definitive covalent binding of 3BP to HK-2 was shown by Chen *et al* in 2009[60]. Ganapathy-Kanniappan and colleagues[28] used [14C]-3BP to show that 3BP covalently binds ('pyruvylates') to GAPDH and inactivates it. These

researchers reported dose-dependent ATP depletion and paradoxical increase in intracellular lactate levels. The antioxidants GSH[30,32] and NAC[32], as well as acetyl-CoA[32], crucial for the biosynthesis of a range of metabolites, are all thiol-based and have been shown to react with 3BP. Depletion of ATP has been consistently reported, while the mode of cell death is controversial among publications[35,61]. Ganapathy-Kanniapan *et al.* argued that it is an apoptotic process in hepatocellular carcinoma cells whereas Sun et al. argue that it is via a necroprotic and apoptotic mechanism. Valenti and colleagues, working with PC-3 prostate cancer cells, found necrosis as the primary mechanism of cell death[62]. Other proposed targets include glutamate dehydrogenase (GDH)[63], succinate dehydrogenase (SDH)[64], ribonuclease, macrophase migration inhibitory factor[65], pyruvate dehydrogenase (PDH)[66], vacuolar H^+-ATPase[67] and sarco/endoplasmatic reticulum Ca^{2+}-ATPase[68].

Given that knowledge of the effect on individual targets in different systems has now accumulated, an unbiased, untargeted metabolomics analysis was deployed here to elucidate some of the metabolic effects of 3BP in the TNBC cell lines used. Recent work on 3BP by other groups has also adopted a broader approach, rather than focusing on particular enzymatic targets. Ganapathy-Kanniappan *et al.* confirmed GAPDH inhibition by showing approximately 70% decrease in GAPDH enzymatic activity by 100 μM 3BP (as in the current study) and direct binding of [14C]-3BP to the enzyme. These workers also performed a wider investigation to show that in two hepatocellular carcinoma cell lines the translation globally inhibited, and cell death is induced by an apoptotic process[35]. While the work in this thesis was in progress, Liberti *et al.*[31] published their work on koningic acid, another GAPDH inhibitor, which they compared with glycolytic inhibitors including 3BP in HCT116 cells. Their metabolomic analysis showed that 3BP causes a dose-dependent (0-500 μM) perturbation on the lower part of glycolysis, TCA cycle and biosynthesis of fatty acids. This profile with 3BP was different to that achieved with other such inhibitors, notably, another halogenated monocarboxylate, iodoacetate. Last year, Darabedian *et*

al[69]. published their work on an alkyne derivative of 3BP and showed it binds to several proteins other than GAPDH, and indeed concluded that it was not necessarily involved in glycolysis at all. Yadav et al, conducted *in silico* molecular docking calculations and also came to conclude that 3BP has several metabolic targets[70]. Overall, it seems that 3BP still attracts a lot of interest as a cancer therapeutic and several groups have come to realise that the pleiotropic actions of this molecule can more effectively be approached by larger scale experiments such as genetic screens, proteomics and metabolomics. These findings are all in accordance with the data presented in this thesis. Notably, none of the aforementioned studies characterised or controlled for the role of the MCT1 as rigorously as in the studies reported here.

3.6.5 Effects on glycolysis, TCA and PPP

The first crucial step for glucose metabolism is the phosphorylation of glucose to glucose-6-phosphate (glucose-6P) via phosphate transfer from ATP, which traps glucose in the cell. Glucose-6P can then enter the glycolytic pathway and mitochondrial metabolism (TCA followed by the electron transport chain) to be used primarily for energy generation in the form of ATP, or shunted into the PPP for the generation of biosynthetic intermediates and maintenance of redox homeostasis[34]. Current results show that ATP was indeed decreased up to $\log_2(FC)=-0.89$ in BT20 cells, but not in MDA-MB-231 cells or MCT1-null cells. This level of depletion is comparable to the level recently reported by Byrne *et al.*[32], who found that 100 μM 3BP reduced ATP production by 60% after 1.5 h treatment in endometrial cancer cells, while Birsoy *et al.*[1], who worked with leukemia cells found almost complete hindrance of ATP production with 80 μM 3BP. Ko *et al.* also showed complete arrest of ATP production in hepatic carcinoma cells starting at 30 μM with corresponding dramatic decrease in cell viability[71]. Indeed, it could be concluded that sensitivity to 3BP is very cell line-dependent, and the relative contributions of different enzymes/pathways to the final outcome also varies markedly. Hence, although 3BP can readily alkylate a range of

nucleophiles in cell free conditions, there is context dependency to which reactions will predominate intracellularly.

Glucose phosphorylation is catalysed by hexokinase. There are four isoforms of this enzyme in human cells, which differ in their expression patterns, subcellular localisations, and catalytic/regulatory properties[60]. HK-1 and HK-2 localise mostly on the outer mitochondrial membrane, HK-3 in a perinuclear compartment and HK-4 is cytosolic in liver and pancreatic cells. Isoform HK-2 is frequently upregulated in cancer. It is strategically located on the outer mitochondrial membrane to shunt glucose into glycolysis, and is thus correlated with the 'Warburg effect' and plays a role in evading apoptosis via association with the mitochondrial voltage-dependent anion channel (VDAC)[59,72].

HK-2 is considered one of the glycolytic targets of 3BP[60], along with GAPDH[28,29,58]. With the current approach, fructose-6P and glucose-6P cannot be distinguished. Hence a decrease in the concentration in either of these metabolites can not be detected, which suggests that HK-2 inhibition might not occur. Jardim-Messede *et al.* also came to this finding in their work with isolated mitochondira and HepG2 carcinoma cells. Using 50 or 100 μM 3BP, they concluded that this concentration is not high enough for HK-2 inhibition, although experiments with higher levels were not performed[73].

Glucose-6P and fructose-6P can be diverted to the PPP. Activity of glucose-6P-dehydrogenase (G6DH) is crucial for diverting glucose-6P into the oxidative phase of PPP with conversion of glucose-6P into 6P-gluconolactone with parallel conversion of $NADP^+$ into NADPH. Although 6P-gluconolactone could not be identified, the next intermediate of the oxidative phase, 6P-gluconate was identified and indeed, shown to accumulate over the course of 3BP treatment. This outcome was shared by both BT20 and MDA-MB-231 cells but BT20 cells showed a more pronounced response (**Figure 14**). Fructose-6P enters the PPP as sedoheptulose-7P at the non-oxidative phase of the PPP. Accumulation of this intermediate, as well as ribose-5P,

one of the most important products of PPP were shown to be selective (but not exclusive) to MCT1-expressing cells (**Figure 14**). This outcome was consistent in both data sets, comparing between MDA-MB-231 and BT20 cells, and comparing between wild-type BT20 cells and those transfected with siRNA against MCT1.

Simultaneously, the glycolytic intermediate fructose-1,6P_2 was shown to have substantial accumulation in MCT1-expressing cells. Fructose-1,6P_2 is upstream of GAPDH and downstream of HK-2. Combined with the build-up of PPP intermediates, these results imply that glucose phosphorylation by HK-2 proceeds to a significant extent. Partial inhibition cannot be excluded, as accumulation of metabolic intermediates may result from downstream inhibition, as is clear in the case of fructose-1,6P_2. GAPDH products cannot be detected but the selective accumulation of fructose-1,6P_2, one step upstream from GAPDH is in agreement with the well-established inhibition of this enzyme by 3BP[29,74].

DHA and its phosphate, DHAP, form the bridge between glycolysis and fatty acid synthesis. DHAP can be converted to glycerol-3P, the backbone of triglycerides, in a reversible step requiring NADH as a co-factor (NAD^+ to go backwards). With the current data, it is unclear what the effect is on these metabolites and subsequent fatty acid metabolism. At the final time point (60 min), a slight but statistically significant increase of glycerol-3P and DHAP appears in BT20 cells (**Figure 14**). For fatty acid synthesis, acetyl-CoA is required, which has been shown to also directly react with 3BP[32], as per other compounds containing a sulfhydryl moiety. It could be anticipated that the decrease in NADH, as shown here, combined with the 'pyruvylated' CoA, would result in a decrease in fatty acid synthesis, which could be interesting to investigate in the future.

Moving into the mitochondria, the TCA cycle is the common gate to the oxidative metabolism of many organic fuels, including pyruvate from glycolysis, but also amino-acids and fatty acids that enter the cycle in the form of acetyl-CoA. As a first step, a 4-carbon entity, oxaloacetate is condensed with the 2-carbons from acetyl-CoA to give the first 6-carbon

intermediate, citrate. Citrate can then be isomerised to isocitrate and continues into the TCA cycle, or it can serve other purposes e.g. contribute to fatty acid synthesis. Overall, the TCA produces high energy electrons in the form of 3 NADH equivalents and 1 $FADH_2$, to be used by the ETC for energy production, along with 1 eq of GTP and 2 eq of CO_2 for the oxidative decarboxylation of citrate. The TCA is fuelled by glutamine catabolism, and since glutamine is plentiful in the media, TCA could be expected to proceed even if glycolysis is inhibited. As Jardim-Messeder *et al.* recently showed using HepG2 cells, glutaminolysis is not directly inhibited by 3BP (100 uM) and it can continue to fuel the TCA[73]. Furthermore, the TCA can be fuelled by fatty acids at the citrate step, which may also help explain why after the 1 h treatment with an intermediate concentration of 3BP (100 μM) used here, no major changes in the TCA were observed.

PPP is one of the pathways most clearly affected with selectivity towards the MCT1-expressing cells (**Figure 14**) observed. PPP is intercalated with glycolysis, hence its connection to energy metabolism, while its primary purpose is generation of reducing equivalents in the form of NADPH and activated 5-carbon sugars as nucleotide precursors. When there is more need for energy production, PPP can feed glycolysis at the fructose-6P or glucose-6P point, while it can proceed with the production of NADPH and ribose-5P when the balance is leaning towards biosynthetic intermediates and protection from oxidative stress. Notably, NADPH is required for the recycling of GSSG (oxidised glutathione) back to GSH (reduced glutathione). PPP appeared with significant selective accumulation of intermediates, especially the later ones (i.e. the 7-carbon containing metabolites). PPP is controlled at the first (irreversible) step of the conversion of glucose-6P into gluconolactone-6P which is in turn positively impacted by the levels of $NADP^+$(**Figure 14**). Gluconate-6P, the next metabolite in the process, is clearly accumulating in MCT1-positive cells, implying that the conditions are met for the PPP to proceed. Importantly, the interplay between PPP and glycolysis can be adjusted depending on the needs of the cell (NADPH, ribose-5P or ATP). From the accumulation of intermediates, it seems that it is shifted

towards the synthesis of NADPH and ribose-5P, which could be the combined outcome of inhibition of GAPDH not permitting reversal to ATP, and consumption of the produced NADPH, which cannot be seen directly but could be anticipated since the thiol-containing antioxidants are being consumed.

These data sets, essentially present snapshots of metabolite abundance at certain time points, and would therefore be complemented by metabolic flux analysis. Labelling of selected nutrients with heavy isotopes (typically ^{13}C, ^{15}N, and ^{2}H) and following the labelling of metabolites downstream allows the flow of intermediates to be followed through metabolic pathways. This approach has not yet been published for 3BP response. As for metabolomics, this can be done with either MS or nuclear magnetic resonance (NMR) spectroscopy. The two techniques are not interchangeable, as metabolic flux analysis does not provide information on the metabolite levels, provided by metabolomics[49]. Comparison between control cells and 3BP treated cells of [13C]-glucose flux would be able to determine the extent of the contribution of HK-2 inhibition.

3.6.6 Effects on antioxidants

There are several reports suggesting that 3BP reacts with glutathione and is subsequently de-activated intracellularly or in cell-free systems[30,58,75]. These results align with the finding reported here (**Figures 15** and **18**). In fact, the putative level of glutathione has been shown to define the level of sensitivity of the cell to 3BP treatment, and glutathione has been proposed as a potential 'antidote' for 3BP toxicity[58,76]. This suggests that MCT1 is not the only determining factor for 3BP toxicity. Glutathione and NAC, both thiol-containing antioxidants, can rescue hepatocellular carcinoma cell line HepG2 from 3BP toxicity[77]. In the present study, the concentration of 3BP was not varied. Instead, a time-course experiment was carried out at a concentration close to the IC50 for the BT20 cells. Interestingly, glutathione depletion peaked at 15 min but then partially recovered at later time points. BT20 cells were richer in glutathione at baseline, however depletion

was still more profound than that in MDA-MB-231 cells. In MCT1-null cells glutathione levels were not affected at all.

NAC was not identified in the first data set comparing BT20 and MDA-MB-231 cells. Comparing between MCT1-expressing and siMCT1 treated BT20 cells, NAC followed a similar trend to that observed for glutathione, although its concentration decreased even in the siMCT1 treated BT20 cells ($log_2(FC)=-1.28\pm0.09$ for BT20 cells, 60 min treatment and $log_2(FC)=-0.60\pm0.07$ for siMCT1-BT20 cells, 60 min treatment). This finding could suggest that NAC more readily reacts with 3BP or it could be a function of absolute concentrations. With the current data, it cannot be determined whether the cells are richer in NAC or glutathione as this would require a standard curve using the LC-MS/MS system for each compound (relative peak intensity cannot be used to compare concentrations of different compounds).

Hydride donors such as the enzyme co-factors NADH and NADPH are regulators of the redox capacity of the cell. Importantly, these compounds cannot be directly 'pyruvylated', in a manner similar to NAC and GSH as they do not contain a sulfhydryl group. NADH abundance was found to be reduced, and potentially starting to recover at the end of the 3BP incubation time. NADH's main functions are in energy production, while NADPH is the main nicotinamide adenine dinucleotide contributing in reductive biosynthesis and redox homeostasis. Cytosolic NADPH is recycled (from NADP) via the malic enzyme 1 (ME1), isocitrate dehydrogenase 1 (IDH1) and the oxidative phase of PPP, which is the main contributor[78]. Accumulation of PPP intermediates, especially the later ones (i.e. sedoheptulose phosphates) in the non-oxidative phase, suggest that PPP is proceeding and hence, NADPH is produced. However, it is not clear whether NADPH is generated by ME1, which catalyses the conversion of malate to pyruvate. Malate, the ME1 substrate, does accumulate. Direct measurement of NADPH by a colorimetric assay, as well as by measurement of total thiol content and ROS would help to build a more complete picture regarding 3BP effect on redox homeostasis. As others have shown for various cell lines, a 'rescue'

study would also be valuable[58] . Proving that 3BP reacts with glutathione and other antioxidants does not necessarily mean that this is how it causes toxicity and it might be one of several contributing factors. This would be the case if glutathione, NAC or NADPH can rescue the cell from 3BP treatment. Crucially, thiol-based and non-thiol antioxidants act in different ways with respect to 3BP. Thiol-based compounds directly react with 3BP (stoichiometric inhibition), therefore they presumably do not allow it to exert its other functions.

3.6.7 Nucleotide synthesis is selectively inhibited in MCT1-expressing cells

Nucleotides have multiple roles in cells, other than being activated precursors for the synthesis of nucleic acids, DNA and RNA. The nucleoside triphosphate ATP is the universal energy currency in biology, acting as a phosphate donor. GTP can also be used as an energy source but is reserved for selected processes. Nucleotide derivatives, such as UDP-glucose constitute important biosynthetic intermediates for other macromolecules, such as glucagon. Nucleotides also participate in cellular signalling transduction, e.g. cAMP and cGMP are intra- and inter-cellular second messengers[34].

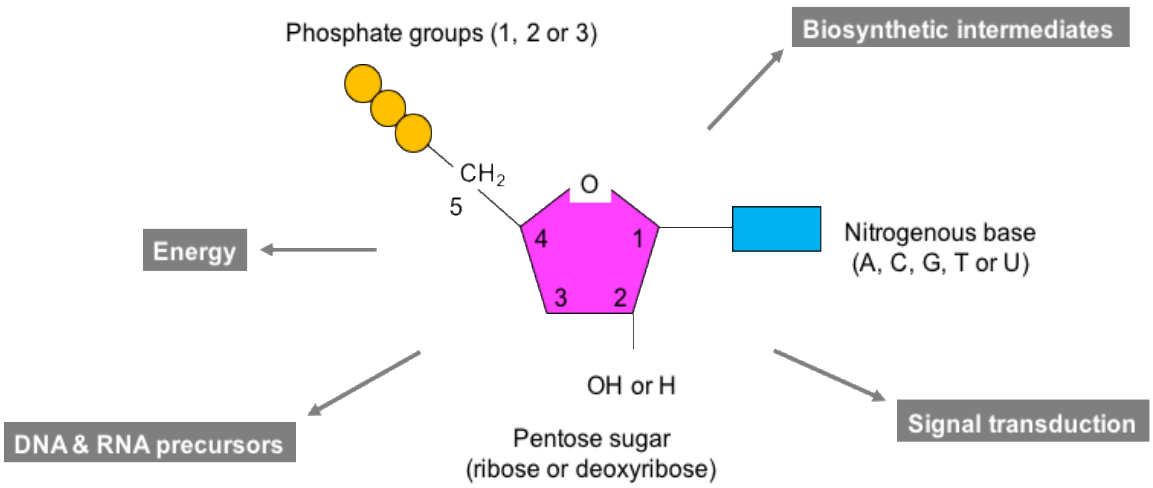

Figure 22 Structure and role of nucleotides. Nucleotides consist of a pentose sugar (ribose or deoxyribose), a nitrogenous base (purine or pyrimidine) and 1-3 phosphate groups. Nucleotides are the immediate precursors of nucleic acids, they act as energy sources and participate in signal transduction. A: Adenine, C: Cytosine, G: Guanosine, T: Thymine and U: Urasil.

Proliferating cells have to commit to *de novo* nucleotide biosynthesis, which is a complex process requiring input from glycolysis and PPP, while non-essential amino acids are utilised for the construction of the bases and methyl groups are donated from the one carbon/folate pool[49,79]. To put the metabolic changes in context, the requirements for nucleotide synthesis are explained (**Figure 22**). A nucleotide is composed of three building blocks: five-carbon sugar (ribose or deoxyribose), a nitrogenous base and at least one phosphate group. As the generic nucleotide structure (**Figure 22**) suggests, nucleotide biosynthesis requires a nitrogen source, which comes from asparagine and glutamine side chains, while the ring structure is built from glycine and aspartate. The sugar comes from the PPP product, ribose-5P (in the activated form, phosphoribosylpyrophosphate (PRPP)). Nucleotides can be synthesized *de novo*, starting with PRPP and amino-acids, or through anaplerosis, starting with PRPP and a pre-synthesized base. Glutamine is an indispensable form of reduced nitrogen required for nucleotide synthesis. For the production of 1 eq of uracil or thymine, 1 eq of glutamine is needed. Cytosine and adenine cost the cell 2 eq of glutamine, while *de novo* synthesis of a guanine base requires 3 eq[34,79]. Crucially, cells growing in supplemented culture media have unrestricted access to glutamine, which is not necessarily the case *in vivo*. Perhaps as a consequence of saturating levels in the media glutamine and glutamate concentrations remain unaffected during 3BP treatment (as seen in **Figure 18)**. Other than glutamine, aspartate and glycine are also utilised for the synthesis of the purine and pyrimidine bases and their concentration is at steady state too (data not shown). The biosynthesis of nucleotide bases is summarised in **Figure 23**.

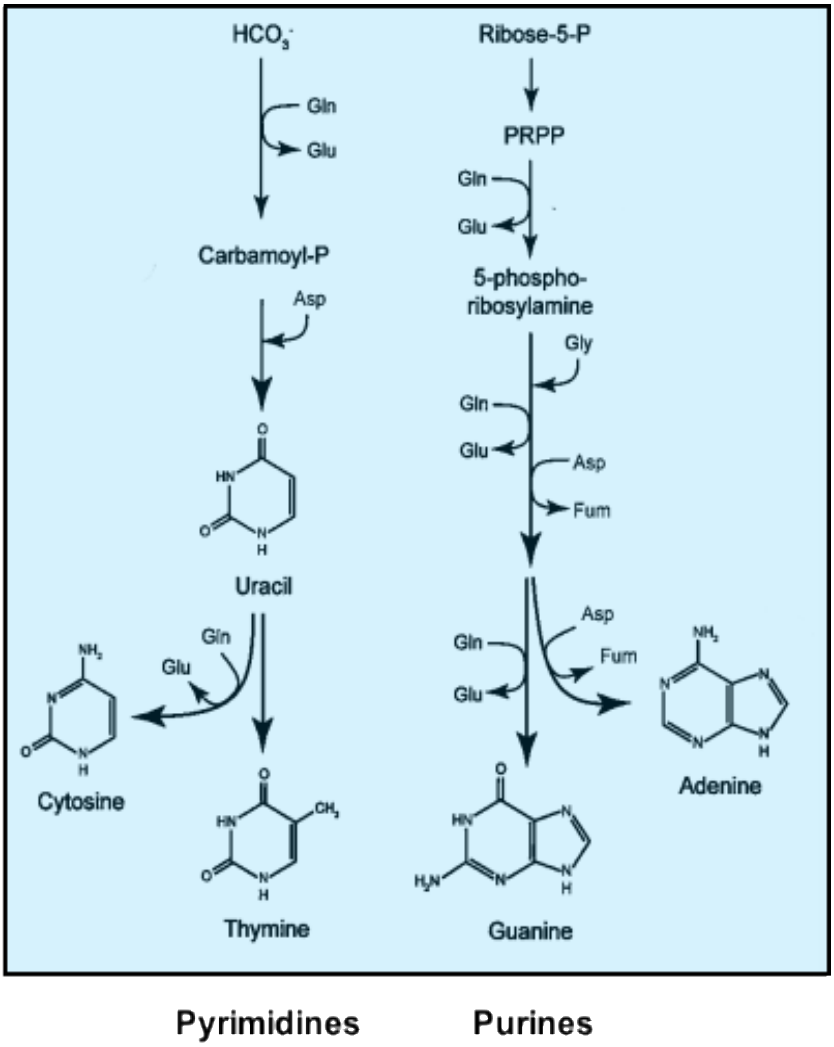

Figure 23 Synthesis of purine and pyrimidine base. Figure adapted from Pavlova N. and Thompson C., 2016.

The effects of 3BP on nucleotide mono-, bi- and tri-phosphate levels have been consistent between the BT20 cells v MDA-MB-231 and the BT20 vs siMCT-BT20 data sets, with only a few exceptions (GMP, dAMP and CDP). Overall, nucleotide biosynthesis decreased in BT20 cells in both data sets. It was found that ATP was decreased significantly within one hour of treatment. In both studies the decrease was statistically significant and exclusive to MCT1-expressing cells

but moderate (less than two-fold), which might suggest that ATP depletion is not the only contributing factor in the substantial toxicity which is already observed at short time points (**Appendix, Figure A2**). Nucleotide synthesis requires aspartate, which is derived from the TCA cycle through the transamination of oxaloacetate[79], a TCA cycle intermediate. Interestingly, TCA metabolites were not severely affected by treatment apart from citrate which dramatically decreased in the early time points and then recovered by 60 min. Oxaloacetate levels showed a moderate decrease in the first data set and less so in the second. Aspartate is also a metabolite of glutamine and since glutamine is available, it is not expected to be markedly affected. At the same time, PPP is proceeding and ribose-5P/PRPP continue to accumulate. Therefore, in terms of metabolic intermediates, the only one lacking is ATP. Direct inhibition of enzymes involved in nucleotide biosynthesis is also possible, something that has not been reported yet but could be investigated.

3.6.8 Oxidative or glycolytic?

It was hypothesized that since glycolysis is, at least to some extent, compromised by 3BP, cell metabolism would lean more towards mitochondrial oxidative metabolism, which can be fuelled by lactate/pyruvate and glutamine. OCR and ECAR were measured using a Seahorse XF96 analyser set to acquire 5 consecutive measurements after overnight incubation with a low (20 μM) concentration of 3BP. Also, baseline measurements were acquired under the same conditions from untreated wells. Baseline measurement is useful to elucidate whether the cells are different in terms of oxygen consumption to start with. 3BP has been suggested to be toxic toward glycolytic cells. Taking this study forward, and given that effects more global than just glycolytic enzyme modulation have been observed, it would be interesting to see if a 'Warburg phenotype' is a prerequisite for sensitivity to 3BP treatment.

Given the long incubation time, a sub-toxic concentration was chosen to explore whether the shift in oxygen consumption precedes the toxic effects. OCR was not affected at all in MCT1-expressing BT20 or siMCT1-BT20 cells and the small increase in OCR/ECAR ratio in the MCT1-expressing BT20 cells can be attributed to the incremental decrease in ECAR in this cell line. Time limitations did not allow further investigation of the effects of 3BP on OCR and ECAR. However, it may be that this part deserves further exploration, with a wider range of doses and incubation times, while the use of cell lines with different basal metabolism would explain the relative importance of glycolysis over OXPHOS in sensitising the cell towards 3BP.

3.7 Conclusions & future directions

This chapter explored the sensitivity of TNBC cell lines to 3BP, an emerging therapeutic targeting metabolism. In accordance with current evidence suggesting that MCT1 is required for 3BP toxicity, an MCT1-expressing (BT20) and an MCT1-null cell line (MDA-MB-231) were selected. Differential, MCT1-dependent sensitivity was confirmed in these cell lines and further validated with the use of MCT1-inhibitor and siRNA-mediated silencing of the transporter, both of which partially reversed 3BP toxicity. The short-term metabolic effects of 3BP treatment on selected TNBC cell lines and their dependence on MCT1 was then profiled. To this end, untargeted metabolomics provide a high throughput, unbiased approach. At the time of writing, metabolomics analysis of 3BP-treated breast cancer cells has not been carried out before. The novel findings reported here include that several pathways are substantially affected, notably, but certainly not limited to, glycolysis. In particular, significant accumulation of PPP metabolites, inhibition of nucleotide synthesis, antioxidant depletion and various effects on the TCA cycle was observed. Most of these effects showed a statistically significant difference in MCT1-expressing cells. Finally, the effect of 3BP on oxygen consumption and media acidification rate was

investigated, as a measure of oxidative and glycolytic metabolism respectively. Marked changes were not observed, most likely because the chosen concentration was too low.

Upregulation of MCT1 has been found in TNBC. Given the proven selectivity of 3BP towards MCT1-expressing cells and the powerful multi-targeted effects it has on their metabolism, 3BP can be considered as a possible therapeutic for this cancer. Nevertheless, it needs to be appropriately formulated to target its reactivity to the tumour site. The next chapter will investigate the development of a liposome-based delivery strategy for this compound.

3.8 References

1. Birsoy, K. *et al.* MCT1-mediated transport of a toxic molecule is an effective strategy for targeting glycolytic tumors. *Nat. Genet.* **45**, 104–8 (2013).
2. Breast cancer statistics | Cancer Research UK. https://www.cancerresearchuk.org/health-professional/cancer-statistics/statistics-by-cancer-type/breast-cancer.
3. Perou, C. M. *et al.* Molecular portraits of human breast tumours. *Nature* **406**, 747–752 (2000).
4. Yadav, B. S., Chanana, P. & Jhamb, S. Biomarkers in triple negative breast cancer: A review. *World J. Clin. Oncol.* **6**, 252–63 (2015).
5. Molecular Subtypes of Breast Cancer. https://www.breastcancer.org/symptoms/types/molecular-subtypes.
6. Hollestelle, A. *et al.* Distinct gene mutation profiles among luminal-type and basal-type breast cancer cell lines. *Breast Cancer Res. Treat.* **121**, 53–64 (2010).
7. Kim, S., Kim, D. H., Jung, W.-H. & Koo, J. S. Metabolic phenotypes in triple-negative breast cancer. *Tumor Biol.* **34**, 1699–1712 (2013).

8. Perou, C. M. Molecular Stratification of Triple-Negative Breast Cancers. doi:10.1634/theoncologist.

9. Chavez, K. J., Garimella, S. V & Lipkowitz, S. Triple negative breast cancer cell lines: one tool in the search for better treatment of triple negative breast cancer. *Breast Dis.* **32**, 35–48 (2010).

10. Cao, M. D. *et al.* Metabolic characterization of triple negative breast cancer. *BMC Cancer* **14**, 941 (2014).

11. van Geldermalsen, M. *et al.* ASCT2/SLC1A5 controls glutamine uptake and tumour growth in triple-negative basal-like breast cancer. *Oncogene* **35**, 3201–3208 (2016).

12. Pinheiro, C. *et al.* Monocarboxylate transporter 1 is up-regulated in basal-like breast carcinoma. *Histopathology* **56**, 860–7 (2010).

13. Pinheiro, C. *et al.* GLUT1 and CAIX expression profiles in breast cancer correlate with adverse prognostic factors and MCT1 overexpression. *Histol. Histopathol.* **26**, 1279–86 (2011).

14. Hong, C. S. *et al.* MCT1 Modulates Cancer Cell Pyruvate Export and Growth of Tumors that Co-express MCT1 and MCT4. *Cell Rep.* **14**, 1590–1601 (2016).

15. Johnson, J. M. *et al.* MCT1 in Invasive Ductal Carcinoma: Monocarboxylate Metabolism and Aggressive Breast Cancer. *Front. Cell Dev. Biol.* **5**, 1–8 (2017).

16. Ko, Y.-H. *et al.* TP53-inducible Glycolysis and Apoptosis Regulator (TIGAR) Metabolically Reprograms Carcinoma and Stromal Cells in Breast Cancer. *J. Biol. Chem.* **291**, 26291–26303 (2016).

17. Li, Z. *et al.* Monocarboxylate transporters in breast cancer and adipose tissue are novel biomarkers and potential therapeutic targets. *Biochem. Biophys. Res. Commun.* **501**, 962–967 (2018).

18. Di Cosimo, S. Lonidamine: efficacy and safety in clinical trials for the treatment of solid

tumors. *Drugs Today (Barc.)* **39**, 157–174 (2003).

19. Study of the Efficacy and Safety of Lonidamine for the Treatment of Symptomatic Benign Prostatic Hyperplasia - Full Text View - ClinicalTrials.gov. https://clinicaltrials.gov/ct2/show/NCT00435448?term=lonidamine&rank=1.

20. A Phase I Trial of AZD3965 in Patients With Advanced Cancer. *Clinicaltrials.Gov* 20130201 (2013).

21. Plummer, R. *et al.* 50OA first-in-human first-in-class (FIC) trial of the monocarboxylate transporter 1 (MCT1) inhibitor AZD3965 in patients with advanced solid tumours. *Ann. Oncol.* **29**, (2018).

22. Glick, M., Biddle, P., Jantzi, J., Weaver, S. & Schirch, D. The antitumor agent 3-bromopyruvate has a short half-life at physiological conditions. *Biochem. Biophys. Res. Commun.* **452**, 170–173 (2014).

23. Fischer, G., Sieber, M. & Schellenberger, A. The carbonyl reactivity of 3-bromopyruvate and related compounds. *Bioorg. Chem.* **11**, 478–484 (1982).

24. Meloche, H. P. Bromopyruvate Inactivation of 2-Keto-3-deoxy-6-phosphogluconic Aldolase. I. Kinetic Evidence for Active Site Specificity. *Biochemistry* **6**, 2273–2280 (1967).

25. Göthe, P. O. & Nyman, P. O. Inactivation of human erythrocyte carbonic anhydrases by bromopyruvate. *FEBS Lett.* **21**, 159–164 (1972).

26. Chang, G. & Hsu, R. Y. The substrate analog bromopyruvate as a substrate, an inhibitor and an alkylating agent of malic enzyme of pigeon liver. *Biochem. Biophys. Res. Commun.* **55**, 580–587 (1973).

27. Ko, Y. H., Pedersen, P. L. & Geschwind, J. F. Glucose catabolism in the rabbit VX2 tumor model for liver cancer: characterization and targeting hexokinase. *Cancer Lett.* **173**, 83–91 (2001).

28. Ganapathy-Kanniappan, S. *et al.* Glyceraldehyde-3-phosphate dehydrogenase is pyruvylated

during 3-bromopyruvate mediated cancer cell death. *Anticancer Res.* **29**, 4909–4918 (2009).

29. Shoshan, M. C. 3-bromopyruvate: Targets and outcomes. *J. Bioenerg. Biomembr.* **44**, 7–15 (2012).

30. Sadowska-Bartosz, I., Szewczyk, R., Jaremko, L., Jaremko, M. & Bartosz, G. Anticancer agent 3-bromopyruvic acid forms a conjugate with glutathione. *Pharmacol. Reports* **68**, 502–505 (2016).

31. Liberti, M. V *et al.* A Predictive Model for Selective Targeting of the Warburg Effect through GAPDH Inhibition with a Natural Product. *Cell Metab.* **26**, 648-659.e8 (2017).

32. Byrne, F. L. *et al.* Metabolic vulnerabilities in endometrial cancer. *Cancer Res.* **74**, 5832–5845 (2014).

33. Khan, A. A. *et al.* Transfection of small RNAs globally perturbs gene regulation by endogenous microRNAs. *Nat. Biotechnol.* **27**, 549–55 (2009).

34. Berg, J. M., Tymoczko, J. L. & Stryer, L. *Biochemistry.* (2006).

35. Ganapathy-Kanniappan, S. *et al.* 3-Bromopyruvate Induces Endoplasmic Reticulum Stress, Overcomes Autophagy and Causes Apoptosis in Human HCC Cell Lines. *Anticancer Res.* **30**, 923–936 (2010).

36. Halestrap, A. P. Monocarboxylic Acid Transport. *Compr. Physiol.* **3**, 1611–1643 (2013).

37. Doherty, J. R. J. & Cleveland, J. L. J. Targeting lactate metabolism for cancer therapeutics. *J. Clin. Invest.* **123**, 3685–3692 (2013).

38. Kennedy, K. M. & Dewhirst, M. W. Tumor metabolism of lactate: the influence and therapeutic potential for MCT and CD147 regulation. *Futur. Oncol.* **6**, 1–32 (2010).

39. Pinheiro, C. *et al.* Role of monocarboxylate transporters in human cancers: State of the art. *J. Bioenerg. Biomembr.* **44**, 127–139 (2012).

40. Latif, A. *et al.* Monocarboxylate Transporter 1 (MCT1) is an independent prognostic biomarker in endometrial cancer. doi:10.1186/s12907-017-0067-7.

41. Pinheiro, C. *et al.* Increased expression of monocarboxylate transporters 1, 2, and 4 in colorectal carcinomas. (2008) doi:10.1007/s00428-007-0558-5.

42. Martinho, O. *et al.* Monocarboxylate transporters (MCTs) in gliomas: expression and exploitation as therapeutic targets. **15**, 172–188 (2013).

43. Dimmer, K. S., Friedrich, B., Lang, F., Deitmer, J. W. & Bröer, S. The low-affinity monocarboxylate transporter MCT4 is adapted to the export of lactate in highly glycolytic cells. *Biochem. J.* **350 Pt 1**, 219–27 (2000).

44. Hui, S. *et al.* Glucose feeds the TCA cycle via circulating lactate. *Nat. Publ. Gr.* **551**, (2017).

45. Sonveaux, P. *et al.* Targeting lactate-fueled respiration selectively kills hypoxic tumor cells in mice. *J. Clin. Invest.* (2008) doi:10.1172/JCI36843.however.

46. Fang, J. *et al.* The H+-Linked Monocarboxylate Transporter (MCT1/SLC16A1): A Potential Therapeutic Target for High-Risk Neuroblastoma. doi:10.1124/mol.106.026245.

47. Koukourakis, M. I., Giatromanolaki, A., Bougioukas, G. & Sivridis, E. Lung cancer: An organized cellular and metabolic domain Lung Cancer A Comparative Study of Metabolism Related Protein Expression in Cancer Cells and Tumor Associated Stroma. *Cancer Biol. Ther.* **6**, 1476–1479 (2007).

48. Zu, X. L. & Guppy, M. Cancer metabolism: facts, fantasy, and fiction. *Biochem. Biophys. Res. Commun.* **313**, 459–465 (2004).

49. DeBerardinis, R. J. & Chandel, N. S. Fundamentals of cancer metabolism. *Sci. Adv.* **2**, e1600200 (2016).

50. Asada, K. *et al.* Reduced Expression of GNA1and Silencing of MCT1 in Human Breast Cancers. *Oncology* **64**, 380–388 (2003).

51. Baltazar, F. *et al.* Monocarboxylate transporters as targets and mediators in cancer therapy response. *Histol. Histopathol.* **29**, 1511–1524 (2014).

52. Morais-Santos, F. *et al.* Differential sensitivities to lactate transport inhibitors of breast

cancer cell lines. *Endocr. Relat. Cancer* **21**, 27–38 (2014).

53. Sadowska-Bartosz, I., Soszyński, M., Ułaszewski, S., Ko, Y. & Bartosz, G. Transport of 3-bromopyruvate across the human erythrocyte membrane. *Cell. Mol. Biol. Lett.* (2014) doi:10.2478/s11658-014-0189-1.

54. Curtis, N. J. *et al.* Pre-clinical pharmacology of AZD3965, a selective inhibitor of MCT1: DLBCL, NHL and Burkitt's lymphoma anti-tumor activity. *Oncotarget* **8**, 69219–69236 (2017).

55. Morais-Santos, F. *et al.* Targeting lactate transport suppresses in vivo breast tumour growth. *Oncotarget* **6**, (2015).

56. Gan, L. *et al.* Metabolic targeting of oncogene MYC by selective activation of the proton-coupled monocarboxylate family of transporters. *Oncogene* **35**, 3037–3048 (2016).

57. Bartmann, C. *et al.* Beta-hydroxybutyrate (3-OHB) can influence the energetic phenotype of breast cancer cells, but does not impact their proliferation and the response to chemotherapy or radiation. *Cancer Metab.* **6**, 8 (2018).

58. El Sayed, S. M. *et al.* The promising anticancer drug 3-bromopyruvate is metabolized through glutathione conjugation which affects chemoresistance and clinical practice: An evidence-based view. *Med. Hypotheses* **100**, 67–77 (2017).

59. Mathupala, S. P., Ko, Y. H. & Pedersen, P. L. Hexokinase-2 bound to mitochondria: cancer's stygian link to the 'Warburg Effect'; and a pivotal target for effective therapy. *Semin. Cancer Biol.* **19**, 17–24 (2009).

60. Chen, Z., Zhang, H., Lu, W. & Huang, P. Role of mitochondria-associated hexokinase II in cancer cell death induced by 3-bromopyruvate. *Biochim. Biophys. Acta - Bioenerg.* **1787**, 553–560 (2009).

61. Sun, Y. *et al.* Mechanisms underlying 3-bromopyruvate-induced cell death in colon cancer. *J. Bioenerg. Biomembr.* **47**, 319–29 (2015).

62. Valenti, D., Vacca, R. A. & de Bari, L. 3-Bromopyruvate induces rapid human prostate cancer cell death by affecting cell energy metabolism, GSH pool and the glyoxalase system. *J. Bioenerg. Biomembr.* **47**, 493–506 (2015).

63. Baker, J. P. & Rabin, B. R. Effects of Bromopyruvate on the Control and Catalytic Properties of Glutamate Dehydrogenase. *Eur. J. Biochem.* **11**, 154–159 (1969).

64. Sanborn, B. M., Felberg, N. T. & Hollocher, T. C. The inactivation of succinate dehydrogenase by bromopyruvate. *Biochim. Biophys. Acta - Enzymol.* **227**, 219–231 (1971).

65. Bendrat, K. *et al.* Biochemical and mutational investigations of the enzymatic activity of macrophage migration inhibitory factor. *Biochemistry* **36**, 15356–62 (1997).

66. Korotchkina, L. G., Showkat Ali, M. & Patel, M. S. Involvement of alpha-cysteine-62 and beta-tryptophan-135 in human pyruvate dehydrogenase catalysis. *Arch. Biochem. Biophys.* **369**, 277–87 (1999).

67. Dell'Antone, P. Inactivation of H+-vacuolar ATPase by the energy blocker 3-bromopyruvate, a new antitumour agent. *Life Sci.* **79**, 2049–55 (2006).

68. Jardim-Messeder, D., Camacho-Pereira, J. & Galina, A. 3-Bromopyruvate inhibits calcium uptake by sarcoplasmic reticulum vesicles but not SERCA ATP hydrolysis activity. *Int. J. Biochem. Cell Biol.* **44**, 801–7 (2012).

69. Darabedian, N., Chen, T. C., Molina, H., Pratt, M. R. & Scho¨, A. H. Bioorthogonal Profiling of a Cancer Cell Proteome Identifies a Large Set of 3-Bromopyruvate Targets beyond Glycolysis. (2018) doi:10.1021/acschembio.8b00743.

70. Yadav, S. *et al.* Molecular docking studies of 3-bromopyruvate and its derivatives to metabolic regulatory enzymes: Implication in designing of novel anticancer therapeutic strategies. *PLoS One* **12**, e0176403 (2017).

71. Ko, Y. H. *et al.* Advanced cancers: eradication in all cases using 3-bromopyruvate therapy to deplete ATP. (2004) doi:10.1016/j.bbrc.2004.09.047.

72. Mathupala, S. P., Rempel, A. & Pedersen, P. L. Glucose catabolism in cancer cells: identification and characterization of a marked activation response of the type II hexokinase gene to hypoxic conditions. *J. Biol. Chem.* **276**, 43407–43412 (2001).

73. Jardim-Messeder, D. & Moreira-Pacheco, F. 3-Bromopyruvic Acid Inhibits Tricarboxylic Acid Cycle and Glutaminolysis in HepG2 Cells. *Anticancer Res.* **36**, 2233–41 (2016).

74. Dell'Antone, P. Targets of 3-bromopyruvate, a new, energy depleting, anticancer agent. *Med. Chem. (Shāriqah (United Arab Emirates))* **5**, 491–6 (2009).

75. Sadowska-Bartosz, I. & Bartosz, G. Effect of 3-bromopyruvic acid on human erythrocyte antioxidant defense system. *Cell Biol. Int.* 1285–1290 (2013).

76. Baghdadi, H. H. Targeting Cancer Cells using 3-bromopyruvate for Selective Cancer Treatment. *Saudi J. Med. Med. Sci.* **5**, 9–19 (2017).

77. Korga, A., Ostrowska, M., Iwan, M., Herbet, M. & Dudka, J. Inhibition of glycolysis disrupts cellular antioxidant defense and sensitizes HepG2 cells to doxorubicin treatment. *FEBS Open Bio* **9**, 959–972 (2019).

78. Chen, L. *et al.* NADPH production by the oxidative pentose-phosphate pathway supports folate metabolism. *Nat. Metab.* **1**, 404–415 (2019).

79. Pavlova, N. N. & Thompson, C. B. The Emerging Hallmarks of Cancer Metabolism. *Cell Metab.* **23**, 27–47 (2016).

4 Liposomal 3BP

4.1 Abstract

In the previous chapter, it was shown that 3-bromopyruvate (3BP) is a promising compound for metabolic targeting of tumour cells that overexpress MCT1. Albeit promising, 3BP has not entered clinical use with the exception of two case reports. Based on the molecular structure of 3BP and available literature, this can be attributed to its instability and high reactivity in physiological conditions, which can result in off-target toxicity and only a small fraction of injected dose reaching the tumour.

In this chapter, the encapsulation of 3BP in liposomes as a way to minimise toxicity and optimise efficacy is described. A triggered release strategy was employed to maximise the availability of 3BP to the target cells at short time points post injection (p.i.). For this, a combination of cavitation-sensitive liposomes, microbubbles as cavitation agents and externally applied focused ultrasound (FUS) were used.

4.2 Introduction

Although 3BP has shown very encouraging results *in vitro*, inducing major metabolic disruption and cytotoxicity selectively to cells overexpressing MCT1, its clinical translation is challenging because of the reactive nature of this compound. This is particularly true when it comes to systemic administration of the agent. Intravenous infusion of 3BP causes a burning sensation to the veins[1]. Glutathione and other thiol-rich components of the blood such as proteins and peptides can react with the compound[2,3], potentially resulting in either its de-activation or off-target toxicities[4]. Finally, as a hydrophilic small molecule its pharmacokinetics do not favour tumour accumulation.

Systemic treatment with unformulated (crude) 3BP can result in serious toxicity and even death[1,5,6], according to the limited existing evidence in this regard, there seems to be a dose-dependent liver and kidney toxicity[7–9]. Encapsulating 3BP in various carriers has been suggested as a way to overcome these challenges and expand the therapeutic window of this promising compound[4,9–11].

Liposomes were the first nanocarriers (NC) to enter clinical practice with the approval of Doxil, a liposomal formulation of doxorubicin, in 1995. Since then, various liposomal formulations have been approved or are now in clinical trials for a variety of indications including cancer[12]. Liposomes present several advantages compared to other NCs. They are versatile, able to carry both hydrophilic and lipophilic payloads in their aqueous core and lipid shell respectively, they are easily synthesised and amenable to surface modifications e.g. attachment of vectors for biological targeting.

However, reliance on the enhanced permeability and retention (EPR) effect for tumour accumulation is a common feature of many NCs, including liposomes. The contribution of EPR has recently been challenged because it is associated with a high degree of inter-patient, inter- and intra-tumour variability, inefficiency of NC accumulation (reported 0.7% across several types of carriers)[13] and, most importantly, poor penetration of NC into the tumour[14–16]. Further, liposomes are designed to be stable in the blood circulation, but this might compromise their ability to efficiently release the therapeutic once at the target.

In response to these challenges, several stimulus-responsive carriers have been developed, to improve carrier accumulation at the target site and release of the therapeutic payload [17,18]. We opted for a cavitation-sensitive liposomal formulation, designed to be co-administered with microbubbles (MBs), as cavitation agents and to subsequently release 3BP in the tumour vasculature in response to externally applied FUS. Ultrasound is a broadly available, economical and non-invasive modality currently used in the clinic for both diagnosis and treatment. In the

context of triggered release from liposomes, ultrasound has recently shown very encouraging outcomes in the TARDOX clinical trial in which ultrasound-induced hyperthermia was used to release doxorubicin from a heat-sensitive liposomal formulation, Thermodox[19]. Similar to the TARDOX design, our strategy does not rely on passive accumulation via EPR of long-circulating liposomes, but rather, on triggered release of 3BP soon after injection, and then reliance on the ability of the small molecule to diffuse into the tumour. This approach is particularly suited to 3BP because of its short half-life[20]. Previous experience with cavitation-triggered release has confirmed the feasibility of this approach[21].

4.3 Aims

The specific aims for this Chapter were:

- To synthesise and characterise empty and 3BP-loaded liposomes
- To develop a method for the quantification of 3BP following encapsulation in liposomes
- To assess selectivity of efficacy in MCT1-positive and negative models *in vitro*
- To encapsulate a fluorescent dye and assess liposome biodistribution *in vivo*

4.4 Materials & Methods

4.4.1 Liposome synthesis

1,2-dipalmitoyl-sn-glycero-3-phosphocholine (DPPC), 1-myristoyl-2-stearoyl-sn-glycero-3-phosphocholine (MSPC) and 1,2-distearoyl-sn-glycero-3-phosphoethanolamine-N-[methoxy(polyethylene glycol)-2000] (ammonium salt) (DSPE-PEG2000) 25 mg/mL solutions in chloroform were combined at a molar ratio 93:2.8:4.2. The solvent was removed by overnight drying under high vacuum at room temperature. The dry lipids were then dissolved in cyclohexane

(1 mL for 12.05 mg lipid) and lyophilised to form a dry lipid pellet (–50°C, 100 mTorr, 2 days using a VirTis Lyostar Advantage Plus EL-85, SP Scientific, Pennsylvania, USA). The lipid films were stored at 4°C. The chemical structure of the lipids is shown in **Table 3**.

A pH gradient was required for active loading of 3BP which is a carboxylic acid (pKa = 1.84), whereas the core of the liposome is alkaline and the surrounding medium is strongly acidic (**Figure 24**). Liposomes were formed by hydration of the pre-formed lipid film with sodium bicarbonate buffer (0.84% w/v, pH 8.4, 350 μL) at 55°C followed by extrusion (7 times) through a 100 nm membrane at the same temperature. For external buffer exchange, size exclusion chromatography (SEC) was used with Sephadex G25 column (GE Healthcare, Buckinghamshire, UK) as the stationary phase and 0.1 M HCl as the mobile phase. 3BP was dissolved in the 0.1 M HCl solution and incubated with the liposomes for 3 h at room temperature for loading (2.5:1 3BP to lipid mass ratio). Liposomes were purified by a second SEC step through a Sephadex G25 column and eluting with PBS.

Table 3 Chemical structure of phospholipids used for liposome synthesis.

Lipid name	Lipid structure
1,2-dipalmitoyl-sn-glycero-3-phosphocholine (**DPPC**)	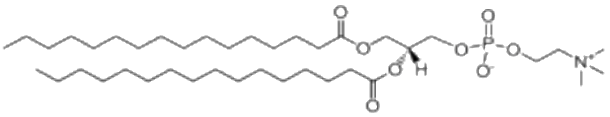
1,2-distearoyl-sn-glycero-3-phosphoethanolamine-N-[methoxy(polyethylene glycol)-2000] ammonium salt (**DSPE-PEG(2000)**)	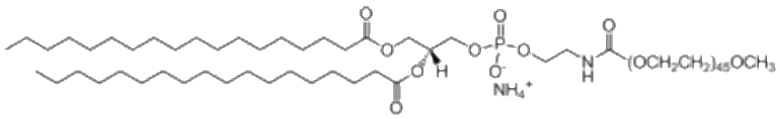
1-myristoyl-2-stearoyl-sn-glycero-3-phosphocholine (**MSPC**)	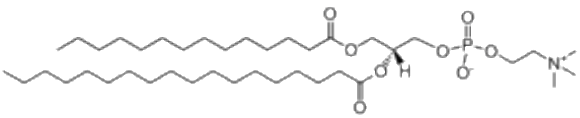

LP were loaded with a fluorescent dye for the assessment of *in vivo* distribution. Sulfonated cyanine-5 (sulfo-Cy5), the hydrophilic derivative of the commonly used fluorescent dye cyanine-5 was chosen. Sulfo-Cy5 was encapsulated in the liposomes by a passive loading technique, whereby the lyophilised lipid film was hydrated with 350 µL sulfo-Cy5 solution (1 mg/mL) and extruded in the same way as for 3BP loading. The liposome was purified using a G25 column with PBS as the mobile phase.

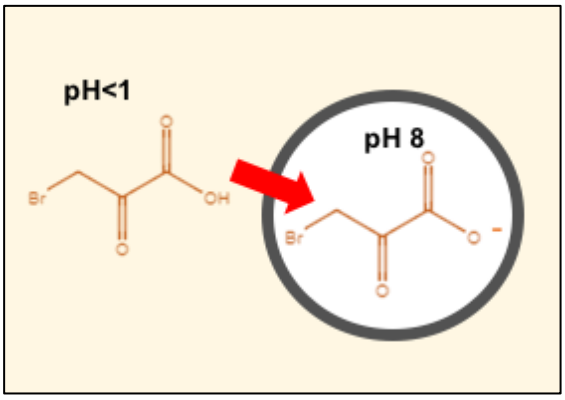

Figure 24 Graphical representation of the active loading technique. 3BP, an organic acid (pKa 1.84) is ionised in strongly acidic conditions (HCl 0.1 M). In an unionised form, it can cross the lipid bilayer of pre-formed liposomes. The liposomal core is mildly alkaline ($NaHCO_3$ 0.84%w/v) which results in ionisation and therefore entrapment of 3BP.

4.4.2 Liposome characterisation

4.4.2.1 Size and zeta potential

To measure the size and zeta potential, 10 µL of the LP emulsion was diluted in 990 µL water. The hydrodynamic diameter of the liposomes (z-average) and polydispersity index (PDI) were determined by dynamic light scattering (DLS) using a Zetasizer Nano ZS instrument (Malvern Instruments, UK). Zeta potential measurements were carried out using a disposable folded capillary Zeta cell filled with the liposome emulsion in MilliQ™ water at 20°C according to

the manufacturer's instructions (Malvern Instruments, UK). Zeta potential was calculated from the electrophoretic mobility of the liposomes using the Smoluchowski approximation.

4.4.2.2 Toxicity

The toxicity of blank liposomes was assessed in MTT assays. Briefly, MDA-MB-231 and BT20 cells were seeded in 24-well plates (50,000 cells/well) the day before treatment and allowed to adhere overnight. Cells were exposed to a range of liposome concentrations (10, 20 and 40 μL liposome per 1 mL growth media), reflecting the concentrations used in subsequent *in vitro* experiments. As a control, Sonovue MBs were also added at the standard concentration employed throughout the *in vitro* studies (10 μL/mL growth media). Cells were incubated at 37°C for 24 h and then assayed as previously described. The results were expressed as the ratio of the absorbance of the treated cells over the absorbance of untreated control for each cell line. All chemicals were purchased from Sigma-Aldrich, UK, unless stated otherwise. MilliQ™ water was used in all applications unless stated otherwise.

4.4.2.3 Stability

Blank liposomes were prepared as described in the previous section. Stability was assessed by measuring the size distribution and PDI of the liposomal formulation following incubation at 4°C, room temperature and 37°C. The final liposome suspension was divided in equal parts (100 μL each) and incubated in 1.5 mL tubes for 24 or 48 hours. A DLS measurement was made of the freshly prepared suspension and following incubation as previously described. The results were presented as the ratio of the size or PDI value obtained for the treated liposome over the value obtained directly after liposome preparation.

4.4.3 Quantification of 3BP

To quantify the amount of encapsulated 3BP, a 60 μL aliquot was vortexed vigorously with an equal volume of chloroform followed by centrifugation (14,000 rpm, 30 min, 4 °C, Eppendorf

5417R centrifuge equipped with F54-30-17 fixed angle rotor) to extract 3BP in the aqueous phase. High performance liquid chromatography (HPLC) was used to quantify the encapsulated 3BP. A C18 reverse phase column (XBridge™ C18, Waters, Belgium) was used as a stationary phase and 3BP (20 μL injection volume) was eluted with an isocratic 90:10 mixture of water and acetonitrile respectively, both acidified with 0.1% v/v trifluoroacetic acid (TFA) at a flow rate of 0.75 mL/min and run time of 10 min. 3BP was quantified using the 230 nm absorbance peak. To generate a standard curve, blank liposomes were used for the extraction process and the aqueous phase was spiked with 3BP to generate final concentrations of 0, 5, 10, 20, 50, 100, 500 and 1000 μg/mL.

4.4.4 *In vitro* ultrasound exposure

The liposomes used for the experiments described in this chapter were designed to be cavitation-sensitive, so that payload release is significantly enhanced by exposure to cavitation agents and ultrasound operated at clinically-relevant settings. An improved version of a previously published in-house built system for acoustic transfection (SAT)[22], named SAT2, was employed for ultrasonic exposures. The SAT2 system allows the cavitation activity to be monitored in real time and *in situ* ultrasonic field characterisation. Neither of theses features were available in the original SAT design. The SAT2 system was designed by Dr. Michael Gray (Institute of Biomedical Engineering, Oxford University). As shown in **Figure 25**, ultrasound treatment using the SAT2 system is carried out in a water tank containing approximately 900 mL of degassed, de-ionised water. The main features of the system are, from bottom to top, a 1 MHz ultrasound transducer at the bottom of the tank (Imasonic 8233 A101, 40 mm diameter, 120 mm radius of curvature), a purpose-built sample holder and an acoustic absorber. Cavitation activity in the sample was monitored for all experiments using a passive cavitation detector (PCD) fitted at the top of the tank (7.5 MHz centre frequency; V320 Panametrics, Olympus). Cells and/or treatment agents, such as MBs and liposomes, were placed in a cell culture dish (35 mm, high wall μ dish; Ibidi,

Germany) fitted to a lid molded from poly(dimethylsiloxane) (PDMS, Sylgard 184; Dow Corning, New York, USA), which is referred to as a 'sonolid' hereafter. Engineering details of the construct are provided in Carugo *et al.*[22] For the experiments reported in this chapter, the optimised lid thickness (1.5 mm) and expanded radial dimensions were used to achieve optimal field uniformity upon exposure to a broad incident US beam. The sample was fitted upside-down (bottom of the dish facing away from the transducer) in the sample holder. The ultrasound transducer was driven by a 1 MHz sinusoidal signal (3000 cycles, 10 ms burst period) from a function generator passed through a 1.9 MHz low-pass filter and amplified 55 dB by a radiofrequency amplifier (1040L, E&I Ltd., NY, USA). The bottom of the culture dish is sufficiently thin (0.18 mm) to allow transmission of harmonic and broadband cavitation signals without significant attenuation. Acoustic emissions received by the PCD were high-pass filtered (F5081-2P0, Allen Avionics, Mineola, NY, USA), pre-amplified (SR445A, SRS, Sunnyvale, CA, USA), digitised (Handyscope HS3, TiePie Engineering, Netherlands) and fed to a laptop computer disk. PCD time series data sets were analysed in Matlab (Mathworks, MA, USA) using Welch's method for power spectrum calculation, implemented with temporal windows of 80 μs (2.5% of typical source drive pulse length) with 50% window overlap.

The aim of this set of experiments was to assess whether 3BP is released from the liposome upon exposure to ultrasound in the presence of cavitation agents, and the endpoint was the assessment of toxicity in MCT1-expressing cells. The experiments were conducted in two ways. In Design 1, cells were seeded in 35 mm culture μ dishes and incubated overnight. 3BP-liposomes or an equal volume of blank liposomes and 100 μL fresh Sonovue were added directly to the dish containing the cells. The Ibidi lid was replaced by a 'sonolid' and the dish was filled with complete DMEM using a syringe, so that no air bubbles remained (10 mL). The dish was inverted and placed on the holder of the SAT2 tank, so that the cells, adherent to the bottom of the plate, faced upwards, with the sonolid between the transducer and the cells. The distance between the sonolid

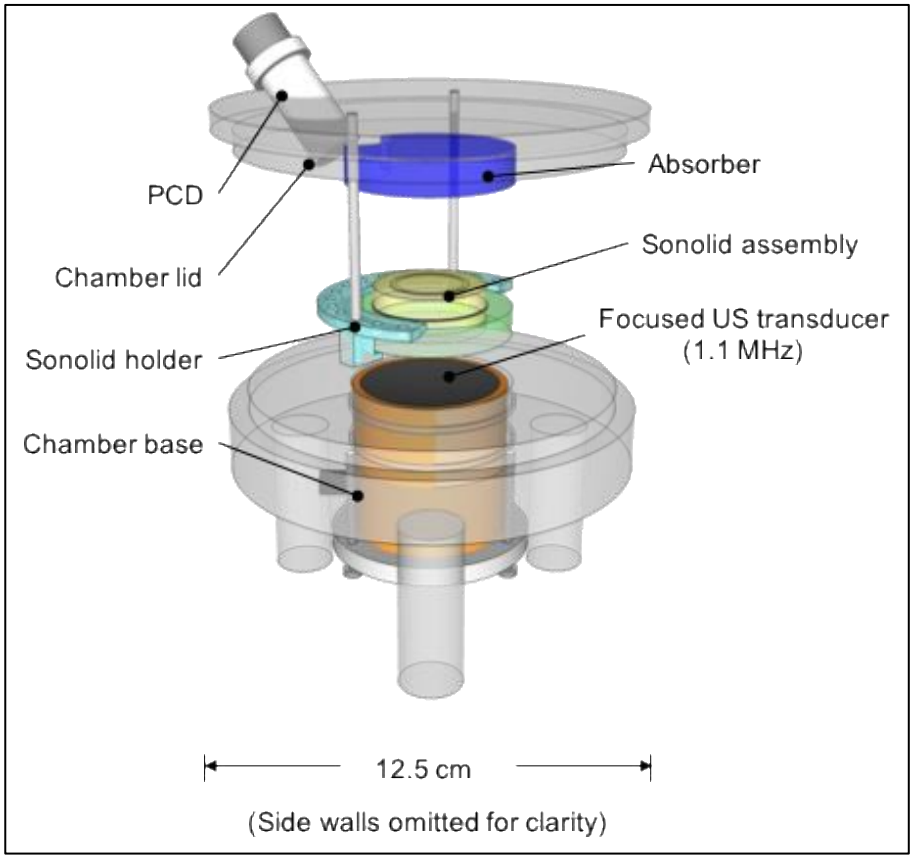

Figure 25 Main parts of SAT2, the device used for in vitro ultrasound exposures. The SAT2 is composed of a cylindrical water chamber at the bottom of which focused ultrasound (US) transducer is fitted. The sample, in an inverted 35 mm cell culture dish sealed with an ultrasound transparent lid ('sonolid') is placed in a holder 32 cm above the transducer. A passive cavitation detector (PCD) receives the acoustic emissions from the sample and feeds them to a computer equipped with TiePie softeware (TiePie Engineering, Netherlands) for processing.

and transducer was 32 mm so that the US beam was focused close to the cells. Cells were treated for 20 s (242 mVpp amplitude in waveform generator resulting in 0.3 MPa pressure, 3000 cycles and 10 ms pulse repetition period). After sonication, 4 mL of the treatment medium was removed and the Ibidi lid was placed back on the dish. Cells were incubated at 37°C for 24 hours and their viability was assessed in an MTT assay.

In **Design 2**, 4 x 10^5 cells/well were seeded in a 6-well plate and the liposomes were treated separately in the SAT2 as described for **Design 1**. Immediately after treatment, 2 mL of medium was replaced in each well. Cells were incubated for 24 h, the medium was removed and cell viability was assessed in an MTT assay. Shear stress from bubble cavitation can facilitate drug delivery either by acting on the cell membranes to temporarily increase their permeability (a phenomenon termed 'sonoporation') or by acting on the liposomes to trigger payload release. This experimental design was introduced later to prevent cell detachment due to ultrasound exposure and exclude drug delivery due to sonoporation. Although sonoporation has been used to drive drug directly into target, that was not the intent in this experimental set-up which was designed to simulate a situation in which the cavitation agents do not come in close proximity to the tumour cells. Rather, they stay in the blood circulation and their role is to cause local drug release from co-injected liposomes upon exposure to ultrasound.

4.4.5 *In vivo* biodistribution

Tumour-free female athymic nude mice were randomly allocated to two groups (n = 3 per group) and under anaesthesia received by intravenous injection either 50 μL purified liposomal sulfo-Cy5 (1.2 mg lipid) or an equivalent amount of free Cy5 dye in PBS. Mice were imaged at 30 min, 60 min and 24 h using the IVIS Spectrum imaging system (Perkin Elmer, MA, USA) with 640/680 filters for excitation and emission respectively. Images were analysed using the IVIS software.

4.5 Results

4.5.1 Synthesis and characterisation of liposomes

Empty ("blank") liposomes were synthesised in the same way as 3BP-loaded liposomes, but with omission of 3BP in the external acidic solution (0.1 M HCl buffer). The size distribution and zeta potential of blank and 3BP-loaded liposomes was measured by DLS. Liposomes of appropriate size, size distribution and zeta potential were synthesised (PDI < 0.2 was required for the system to be regarded as monodisperse). Further, the stability of the liposomes over 2 days was assessed by measuring the change in average size (z-average) and size distribution (PDI) after incubation at 4°C, room temperature and 37°C. Liposomes were stable, with the exception of those incubated at 37°C the size of which had diminished by 2 days (approximately 5%). This was not regarded as a problem, since liposomes are intended to release their payload shortly after administration. The physicochemical characteristics of the blank and 3BP-loaded liposomes are presented in **Figure 26**.

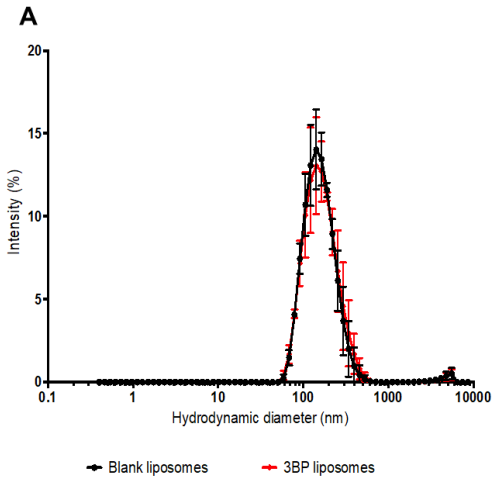

B

Sample	Size (z-average, nm)	PDI	Zeta potential (mV)
Blank liposomes	143.9±8.4	0.15±0.07	-17.4
3BP liposomes	145.3±8.5	0.14±0.05	-16.1

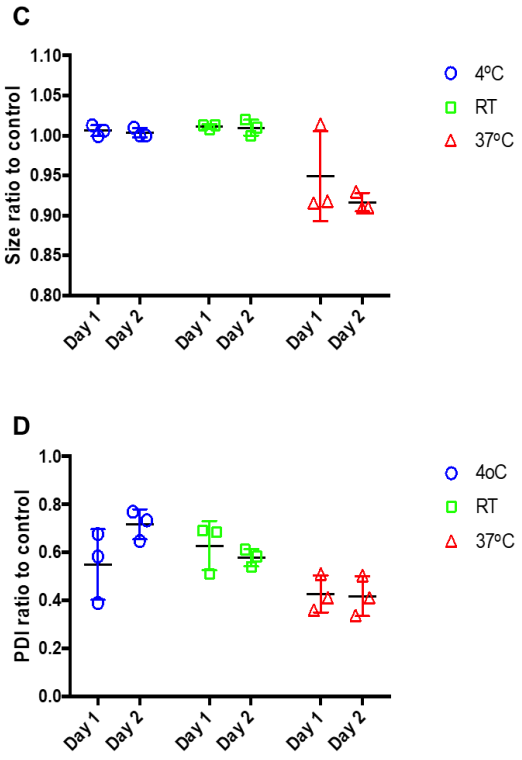

Figure 26 Physicochemical properties of liposomes (a) size distribution by intensity measured by dynamic light scattering (DLS) of freshly prepared empty ('blank') or 3BP-containing liposomes, (b) average size, polydispersity index (PDI) and zeta potential of freshly prepared empty ('blank') or 3BP-containing ('3BP') liposomes, (c) and (d) liposome average size and PDI change respectively after incubation in phosphate-buffered saline at different temperature 4ºC, 25ºC ('RT') or 37ºC. N=3 for all studies. The results were analysed using Prism 7 software (Graphpad, CA, USA). Error bars represent the standard deviation.

Blank liposomes and Sonovue, which was used as a cavitation agent, were found to be non-toxic in MDA-MB-231 and BT20 cells at the concentrations used for all experiments in this chapter (**Figure 27**).

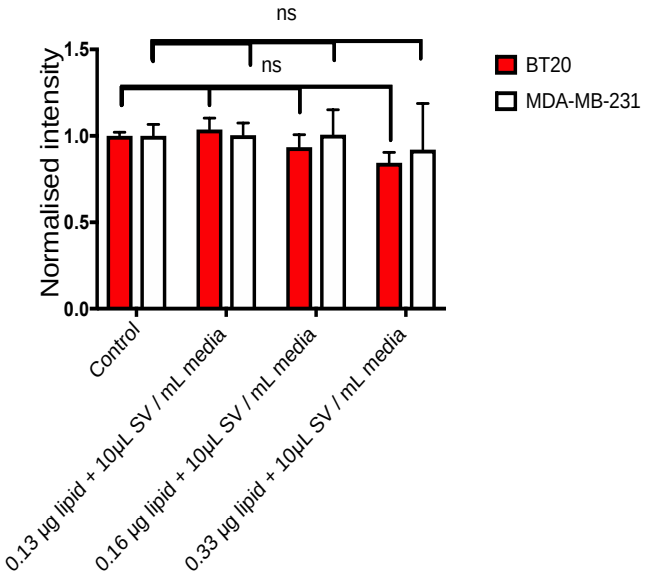

Figure 27 Evaluation of blank liposome toxicity. Toxicity of blank liposomes and Sonovue microbubbles (SV) tested on MDA-MB-231 and BT20 cells, at a concentration range that includes the concentrations used for further experiments.

4.5.2 Encapsulation of 3BP

The volume of the liposomal formulation to be used for cell treatment was determined by disrupting an aliquot of liposomes with chloroform and analysing the aqueous phase by HPLC. 3BP content was then determined from the standard curve and the corresponding volume of the liposomal formulation was used for cell treatments (**Figure A1, Appendix**). Encapsulation efficiency was up to 3-8% of the initial concentration corresponding to 1.3 mg/mL (8.3 mM) of neat formulation (approximately 0.1 mg 3BP for 12 mg lipid assuming that no lipid loss occurs during the process).

4.5.3 *In vitro* ultrasound exposure

Originally, the experimental design involved exposure of dishes with adherent cells to the treatment agents and ultrasound (**Design 1**). The results presented in **Figure 28** confirm that 3BP is not toxic when encapsulated, even to BT20 cells. However, ultrasound treatment seemed to

incur a lot of apparent toxicity, even for cells treated with blank liposomes (viability reduced to 39.3 ± 12.3% compared to 'no ultrasound' control). Liposomes of this composition are not toxic, hence we concluded that this apparent toxicity was caused by detachment of cells due to the ultrasound. This design was also thought to be sub-optimal due to the fact that it does not recapitulate the *in vivo* setting as closely as possible *in vitro*: target cells are not supposed to be directly exposed to the intact liposomes, cavitation agents and ultrasound for this drug delivery

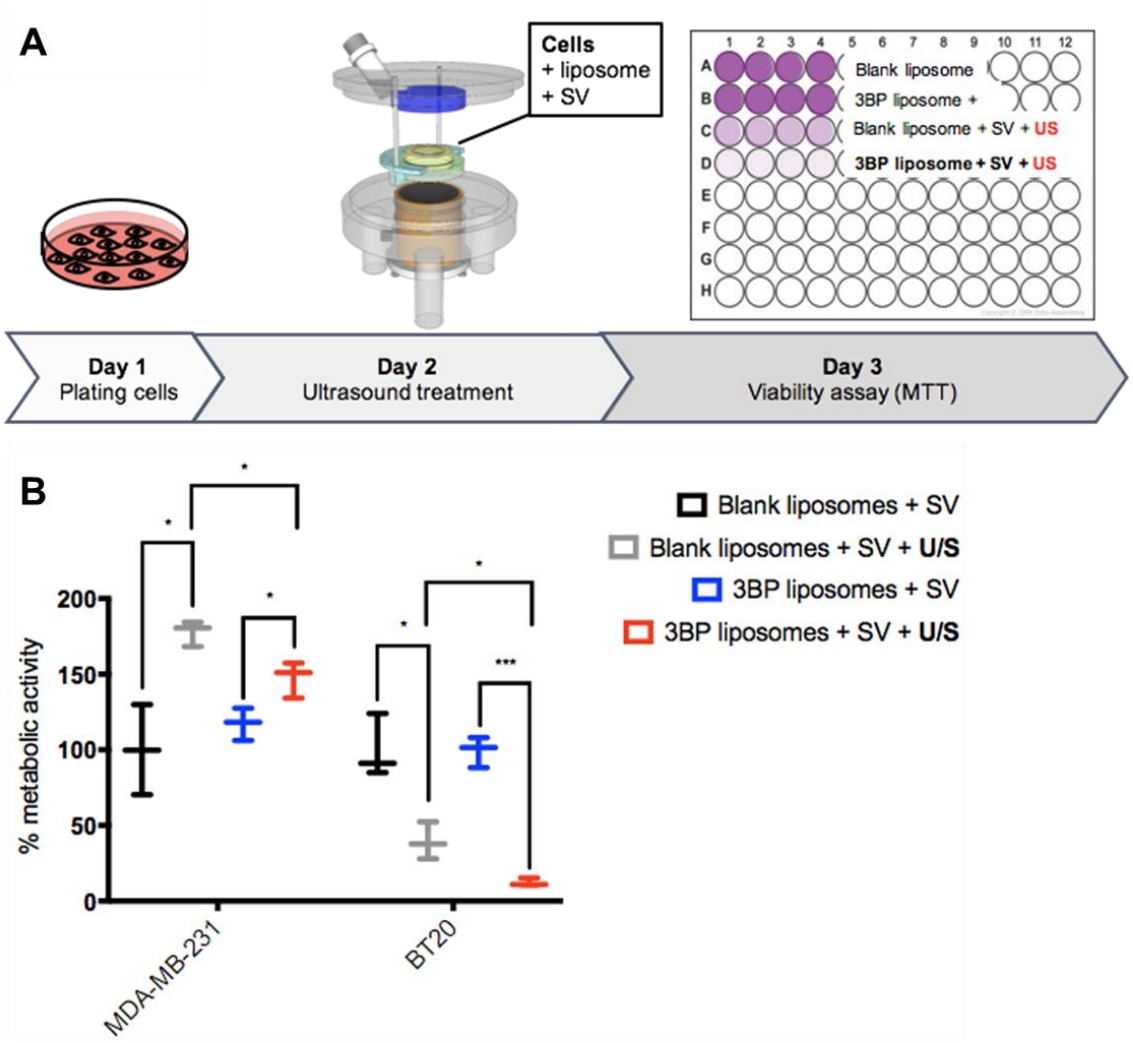

Figure 28 Experimental Design 1 for *in vitro* treatment of cells with liposomal 3-bromopyruvate (3BP) and ultrasound (U/S). (a) Graphical representation of the experimental procedure. Cells are seeded in 33 mm µ-cell culture dishes the day prior to the experiment. Growth medium supplemented with liposomes and SonoVue (SV, 0.25 mg/mL) replaces the normal growth medium and the dish is treated with ultrasound in the SAT2 device. Cells are then incubated for 24 h and their viability is measured with an MTT assay. For full details see Methods. (b) % cell viability 24 h post-exposure normalised to 'no ultrasound' control for each cell group.

strategy. Rather, 3BP release occurs in the bloodstream and the free compound diffuses through the extracellular space and reaches the cells where it is taken up via MCT1.

Therefore, although **Design 1** confirmed that 3BP is stably encapsulated in the liposomes and released upon ultrasound treatment, we optimised the design to better recapitulate the clinical situation and to distinguish between the effects of the compound and exposure to ultrasound.

Briefly, the improved design comprised treatment of the liposomes and MBs with ultrasound separately, and then the resulting suspension distributed to wells seeded with cells. It was confirmed that 3BP reduces the viability of MCT1-expressing cells significantly more than non-MCT1-expressing cells (viability reduced to 52.8% ± 4.1 in BT20 cells, $P<0.001$), when the liposomes are treated with ultrasound in the presence of cavitation agents, as demonstrated in **Figure 29**.

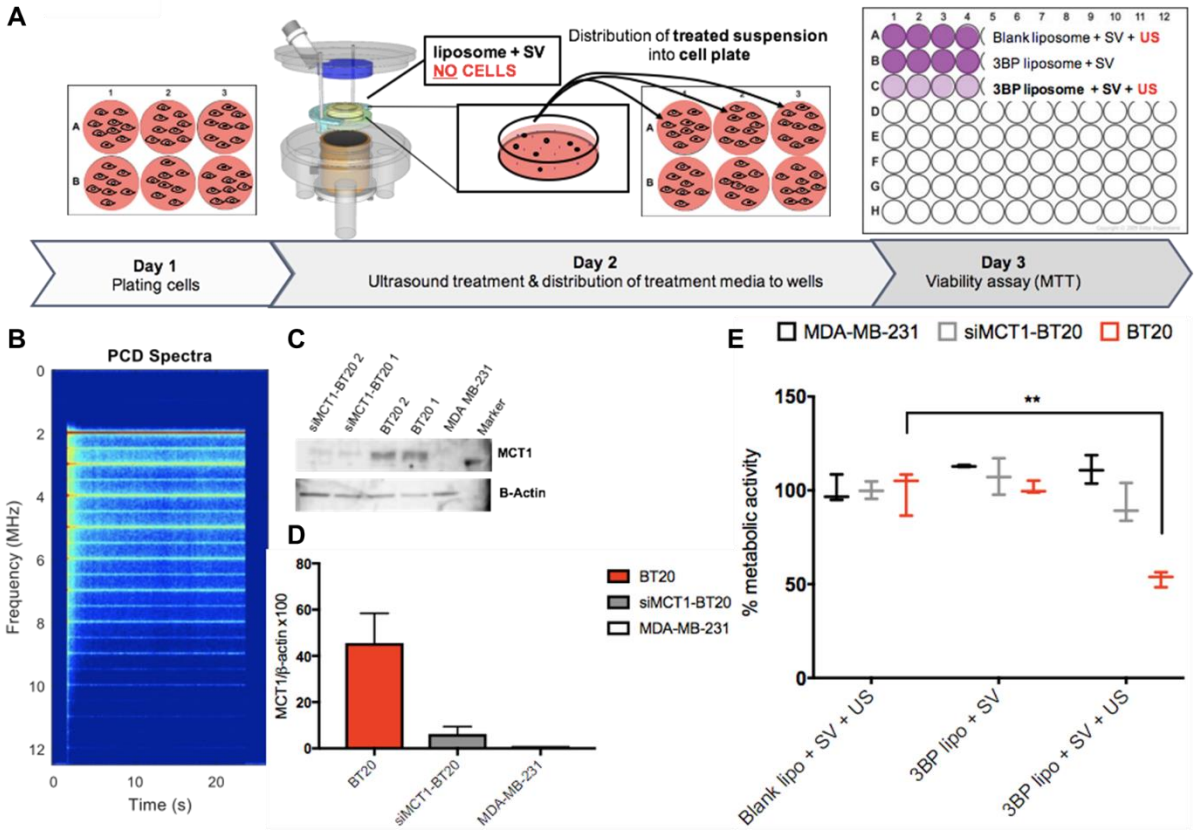

Figure 29 Experimental Design 2 for *in vitro* treatment of cells with 3-bromopyruvate (3BP) and ultrasound (US). (a) Graphical representation of the experimental procedure. Briefly, cells are seeded in a 6-well plate the day prior to the experiment. The following day, growth medium supplemented with liposomes and SonoVue (SV, 0.25 mg/mL) is treated in a cell-free 35 mm μ-cell culture dish in the SAT2. The treated solution is then distributed into the cells. Cells are incubated for 24 h and their viability is assessed with an MTT assay. (b) Representative passive cavitation detection (PCD) spectrum of SV (20 s exposure, 1.1 MHz, 0.3 MPa, 3,000 cycles). (c)Western blot analysis for the evaluation of siRNA-mediated silencing efficiency in BT20 cells and (d) quantification of optical density as a ratio to β-actin. (e) % metabolic activity as a measure of cell viability 24 h post-exposure normalised to blank liposome control for each cell group (n=3). Error bars represent the standard deviation. *P<0.05, ** P<0.01. Western blotting(d) and metabolic activity (e) data were analysed using Prism 7 software (GraphPad, CA, USA). MatLab software (Mathworks, MA, USA) was used to plot PCD spectra (b). For full details, please refer to methods.

4.5.4 *In vivo* biodistribution in tumour-free mice

A pilot experiment was conducted using free sulfo-Cy5 dye and sulfo-Cy5-loaded liposomes. Mice were injected in the tail vein with 50 μL liposome or free dye solution. The initial amount selected for this study was 40 μg dye based of the amount encapsulated in the liposomes. Since we had not injected this formulation before, we decided to start with two mice, one injected with 40

μg/50 μL free dye and one with the equivalent amount of liposomes, corresponding to 1.2 μg total lipid. The injection failed in mouse 2 (liposomes) and the mouse was excluded from the study. We speculated that this was because the emulsion was too viscous and we decided to try 1:2 dilution for mouse 3. The emulsion seemed to be still viscous as it was not moving normally upwards from the tail. We decided to dilute 1:3 and the mice 4, 5 and 6 received 1:3 diluted liposomal formulation (10.3 μg dye, 50 μL injection volume, 0.4 μg lipid). Mice were imaged using the IVIS Spectrum system operating with 640/680 excitation/emission filters at the epiluminescence mode. The selected time points for imaging were 30 min, 60 min and 1 day. Animals were kept under anaesthesia throughout the study, up to 2.5 hours. Mice 5 and 6 were imaged using the FLIT mode to obtain 3-dimensional images. Treatment is summarised in **Table 4** and 60 min and 24 h imaging of mouse 6, injected with liposomes, are shown in **Figure 30**.

Although the biodistribution results from this experiment have no statistical power, a safe concentration of liposomal emulsion was determined along with a sulfo-Cy5 concentration appropriate for imaging. The current results from two mice (5 and 6, only 6 shown) indicate that the liposome accumulates in the liver within the first hour post injection. Liver accumulation is expected for liposomal formulations. High fluorescence background was observed in all mice which made the epifluorescence 2D images inconclusive. In future studies, lower concentration of the dye could be employed and the mice could be on 'low-fluorescence' diet for longer.

Table 4 Summary of treatments used in the pilot biodistribution study.

Mouse	Included?	Injectable	Quantity of injectable	Imaging
1	No	Sulfo-Cy5 liposomes in PBS	41 µg dye, 1.2 µg lipid in 50 µL PBS	Yes, but not used.
2	Yes	Sulfo-Cy5 in PBS	41 µg dye in 50 µL PBS	30 min, 60 min and 1 day, epiluminescence. 3D (FLIT) imaging at 1 day.
3	No	Sulfo-Cy5 liposomes in PBS	20.5 µg dye, 0.6 µg lipid in 50 µL PBS	Yes, but not used.
4	Yes	Sulfo-Cy5 liposomes in PBS	13.6 µg dye, 0.4 µg lipid in 50 µL PBS	30 min, 60 min and 1 day, epiluminescence. 3D (FLIT) imaging at 60 min and 1 day.
5	Yes	Sulfo-Cy5 liposomes in PBS	13.6 µg dye, 0.4 µg lipid in 50 µL PBS	30 min, 60 min and 1 day, epiluminescence. 3D (FLIT) imaging at 60 min and 1 day.
6	Yes	Sulfo-Cy5 liposomes in PBS	13.6 µg dye, 0.4 µg lipid in 50 µL PBS	30 min, 60 min and 1 day, epiluminescence. 3D (FLIT) imaging at 60 min and 1 day.

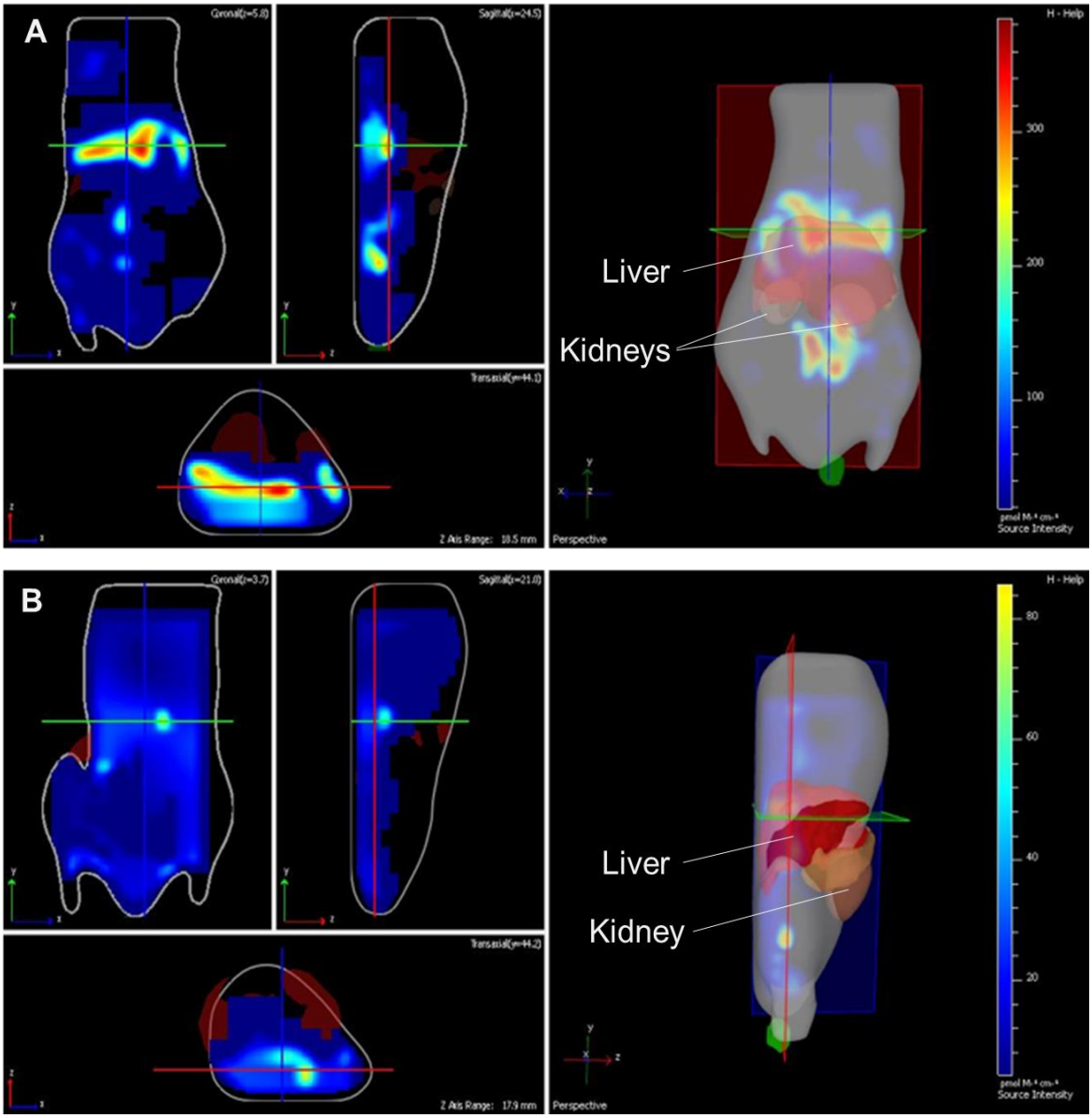

Figure 30 Liposome biodistribution. Imaging 60 min (a) and 24 h (b) of mice injected with sulfo-Cy5 loaded liposomes using the IVIS Spectrum system (Perkin Elmer, MA, USA) operating at the FLIT mode for 3D imaging and using 640/680 excitation emission filters for acquisition. Female nude mouse and organs (liver, spleen and kidneys) phantom added artificially upon analysis to facilitate the localisation of the signal. Images were analysed by the Living Image software (Perkin Elmer, MA, USA).

4.6 Discussion

Recognising the challenges in the systemic treatment with 3BP, the feasibility of employing cavitation-sensitive liposomes in combination with MBs and extracorporeal FUS to overcome some of these challenges was explored.

4.6.1 The approach

Liposome stability while in the circulation has long been recognised as a desirable attribute[12]. It has also been established that triggering the release of the therapeutic once the liposome reaches the target tissue, to make the drug bioavailable, can significantly improve therapeutic efficacy[23]. In an attempt to harness the pharmacokinetic benefits of a nano-sized carrier while in circulation and retain the more favourable distribution profile of a small molecule within the tumour mass, a triggered release approach was developed. In fact, 3BP is ideal for this approach since there is a transporter for its selective uptake into the target cells (MCT1) and the acidic pH of the tumour accelerates the transport[24,25]. A small hydrophilic molecule like 3BP cannot be retained in the tumour for long, unlike a macromolecule or a liposome would by exploitation of the dysfunctional lymphatics. It could be argued that the remaining 3BP either in liposomes that were not ruptured and are still circulating or free 3BP that did not enter the target cells could cause toxicity to surrounding tissues and hence defeat the purpose of using a delivery system in the first place. However, it is expected that in the particular case of 3BP and given that ultrasound is applied shortly after administration, the 'unused' 3BP will slowly degrade thanks to its short half-life, most of it in the liposomes, before being able to cause toxic effects. However, the feasibility, efficacy and safety of the *in vivo* application of this approach remains to be investigated in the future.

4.6.2 The formulation

3BP has shown great promise *in vitro*, both in our hands and in the hands of others[10]. Evidence that 3BP is active *in vivo* comes from the success of local treatment attempts, where the concerns associated with chemical inactivation of the compound while in the blood stream and off-target toxicity are effectively eliminated. Early evidence comes from Geschwind *et al.* who successfully treated liver VX2 tumours in rabbits via direct intra-arterial infusion of 3BP solution with no damage to healthy liver tissue or other organs as shown by histology[26]. The same group investigated the treatment of subcutaneous and intraperitoneally implanted hepatocellular carcinoma (HCC) tumours in rats. Repeated intratumoural or intraperitoneal injections of 3BP resulted in regression or even eradication of tumours without toxic effects[27]. An interesting study by Zhang *et al.* comparing administration of 3BP solution by oral gavage and aerosol for the treatment of lung tumours found it effective in both cases but causing mild liver toxicity in the case of the oral administration[28]. This study was followed up with another report by the same group examining the combination of 3BP with rapamycin[29]. Sadly, the authors did not explore the extent of systemic release of 3BP from the lung when administered by aerosol. Yamada and colleagues recently reported effective topical treatment of melanoma *in vitro* and in mice without any evidence of toxicity in the surrounding healthy cells[30]. Another case of successful topical treatment utilising a delivery system comes from Wicks *et al.* who implanted a 3BP releasing polymer wafer intra-cranially in rats to treat gliomas[31].

Two clinical case studies have been reported to date. Ko and colleagues treated a 16-year old male patient with liver cancer when other treatment options had been unsuccessful. 'Specially formulated' 3BP was administered via 'trans-catheter intra-arterial bolus injection'. The patient was able to survive longer than expected but eventually passed away 2 year post diagnosis due to disease progression[5]. Given the encouraging results of this study, PreScience Labs, an U.S. company founded by one of the researchers undertaking the treatment of the liver cancer patient in 2012,

received approval for a phase I clinical trial from the Food and Drug Administration in 2013, but the study was never commenced because of lack of funding[6]. El Sayed and colleagues treated a 28-year old male patient with stage IV melanoma. They found minimal anticancer efficacy of unformulated 3BP when administered together with paracetamol to deplete glutathione[1]. As the authors of this study conclude, 3BP would benefit from a drug delivery system and should not be administered to patients in a crude form[4,6]. Unfortunately, this warning did not prevent the death of three cancer patients in Germany treated with 3BP – allegedly in inappropriate regimens – at an 'alternative medicine' clinic[6,32].

Taken together, the current evidence converges to the use of a drug delivery system to protect 3BP from chemical deactivation while in circulation, while simultaneously protecting the healthy tissues from 3BP toxicity. Liposomes were the first NCs to enter the clinic and since then several untargeted, targeted and stimuli-responsive formulations have been licensed or entered clinical trials for a variety of indications including cancer[12,23]. A major criticism, however, is that they cannot penetrate the tumour efficiently and hence the therapeutic remains in the perivascular space rather than the core of the tumour. We hoped to tackle this challenge by releasing the therapeutic locally in the tumour vasculature.

3BP is a hydrophilic, ionisable molecule which makes it suitable for active loading into the aqueous core of the liposome by pH gradient. 3BP is weak organic acid (pKa 1.84) and is therefore uncharged only in strongly acidic conditions, and ionised (negatively charged) in alkaline or neutral pH. Based on this property, active loading was employed whereby uncharged 3BP dissolved in acidic buffer can more easily cross the lipid bilayer while once in the liposomal core, which is alkaline, it is negatively charged and hence trapped inside. This strategy worked sufficiently well for *in vitro* experiments with cells, although the encapsulation efficiency was quite low. The aim of active loading is to achieve higher concentration inside the liposome, while passive loading can achieve at most the same concentration as in the external phase since the liposomes entrap some

of it while forming. The low encapsulation of 3BP could be attributed to the fact that even in the uncharged form, it is a small, polar carboxylic acid with cLogP = -5.7 (highly hydrophilic)[33]. In vitro, we have more flexibility with the concentration of liposomes we could use so the low 3BP content was not problematic. In order to proceed with therapy studies *in vivo*, it would be desirable to optimise encapsulation in the liposome. Realising that active loading might not be optimal for this application, re-assessing the efficiency of passive loading could be valuable.

The consistency of the formulation used here is similar to that of other stimulus-responsive liposomes. Cholesterol-free (i.e. 'looser') lipid membrane was used. DPPC is the main constituent of the liposomal membrane. This is a symmetrical phosphatidylcholine, carrying saturated fatty acids which results in a cylindrical shape of the molecule and therefore tight packing of the fluid membrane. It has a high transition temperature (T_m= 55 °C) and provides stability to the vesicle. DSPE-PEG2000 is used to provide longer circulation time and 'loosening' of the packing. This lipid usually constitutes up to 5% of the formulation in order to avoid the severe destabilisation of the membrane occurring at higher amounts. MSPC is an asymmetrical PC used to 'loosen' the packing and lower the T_m, overall resulting in a 'leakier' liposome amenable to triggered release. Another option for this purpose, used in thermosensitive formulations, is the use of lyso-lipids, which could be investigated in future studies.

Liposomes exhibited appropriate size (140-150 nm) consistently between batches and negative zeta potential as expected by the use of phospholipids. These liposomes retained their size and size distribution for at least 24 h after preparation at 4°C and room temperature, while they seemed to shrink at 37°C. Although long circulating liposomal formulations are expected to be stable at 37°C for longer (at least 6 hours to exploit EPR), these liposomes are intended for drug release shortly after administration, therefore they are not required to be stable for as long. Stability at storage conditions (e.g. fridge) is important because it allows for more temporal flexibility between the time the formulation is prepared and used. This is also important for

experiments that need to be staggered, in which case a stable formulation allows for the use of the same batch for all experimental replicates. In this chapter, physicochemical stability of the liposomes is shown. However, the rate of release in the presence or absence of ultrasound has not been shown. This formulation was originally developed for the delivery of ^{111}In-labelled human epidermal growth factor ([111In]In-DTPA-hEGF) to breast tumours overexpressing EGF receptor (EGFR). Direct evidence of enhanced release of the radiopharmaceutical upon ultrasound treatment is provided in the manuscript of that study (under review at the time of writing) and has been reproduced in this document (**Figure 31**). Characterisation of the release profile in the absence and presence of ultrasound should be performed.

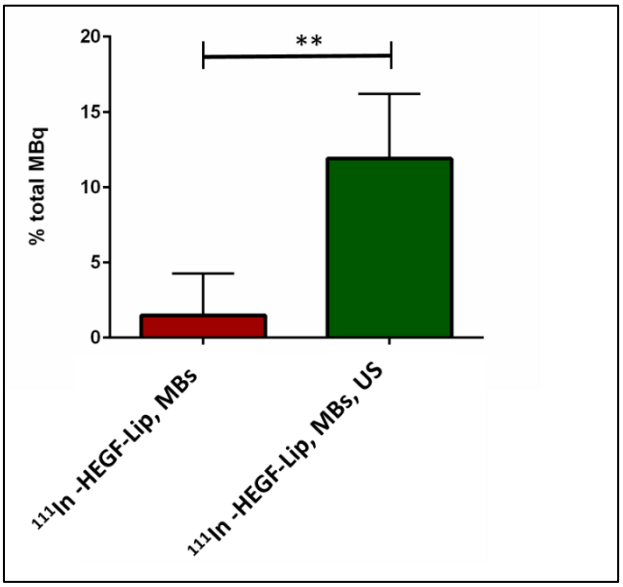

Figure 31 Cavitation triggered released of a peptide from liposomes. Enhanced release of [111In]In-hEGF from liposomes upon exposure to ultrasound using the same conditions as used In this work. Unpublished data reproduced with the permission of Dr J. Owen, who is the first author of this manuscript.

Nonetheless, indirect but robust evidence of drug release and ultrasound-responsiveness of the liposomes is provided by the cell viability studies presented in **Figures 28** and **29**. Indeed, in the absence of ultrasound stimulation, no toxicity was observed in the MCT1-expressing cells

suggesting release below the toxic levels. Notably, 3BP concentration of approximately 40 μM or more is required for evident toxicity in BT20 cells so this result does not exclude the possibility of significant release in the absence of ultrasound treatment.

In this work, we selected a clinically approved ultrasound contrast agent, SV. SV is phospholipid shell, sulphur hexafluoride-filled MB formulation licensed for diagnostic purposes only to enhance the echogenicity of blood or urine in ultrasound scans[34]. An important advantage of cavitation-triggered drug release is that the use of MBs allows for non-invasive real-time monitoring of the external stimulus, that is cavitation. The obvious benefit of using SV is that it is a standardised, ready-to-use formulation which reduces the variability between experiments and eliminates the need for further characterisation of the cavitation agents. Indeed, cavitation was detected as the harmonic and ultraharmonic signal (integer and half-integer multiples of the 1.1 MHz frequency of the FUS transducer) caused by bubble scattering, as well as broadband noise indicating bubble collapse (green/light blue fill between the harmonics and ultraharmonics) as shown in **Figure 29B** for a representative ultrasound exposure. For all experiments in this chapter ultrasound exposure lasted 20 s. Although sonication could be prolonged *in vitro* for as long as SV cavitation occurs, 20 s is a relevant time duration for future *in vivo* experiments. In our recent publication[35], we have shown that SV is replenished approximately every 20 s in mice, so the ultrasound beam sees new bubbles thanks to the blood flow, which is not the case in our *in vitro* set up. Also, SV bubbles are very short-lived, which is also apparent from **Figure 29B.** Although the sonication time is only 20 s, it is already evident that the size distribution of the bubbles changes as the higher frequency signal fades indicating that smaller bubbles coalesce to make bigger ones. SV, like other cavitation agents in the micron size range, is restricted in the vasculature therefore the cavitation effects are dependent on tumour perfusion. Poorly vascularised tumours cannot receive maximum benefit from this strategy, hence there is value in checking the perfusion of the tumour model as concluded by Thomas *et al*[35]. Investigation of the use of longer-lived cavitation

agent, like polymeric MBs[36,37], as well as smaller ones that could extravasate and continue to cavitate in the tumour tissue could improve drug release and are worth investigating.

4.6.3 The treatment

In vitro experiments with ultrasound were performed using an in-house designed and built device that is compatible with cell culture[22]. Two experimental designs were developed to evaluate whether the ultrasound selectively enhances the delivery of 3BP to the MCT1-expressing cells. Ultrasound-induced cavitation of MBs can enhance delivery in two ways. Shear stress can act on the liposome membrane causing rupture of the vesicle and release of its contents or, alternatively, temporarily increase the permeability of the cell membranes, a phenomenon termed sonoporation.

In the original design (**Design 1**), cells were plated directly in the treatment dish. This study showed no reduction in cell viability following treatment with blank or 3BP-loaded liposomes in the absence of ultrasound in MCT1-positive and negative cells, confirming that the release of the compound, if any, is lower than the level required for toxicity in the 3BP-sensitive cell line (BT20). Ultrasound treatment did not reduce the viability of MDA-MB-231 cells. Rather, we saw an increase in cell metabolic activity, which cannot be correlated with increased number of viable cells since the results were normalised to untreated control of the same cell line. This effect was not intentional but does not compromise the outcome of this study. Conversely, BT20 cells showed sensitivity to ultrasound and/or cavitation in the absence of 3BP. This could be an artefact resulting from cell detachment rather than direct toxicity. Detached cells would be counted as dead because they would be removed at the washing steps. Still, treatment with 3BP-loaded liposomes and ultrasound proved significantly more toxic than treatment with 3BP-loaded liposomes without ultrasound and treatment with blank liposomes and ultrasound.

Design 2 was developed, firstly, to unambiguously prove that the enhanced toxicity of the 3BP-loaded liposome and ultrasound combination treatment results from 3BP release from the

liposome rather than sonoporation. It is, after all, possible that one cell line is more amenable to sonoporation than the other one. To completely exclude differences in cell sensitivity to any of the treatment components, **Design 2** also incorporates siMCT1-BT20 cells, with minimal expression of the transporter as confirmed by WB analysis. Secondly, it was recognised that the *in vivo* setting is not recapitulated by **Design 1**. Microbubbles are too bulky to extravasate from the blood vessels and therefore the cavitation events happen in the vessels – tumour cells themselves are never in proximity with the cavitating bubble. To mimic this *in vivo* setting, we spatio-temporally separated the cavitation and release events from the cells. In **Design 2**, media is supplemented with liposomes and microbubbles, treated with ultrasound and the treated media is used for cell treatment. In this way, observed reductions in cell viability are due to 3BP release rather than sonoporation. Indeed, all control groups were unaffected by treatment. The only group with significantly compromised viability was the wild-type BT20 cell group treated with 3BP-loaded liposomes and ultrasound, providing strong evidence that the liposomes respond to ultrasound and release their payload without otherwise affecting the cells.

To the best of our knowledge, this formulation combined with cavitation-triggered release has not been presented before. There is a limited number of publications reporting successful delivery systems for 3BP. In particular, micro-encapsulated 3BP has shown promising results *in vitro* and *in vivo* for the treatment of orthotopic pancreatic tumours in mice[11]. EGFR-targeted liposomal formulation of 3BP has shown promise *in vitro* in the treatment of cells growing in 2D and 3D. Interestingly, these researchers aimed for the treatment to be independent from the MCT1 expression status of the cell. However, in their case, treatment efficacy is dependent on the expression of EGFR. Both targets present great therapeutic opportunities especially in the case of TNBC, which lacks the molecular targets of hormone-dependent and HER2-positive breast tumours. It could be argued that it is better use of both targets in a cancer type so urgently in need of effective targeted treatments, rather than favouring the one against the other. Needless to say,

targeted and long-circulating liposomes come with the afore-mentioned limitations. In a recently published study from our group, we have shown that despite the successful uptake of EGFR-targeted liposomes *in vitro*, their fast clearance *in vivo* (less than 20 min) significantly compromised tumour uptake in vivo. However, tumour uptake almost doubled with ultrasound treatment[38]. While the current work was ongoing, Zhang and colleagues published very encouraging results showing systemic treatment with liposomal 3BP, providing proof-of-concept for the up to then speculative arguments that liposomes could improve the therapeutic window of 3BP[39]. This study also employed targeted liposomes. Unlike the design used by Gandham *et al.* who targeted the liposome against EGFR found on tumour cells, and thus requiring internalisation of the liposome, Zhang's study employed a vascular target and aimed for the drug to be released in the tumour vasculature. However, their liposome relied on passive release without an external or intrinsic stimulus.

4.7 Conclusions & future directions

Accumulated experience with 3BP has shown it to be a clearly potent but quite controversial compound, due to its reactive nature. Sadly, inappropriate use of unformulated 3BP resulted in the death of three cancer patients. This tragic event highlighted more than ever that it is imperative for this compound to be properly formulated for its use to be safe and effective. Taken together, the data presented in this chapter provide evidence that the encapsulation of 3BP in non-toxic, cavitation-sensitive liposomes of appropriate physicochemical properties is a feasible and promising strategy for the systemic administration of the compound. Liposomes of similar compositions are already in the clinic or in clinical trials, while the cavitation agents employed here, SV, are routinely used in clinical practice for diagnostic purposes. In mice, liposomes followed by fluorescence imaging induced no side effects in concentrations that would be used for treatment.

Ultrasound equipment for diagnosis and treatment is readily available in the clinic. Therefore, this could be a viable therapeutic approach for cancer patients in the future.

If this study were to be taken forward, we would more formally examine the release profile of the liposomes *in vitro* and *in vivo*. A fluorescent dye like sulfo-Cy5 can be used for this purpose. The encapsulation efficiency of 3BP in the liposomes should be optimised to ensure that the minimum concentration of lipid is injected to the animal for a therapeutic study. Importantly, a therapeutic study would require multiple injections of the compound over several days so it is best practice to minimise the excipients involved in the formulation. Establishing an *in vivo* tumour model for these studies is of prime importance. BT20 cells, although they grow well *in vitro*, have been challenging to grow as a xenograft. Overall, I hope to overcome these challenges and explore the potential of the presented strategy.

4.8 References

1. El Sayed, S. M. *et al.* Safety and outcome of treatment of metastatic melanoma using 3-bromopyruvate: a concise literature review and case study. *Chin. J. Cancer* **33**, 356–64 (2014).
2. Fan, T. *et al.* Tumor Energy Metabolism and Potential of 3-Bromopyruvate as an Inhibitor of Aerobic Glycolysis: Implications in Tumor Treatment. *Cancers (Basel).* **11**, (2019).
3. Sadowska-Bartosz, I., Szewczyk, R., Jaremko, L., Jaremko, M. & Bartosz, G. Anticancer agent 3-bromopyruvic acid forms a conjugate with glutathione. *Pharmacol. Reports* **68**, 502–505 (2016).
4. El Sayed, S. M. Enhancing anticancer effects, decreasing risks and solving practical problems facing 3-bromopyruvate in clinical oncology: 10 years of research experience. *Int. J. Nanomedicine* **13**, 4699–4709 (2018).
5. Ko, Y. H. *et al.* A translational study 'case report' on the small molecule 'energy blocker' 3-bromopyruvate (3BP) as a potent anticancer agent: From bench side to bedside. *J. Bioenerg.*

Biomembr. **44**, 163–170 (2012).

6. Feldwisch-Drentrup, H. Candidate cancer drug suspected after death of three patients at an alternative medicine clinic. *Science (80-.).* (2016) doi:10.1126/science.aah7192.

7. Chang, J. M. *et al.* Local toxicity of hepatic arterial infusion of hexokinase II inhibitor, 3-bromopyruvate: In vivo investigation in normal rabbit model. *Acad. Radiol.* **14**, 85–92 (2007).

8. Pan, Q. *et al.* Hepatotoxicity and nephrotoxicity of 3-bromopyruvate in mice. *Acta Cir. Bras.* **31**, 724–729 (2016).

9. Zhang, Y. *et al.* Suppression of Tumor Energy Supply by Liposomal Nanoparticle-Mediated Inhibition of Aerobic Glycolysis. *ACS Appl. Mater. Interfaces* **10**, 2347–2353 (2018).

10. Gandham, S. K., Talekar, M., Singh, A. & Amiji, M. M. Inhibition of hexokinase-2 with targeted liposomal 3-bromopyruvate in an ovarian tumor spheroid model of aerobic glycolysis. *Int. J. Nanomedicine* **10**, 4405–23 (2015).

11. Chapiro, J. *et al.* Systemic Delivery of Microencapsulated 3-Bromopyruvate for the Therapy of Pancreatic Cancer. *Clin Cancer Res. Clin Cancer Res* **20**, 6406–6417 (2014).

12. Bulbake, U., Doppalapudi, S., Kommineni, N. & Khan, W. Liposomal formulations in clinical use: An updated review. *Pharmaceutics* **9**, 1–33 (2017).

13. Wilhelm, S. *et al.* Analysis of nanoparticle delivery to tumours. *Nat. Rev. Mater.* **1**, 1–12 (2016).

14. Stylianopoulos, T., Munn, L. L. & Jain, R. K. Reengineering the Tumor Vasculature: Improving Drug Delivery and Efficacy. *TRENDS in CANCER* **4**, 258–259 (2018).

15. Sriraman, S. K., Aryasomayajula, B. & Torchilin, V. P. Barriers to drug delivery in solid tumors. *Tissue barriers* **2**, e29528 (2014).

16. Ziemys, A. & Ferrari, M. Transport barriers and oncophysics in cancer treatment. *TRENDS in CANCER* **4**, 277–280 (2018).

17. Mura, S., Nicolas, J. & Couvreur, P. Stimuli-responsive nanocarriers for drug delivery. *Nat. Publ. Gr.* **12**, (2013).

18. Torchilin, V. P. Multifunctional, stimuli-sensitive nanoparticulate systems for drug delivery. *Nat. Rev. Drug Discov.* **13**, 813–827 (2014).

19. Lyon, P. C. *et al.* Safety and feasibility of ultrasound-triggered targeted drug delivery of doxorubicin from thermosensitive liposomes in liver tumours (TARDOX): a single-centre, open-label, phase 1 trial. *Lancet Oncol.* (2018) doi:10.1016/S1470-2045(18)30332-2.

20. Glick, M., Biddle, P., Jantzi, J., Weaver, S. & Schirch, D. The antitumor agent 3-bromopyruvate has a short half-life at physiological conditions. *Biochem. Biophys. Res. Commun.* **452**, 170–173 (2014).

21. Graham, S. M. *et al.* Inertial cavitation to non-invasively trigger and monitor intratumoral release of drug from intravenously delivered liposomes. *J. Control. Release* **178**, 101–107 (2014).

22. Carugo, D., Owen, J., Crake, C., Lee, J. Y. & Stride, E. Biologically and acoustically compatible chamber for studying ultrasound-mediated delivery of therapeutic compounds. *Ultrasound Med. Biol.* **41**, 1927–1937 (2015).

23. Allen, T. M. & Cullis, P. R. Liposomal drug delivery systems: From concept to clinical applications. *Adv. Drug Deliv. Rev.* **65**, 36–48 (2013).

24. Sadowska-Bartosz, I., Soszyński, M., Ułaszewski, S., Ko, Y. & Bartosz, G. Transport of 3-bromopyruvate across the human erythrocyte membrane. *Cell. Mol. Biol. Lett.* (2014) doi:10.2478/s11658-014-0189-1.

25. Azevedo-Silva, J. *et al.* The cytotoxicity of 3-bromopyruvate in breast cancer cells depends on extracellular pH. *Biochem. J.* **467**, 247–258 (2015).

26. Geschwind, J.-F. H., Ko, Y. H., Torbenson, M. S., Magee, C. & Pedersen, P. L. Novel therapy for liver cancer: direct intraarterial injection of a potent inhibitor of ATP

production. *Cancer Res.* **62**, 3909–13 (2002).

27. Ko, Y. H. *et al.* Advanced cancers: eradication in all cases using 3-bromopyruvate therapy to deplete ATP. (2004) doi:10.1016/j.bbrc.2004.09.047.

28. Zhang, Q. *et al.* Aerosolized 3-Bromopyruvate Inhibits Lung Tumorigenesis without Causing Liver Toxicity. *Cancer Prev. Res.* **5**, 717–725 (2012).

29. Zhang, Q. *et al.* Enhanced antitumor activity of 3-bromopyruvate in combination with rapamycin in vivo and in vitro. *Cancer Prev. Res. (Phila).* **8**, 318–26 (2015).

30. Yamada, M. *et al.* Topical 3-bromopyruvate is a novel targeted therapy for melanoma in a preclinical model. *J. Dermatol. Sci.* **92**, 134–142 (2018).

31. Wicks, R. T. *et al.* Local delivery of cancer-cell glycolytic inhibitors in high-grade glioma. *Neuro. Oncol.* **17**, 70–80 (2015).

32. Lowe, D. Bromopyruvate Revealed - In the Pipeline. *Science translational medicine* https://blogs.sciencemag.org/pipeline/archives/2018/11/14/bromopyruvate-revealed.

33. Yadav, S. *et al.* Molecular docking studies of 3-bromopyruvate and its derivatives to metabolic regulatory enzymes: Implication in designing of novel anticancer therapeutic strategies. *PLoS One* **12**, e0176403 (2017).

34. SonoVue 8 microlitres/ml, powder and solvent for dispersion for injection - Summary of Product Characteristics (SmPC) - (eMC). https://www.medicines.org.uk/emc/product/1539/smpc.

35. Thomas, E. *et al.* Ultrasound-mediated cavitation enhances the delivery of an EGFR-targeting liposomal formulation designed for chemo-radionuclide therapy. *Theranostics* **9**, 19 (2019).

36. Jablonowski, L. J. *et al.* Balancing stealth and echogenic properties in an ultrasound contrast agent with drug delivery potential. *Biomaterials* **103**, 197–206 (2016).

37. Eisenbrey, J. R. *et al.* Development and optimization of a doxorubicin loaded poly(lactic

acid) contrast agent for ultrasound directed drug delivery. *J. Control. Release* **143**, 38–44 (2010).

38. Thomas, E. *et al.* Ultrasound-mediated cavitation enhances the delivery of an EGFR-targeting liposomal formulation designed for chemo-radionuclide therapy. *Theranostics* **9**, 19 (2019).

39. Zhang, Y. *et al.* Suppression of Tumor Energy Supply by Liposomal Nanoparticle-Mediated Inhibition of Aerobic Glycolysis. (2017) doi:10.1021/acsami.7b16685.

5 A radiolabelled lactate mimetic: ^{123}I-HPLA

5.1 Abstract

In this chapter, the application of the 'Trojan horse' approach, successfully employed in the case of 3BP, is investigated for the delivery of targeted radionuclide therapy (TRT) to cancer cells. The first challenge encountered was the small size of lactate and pyruvate comprised of only three carbon atoms, hence attachment of a chelator and a radio-metal would result in an entity with different chemical properties. Given that a large halogen, bromine, does not impair the selectivity of 3BP toward MCT1, it was hypothesised that radio-iodine, a commonly used radio-halogen, could be substituted for bromine without loss of specificity.

Here, the synthesis of this proposed compound, followed by its purification, *in vitro* and *in vivo* investigation are presented.

5.2 Introduction

5.2.1 Targeted radionuclide therapy (TRT)

Together with chemotherapy, external beam radiotherapy (EBRT) constitute the mainstay of treatment for patients with tumours that cannot be cured by surgery alone. One of the main limitations of these treatments is the associated toxicity due to off-target effects. Targeted radionuclide therapy (TRT) is the selective irradiation of cancer cells by the administration of a radionuclide. In combination with the development of molecularly targeted agents and carriers, TRT offers a unique opportunity to provide selective irradiation of the tumour without damaging healthy organs[1,2]. Often, agents used for TRT are theranostic, meaning that depending on the radioiosotope or the dose of radioactivity administered, they can be used for treatment or imaging

via positron emission tomorgraphy (PET) or single-photon emission computed tomography (SPECT) for initial diagnosis or monitoring of the disease[2].

The first radionuclide to be used in the clinic was radio-iodine, which has been used for decades for the treatment of thyroid cancer[3,4]. Targeting capacity in this case is inherent to the radionuclide – iodine naturally accumulates in the thyroid. Similarly, strontium, administered as $^{89}SrCl_2$, acts as a calcium mimetic and accumulates in bones, serving as a palliative treatment in cancer patients with bone metastases[3,5]. Most radionuclides however, have no inherent targeting capacity and rely on targeting vectors for selective accumulation at the target tissue and, if appropriate, selective cellular uptake[5].

TRT has shown immense promise as a therapeutic modality both in clinical and preclinical applications. Established treatments include radioimmunotherapy for lymphoma using ^{90}Y-itritumomab tiuxetan, small molecule treatment of neuroblastoma with ^{131}I-MIBG and prostate cancer with $^{223}RaCl_2$[2]. Moreover, positive outcomes of the NETTER 1 phase III clinical trial of ^{177}Lu-octreotide (Lutathera) led to its approval by the FDA last year, offering a new treatment option for patients with mid-gut neuroendocrine tumours[6–10]. ^{212}Pb-TCMC-trastuzumab was shown to be safe in phase I clinical trials in patients with intraperitoneal HER2-positive metastases[11], while it has shown significant survival benefit in pre-clinical studies[12]. ^{177}Lu-prostate-specific membrane antigen (PSMA) therapy is under clinical investigation at the time of writing[13], and PSMA-targeted radio-ligands binding α or β emitters are being explored[9,14,15]. An α emitter-labelled anti-PDL1 antibody is under pre-clinical development[16]. Additionally, a range of nanocarriers with TRT cargo have been investigated for the delivery of radionuclides to solid tumours, including polymeric[17], protein-based[18] and inorganic nanoparticles[19], liposomes[20] and polymer-radionuclide conjugates[21,22].

5.2.2 Delivery considerations for TRT

Delivery challenges associated with non-radioactive cancer therapeutics are also applicable to TRT. These arise from the physicochemical properties of the therapeutic and can result in poor pharmacokinetics and unfavourable biodistribution, or posed by the tumour, with dense extracellular matrix and high interstitial pressure being the most prominent[23,24]. When it comes to radiopharmaceuticals however, additional factors must be taken into account. The properties of the carrier should be matched to those of the radionuclide at multiple levels such as the spatial distribution in the target tissue, kinetics, chemistry and formulation process[25].

Different radionuclides vary in emission type (α, β^-, β^+/positron, Auger electrons or γ-radiation), which in turn determines the penetration range and linear energy transfer (LET). Auger electron emitters (e.g. ^{125}I and ^{99m}Tc) have the shortest penetration range (2-500 nm) accompanied by high LET (4-26 keV/ μm)[5]. They are used to minimise collateral damage, but they present with additional challenges as they require homogeneous distribution and intracellular delivery[26]. Alpha (α) emitters (e.g. ^{213}Bi, ^{223}Ra, ^{211}At, ^{225}Ac) have a penetrating range extending to a few cell diameters (50-100 μm in soft tissue) and high LET (80–100 keV/μm), hence they are appropriate for treating small lesions and metastases[5,26]. Positron (β^+) emitters are commonly used for imaging purposes via PET with the prominent example of ^{18}F-fluorodeoxyglucose (FDG). They are high energy, short-lived isotopes with a penetrating range of 0.2-8 mm. Longer lived nuclei such as ^{89}Zr ($t_{1/2}$ = 3.3 days) are also being investigated[26]. By far the most commonly used in therapy are the beta (β^-)-emitting radionuclides, which have a longer penetrating range (1-500 mm) and low LET (0.2 keV/mm)[5,26]. Beta particles are therefore less demanding in terms of homogeneous delivery, but the trade-off is that they are more likely to cause damage to healthy tissues.

Considering the particular features of each radionuclide, the selection of the carrier needs to address the two following parameters:

5.2.2.1 Spatial requirements which depend on the penetration depth

For highest impact, Auger emitters need to be in close proximity to the target organelle or macromolecule, which is typically nuclear DNA but could be the mitochondrial DNA as well[1]. Therefore, Auger emitters require a mechanism of intracellular targeting e.g. membrane receptors that translocate to the nucleus. One such example is EGFR, which has been targeted using liposomes externally decorated with ^{111}In-labelled epidermal growth factor (^{111}In-EGF)[27,28]. For beta emitters, on the other hand, cell membrane localisation can be sufficient such as in the case of the radioligand ^{177}Lu-PSMA, which targets the extracellular part of PSMA[29].

5.2.2.2 Radionuclide half-life

Half-life is a crucial factor when considering the purpose of the radiopharmaceutical (imaging or treatment), the preparation of the formulation and the kinetics of the therapeutic in the body. Generally, short half-life coupled with fast biological clearance are ideal for imaging agents, which minimises toxicity potential, optimises contrast and is more practical for the patient and their family. For TRT, however, longer retention of the radiopharmaceutical at the target site is required and a half-life spanning of a few days is desirable.

The time it takes for the preparation of the radiotherapeutic and its *in vivo* kinetics should match the half-life of the radionuclide. Ideally, addition of the radioactivity is achievable in a single and final step of the synthetic and/or formulation process. This has the additional advantage of minimising handling of radioactive material. Bifunctional, amine-based chelators provide a platform for the radiolabelling of peptides, antibodies and nanocarriers with radio-metals. The macromolecule or carrier can be functionalised with the chelator and the radiolabelling is then a quick and facile process involving addition of the radio-metal salt in aqueous buffers[26], followed by purification by size exclusion chromatographic techniques or filtration. In contrast, radio-halogens require covalent bond formation. Radio-iodine is the only halogen for which there is a simple and standardised method of radiolabelling. It requires the presence of an aromatic ring

usually provided by tyrosine residues on peptides[26,30,31]. A frequent challenge with radio-iodinated compounds is the metabolic detachment of iodine in the body and accumulation of iodine in tissues expressing the sodium-iodide symporter (NIR), particularly the thyroid[25,32].

5.2.3 A radiolabelled compound to target MCT1

PET tracers have been used for imaging cancer metabolism in the clinic and for research. In particular, the use of ^{18}F-FDG for PET imaging has dominated the field[33,34]. FDG is a fluorinated glucose analogue that is taken up by the glucose transporter but cannot be further metabolised. Its use is based on the 'Warburg effect', that is upregulated glycolysis even in aerobic conditions, a phenotype exhibited by many cancers. However, transformative advances in cancer metabolism have shown that it is deregulated in multiple ways, involving several metabolites, which have not yet been exploited for imaging or TRT. Anti-1-amino-3-^{18}F-fluorocyclobutane-1-carboxylic acid (FACBC), a synthetic ^{18}F-labelled amino-acid was approved by the Food and Drug Administration (FDA) in 2016 for the detection of recurrent prostate cancer. Glutamine was first radiolabelled in 2011 with ^{11}C and ^{18}F[33], while other amino-acids, tyrosine and methionine labelled with ^{11}C have also been investigated[35,36]. Nucleotides labelled with radio-iodine, ideally suited to deliver radioactivity to DNA, have been reported[37]. Lately, an ^{18}F-lactate derivative was also synthesised, which constitutes an exciting development given the central role of lactate in cancer metabolism[38].

There is a special challenge with utilising metabolite analogues as radiopharmaceuticals which is that metabolites are small molecules, many of them composed of a 2-6 carbon skeleton (sugars, amino-acids, small monocarboxylates). Commonly used chelators are either macrocyclic aminopolycarboxylic systems like DOTA ($C_{16}H_{28}N_4O_8$, 404.420 g/mol) or acyclic like DTPA ($C_{14}H_{23}N_3O_{10}$, 393.3 g/mol)[26] and would substantially change the physicochemical properties of most metabolites. Therefore, direct covalent binding of non-metal elements is needed. Metabolites labelled with carbon or hydrogen isotopes would have the advantage of sharing the same

properties as the native molecule. Fluorine, however, has dominated the field because its size is similar to that of hydrogen, but, unlike labelling with ^{11}C, the end product is not the same. This potentially limits downstream metabolism of the tracer (as with ^{18}F-FDG), thus removing the complexity associated with participation of the metabolite in several pathways and therefore, simplifying the measurement of uptake. Moreover, inhibition of downstream metabolism, as in the case of glucose analogues, could be therapeutic.

^{18}F is an excellent imaging agent but not a therapeutic radioiosotope. Iodine, a much larger and less electronegative halogen, presents several advantages which explain why it is the only non-metal isotope used in the clinic. First, it has a stable isotope (^{127}I) and three readily available radioisotopes with different properties (^{123}I, ^{125}I, ^{131}I), which can form a theranostic pair, with a ^{123}I-labelled and $^{131/125}$I-labelled compound serving as a tracer and therapeutic agent respectively. Also, radioiodination reaction schemes have been developed, albeit mostly relying on the presence of an aromatic ring on the substrate[30,31,39]. The properties (half-life and emissions) and main clinical applications of iodine isotopes are summarised in **Table 5**.

MCT1 is highly expressed by many cancers[40], while its relatively wide substrate specificity[41,42], that includes aromatic and halogenated monocarboxylates, makes it a potentially suitable target for radioiodinated substrates.

Table 5 Iodine isotopes and their properties.

Isotope	Half-life	Emissions	Imaging
^{127}I	N/A (stable)	N/A	N/A
^{123}I	13.3 h	γ, Auger electrons	SPECT
^{125}I	60.2 d	Auger electrons, γ	SPECT
^{131}I	8.01 d	β, γ	SPECT

5.3 Aims

The aims of this chapter were:

- To radioiodinate an aromatic lactate derivative, HPLA
- To develop a chromatographic method for the purification of the iodinated compound (I-HPLA)
- To investigate the uptake of I-HPLA by MCT1-positive and -negative cell lines
- To explore the *in vivo* behaviour of I-HPLA
- To encapsulate I-HPLA in liposomes.

5.4 Materials & Methods

5.4.1 Synthesis of I-HPLA

A solution of p-hydroxyphenyllactic acid (HPLA) was prepared by dissolving 2 mg in 100 μL PBS. HPLA solution (15 μL) was transferred into the reaction tube (Pierce pre-coated iodination tubes, Fisher Scientific, UK), quickly followed by the addition of sodium iodide-123 (^{123}I-NaI in sodium hydroxide solution, GE Healthcare, Belgium). The addition of radioiodide was done by rinsing the stock vial three times with 15 μL PBS. The stock vial contains 37 MBq in 1-1.3 μL sodium hydroxide aqueous buffer to minimise volatility. The reaction tube contains a total of 60 μL (or up to 100 μL if more washes of the stock vial are required to remove as much radioactivity as possible). Iodide undergoes oxidation once in the reaction tube so the tube is sealed immediately after the addition of ^{123}I-NaI. The reaction is allowed to proceed for 60 min, and then quenched by transfer of the reaction mix into a clean Eppendorf tube.

The phenolic ring becomes more activated towards further substitution reaction after the attachment of the first iodine atom, so two iodination products are expected with different lipophilicities – double iodination resulting in more lipophilic product. The hydroxyl group activates the ring towards electrophilic aromatic substitution, hence a phenolic starting material was selected over phenyl-lactate. Hydroxyl group also directs further substitution to the ortho- and para- position. Para-position is already occupied by the lactate moiety therefore the expected products are those of ortho-iodination (positions 3 and 5). The chemical structures of the starting material (HPLA) and those of the expected mono- and di-iodination products (I-HPLA and I_2-HPLA) are presented in **Figure 32**.

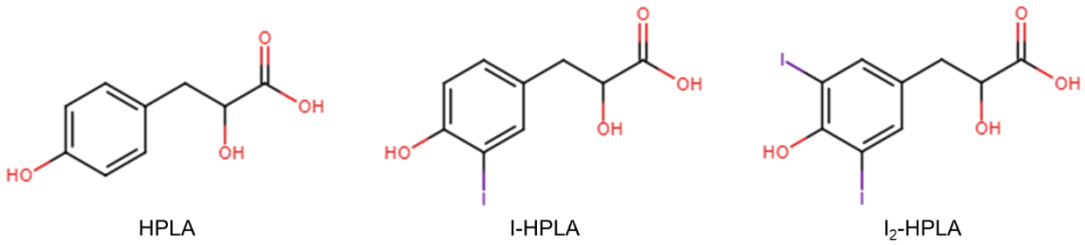

Figure 32 Chemical structures of the starting material, p-hydroxyphenyllactic acid (HPLA) and the mono- and di-iodination products (I-HPLA and I_2-HPLA, respectively).

5.4.2 Analysis and purification of I-HPLA

To check the reaction has proceeded, a small aliquot of the reaction mix was analysed with reversed phase-high pressure liquid chromatography (RP-HPLC) (2 µL / 0.5-1 MBq in 20 uL PBS). For further *in vitro* or *in vivo* experiments, ^{123}I-HPLA was synthesised on the day of the experiment, a small aliquot (2 µL in 20 µL PBS) was analysed by HPLC as a test, followed by purification of the radioactive compound by the same method. The injection volume varied depending on the experiment and it could be manual (for larger volumes and high activity) or a standard 20 µL injection via the autosampler.

For HPLC analysis and purification, the column was equilibrated and a blank water injection was run prior to any sample. HPLC is operated using an XBridge C-18 column (Agilent, CA, USA) at room temperature. A 20 min gradient of 1-99% water-acetonitrile acidified with 0.1% formic or trifluoroacetic acid (TFA) is used. When first developing the reaction and analysis method, TFA was employed. However, when assays with treated cells were commenced, it was noticed that the combination of acetonitrile and presence of acid caused cytotoxicity. For this reason, a switch to formic acid, which is less toxic, was made. Notably, the column was changed from 4.6 x 150 mm to one of the same type but smaller: 3.5 μm particle size and 3.0 x 150 mm dimensions. This shifted the retention times to approximately 2 min earlier. Following the analysis of a small aliquot, the reaction mix was run using the same method and gradient, and the radio-peak collected for use in subsequent experiments. For the assessment of radiochemical purity, product from a non-radioactive (^{127}I) and radioactive (^{123}I) reaction were purified and run on HPLC. The purified non-radioactive product was analysed using mass spectrometry (MS) to verify which peak corresponded to the starting material, and which to mono- and di-iodinated products.

In RP-HPLC, polar compounds interact weakly with the stationary phase (which is non-polar) and elute quickly. In contrast, the interaction of less polar compounds with the stationary phase is stronger, and therefore elute later.

5.4.3 Radiochemical stability of I-HPLA

The purified compound was diluted in PBS and stored for 24 h at room temperature, 4°C or 37°C and then analysed by HPLC as described in the previous section.

5.4.4 Optimisation of the reaction time

The 'Iodogen reaction' is intended mainly for the iodination of water-soluble macromolecules and cells, which tend to have complex structures with chemical groups potentially

sensitive to the oxidising environment of the reaction[30]. Hence, the recommended reaction time by the manufacturer is 5-15 min[43]. Here, the target compound is a small molecule with only a single aromatic ring available for iodination and other functional groups (hydroxyl, carboxyl) not known to be sensitive under the reaction conditions. It was therefore hypothesised that increasing the reaction time will increase the yield. To assess this, non-radioactive I-HPLA was synthesised and purified as described in sections 5.4.1 and 5.4.2 respectively. Then, 20 μL aliquots of the reaction solution were collected at several time points (5, 10, 30 and 60 min). The AUC of each reactant or product peak at 230 nm wavelength was plotted against time in minutes.

5.4.5 Cellular uptake of I-HPLA

BT20 and MDA-MB-231 cells were seeded to 80-90% confluency (5 x 10^4 cells/well in 24 well plate). The following day medium from each well was replaced by 1 mL fresh medium. Cells were exposed to purified ^{123}I-HPLA (0.5-1.5 MBq/well) for 2 or 24 h in normal growth conditions. The medium was then removed and cells were washed three times with PBS and lysed with RIPA buffer supplemented with protease inhibitor on ice. The lysates were collected and the wells were rinsed once with RIPA and the rinse was added to the lysate. Radioactivity in the lysates was measured using an automated Wizard gamma counter (Perkin Elmer, Waltham, MA, USA). Protein content in the lysates was assessed by BCA assay (see **Chapter 2, section 2.2**) and radioactivity was normalised per mg of protein to account for differences in cell number. Due to the short half-life of ^{123}I, using absolute values of normalised activity (CPM/μg of protein) to compare between different experimental sessions would be challenging. Hence, the results were plotted as ratios of normalised activity in the lysate of the MCT1-positive cells (BT20) to normalised activity in the lysate of the MCT1-negative cells (MDA-MB-231), to show the MCT1-dependent difference in uptake.

5.4.6 *In vivo* tumour growth

All *in vivo* procedures were conducted in accordance with the Animals Scientific Procedures Act of 1986 (UK) (Project License Number 30/3115 and P13B66CD9 issued by the Home Office) and protocols approved by the Committee on the Ethics of Animal Experiments of the University of Oxford. Female athymic nude mice (6–8 weeks old, average weight of 25 g) were purchased from Charles River. To obtain BT20 xenografts, $4x10^6$ cells were mixed 1:1 with Matrigel (final volume 200 μL) and injected subcutaneously (s.c.) in the right flank. Mice were monitored at least once weekly for the appearance of tumours which were measured using callipers.

The primary goal of this pilot experiment was to collect information about the growth and vascularity of BT20 tumours as xenografts. Xenografts are the easiest and most commonly used tumour models for *in vivo* experiments such as those carried out here.

5.4.7 *In vivo* biodistribution and pharmacokinetic studies

Blood clearance was evaluated using SPECT imaging of the thoracic area. The experiment was designed so that the same mice could be used for pharmacokinetics and biodistribution. Mice (n=3) were anaesthetised with isoflurane, cannulated via the lateral tail vein and placed in a bespoke cradle. Each animal received ^{123}I-HPLA solution in PBS (4-6 MBq, 200 μL, pH 5) intravenously, followed by 60 μL saline to flush the cannula and imaged for approximately 50 min, acquiring 200 frames of 30 s focused on the heart. At the end of the SPECT session, a full body CT and SPECT scan was performed. At 1.5 h post-injection, the animals were euthanised, the organs and xenografts were harvested, weighed and the amount of radioactivity was counted using an automated gamma counter (HIDEX, Finland). All images were reconstructed using MILabs reconstruction software v3.24 and analysed using PMOD v.3.37 (PMOD Technologies, Zurich, Switzerland).

In order to assess the selectivity of the compound for the tumour over the healthy tissues, 'tumour to muscle' ratio was calculated by dividing the normalised activity (CPM/g of tissue) of the tumour by that of a muscle sample. For this calculation, tissues (including blood) were accurately weighed in pre-weighed tubes placed in the automated gamma counter (HIDEX, Finland). For 'tumour to blood' ratio, total blood volume was assumed to be 2 mL and was calculated in the same was as the 'tumour to muscle'. Total blood volume was assumed to be 2 mL. 'Tumour to blood' ratio is an indication of whether the compound is accumulating in the tumour while in circulation.

5.4.8 Encapsulation of I-HPLA in cavitation-sensitive liposomes

Liposomes were synthesized as described in **chapter 4** for 3BP, but 3BP was replaced by I-HPLA in the external acidic solution during active loading. I-HPLA is more lipophilic than 3BP so it was anticipated that loading would be more efficient. Loading was allowed to proceed for 2 h at room temperature. Loading efficiency was assessed by separation of the liposomes and free compound using size exclusion column chromatography (Sephadex G25 fine, eluted with PBS) and measurement of the radioactivity in the liposomal fraction using an automated Wizard gamma counter.

5.5 Results

5.5.1 Synthesis of I-HPLA: reaction analysis

Radioiodination under oxidative conditions via the 'iodogen' method was employed for the synthesis of ^{127}I-HPLA ('cold') and ^{123}I-HPLA ('hot'). Starting materials were clearly separated from the products, as apparent from the chromatographic traces of the starting materials and the crude reaction mix, presented in **Figure 33**. The 'cold' reaction generated two products. Since iodination increases the lipophilicity of the compound, it was expected that iodination products

will elute later than the starting materials and that if there are more than one products, the mono-iodinated one will elute first[31]. Mono-iodination can take place on either of the ortho-positions and there is no control over which one will be iodinated[30]. Since this molecule is intended to act as a carrier for the radio-iodine, this lack of control is not a concern.

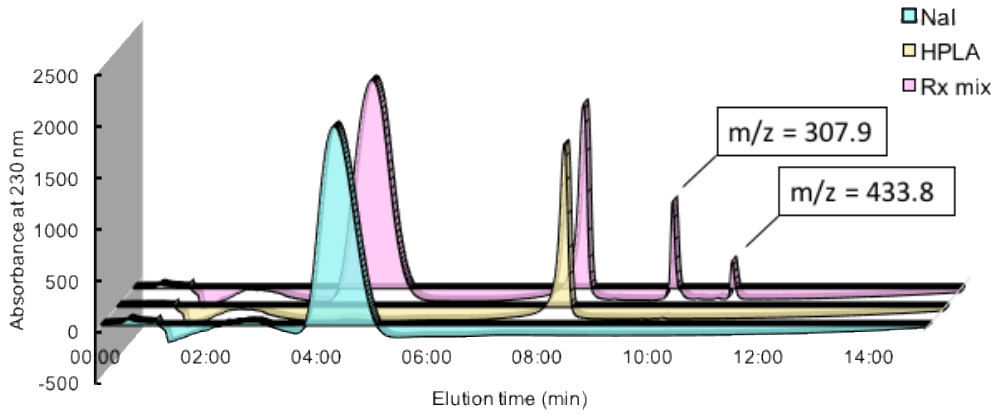

Figure 33 Chromatographic trace showing starting materials and products involved in I-HPLA synthesis. Crude reaction mix (20 µL) in PBS was analysed by reversed phase-high performance liquid chromatography (RP-HPLC) and the eluting compounds were detected by an ultraviolet detector set at 230 nm. Each trace corresponds to an independently run sample. From front to back: in blue, sodium iodide (NaI 1 mg/mL in PBS), in yellow, p-hydroxyphenyllactic acid (HPLA 1 mg/mL in PBS) and in pink, crude reaction mix after 60 min incubation. HPLC was operated with a C18 column, 1-99% water-acetonitrile gradient acidified with trifluoroacetic acid, 1 mL/min, 20 min. For full details, see methods.

The 'iodogen' method of radio-iodination is commonly employed for the iodination of hydrophilic compounds, which can be sensitive to prolonged exposure to oxidative environment. HPLA, however, is not expected to degrade under these conditions, therefore, the possibility of increasing the yield of the reaction by increasing the reaction time was investigated. AUC of HPLA and the products is higher at 280 nm, which is where the aromatic ring absorbs, but sodium iodide cannot be seen at this wavelength, which is why the 230 nm trace is presented in **Figure 34**. The reaction yield was found to increase if the reaction is allowed to proceed for longer than 5-15 min.

In particular, the AUC of 'product 1', which corresponds to the mono-iodinated compound (I-HPLA) almost tripled by 60 min as compared to 5 min (**Figure 34B**). Therefore, the radio-iodination reaction time was set at 60 min to maximise the yield.

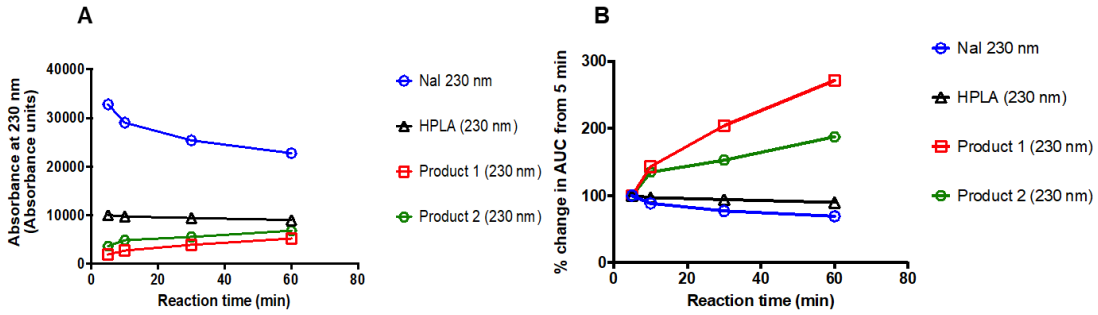

Figure 34 Optimisation of I-HPLA reaction yield. (A) Area under the curve (AUC) of chromatographic peaks of reagents (sodium iodine, NaI, and p-hydroxyphenyllactic acid, HPLA) and products 1 and 2 over time. (B) % change in AUC of reagents and products from 5 min reaction time, which is the recommended time for radio-iodination.

Reaction of excess HPLA with ^{123}I-NaI (37 MBq) produced a single radioactive compound, as shown in the combined UV and radioactive HPLC traces in **Figure 35**.

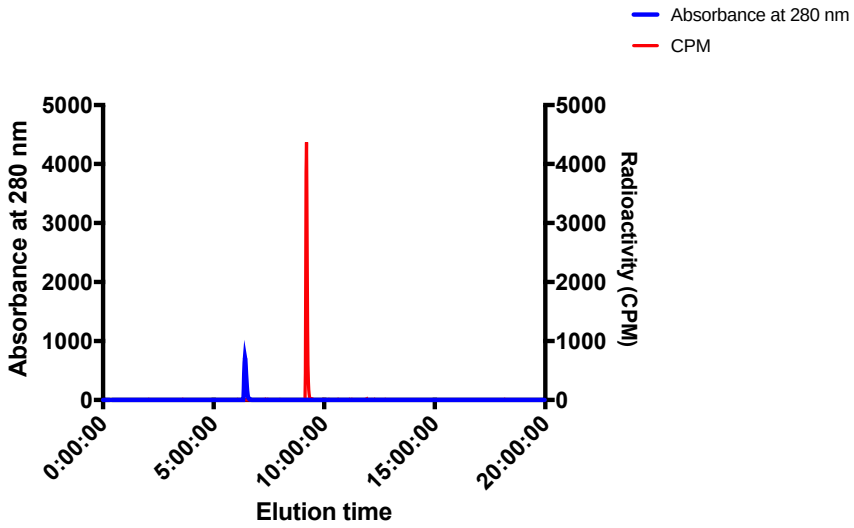

Figure 35 Purification of ^{123}I-HPLA. Chromatographic separation of unreacted starting materials and products of HPLA reaction with ^{123}I-NaI in PBS using HPLC equipped with a C18 column. Blue trace corresponds to the UV detector (280 nm) and red trace corresponds to the radioactivity detector of the radio-HPLC system. The graph was plotted using Prism 7 software (GraphPad, CA, USA). For full details, please refer to methods.

Notably, no ^{123}I-NaI peak in the dead volume of the column was detected, confirming that all iodine reacted. Since no ^{123}I-NaI peak or other radioactive peak was observed, losses from the added activity were attributed only to transfer between different containers and radioactive decay.

To confirm that the radio-iodination and the 'cold' iodination products are identical, the corresponding purified solutions were mixed together and co-injected for HPLC analysis. The UV peak (280 nm) corresponding to the 'cold' product coincides with the radioactive peak arising from the 'hot' product, suggesting that the two compounds are the same (**Figure 36**). Additionally, no other peaks are seen on the chromatograms, confirming the radio-chemical purity of the compound (**Figure 36**).

Here the HPLA and product peaks have drifted to earlier retention times. This can be explained by the decreasing efficiency of the column with repeated use, replacement of HPLC column and the use of trifluoroacetic acid (TFA) or formic acid (FA) to acidify the mobile phase. The chromatogram in **Figure 35** is representative of experiments where the compound was used in subsequent experiments. FA shifted all compounds to shorter retention times.

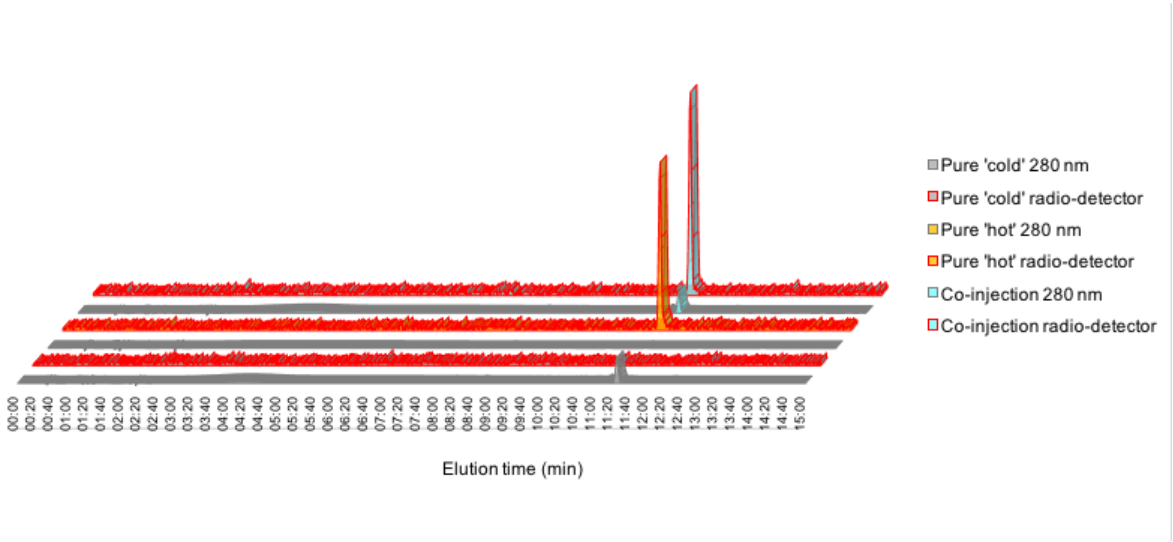

Figure 36 Radio-chemical purity of ^{123}I-HPLA. Reversed phase – high performance liquid chromatography (RP-HPLC) traces are shown. Ultraviolet (UV) signal at 280 nm is shown in grey outline and radioactivity signal is shown in red outline. Starting from the front: Purified non-radioactive I-HPLA (pure 'cold' in grey), prurified ^{123}I-HPLA (pure 'hot' in yellow) and co-injection of both solutions in cyan. HPLC was operated using a C18 column with 1-99% water-acetonitrile gradient acidified with formic acid, 1 mL/min flow rate. For full details, see methods. The graph was plotted using Microsoft Excel (Microsoft Corporation, Washington, USA).

5.5.2 Radiochemical stability of I-HPLA

Freshly synthesised and purified ^{123}I-HPLA was diluted in PBS and incubated at room temperature, 4°C or 37°C for 24 h. This time point was selected because it is the longest relevant time point for *in vitro* and *in vivo* studies using ^{123}I, which has a half-life of 13.3 h. At the end of the incubation time, 20 µL solution was injected for HPLC analysis. No detectable degradation, particularly, detachment of radio-iodide was found, as shown in **Figure 37**.

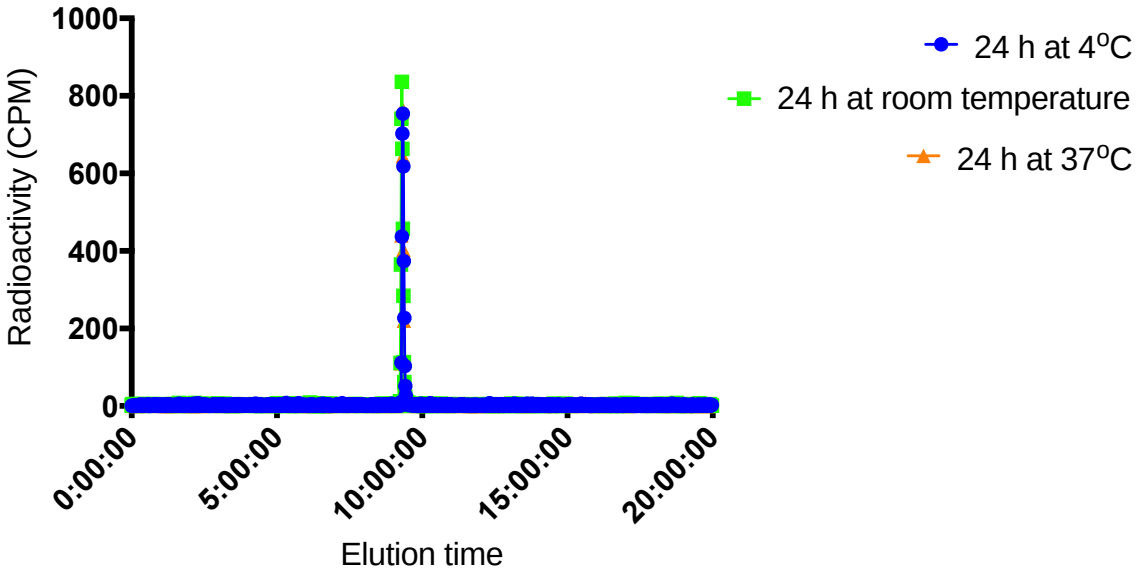

Figure 37 Radiochemical stability of ^{123}I-HPLA at 4°C, room temperature and 37°C. Freshly synthesised and purified ^{123}I-HPLA was incubated for 24 h at 4°C, room temperature or 37°C and then analysed by reversed phase-high performance liquid chromatography (RP-HPLC). The radioactivity trace for each sample (peaks in counts per minute, CPM) is presented. Blue, green and orange trace correspond to 4°C, room temperature and 37°C incubation for 24 h. HPLC was operated using a C18 column with 1-99% water-acetonitrile gradient acidified with formic acid, 1 mL/min flow rate. For full details, see methods. Graph was plotted using Prism 7 software (GraphPad, CA, USA).

5.5.3 Uptake studies

In contrast to lactate, pyruvate and 3BP, the structure of I-HPLA results in higher lipophilicity, arising from the phenolic ring and the attached iodide. Also, the size of the molecule is significantly bigger. Therefore, uptake was tested in TNBC cell lines with high and low MCT1 expression.

From uptake results presented in **Figure 38**, it is clear that BT20 cells internalise significantly more radioactivity ($P<0.05$) than MCT1-null MDA-MB-231 cells. The difference in uptake is higher on average for the 2 h incubation time, with the maximum difference reaching 8-fold for 1.5 MBq ($P<0.001$). However, although the absolute amount taken up increases with increased dose (data not shown), the uptake ratio did not appear to be increasing consistently with increasing dose. Smaller doses did not present with significant difference between the cell lines, potentially

due to the 'stickiness' of the cell culture plates. Overnight incubation resulted in a decrease in the difference of internalised radioactivity between the two cell lines, reaching up to 2.5-fold, but still, significant difference ($P<0.05$) can be observed. A possible explanation for this decrease could be that the compound not being retained, or alternatively, that the iodide is cleaved off from the parent compound and excreted.

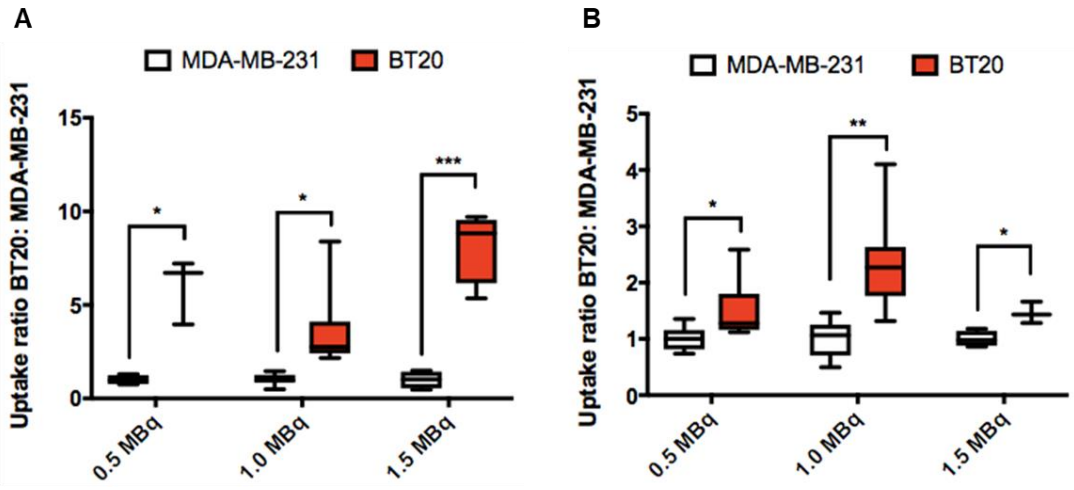

Figure 38 Uptake of ^{123}I-HPLA by breast cancer cell lines. BT20 (red) and MDA-MB-231 cells (white), which present high and low MCT1 expression respectively, were incubated with increasing concentration of ^{123}I-HPLA (0.5, 1.0 and 1.5 MBq/mL) for (A) 2 h or (B) 24 h (n=3). At the end of the incubation time, the cells were washed three times with PBS, lysed and the radioactivity in the lysate was measured using an automated gamma counter (Wizard counter, Perkin Elmer, Waltham, MA, USA). Results are presented as ratios of normalised activity (counts per minute/ µg of protein) in BT20 lysates over MDA-MB-231 lysates. Statistical analysis was performed using Prism 7 (Graphpad Software, CA, USA). *P<0.05, **P<0.01, ***P<0.001, n=3.

5.5.4 *In vivo* tumour growth

No significant tumour growth was observed for several weeks while the tumours of three mice started growing at 8 weeks. Tumour perfusion was investigated using contrast-enhanced ultrasound imaging. Only two tumours showed substantial signal enhancement compared to baseline (3- and 6-fold) which implies that the tumours were not actively growing or were poorly perfused. Mice were used 9 weeks post inoculation for a pilot pharmacokinetic and biodistribution study. The largest tumour at that point was 60 mm^3 and the smallest 15 mm^3. The *in vivo* model needs to be optimised for future studies or, if growth and/or perfusion are inconsistent, an

alternative model will be sought. Graph presenting the tumour growth and best perfused tumours are shown in the **Appendix (Figure A3).**

5.5.5 *In vivo* pharmacokinetic and biodistribution studies

The primary objective of this pilot *in vivo* experiment was to assess the feasibility of the process and the safety of the injected solution. The secondary objective was to acquire preliminary data on the radioactivity requirements for imaging, clearance of the compound, biodistribution and any intrinsic targeting capacity. Also, a known challenge with iodine-based radiopharmaceuticals is metabolic detachment of the radio-iodine and accumulation at the thyroid[44]. For animal experiments, this issue was addressed by adding potassium iodide (KI) in the drinking water the day before the experiment to saturate the thyroid. Since this was a pilot experiment with one of its objectives being to assess the behaviour of the compound, it was decided not to add the potassium iodide pre-treatment in order to assess whether the issue of iodine detachment is present.

^{123}I-HPLA was synthesised on the day of the experiment. Compared to routine synthesis for *in vitro* experiments, further limitations were posed for *in vivo* use to minimise the chance of encountering welfare issues. In particular, the limitations were on the upper limit of injection volume, pH of injected solution and acetonitrile content. Empirically, 5 MBq injection is known to be a sufficient amount for acquiring SPECT data. Maximum intravenous injection volume per mouse is 200 μL and target pH was >5. Acetonitrile LD_{50} has been measured in rats and found to vary between 170-520 mg/kg, but for this experiment calculations were based on 200 mg/kg and considering 20 g as the weight of each mouse, although the mice used in this study were heavier (approximately 25 g). Acetonitrile causes late-onset toxicity through the metabolic release of cyanide in the body.

To meet these requirements, the full reaction solution (60 μL) was injected manually to the HPLC for purification, allowed for acetonitrile evaporation for approximately 1 h. The solution was then diluted to 200 μL per mouse and pH was checked to be >5, resulting with 5 MBq/200 μL injection volume. The solution was injected slowly, while mouse breathing was checked. No adverse effects were noticed.

The highest amount of radioactivity was found in the stomach, followed by the kidneys and small intestine (7.7x 10^6, 2.9 x 10^6 and 2.3 x 10^6 CPM/g respectively). Radioactivity in the thyroid was found to be 2.2 x10^6 CPM/g based on two mice from which the thyroid could be isolated. The tumour/muscle ratio (5.78 ± 0.96 at 1.5 h) indicates differential uptake in tumour over normal tissue. Low tumour/blood ratio (0.62 ± 0.34 at 1.5 h) indicates a highly hydrophilic compound which preferentially distributes in the blood. Autoradiography showed weak signal which was, however, fairly homogeneously distributed throughout the tumour mass (image from tumour centre shown in **Figure 39**). Given that these tumours were poorly vascularised but quite small, this can be attributed to diffusion. Full body SPECT at 1 h showed accumulation in the bladder, which is the only organ that generated signal. This is indicative of the fast clearance of the compound in the urine and in agreement with the low tumour/blood ratio.

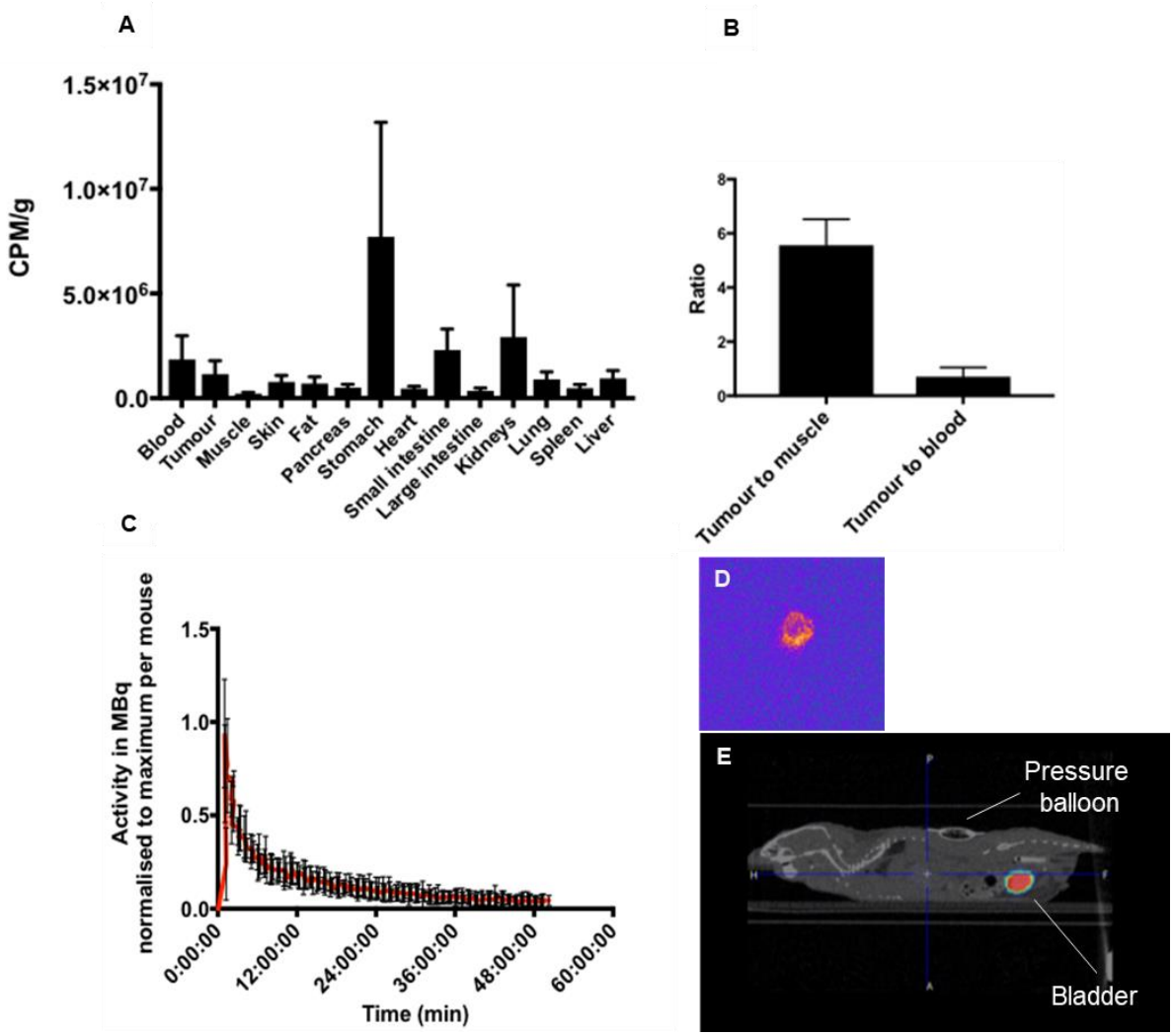

Figure 39 ***In vivo*** **characterisation of ^{123}I-HPLA**. (A) Biodistribution of ^{123}I-HPLA (5 MBq in PBS, pH 5) at 1.5 hours post-injection in female nude mice. (B) Ratios of 'tumour to blood' and 'tumour to muscle', (C)^{123}I-HPLA blood clearance measured by single photon emission computed tomography (SPECT) imaging focused on the heart area. (D) Representative autoradiography showing the distribution of ^{123}I-HPLA in a slice at the centre of the tumour 1.5 h post-injection. (E) Representative full body SPECT/CT image (lateral view) acquired 1 h post injection of ^{123}I-HPLA. A pressure balloon was used to monitor the breathing of the animal during imaging. Statistical analysis was performed using Prism 7 software (GraphPad Software, CA, USA), n=3, error bars represent standard deviation.

5.5.6 Encapsulation of I-HPLA in cavitation-sensitive liposomes

Size exclusion column chromatography was used to purify ^{123}I-HPLA-liposomes, with clear separation of the liposomal fraction in the dead volume (fractions 7-13) and the free compound eluting in a broad peak in fractions 27-39 (**Figure 40)**. Radio-synthesis, purification of ^{123}I-HPLA, encapsulation and purification of the liposomes were all performed on the same day, therefore it is unlikely that there is free iodide in fractions 27-39. As **Figure 40** shows (pink trace), the liposomal aliquot showed the same retention and no free compound peak was detected. Encapsulation efficiency was calculated by measuring the liposomal and free compound fractions using a Capintec well counter and found to be 30-40%.

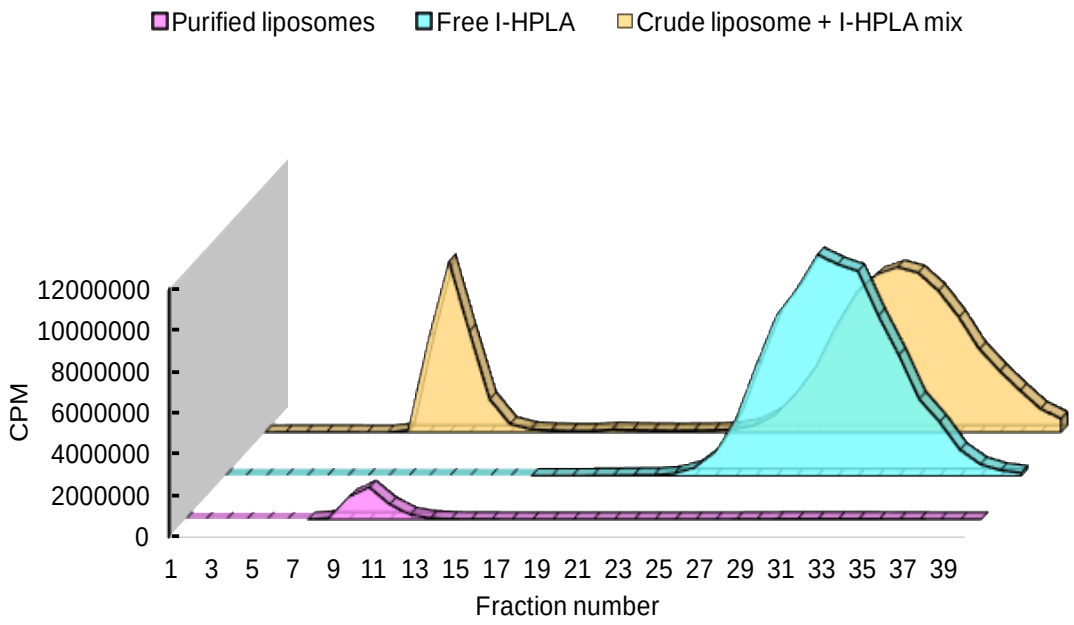

Figure 40 Purification of ^{123}I-HPLA loaded liposomes. Size exclusion chromatography traces of crude liposome mix (yellow), free ^{123}I-HPLA (cyan) and purified ^{123}I-HPLA containing liposome suspension (pink). Each fraction collected was 100 µL, except the first one which was 200 µL. Sephadex G25 column was used as the stationary phase and PBS was used as the mobile phase. Graph was plotted using Microsoft Excel (Microsoft Corporation, Washington, USA).

5.6 Discussion

In this section, the feasibility of exploiting MCT1 transport of small monocarboxylates for the delivery of TRT to TNBC cell lines was explored. MCT1 does not exhibit high substrate specificity but its main physiological substrates are L-lactate, pyruvate and β-hydroxybutyrate. More lipophilic monocarboxylates which physiologically arise from the transamination of amino-acids, such as 3-phenyl-pyruvate (from phenylalanine) and α-ketoisocaproate (from leucine), are also transported via MCT1[41,42]. However, the hydrophobic alkyl chain of these compounds interferes with their release from the transporter, making transport slower. Interestingly, the K_m value of MCT1 for the halogenated monocarboxylate chloropropionate is lower than that for lactate (Km = 4.5 mM) and equal to that for pyruvate (Km = 0.7 mM)[42]. MCT1 also mediates the transport of halogenated lactate/pyruvate derivatives such as ^{18}F-fluorolactate[38] and 3BP[45]. Larger substrates include 4-phenyl-butyrate, valproate, salicylate, and statins, while prodrugs of gabapentin and R-baclofen have been specifically designed to take advantage of the high intestinal MCT1 expression to improve their bioavailability[41,46]. Taking these different sources of information together, it was concluded that the choice of substrate, HPLA, and radionuclide, ^{123}I, were suitable and that ^{123}I-HPLA would likely be transported by MCT1.

5.6.1 Iodination reaction

Iodine volatility seriously limits the chemistry that can be applied especially under aqueous conditions. Aliphatic carbons, such as C-3 on lactate/pyruvate, require prior activation (e.g. formation of stannylated precursor) so that iodination under mildly oxidising conditions becomes possible. Radio-iodination via electrophilic aromatic substitution is a commonly used method for labelling proteins, peptides and small molecules[39,44]. 'Iodogen' is a milder oxidising agent than Chloramine-T, the other commonly used radio-iodination reagent, and it is insoluble in water[39]. 'Iodogen' is not directly involved in the reaction, it acts to oxidise iodide (I^-) to an electrophilic

species, iodous ions ('I^+') which can attack the electron-rich aromatic ring[43]. Substituents already bonded to the aromatic ring affect the rate and position of further substitution. Substituents can withdraw or donate electrons to the ring via inductive or resonance effect. The first step of the reaction mechanism is the formation of the positively charged arenium ion. Electron-donating substituents stabilise the arenium ion, therefore activating the ring towards further substitution. In contrast, electron-withdrawing substituents destabilise the arenium ion intermediate and make further substitution less favourable. Electron-donating substituents are ortho/para-directing while electron-withdrawing substituents are meta-directing (least effect on this position). Hydroxyl group (-OH) exhibits a weak inductive effect pulling electrons to the heteroatom, but it releases electrons via a strong resonance effect. It is therefore, a strong electron-donating, ortho/para-directing substituent[47]. The para-position is already occupied by another substituent, an alkyl group. Alkyl groups are weak electron-donors by inductive effect but directing further reaction to ortho/para position with regard to them[47]. Hydroxyl group dominates and iodination on tyrosine is known to happen on the ortho-position with regards to the hydroxyl group[43]. This explains why in the case of radio-iodination, where the HPLA is in large excess, we only get a single iodination product. In the case of the 'cold' reaction, two products were obtained. Given the clear separation of these products, which arises from a difference in lipophilicity, these products are more likely to be mono- and di-iodination products at the two ortho positions with regards to the hydroxyl group. The possibility of having two mono-iodinated products on the ortho- and meta-position is less likely and also not supported by the chromatogram – the products would have very similar retention times. Further characterisation with NMR would be desirable. NMR requires, however, a substantial amount of the compound (a few mg), which requires scale-up of the reaction and a change of the RP-HPLC column – from analytical column to semi-preparative.

For this work, pre-coated iodination tubes were selected. Pre-coated tubes constitute safe, convenient and ready-to-use reaction vessels. The reaction is easily terminated by transferring the

solution into a clean container. Quenching of the reaction with addition of excess cold iodide or tyrosine analogues is also possible and it increases the safety of iodination of proteins/peptides that only contain few reactive residues[43,44]. However, in this work, the substrate is essentially a tyrosine analogue and it is added in large excess to ensure that all available radioactive iodine reacts. An important limitation is the reaction volume is up to 300 μL, which is dictated by the height of the tube coating. Therefore, scaling up the reaction requires a change of the set-up. For iodination of tyrosine, neutral pH is appropriate (neutral –OH group) while pH adjustment is required for the iodination of other substrates to ensure that the hetoroatom is not protonated and its electrons are available to the aromatic system (imidazole ring of histidine, cytosine of nucleic acids)[43]. HPLA has a similar structure to that of tyrosine and importantly, the phenol moiety is maintained, therefore the reaction was performed in PBS pH 7.2.

Also, changing from TFA to FA accelerated the elution. FA is a weaker acid than TFA (pKa 3.75 and 0.23 respectively). Using 0.1% FA results in pH ≈ 2.7, while the same concentration of TFA results in pH ≈ 2. FA, however, is less toxic than TFA (LD_{50} 700 and 200-400 mg/kg respectively). Therefore, FA was preferred since the resulting solution was intended for use with cells or injected in mice. The identity of the eluted compounds cannot be questioned however. The procedure is standardised and the starting material, HPLA, can act as an informal internal standard since it was there in every experiment so the retention time of the radioactive peak could still be compared to that of HPLA (approximately 3 min difference in retention time with the mono-iodinated product).

Detachment of radio-iodine is a recognised, but not unsurmountable, challenge associated with iodine-based radio-pharmaceuticals. This is generally attributed to metabolic de-iodination (by iodotyrosine dehalogenase 1) rather than chemical instability. To test this, ^{123}I-HPLA was incubated at 4°C, room temperature or 37°C for 24 h post-purification and then analysed by HPLC. The retention time of the radioactive eluate did not change, and no additional peaks were detected

(e.g. free iodide in the dead volume). It can therefore be safely concluded that the compound is radio-chemically stable for the course of all performed experiments. Stability in serum could also be tested.

5.6.2 Cell studies

MCT1 is able to transport a variety of small organic acids, and it is not highly specific to lactic and pyruvic acid. Esterified derivatives are not charged in physiological conditions, hence they can passively diffuse through the lipid bilayer, and selectivity for cells expressing the transporter is lost, as in the case of a perillyl alcohol derivative of 3BP, intentionally synthesised as an ester to widen the applicability of the compound[48].

The question addressed in this chapter is whether, despite the changes conferred by radioiodination, the synthesised lactate derivative can still be selectively taken up by MCT1-expressing cells. It was found that BT20 cells consistently internalised higher activity, reaching approximately 8-fold difference in 2 h but only 2-fold in 24 h. This is an intriguing result that deserves further investigation. It could result from iodine detachment and subsequent ejection of the ion, or retention of the whole molecule could be limited. Difference in internalised activity was consistent but not proportional to the added activity. Transport through MCT1 follows the concentration gradient of the compound in and outside the cells. It would, therefore, be expected that if more compound is added, more will be internalised. In the experiments carried out for this project, there was no statistically significant increase in the internalised activity within the tested concentration range in which difference between the two cell lines could be seen. In very low doses (<0.5 MBq/well) there was overall lower activity in both cell lines. The results have been normalised to 'fold change' rather than absolute CPM reading to enable comparisons between experiments. An important challenge faced initially was the radioactivity sticking to the wells. Increasing cell density minimised this problem and differences between the two cell lines became

clearer, as shown by the presented results. For short incubation times, it is speculated that performing the experiment in Eppendorf tubes will further improve the outcomes (only pilot experiments performed to date).

5.6.3 *In vivo* study

A pilot *in vivo* study was conducted. Primarily, this was a feasibility study to investigate the practical challenges of an *in vivo* experiment. Taking into account the short half-life of ^{123}I (13.3 h), radiosynthesis and purification had to be carried out on the day of the experiment. An alternative option would be to start with much higher radioactivity on the day before the *in vivo* experiment (4x, to account for two half-lives) but this would require handling of a lot more activity than what was needed and it would also reduce the specific activity of the preparation. Second, the compound needs purification via HPLC, which requires the use of acetonitrile and FA, for the currently used method. Although in theory, acetonitrile content below its LD_{50} (170-520 mg/kg) was achievable and the pH could be adjusted, this pilot experiment served to ensure the preparation was safe to inject. Indeed, no side effects were observed. Upon injection, no slowing down of the breath rate or heart rate was observed. Two mice, which were maintained for 24 h, were monitored for late-onset side effects but nothing was noticed. Therefore, it was concluded that the sequence of radio-synthesis, purification and treatment on a single day is achievable and the preparation is safe to inject.

Drug clearance was followed non-invasively via SPECT imaging focused on the heart. The standard way of monitoring drug clearance is by blood collection at different time points. SPECT imaging, as performed in this study, is superior to the standard method in terms of animal welfare (no blood withdrawn, animal imaged under anaesthesia, then euthanised). Also, blood cannot be withdrawn more than twice in 24 h from the same animal. In this respect, monitoring clearance via SPECT reduces the number of animals required since each animal provides data for all time

points. In terms of accuracy, SPECT imaging is essentially continuous (30 s for each frame) while only a few time points (5-6) would be possible with direct blood collection. This method does not completely replace blood collection however. What is measured is radioactivity and not the compound directly. This experiment could be enhanced by collecting blood at the end of the imaging session and analysing it by HPLC to confirm that the compound is intact. Full body SPECT imaging was performed directly after the PK study, on the same mouse. In agreement with the rapid clearance of the compound, most radioactivity was seen in the bladder, implying renal clearance. This is not surprising for a small hydrophilic organic acid like ^{123}I-HPLA. The animals were euthanised, the organs were harvested and the radioactivity was measured. From the biodistribution graph (**Figure 439A**), it is interesting that organs known to exhibit high MCT1 expression in humans (stomach, small intestine) showed higher uptake than most other tissues, with the exception of the kidneys. Organs of high interest for most therapeutics are the liver and kidneys because they are involved in the metabolism and clearance of drugs. In agreement with the rapid clearance and the high radioactivity in the bladder, radioactivity in the kidney was also higher than average. Mice were used in this study when the tumours were still small (14-68 mm^3). However, the tumour-to-muscle ratio, a metric for the selectivity for cancerous over healthy tissue, is 4.95 ± 0.96 which indicates selective uptake. Lastly, tumour-to-blood ratio is 0.65 ± 0.34 indicating that the compound preferentially distributes in the blood, which is in accordance to its hydrophilic nature.

Given the hydrophilic nature of the compound and the existence of tissues in the body that also highly express MCT1, it was hypothesised that ^{123}I-HPLA would benefit from encapsulation in the previously described (**Chapter 4**) cavitation-sensitive liposomes with the aim to locally release the compound at the tumour site. Although time did not allow to progress that far, encapsulation of ^{123}I-HPLA was achieved (approximately 30-40% of added activity, depending on the batch) and purification of the liposomes using a G25 size exclusion column was also successful.

Given the very limited number of studies on stimulus-responsive delivery systems for radiopharmaceuticals[27,49], this is a very exciting avenue to pursue in future studies. Moreover, therapeutic radiopharmaceuticals targeting metabolic liabilities of cancer cells have not been studied before. More studies could be conducted to test the selectivity of the compound for the lactate transporter and if that proves to be the case, changing to a ^{131}I-HPLA would provide a bridge between diagnosis and treatment.

5.7 Conclusion & future directions

In this chapter, development of a radiolabelled lactate derivative was investigated with the aim to use this compound for MCT1-mediated TRT. The 'iodogen' reaction, a standard, safe and facile method of iodination was selected for the radio-iodination of HPLA, a derivative of lactate carrying a phenol moiety available for reaction. Selective uptake of the compound by MCT1-expressing TNBC cells was observed. ^{123}I-HPLA solution (5 MBq) was shown to be safe to inject in mice and sufficient for imaging by SPECT, pharmacokinetic and biodistribution studies. The compound was rapidly cleared (50 min), suggesting that it would benefit from a delivery system to improve its pharamacokinetic profile. ^{123}I-HPLA showed preferential uptake by the tumour and organs that are known to express MCT1 (stomach and intestine). ^{123}I-HPLA-containing liposomes were successfully synthesised via an active loading technique, as used for 3BP in **Chapter 4**.

Scaling up the iodination reaction would enable further characterisation of the iodination products with NMR. Although encouraging results were obtained suggesting that MCT1 might be responsible for I-HPLA uptake, this could be more rigorously proven by siRNA-mediated silencing of the transporter.

5.8 References

1. Pouget, J.-P., Lozza, C., Deshayes, E., Boudousq, V. & Navarro-Teulon, I. Introduction to radiobiology of targeted radionuclide therapy. *Front. Med.* **2**, 12 (2015).
2. Bavelaar, B. M., Lee, B. Q., Gill, M. R., Falzone, N. & Vallis, K. A. Subcellular Targeting of Theranostic Radionuclides. *Front. Pharmacol.* **9**, 996 (2018).
3. Gabriel, M. Radionuclide therapy beyond radioiodine. *Wiener Medizinische Wochenschrift* **162**, 430–439 (2012).
4. Beierwaltes Background, W. H. The History of the Use of Radioactive Iodine. (1938).
5. Jackson, M. R., Falzone, N. & Vallis, K. A. Advances in Anticancer Radiopharmaceuticals. (2013) doi:10.1016/j.clon.2013.06.004.
6. Strosberg, J. *et al.* Phase 3 Trial of 177 Lu-Dotatate for Midgut Neuroendocrine Tumors. *N. Engl. J. Med.* **376**, 125–135 (2017).
7. Dekempeneer, Y. *et al.* Targeted alpha therapy using short-lived alpha-particles and the promise of nanobodies as targeting vehicle. *Expert Opin. Biol. Ther.* **16**, 1035–1047 (2016).
8. Vaidyanathan, G. & Zalutsky, M. R. Applications of 211At and 223Ra in targeted alpha-particle radiotherapy. *Curr. Radiopharm.* **4**, 283–94 (2011).
9. Kiess, A. P. *et al.* (2S)-2-(3-(1-Carboxy-5-(4-211At-Astatobenzamido)Pentyl)Ureido)-Pentanedioic Acid for PSMA-Targeted α-Particle Radiopharmaceutical Therapy. *J. Nucl. Med.* **57**, 1569–1575 (2016).
10. Vaidyanathan, G., Boskovitz, A., Shankar, S. & Zalutsky, M. R. Radioiodine and 211At-labeled guanidinomethyl halobenzoyl octreotate conjugates: Potential peptide radiotherapeutics for somatostatin receptor-positive cancers. *Peptides* **25**, 2087–2097 (2004).
11. Meredith, R. F. *et al.* Safety and Outcome Measures of First-in-Human Intraperitoneal α Radioimmunotherapy With 212Pb-TCMC-Trastuzumab. *Am. J. Clin. Oncol.* **41**, 716–721

(2018).

12. Yong, K. & Brechbiel, M. Application of 212Pb for Targeted α-particle Therapy (TAT): Pre-clinical and Mechanistic Understanding through to Clinical Translation. *AIMS Med. Sci.* **2**, 228–245 (2015).

13. Radiometabolic Therapy (RMT) With 177Lu PSMA 617 in Advanced Castration Resistant Prostate Cancer (CRPC) - Full Text View - ClinicalTrials.gov. https://clinicaltrials.gov/ct2/show/NCT03454750.

14. Eiber, M. *et al.* Prostate-Specific Membrane Antigen Ligands for Imaging and Therapy. *J. Nucl. Med.* **58**, 67S-76S (2017).

15. Blue Earth Diagnostics | Blue Earth Diagnostics Expands Oncology Portfolio with Exclusive, Worldwide Licensing of Investigational Radiohybrid PSMA-targeted Agents for Prostate Cancer from Scintomics - Blue Earth Diagnostics. http://www.blueearthdiagnostics.com/blue-earth-diagnostics-expands-oncology-portfolio-with-exclusive-worldwide-licensing-of-investigational-radiohybrid-psma-targeted-agents-for-prostate-cancer-from-scintomics/.

16. Nedrow, J. R. *et al.* Pharmacokinetics, microscale distribution, and dosimetry of alpha-emitter-labeled anti-PD-L1 antibodies in an immune competent transgenic breast cancer model. *EJNMMI Res.* **7**, 57 (2017).

17. Gill, M. R. *et al.* ^{111}In-labelled polymeric nanoparticles incorporating a ruthenium-based radiosensitizer for EGFR-targeted combination therapy in oesophageal cancer cells. *Nanoscale* **10**, (2018).

18. Tian, L. *et al.* Radionuclide I-131 Labeled Albumin-Paclitaxel Nanoparticles for Synergistic Combined Chemo-radioisotope Therapy of Cancer. *Theranostics* **7**, 614–623 (2017).

19. Song, L., Falzone, N. & Vallis, K. A. EGF-coated gold nanoparticles provide an efficient nano-scale delivery system for the molecular radiotherapy of EGFR-positive cancer. *Int. J.*

Radiat. Biol. **3002**, 1–8 (2016).

20. Harrington, K. J. *et al.* Effective Targeting of Solid Tumors in Patients With Locally Advanced Cancers by Radiolabeled Pegylated Liposomes.

21. Du, J., Marquez, M., Hiltunen, J., Nilsson, S. & Holmberg, A. R. Radiolabeling of dextran with rhenium-188. *Appl. Radiat. Isot.* **53**, 443–448 (2000).

22. Lammers, T. *et al.* Polymeric nanomedicines for image-guided drug delivery and tumor-targeted combination therapy. *Nano Today* **5**, 197–212 (2010).

23. Hobbs, S. K. *et al.* Regulation of transport pathways in tumor vessels: role of tumor type and microenvironment. *Proc. Natl. Acad. Sci. U. S. A.* **95**, 4607–12 (1998).

24. Ziemys, A. & Ferrari, M. Transport barriers and oncophysics in cancer treatment. *TRENDS in CANCER* **4**, 277–280 (2018).

25. Gudkov, S. V, Shilyagina, N. Y., Vodeneev, V. A. & Zvyagin, A. V. Targeted Radionuclide Therapy of Human Tumors. *Int. J. Mol. Sci.* **17**, (2015).

26. Peltek, O. O., Muslimov, A. R., Zyuzin, M. V. & Timin, A. S. Current outlook on radionuclide delivery systems: from design consideration to translation into clinics. *J. Nanobiotechnology* **17**, 90 (2019).

27. Thomas, E. *et al.* Ultrasound-mediated cavitation enhances the delivery of an EGFR-targeting liposomal formulation designed for chemo-radionuclide therapy. *Theranostics* **9**, 5595–5609 (2019).

28. Gill, M. R. *et al.* 111In-labelled polymeric nanoparticles incorporating a ruthenium-based radiosensitizer for EGFR-targeted combination therapy in oesophageal cancer cells. *Nanoscale* **10**, 10596–10608 (2018).

29. von Eyben, F. E. *et al.* Third-line treatment and 177Lu-PSMA radioligand therapy of metastatic castration-resistant prostate cancer: a systematic review. *Eur. J. Nucl. Med. Mol. Imaging* **45**, 496–508 (2018).

30. Caplan, S. & Baniyash, M. Radioiodination of Cellular Proteins. *Curr. Protoc. Cell Biol.* **15**, 7.10.1-7.10.13 (2002).

31. Salacinski, P. R. P., McLean, C., Sykes, J. E. C., Clement-Jones, V. V. & Lowry, P. J. Iodination of proteins, glycoproteins, and peptides using a solid-phase oxidizing agent, 1,3,4,6-tetrachloro-3α,6α-diphenyl glycoluril (Iodogen). *Anal. Biochem.* **117**, 136–146 (1981).

32. You, L. *et al.* MicroSPECT imaging of triple negative breast cancer cell tumor xenografted in athymic mice with radioiodinated anti-ICAM-1 monoclonal antibody. *Appl. Radiat. Isot.* **139**, 20–25 (2018).

33. Pantel, A. R., Ackerman, D., Lee, S.-C., Mankoff, D. A. & Gade, T. P. Imaging Cancer Metabolism: Underlying Biology and Emerging Strategies. *J. Nucl. Med.* **59**, 1340–1349 (2018).

34. Sai, K. K. S., Zachar, Z., Bingham, P. M. & Mintz, A. Metabolic PET Imaging in Oncology. *Am. J. Roentgenol.* **209**, 270–276 (2017).

35. Pirotte, B. *et al.* Combined use of 18F-fluorodeoxyglucose and 11C-methionine in 45 positron emission tomography—guided stereotactic brain biopsies. *J. Neurosurg.* **101**, 476–483 (2004).

36. De Reuck, J. *et al.* [Methyl-11C]thymidine positron emission tomography in tumoral and non-tumoral cerebral lesions. *Acta Neurol. Belg.* **99**, 118–25 (1999).

37. Kortylewicz, Z. P., Kimura, Y., Inoue, K., Mack, E. & Baranowska-Kortylewicz, J. Radiolabeled cyclosaligenyl monophosphates of 5-iodo-2'-deoxyuridine, 5-iodo-3'-fluoro-2',3'-dideoxyuridine, and 3'-fluorothymidine for molecular radiotherapy of cancer: synthesis and biological evaluation. *J. Med. Chem.* **55**, 2649–71 (2012).

38. Van Hée, V. F. *et al.* Radiosynthesis and validation of [18F]-3-fluoro-2-hydroxypropionate ([18F]-FLac) as a PET tracer of lactate to monitor MCT1-dependent lactate uptake in tumors. *Oncotarget* (2017) doi:10.18632/oncotarget.14705.

39. Seevers, R. H. & Counsell, R. E. Radioiodination techniques for small organic molecules. *Chem. Rev.* **82**, 575–590 (1982).

40. Pinheiro, C. *et al.* Role of monocarboxylate transporters in human cancers: State of the art. *J. Bioenerg. Biomembr.* **44**, 127–139 (2012).

41. Fisel, P., Schaeffeler, E. & Schwab, M. Clinical and Functional Relevance of the Monocarboxylate Transporter Family in Disease Pathophysiology and Drug Therapy. *Clin. Transl. Sci.* **11**, 352–364 (2018).

42. Halestrap, A. P. The monocarboxylate transporter family-Structure and functional characterization. *IUBMB Life* **64**, 1–9 (2012).

43. Tubes, P. P. I. Pierce ® Pre-Coated Iodination Tubes. *Meridian* **0747**, 1–6.

44. Kameswaran, M., Sarma, H. D. & Dash, A. Preclinical evaluation of 131I-Bevacizumab – A prospective agent for radioimmunotherapy in VEGF expressing cancers. *Appl. Radiat. Isot.* **123**, 109–113 (2017).

45. Birsoy, K. *et al.* MCT1-mediated transport of a toxic molecule is an effective strategy for targeting glycolytic tumors. *Nat. Genet.* **45**, 104–8 (2013).

46. Enerson, B. E. & Drewes, L. R. Molecular Features, Regulation, and Function of Monocarboxylate Transporters: Implications for Drug Delivery. *J. Pharm. Sci.* **92**, 1531–1544 (2003).

47. Dewick, P. M. *Essentials of Organic Chemistry for students of Pharmacy, Medicinal Chemistry and Biological Chemistry*. (2006).

48. Chen, T. C. *et al.* A perillyl alcohol-conjugated analog of 3-bromopyruvate without cellular uptake dependency on monocarboxylate transporter 1 and with activity in 3-BP-resistant tumor cells. *Cancer Lett.* **400**, 161–174 (2017).

49. Van Wamel, A., Bouakaz, A., Bernard, B., Ten Cate, F. & De Jong, N. Radionuclide tumour therapy with ultrasound contrast microbubbles. doi:10.1016/j.ultras.2003.11.013.

6 Polymeric microbubbles: an alternative delivery system

6.1 Abstract

This chapter explores the possibility of making lactate-based polymeric microbubbles to be used both as imaging agents and drug carriers. Small α-hydroxyacids have been extensively used for the synthesis of biocompatible and biodegradable polymers for drug delivery and other medical applications. Gradual hydrolytic degradation of these polymers results in the release of the non-toxic building blocks, such as lactic acid, which are physiological metabolites. As for liposomes, the most commonly investigated drug delivery strategies involve either the encapsulation of one or more therapeutics into a nano/micro-particle or a particle externally decorated with the targeting or therapeutic agent. Here, we set out to explore an alternative strategy, based on the coincidence that α-hydroxy-monocarboxylates, which constitute MCT1 substrates, which may be modified to act as metabolic poisons (see **chapter 3**), are also the building blocks of biodedgradable polymers used for drug delivery. Indeed, lactate-based polymers have been successfully used for gradual lactate release to assist wound healing[1]. Applying the same logic for cancer applications, some of the non-toxic lactate residues could be replaced with toxic lactate mimetics, analogous to 3BP, which is where this work may be taken in the future.

6.2 Introduction

This final chapter of this thesis reports an investigation of the feasibility of synthesising a biodegradable ultrasound contrast agent (UCA) with a monocarboxylate therapeutic co-

polymerised into its polymeric shell and released locally as the polymer degrades. This should provide an ultrasound responsive formulation that is also the agent which provides the therapeutic molecule.

This concept developed through the observation that to target the monocarboxylate transporter via a 'Trojan horse' approach, monocarboxylates could be employed – 3BP or ^{123}I-HPLA. As detailed in **chapter 1**, the natural substrates of MCT1 are short-chain organic acids and substitution on the α-carbon is not required but is well tolerated (pyruvate has a carbonyl and lactate a hydroxyl on that position). MCT1 is overexpressed in several cancers but its relatively widespread expression in healthy cells would result in off-target toxicity if such a modified substrate were to be used as a systemically delivered drug without formulation into a carrier[2,3], as in the case for widely used therapeutics such as conventional chemotherapeutics like doxorubicin. This work involved halogenated compounds. Halogens, in particular bromine and iodine which are larger and less electronegative than fluorine and chlorine, are typically good leaving groups in substitution and elimination reactions. Indeed, 3BP is a highly reactive compound and, although ^{123}I-HPLA showed remarkable stability, de-iodination is a regularly encountered challenge with iodine-based radiopharmaceuticals.

Chapter 4 focused on the development of a delivery strategy for 3BP employing established UCAs in combination with co-administered cavitation-sensitive liposomes, made of commonly employed phospholipids. α-Hydroxy-acids such as lactate constitute the building blocks of biodegradable polymers, well suited for nano- and microparticle formulation and, as shown more recently, for formulation of UCAs[4,5]. In this chapter, the first steps were taken to elucidate this little explored opportunity to replace some of these natural metabolites on the polymer skeleton with 'Trojan horses' that are selectively delivered and locally released in the tumour. The first step in this direction was to test whether lactate-based UCAs could rupture into nano-fragments upon ultrasound stimulation and if monomer release could be accelerated by ultrasound. These

questions are the focus of the studies presented in this chapter. In the following introductory section, the currently used UCAs and the rationale for their development is discussed, the polymer properties related to hydrolytic degradation explained, and the research done by others supporting the pursuit of the proposed approach is summarised.

6.2.1 Degradation of lactate-based constructs

Lactic acid-based homo- and co-polymers are commonly used in biomedical applications, including the formulation of drug delivery systems[6–9]. Poly-lactic acid (PLA) and poly(D, L-lactic-*co*-glycolic) acid (PLGA) (**Figure 41**) are considered biocompatible and biodegradable, and can be hydrolysed to non-toxic physiological metabolites. Their physicochemical properties are tuneable, and they can be shaped into films, tablets, spherical or aspherical particles in the micron or submicron size range[1,7,10,11]. These polymers can encapsulate hydrophobic and, to a lesser extent, hydrophilic drugs[12–14], while their surface can be decorated with targeting agents or PEGylated to prolong the circulation time[15,16].

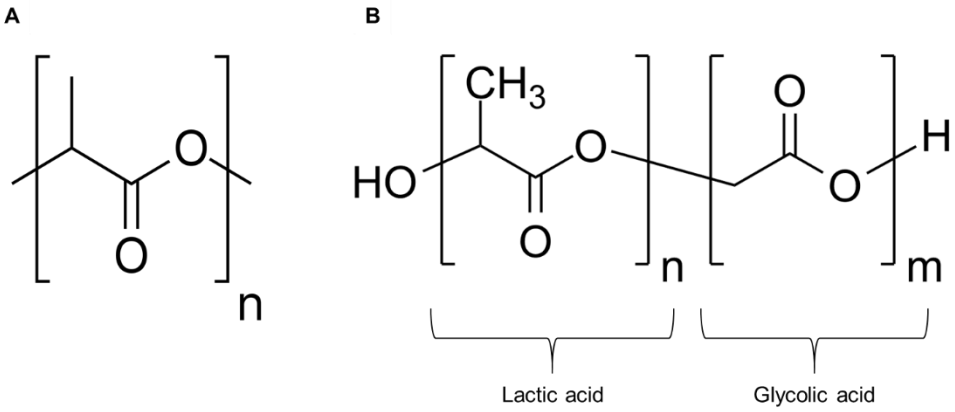

Figure 41 Chemical structures of poly(lactic acid) (PLA) and poly(D,L-lactic-*co*-glycolic acid) (PLGA). PLA (a) is composed from lactic acid building blocks, and PLGA (b) is composed of lactic and glycolic acid building blocks linked together with ester bonds.

The degradation profile of PLAs and PLGAs has been studied in depth and several parameters have been shown to affect the degradation rate of these polymers. These factors, which are catalogued below, are related not only to the material itself, but also the shape and size of the final construct as well as the properties of the degradation media.

6.2.1.1 Material factors

Polymer composition affects the degradation rate. Most commonly, homopolymers of lactic acid (or its cyclic dimer, lactide) or co-polymers with glycolic acid (or its cyclic dimer, glycolide) are utilised for biomedical applications to produce PLA and PLGA. Lactic acid comes in two optical isomers, L- and D-lactic acid. Polymers can be formed by one of these isomers or a mix of both, with or without glycolic acid. Degradation rate decreases with increasing crystallinity[17,18]. Also, glycolic acid bonds are more prone to hydrolysis than those involving lactic acid and polymers with higher glycolic acid content degrade faster[19]. PDLA exhibits the highest crystallinity and the slowest degradation rate, while PLGA with high glycolic acid content (usually up to 50:50) is amorphous and exhibits faster degradation (fastest for PLGA 50:50)[1711,19].

Polymer molecular weight (M_w) is another factor affecting degradation rate. In drug delivery applications, the M_w of PL(G)As used generally falls within the 5-150 kDa range. Longer chains degrade slower than shorter ones[20]. This can be explained by the increasing hydrophobicity of the longer polymer chains and also by the fact that autocatalysis of hydrolysis is favoured in shorter polymer chains. There are two proposed mechanisms for polyester hydrolytic degradation. A terminal residue can be cleaved off or, alternatively, the polymer can be split into two shorter chains. Acid monomers then catalyse further hydrolysis, a phenomenon described as autocatalysis[21,22]. Shorter chains result in higher density of terminal carboxylic acid groups, a higher chance of terminal monomer being cleaved off and consequently, more free acid to catalyse further hydrolysis.

It follows that the terminal group also plays a role in the degradation rate. Polymers terminated with free acid will degrade faster than esterified polymers.

6.2.1.2 Construct factors

The size, shape and porosity of the construct will influence the degradation rate[22–24]. Given that PL(G)A consisting of 10 or more monomers is insoluble in water and aqueous buffers, degradation by hydrolysis happens in the solid-liquid interface. Hence, any factor increasing the surface-to-volume ratio of the construct will increase the degradation rate. Accordingly, smaller particles degrade faster than larger ones, films faster than tablets, porous particles faster than particles with smooth surface[22,25] . Indeed, Panyam and colleagues compared the degradation rate of 1 μm diameter particles to 100 nm particles and found that the degradation rate constant for the first, rapid phase is almost three times higher for the 100 nm particles (k1 = 0.028 $day^{-1}$and 0.011 day^{-1}respectively)[22].

6.2.1.3 Media factors

Hydrolytic reactions can be catalysed by both acid and base. Hence, degradation is accelerated in sufficiently alkaline or acidic conditions as compared to neutral pH. Moreover, the temperature of the medium is important. Higher temperature increases the motility of polymer chains and this in turn makes the diffusion of water molecules and water-soluble acids/bases more rapid[11,18].

For the present study, the target construct was a microbubble (MB) of <10 μm diameter designed to be responsive to ultrasound pressures that are achievable and acceptable in current clinical applications. Low molecular weight (15-18 kDa) and intermediate and high molecular weight (25-38 kDa and 38-54 kDa respectively) PLGA were the polymers selected as the building blocks.

6.2.2 Ultrasound contrast agents

In the area of ultrasound contrast agents (UCAs), lipid- and protein-shelled microbubbles (MBs) have been extensively studied, while polymeric contrast agents have received less attention. The first commercially available MB formulation was Albunex® (Mallinckrodt Inc., Hazelwood, MO, USA) which is an air-filled MB formulation stabilised by a thin layer of cross-linked human serum albumin. Its successor, Optison™ (GE Healthcare Inc., Princeton, NJ, USA), was aimed at increasing the stability of bubbles in circulation. To this end, air was replaced with higher MW gas (perfluoropropane, MW 188 g/mol) which is less water-soluble and exhibits lower diffusivity. Later generations of UCAs could be stored as lyophilised powders and resuspended in saline immediately prior to injection, which increased the convenience of use. Phospholipid coating of perfluorocarbon microbubbles offers a good balance between echogenicity and stability, which explains why formulations such as SonoVue® (Bracco, Geneva), Definity® (Bristol-Myers Squibb Medical Imaging Inc., USA) and Sonazoid™ (GE Healthcare Inc., Princeton, NJ, USA) are used in clinical practice as contrast agents for imaging[26].

Still, as concluded by Kwan and Borden[27], gas exchange between the lipid-shelled MBs and the blood occurs within a few minutes post injection. To achieve further prolongation of the MB lifetime in the bloodstream, the phospholipid shell can be replaced by a polymer shell. Polymeric shelled UCAs were pioneered by the Wheatley group, who used biodegradable, non-toxic polyesters such as PLA and PLGA. These could be formulated without stealthing or decorated with polyethyleneglycol (i.e. PEGylated) to prolong the circulation time of the MBs. Polymer shells are more rigid hence the longer circulation time comes at the expense of some of the echogenicity of the bubble. However, these particles, in common with their solid counterparts, can entrap hydrophobic and hydrophilic drugs and can be surface decorated with targeting agents and other therapeutics as well as PEG. Eisenbrey *et al.* have shown *in vitro* that PLGA MBs filled with air collapse in response to ultrasound (20 min exposure at 5 MHz, 0.94 MPa), giving rise to polymer

fragments of a few hundred nm in size[14]. Particles below 400-500 nm are in theory able to cross the hyperpermeable tumour vasculature and enter the tumour tissue, which is the basis of the development of nanocarriers in general. The researchers used a semi-permeable membrane with pore size 400 nm as a model for the leaky tumour vasculature to provide proof-of-concept that these 'nano-fragments' can exploit the EPR effect, similarly to nanocarriers. The theoretical advantage over conventional nanocarriers is that MBs are too large to leave the circulation and access healthy (or inflamed) tissues with porous vasculature, potentially sparing them from toxicity. Instead, they are fragmented at the tumour vasculature achieving higher concentration of the 'nano-fragments' locally, thus maximising the chance of deposition selectively in the tumour.

Monomer release in response to ultrasound, has received limited attention and only with respect to ultrasound exposure involved in the fabrication process of polymeric particles. Also, 'nano-fragment' generation in Eisenbrey's studies constitute encouraging proof-of-concept that ultrasound can induce the collapse of MBs into nano-sized particles, the conditions employed are not realistically achievable when cells are involved (as reported in chapter 4, cells detachement was observed with 20 s, 0.3 MPa), and even less so *in vivo*. Therefore, investigation of milder conditions and shorter sonication exposures would be of interest. Further, monomer release in response to ultrasound, has received limited attention and only with respect to ultrasound exposure involved in the fabrication process of polymeric particles.

6.3 Aims

The aims of this chapter were to achieve:

- Synthesis of gas-entrapping microparticles (microbubbles) from poly(lactic-co-glycolic acid) (PLGA), an FDA-approved, clinically used, biocompatible and biodegradable polymer.
- Physicochemical and acoustic characterisation of the polymeric particles.

- Demonstration that ultrasound treatment can enhance the degradation of the particles and release of the monomer (proof-of-concept).

6.4 Materials & methods

6.4.1 Synthesis of polymeric particles

All chemicals were purchased from Sigma-Aldrich, individual product codes stated. Poly(lactic-*co*-glycolic acid) (PLGA) or poly(lactic acid) (PLA) microbubbles (MBs) were designed to provide a dual role, firstly as cavitation agents and secondly as a therapy delivery system. They were prepared by a modified double emulsion – solvent evaporation technique, adapted from the work developed for polymeric MBs by the Wheatley group[5]. Briefly, polymer (PLA 10-18 kDa: 719978, PLGA 24-38 kDa: 719870, PLGA 38-54 kDa: 26780-50-7, all acid-terminated) and camphor (14875) at a 10:1 mass ratio were dissolved in dichloromethane (DCM) (HPLC grade, 34856). For one batch of MBs, 100 mg PLGA and 10 mg camphor were dissolved in 2 mL DCM. Ammonium carbonate (207861) 4% w/v aqueous solution ($(NH_4)_2CO_3$) was added and sonicated over ice bath (Vibra-cell, Sonics, 60% amplitude, pulse 9 s 'on', 1 s 'off' for 40 s) to form a primary water-in-oil (w/o) emulsion. Ice cold polyvinyl alcohol (PVA) (9-10 kDa, 80% hydrolysed, 360627) 5% w/v aqueous solution (10 mL) was then added and a secondary water-in-oil-in-water (w/o/w) emulsion was formed by homogenisation. Finally, 2% v/v isopropyl alcohol (reagent grade, 190764) (20 mL) was added. The emulsion was transferred into a beaker, covered with perforated foil to allow for gradual solvent evaporation and left under magnetic stirring overnight at room temperature.

DCM evaporation, leaves an insoluble polymer and the originally formed droplets were solid microparticles at this stage. The particles were collected by centrifugation (5,000 rcf, 60 min, 4°C). The resulting pellet was re-suspended with hexane three times and the washed particles were collected by centrifugation, flash-frozen in liquid nitrogen and lyophilized for 48 h. Upon

lyophilisation, camphor and ammonium carbonate sublimate, leaving hollow space which is filled with air after the process is finished.

6.4.2 Characterisation of polymeric particles

6.4.2.1 Size and morphology

For bright field optical microscopy, freshly prepared MB suspension (10 μL) was loaded into each side of the haemocytometer. Images were acquired at 10x and 40x magnification (at least 10 images per sample) using a Leica DM500 microscope (Leica Microsystems GmbH, Germany) connected to a camera (MicroPublisher 3.3 RTV, Imaging, Canada).

Single particle optical sizing (SPOS) was employed for measuring particle size using an AccuSizer 7000AD (Entegris Inc., FL, USA). For each measurement, the sample vessel was flushed with MilliQ water until the particle count was at background level. The vessel was filled with 30 mL water and 100 μL sample (1 mg/mL) was added. The number weighted mean was reported for average size and the size distribution was plotted using Prism 7 (GraphPad Software, USA).

Initial high vacuum SEM images were acquired by Dr Errin Johnson (Dunn School of Pathology, University of Oxford, UK) using a JEOL-6390 SE microscope (Jeol Inc., Tokyo, Japan) with accelerating voltage 2.5 kV. Later, a FEI Quanta Inspect S instrument (FEI company, Oregon, USA) was employed for low vacuum or environmental SEM and the imaging parameters were optimised by Dr Jason Brown (Department of Physics, University of Oxford, UK). For this sensitive sample, a balance needed to be found between acquisition of good resolution images and not degrading the sample (main factors being pressure, electron beam, humidity). Generally, higher vacuum and higher accelerating voltage generate higher quality images. However, the sample was degraded with accelerating voltage between 4-5 kV. Optimal conditions were determined at accelerating voltage 3 kV, chamber pressure 30 Pa and the image parameters were: contrast 81.8%,

enhancement 48.1% and brightness 45.5%, for all sessions. Lyophilised and re-hydrated samples were examined. Dry lyophilised samples with no further processing provided the best quality images. Size of intact particles and particles after sonication was manually measured from the SEM images using ImageJ software.

6.4.2.2 Acoustic characterisation

The purpose of these studies was to investigate whether the polymeric particles respond to ultrasound pressures in line with the medically relevant range. An in-house assembled, previously described setup[28,29] was employed for this study. The setup was designed by Dr Christophoros Mannaris (Institute of Biomedical Engineering, University of Oxford, UK) (**Figure 42**).

The main components of the setup were a focused ultrasound (FUS) transducer (H102, Sonic Concepts, Bothell, WA, USA), a tissue-mimicking flow phantom model with an embedded 1-mm channel through which the sample can flow, and a 7.5 MHz single-element passive cavitation detector (PCD) (V320 Panametrics, Olympus, Waltham, USA) that was used to passively record acoustic emissions generated by cavitation nucleated by the sample. The FUS and PCD were controlled via custom-made software using a graphical programming language (Lab-VIEW, National Instruments, Austin, TX, USA).

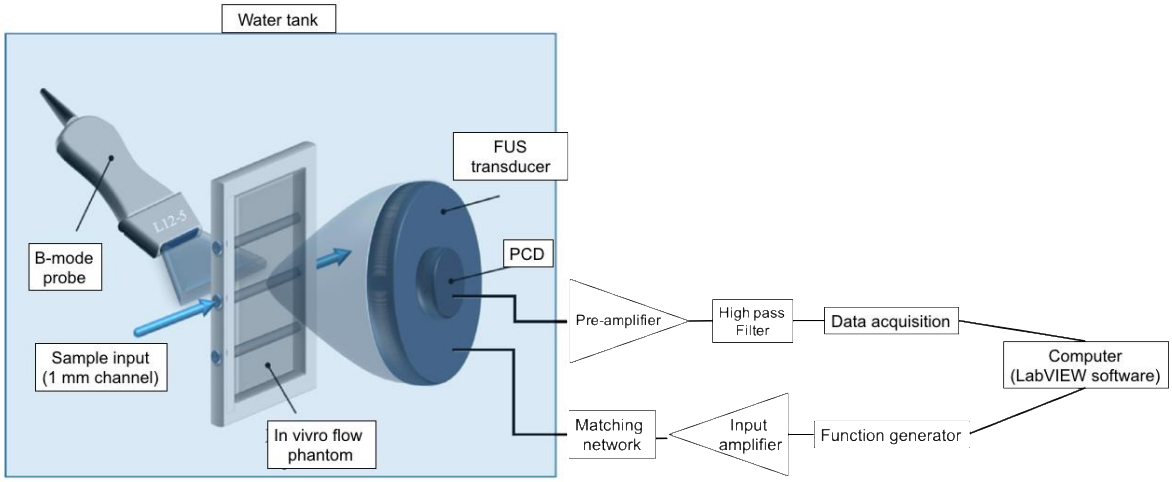

Figure 42 Acoustic characterisation setup. Schematic diagram showing the experimental setup used for the acoustic characterisation of microbubbles (MBs). The ultrasound apparatus is placed in the tank filled with degassed water (omitted for clarity). It consists of the focussed ultrasound (FUS) transducer, passive cavitation detection (PCD) transducer, tissue-mimicking agarose phantom and diagnostic ultrasound imaging device. The signal received by the PCD is high-pass filtered, amplified and recorded and processed on MatLab (MathWorks, Natick, MA, USA). The FUS and PCD transducers are controlled via custom-made software using a graphical programming language (Lab-VIEW, National Instruments, Austin, TX, USA).

The phantom was prepared from degassed hydrogel composed of 1.5% (w/v) ultrapure agarose gel (Invitrogen, Carlsbad, CA, USA) the day before the experiment and maintained at 4°C until needed. For treatment, MBs were freshly dispersed in PBS at a range of concentrations (0.1, 0.01 and 0.001 mg/mL). The sample passed through the 1 mm channel embedded in the agarose phantom at a flow rate of 0.5 mL/min. The FUS transducer of fundamental frequency 1.1 MHz was operated at peak negative pressure from 0.18 MPa up to 3 MPa, 0.18 ms pulse length, 200 cycles. Eluted particles were collected, lyophilised and analysed by SEM. Acoustic data were analysed on MatLab (MathWorks, MA, USA) as previously described[28,29]. Full details of the set-up can be found in references 28 and 29.

6.4.3 Degradation of polymeric particles

Lyophilised IMW PLGA MBs were dispersed in PBS at a 2.5 mg/mL concentration and kept on ice. A 35 mm Ibidi μ-dish (high wall) was filled with the MB suspension and placed in the SAT2 device, as described in **Chapter 4**. The input voltage from the waveform generator was 140 mVpp (corresponding to 0.2 MPa) or 310 mVpp (corresponding to 0.5 MPa). As previously, the ultrasound transducer was driven by a 1.1 MHz sinusoidal signal passed through a 1.9 MHz low pass filter and amplified 55 dB by a radiofrequency amplifier (1040L, E&I Ltd., NY, USA) and the acoustic emissions were recorded and analysed as described in **Chapter 4**.

After treatment, the MB suspension was aliquoted into 1.5 mL micro-centrifuge tubes and placed on a heater-shaker set at 37°C and covered with foil for better heat retention. At each time point, the corresponding tube was centrifuged (14,000 rpm, 30 min, 4°C, Eppendorf 5417R centrifuge equipped with F54-30-17 fixed angle rotor) and the supernatant collected and kept at -20°C awaiting analysis. Lactate measurement using a colorimetric lactate dehydrogenase (LDH)-based assay (MAK064, Sigma-Aldrich, UK) was selected as a simple, sensitive and reliable way to assess monomer release from the degrading polymer (the assay does not detect the polymerised form). Briefly, the supernatants were thawed slowly on ice and a 50 μL aliquot was transferred into each well of a 96-well plate. The 'master mix' containing the enzyme and probe was prepared as per manufacturer's instructions. Solutions of known concentration of lactate (0, 2, 4, 6, 8 and 10 μM) were freshly prepared for each assay and used for the construction of a standard curve. Master mix (50 μL) was added to the standard and test samples and the plate was incubated for 30 min at room temperature in the dark. The plate was read at 570 nm using a plate reader (Infinite 200 Pro, Tecan, Switzerland).

6.5 Results

6.5.1 Low molecular weight PLA particles

With the target construct in mind, in which there is a halogenated lactate derivative (substitution on carbon 3), PLA was the polymer selected originally, to maximise the content of lactate residues for a given MW. For this design, a lactate-based polymer with high degradation rate was required therefore 'uncapped' carboxyl-terminated, low molecular weight (15-18 kDa) polymer was selected. The first question that needed to be answered was whether MBs, i.e. ultrasound-responsive particles, could be formed using such a low MW polymer.

Particles were formed using a double emulsion – solvent evaporation method, as modified by Eisenbrey *et al.* and optimised in house[14]. The obtained particles were smaller than the usually reported size range for MBs (1-8 μm) with a number-weighted mean 0.78 μm measured by SPOS (**Figure 43A)**. However, it was difficult to fully re-disperse the lyophilised powder in water and chunks of material were always present. This is not acceptable for an injectable formulation because it could potentially cause an embolism and, in this case, it would potentially also block the needle. Optical microscopy confirmed the presence of large aggregates embedded within a fibrous matrix (**Figure 43B)**, although there were spherical particles present. Particles not embedded in the matrix were floating – in the haemocytometer, this can be confirmed by seeing the particles at a different focus level from that of the grid.

High vacuum scanning electron microscopy (2.5 kV accelerating voltage) was performed using the lyophilised powder form of the polymer bubbles. The presence of collapsed spherical forms of approximately 1 μm diameter embedded in a solid matrix was confirmed (**figure 43C**). A question was raised, however, as to whether the hollow particles are unstable under vacuum and burst or they are inappropriately shaped to begin with. To try and answer this, milder SEM conditions were tried – environmental and 'low vacuum'. 'Low vacuum' SEM provided good quality images but the result was the same – collapsed <1 μm spheres in a solid matrix (**Figure**

43D). The matrix is likely to be a mix of PVA and PLA not used for particle formation. The concentration of PVA was towards the higher end of the concentration spectrum used for particle formation (5% w/v). PVA is notoriously difficult to remove from the final particle formulation, even after multiple washes.

It was, therefore, concluded that the particles formed by LMW PLA do not present acceptable properties (size and morphology).

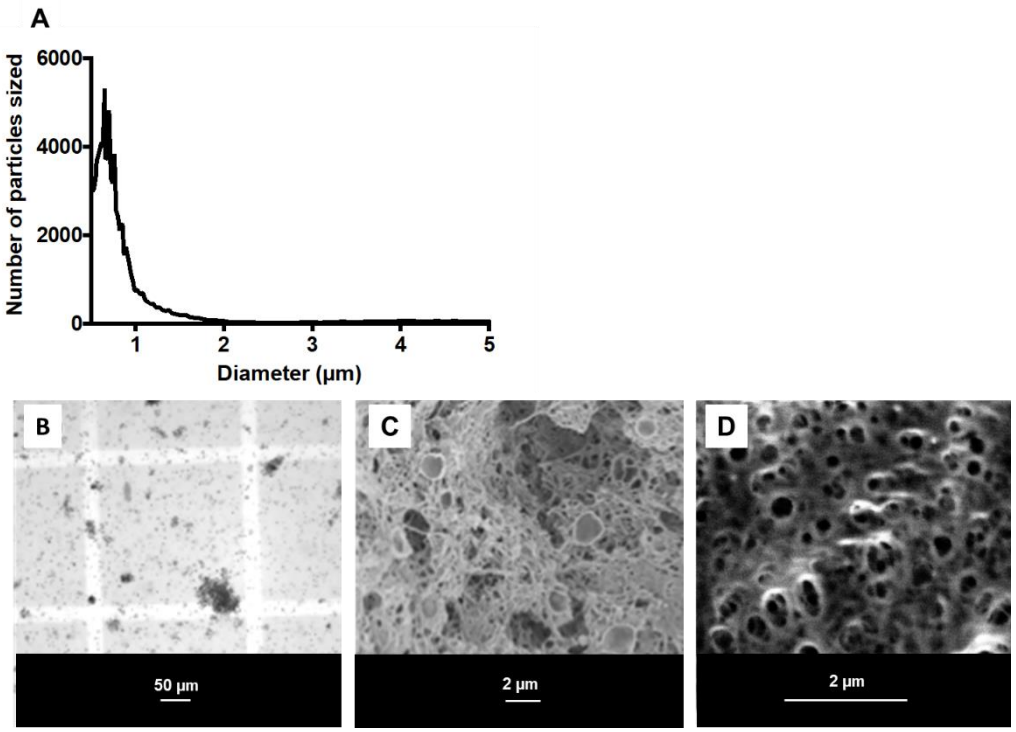

Figure 43 PLA particle characterisation. (A) Size distribution by single particle optical sizing (SPOS). For measurement, 100 µL of 1 mg/mL particle suspension was diluted in the measurement vessel with 30 mL water. (B) Optical microscopy image at 40x magnification. For imaging, 10 µL 1 mg/mL suspension was placed into each side of the hemocytometer. (C) Scanning electron microscopy (SEM) imaging of lyophilised PLA formulation (2.5 kV). (D) Low-vacuum SEM imaging of lyophilised PLA formulation (3 kV, 30 Pa).

6.5.2 PLGA particles

6.5.2.1 Particle characterisation

Introduction of glycolic acid in the polymeric chain results in amorphous material with highest degradation rate effect achieved at 50% content. Therefore, two polymers with different MW were tested. PLGA termed 'intermediate MW' (IMW PLGA) was 24-38 kDa while the one termed 'high MW' (HMW PLGA) was 38-54 kDa. The same procedure was followed for particle preparation but with these polymers, spherical particles of slightly larger number-weighted average diameter (1.01 μm for IMW PLGA and 1.47 μm for HMW PLGA) were formed (**Figure 44**). High vacuum SEM was not attempted and SEM imaging was performed in the 'low vacuum' mode. As apparent from both optical and electron microscopy images of intact particles, the size distribution is quite broad with particles from approximately 0.5 μm to 3 μm (**Figure 44A, B** for HMW MBs and **E, F** for IMW PLGA). This is acceptable in bubble formulations. For instance, SonoVue, which was employed in the two previous chapters, has an even broader size distribution (0.7-10 μm) [30,31]. Differences in size measured by microscopy and SPOS are normal since the two techniques measure different types of diameter. For SPOS, particles are dispersed in water and sizing is calculated based of the scattering of a laser beam. SPOS provides the hydrodynamic diameter of the equivalent spherical particle, even if the actual particle is not a sphere. Therefore, it is not possible to obtain morphological information from this technique but it is more indicative of the apparent size of particles when surrounded by water. Optical bright field microscopy provides the optical diameter in water and, in the case of MBs, also confirms that the particles float (**Figure 44A** and **E** for HMW and IMW PLGA respectively). SEM provides morphological information and the size of dry particles (**Figure 44B** and **F** for HMW and IMW PLGA respectively). Manually measured size from the SEM images was 1.00 ± 0.43 μm for HMW PLGA and 0.68 ± 0.21 μm for IMW PLGA particles. The images shown in **Figure 44** (optical microscopy

and SEM) demonstrate, in accordance with the SPOS data (**Figure 44 I** and **J**), that the sample is free of the aggregates observed for lower MW particles in **Figure 43**. It is noteworthy that these techniques although rather complementary do provide different and independently useful information and so cannot replace one another. Indeed, this analysis is a good demonstration of the value of deploying a range of analytical techniques.

An interesting observation was that SEM showed different particle morphology depending on the MW of the PLGA (**Figure 44B** vs **F**). Specifically, HMW PLGA particles were smooth spheres, while the surface of IMW PLGA particles was rougher and featured one or more cavities. Such differences could substantially impact on the entrapment of gas and therefore the US response of the particles.

MB suspension (0.01 mg/mL) was injected in the agar phantom apparatus described and briefly treated with a series of ultrasound pressures under flow. A B-mode transducer was aligned with the flow channel to obtain contrast enhancement images (**Figures 44D** and **H** for HMW and IMW PLGA particles respectively). The treated particles were collected from the outlet of the device, lyophilised and imaged with low vacuum SEM (**Figure 44C** and **G** for HMW and IMW PLGA particles respectively). Fragments were collected after high pressure ultrasound bursts, so they are not representative of treatment with specific pressures. Lyophilisation can have an effect on the particles, but unfortunately environmental SEM, the only mode that can image wet particles, could not provide enough contrast to create an image. Also, intact MBs, which were lyophilised, were imaged with the same SEM mode which provides evidence that lyophilisation does not destroy the particles (**Figure 44B** and **F**). This study confirmed a crucial point for this strategy: ultrasound treatment decreased the size of the particles: 1.00 ± 0.43 μm to 0.48 ± 0.18 μm for HMW PLGA and 0.68 ± 0.21 μm to 0.55 ± 0.14 μm, as calculated from the SEM images manually using ImageJ.

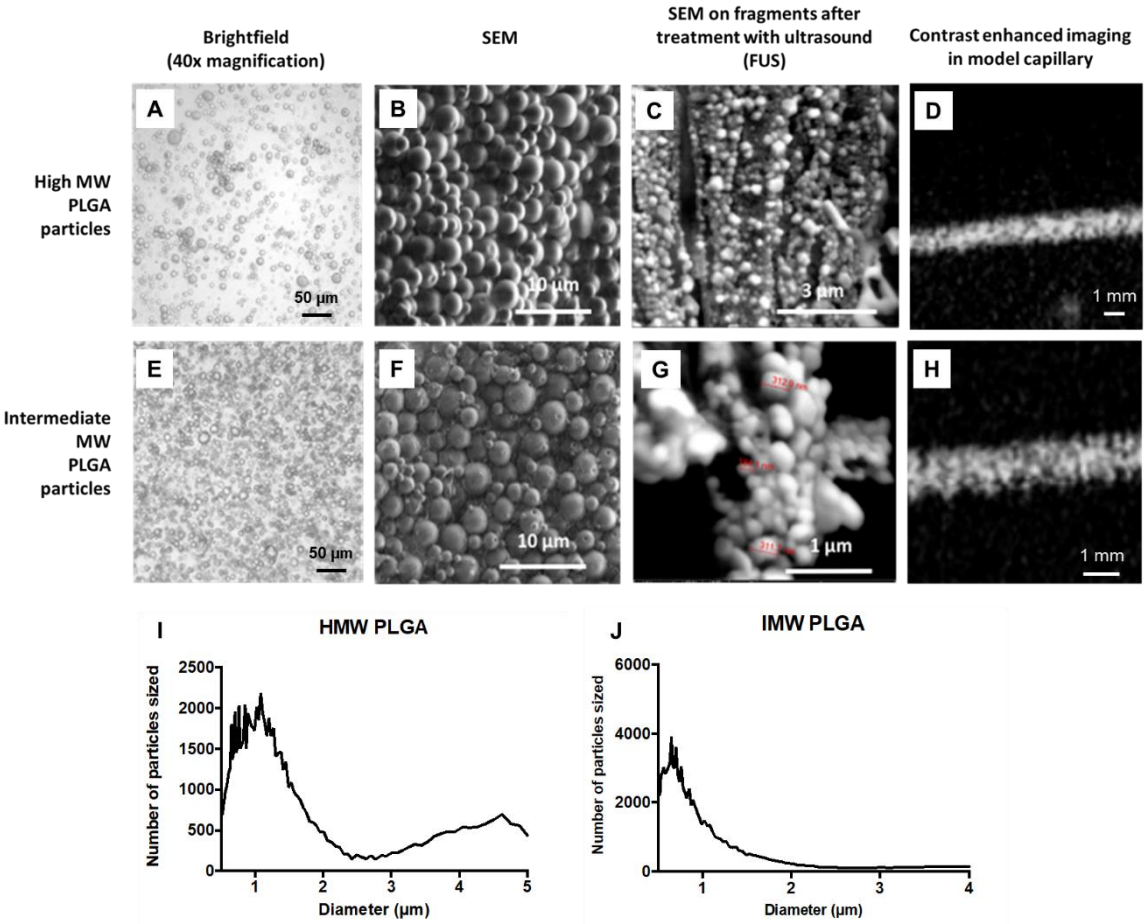

Figure 44 Characterisation of poly(lactic-*co*-glycolic acid) particles. (A) Optical microscopy image (40x magnification) of 10 µL 1 mg/mL 'high' Mw (HMW) particle suspension in water placed into each side of the hemocytometer. (B) Low vacuum SEM image of HMW PLGA particles, (C) Low vacuum SEM image of sonicated HMW particle suspension and (D) B-mode ultrasound imaging of HMW particles in a 1 mm channel across an agarose phantom. (E)-(H) Equivalent images of the 'intermediate' MW (24-38 kDa) PLGA particles, (I) and (J) Size distribution of 'high' Mw (38-54 kDa) and 'intermediate' MW (24-38 kDa) PLGA particles measured by single particle optical sizing (SPOS). For measurement, 100 µL 1 mg/mL particle suspension was diluted in the measurement vessel of the Accusizer instrument which is filled with 30 mL water..

On the basis of these results, it was decided that IMW PLGA particles would be taken forward since they were more likely to present with faster degradation and improved acoustic response. Further acoustic characterisation was performed in the same agar phantom apparatus, using 0.1, 0.01 and 0.001 mg/mL IMW PLGA suspension in PBS. Out of a series of acoustic pressures tested, two were selected to represent a 'low' and a 'high' pressure setting, while the other conditions were kept the same. The top spectra at different concentrations (**Figure 45A**) show

that at 0.18 MPa pressure, particles cavitate in a non-inertial manner, as evident from the harmonic emissions, i.e. emissions which are harmonics of the driving frequency caused by stable oscillation of bubbles around their radius. The fundamental frequency of the transducer was 1.1 MHz, and a filter was used to exclude the frequencies below 4 MHz. Therefore, harmonics seen at 4.4, 5.5 MHz and further x1.1 multiples are evidence of non-inertial cavitation in the sample. Broadband noise (blue) and harmonic/ultra-harmonic emissions make up the total signal (red) (**Figure 45A**). In contrast, higher pressure (0.77 MPa) resulted mainly in inertial cavitation (**Figure 45B**), evident by the broadband noise (blue), at all concentrations. Under flow, the ultrasound beam is presented

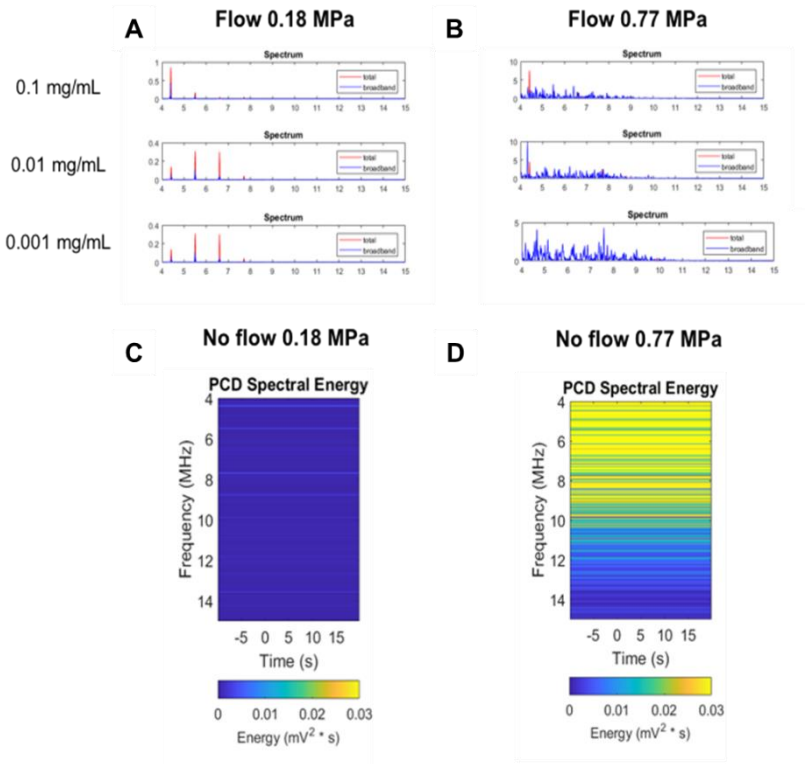

Figure 45 Acoustic characterisation of intermediate molecular weight microbubbles (IMW MBs). (A) and (B) Cavitation spectrum at 'low' (0.18 MPa) and 'high' (0.77 MPa) pressure of different concentrations (0.1, 0.01 and 0.001 mg/mL) of MBs under 0.5 mL/min flow in a 1 mm diameter channel across a 1.5% agarose tissue-mimmicking phantom. (C) and (D) Cavitation activity of IMW MBs as a function of time (in seconds) at 'low' and 'high' ultrasound pressures. PLGA is poly-(lactic-co-glycolic acid) 24-38 kDa. Ultrasound parameters used were 1.1 MHz driving frequency, 0.18 ms pulse length, 200 cycles at 0.18 or 0.77 MPa pressure. These graphs were plotted using MatLab software (MathWorks, MA, USA)

with fresh bubbles while when the flow is arrested the same bubbles are treated for the whole duration. The waterfall graphs (**Figure 45C** and **D**) show acoustic energy distribution at 0.01 mg/mL concentration across different frequencies and for the full 20 second treatment duration. The graphs show that non-inertial (0.18 MPa) or inertial (0.77 MPa) cavitation is maintained.

6.5.2.2 Polymer degradation studies

After selecting the IMW PLGA MBs as the most appropriate starting point and having demonstrated fragmentation in response to ultrasound, the next crucial point was to explore whether ultrasound treatment accelerates the polymer degradation. Two ultrasound pressures close to what was used in **chapter 4** (0.3 MPa) were selected and sonication time was set at 20 s, which was a realistic time duration as explained in **chapter 4**. A frequency of 1.1 MHz, was used as for all experiments and other parameters were set as for SonoVue in **chapter 4**. Treatment with a probe sonicator for 40 s was selected as a 'positive' control as these conditions are a lot harsher than those used for cell and animal treatment. A control sample not exposed to US was also included.

First, the ability of the polymer MBs to nucleate cavitation was confirmed by the PCD spectral energy graphs (**Figure 46A** and **B**). Low pressure (0.2 MPa) gave rise to non-inertial cavitation, as indicated by the harmonic and ultraharmonic signal (integer and half-integer of driving frequency) in **Figure 46A**. Therefore, under these conditions it is expected that only few bubbles would collapse. In contrast, higher pressure (0.5 MPa) resulted in inertial cavitation which is indicated by the broadband signal in **Figure 46B**. According to this cavitation pattern, most bubbles are expected to collapse[28].

Samples were then incubated in micro-centrifuge tubes on a shaker set at 37°C for up to 7 days. For each time point, the solid residue was separated from the solution by centrifugation and the supernatant was analysed using a colorimetric lactate assay. The 'positive' control, treated with

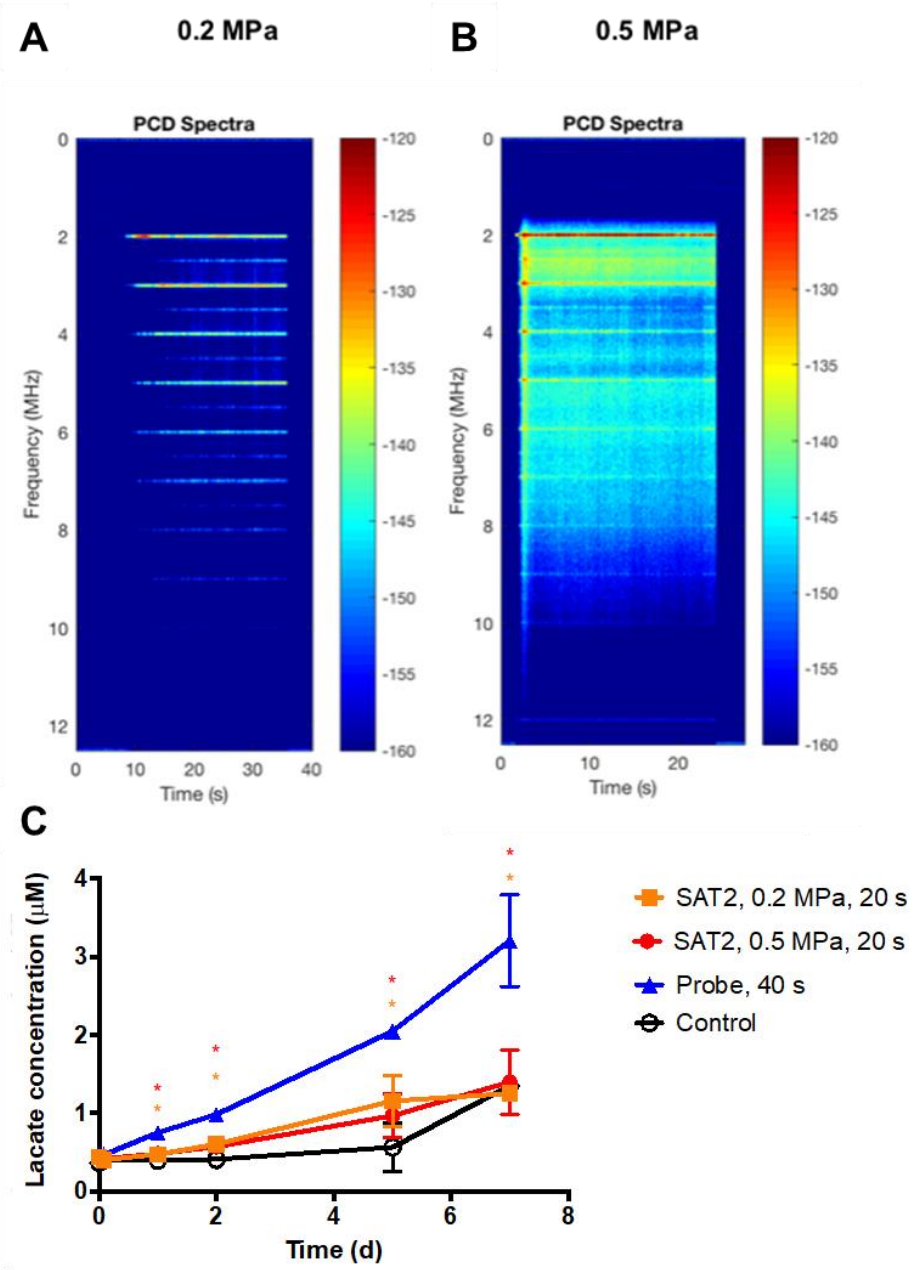

Figure 46 Ultrasound-induced degradation of polymeric microbubbles (MBs). (A) and (B) Cavitation activity of poly(lactic-co-glycolic acid) (PLGA) MBs at 0.2 and 0.5 MPa respectively. (C) Lactate release from PLGA MBs treated with ultrasound (0.2 MPa, 0.5 MPa or probe sonicator) and from untreated control. *P<0.05, where red and orange symbol correspond to the statistical significance of the difference between 0.5 and 0.2 MPa respectively. MatLab software (Mathworks, MA, USA) was used to plot graphs A and B. Prism 7 software (GraphPad, CA, USA) was used to analyse the lactate release data (n=3) and to plot graph C. Error bars represent the standard deviation.

a probe sonicator, showed approximately double the lactate release compared to the untreated control (P<0.05) from t = 1 day onwards. However, the samples treated with 0.2 or 0.5 MPa for

20 seconds did not show significant difference in lactate release compared to control (**Figure 46C**). This experiment showed that in principle, ultrasound can increase monomer release, however the intensity and duration of the treatment needed to be further investigated.

In response, it was decided to sonicate at the 'high' pressure (0.5 MPa) for as long as significant cavitation could be detected (cavitation is recorded in real time). From **Figure 47A**, it is apparent that cavitation is still occurring after 8 min of treatment, but the broadband signal has disappeared. Also, harmonics are seen in the lower frequencies only (2-5 MHz), unlike the harmonic signal at the beginning of treatment which registered at up to 9 MHz. This signifies that the larger bubbles are destroyed during the early stages and leading to a reduction in the mean size of the remaining bubbles. Although direct comparisons cannot be made due to the difference in concentration, persistent cavitation for 8 min without renewal of the bubbles is unlikely to be seen

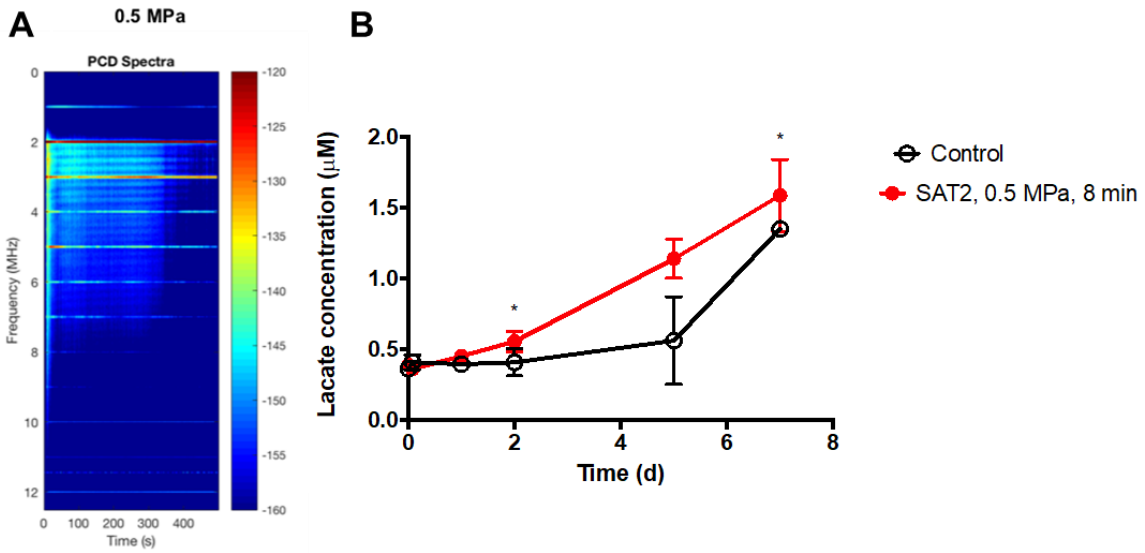

Figure 47 Lactate release from polymeric microbubbles (MBs) following 8 min sonication. (A) Cavitation activity of poly-(lactic-co-glycolic acid) (PLGA) MBs 2.5 mg/mL exposed to 0.5 MPa ultrasound (US) pressure for 8 min in the SAT2 device (please see Methods in Chapter 4 for full details of the device).(B) Lactate release from PLGA bubbles after 8 min ultrasound exposure in the SAT2 device (0.5 MPa, 2.5 mg/mL, n=3). Lactate was measured with a colorimetric assay kit (MAK064-1KT, Sigma Aldrich). PLGA was 24-38 kDa MW. MatLab software (Mathworks, MA, USA) was used to plot graphs A and B. Prism 7 software (GraphPad, CA, USA) was used to analyse the lactate release data (n=3) and to plot graph C. Error bars represent the standard deviation.

with phospholipid formulations and is an important advantage of the polymeric bubbles. This increased exposure duration conditions resulted in slightly higher lactate release ($P<0.05$ for day 2 and 7) compared to the control (**Figure 47B**). Although not optimised, this is an encouraging result showing that clinically relevant ultrasound conditions can accelerate monomer release from a polymeric MB formulation. Further exploration of US parameters, perhaps including an increase in pressure beyond 0.5 MPa, and optimisation of the MB formulation would be important next steps.

6.6 Discussion

Ultrasound-induced acoustic cavitation has been proposed as a strategy to address the challenges of inadequate penetration and distribution throughout the tumour[29,32–35], which are well established factors in the suboptimal efficacy of several cancer therapeutics[33]. Once exposed to ultrasound, gas bubbles dispersed in liquid undergo inertial or non-inertial cavitation depending on the ultrasound parameters[36]. At low pressures, bubbles undergo stable, non-destructive radial oscillations, a process referred to as non-inertial cavitation, while as the applied pressure increases oscillations become increasingly non-linear, leading to rapid expansion and eventually violent collapse of the bubbles, referred to as inertial cavitation[28,36]. Gas bubbles are very short-lived in the blood or aqueous media and are therefore stabilised by protein, lipid, or polymeric shells[37,38].

Bubble cavitation has been used to enhance the delivery of co-administered therapeutics via mechanical[32] or thermal effects[39,40], which can facilitate delivery by temporarily increasing the permeability of the local vasculature[41,42], propelling therapeutics[4,29,43] or triggering drug release from cavitation-sensitive carriers[44]. The latter strategy was the topic of **Chapter 4**. Apart from co-administering cavitation and therapeutic agents, recent research has explored the feasibility of conjugating therapeutic carriers, e.g. liposomes on the ultrasound contrast agent (UCA)[45,46], encapsulation of therapeutics into the shell of UCAs[5,14] and finally, material transfer from the UCA

to the surrounding epithelia[47]. The common denominator of these approaches is that they all point towards the direction of providing an additional role to the UCA, i.e. that of a carrier of therapeutics. The major advantage of these approaches is that they ensure that the therapeutic and the UCA are at the site of action at the same time. Another strength is that the delivery can be visualised in real time, since the UCA can be used for imaging with ultrasound (as evidenced by the B-mode images in **Figure 44** here). Liposome conjugation on the surface of lipid MBs has provided promising results, however it significantly increases the complexity of the formulation and requirements for characterisation. Additionally, it is known that lipid-based MBs, even when filled with perfluorocarbons, are short-lived in circulation. Lipid MBs are excellent imaging agents thanks to the high flexibility of their shell which allows the entrapped gas to oscillate.

However, for drug delivery purposes, longer-lived polymeric agents, which can still provide sufficient contrast at clinically relevant ultrasound pressures might be preferable. In pre-clinical settings, several such particles have been developed, made from biodegradable[10,48] or non-biodegradable polymers[35,49]. The Wheatley group developed smooth surface, high molecular weight PLA and PLGA spheres by modifying conventional emulsification techniques with the addition of sublimating compounds, to provide a hollow chamber, filled with air at the core of the sphere[50,51]. They showed that these particles can have a dual role as UCAs and drug carriers for conventional small molecule chemotherapeutics[14,52]. They went on to show that the PLA (MW 83 kDa) spheres collapse in response to ultrasound (0.94 MPa, 5 MHz frequency, 5000 cycles for 20 min), generating sub-micron fragments able to pass through the pores of an *in vitro* model of the leaky tumour vasculature[14]. Not unlike nanoparticles, PLA half-life was increased by PEGylation[53]. The multiple studies done by the Wheatley group on variations of this idea provided proof-of-concept that polymeric UCAs can act as drug carriers and can generate fragments which can potentially be transferred into the tumour tissue and gradually release the entrapped therapeutic.

However, the 20 min sonication time employed in the studies of Wheatley and colleagues was not in line with what can realistically be expected *in vivo*.

Variations of the double emulsion – solvent evaporation method for polymeric MB fabrication have been used by multiple researchers. This emulsification technique allows for encapsulation of both hydrophilic and hydrophobic drugs, it is amenable to modifications and can be scaled up[50]. The first polymer employed in the work reported in this thesis is PLA. For the current investigation, fast polymer degradation, in the time scale of days, is desirable. High MW PLA, as used by Cochran *et al.*[14] does not meet this requirement and was therefore replaced by PLA of much lower MW (10-17 kDa). Another material factor affecting degradation is the end groups of the polymer, with acid-terminated polymers able to auto-catalyse hydrolysis and therefore facilitating degradation. Hence, the polymer was selected to be acid-terminated. Small particles (<1 μm) were observed under the optical microscope but instead of being free-flowing, they were entrapped into a fibrous matrix. It is speculated that this matrix could arise from a combination of surplus PVA and polymer not involved in particle formation.

Dynamic light scattering (DLS), which is a preferred technique for liposome sizing in **chapter 4** was not appropriate for sizing these particles, and MBs in general.

The first reason for this is the size of these particles. Given the broad size distribution that is expected, 1-8 μm would be an anticipated and acceptable size range for polymer MBs. MBs should not be larger than 8-10 μm because this increases the risk of embolism. DLS measurements are based on Brownian motion, which is a characteristic of nanoparticles and it is therefore ideally suited for nanoparticle size measurements. SPOS is also an optical sizing technique, based on the scattering or diffraction of a laser beam traversing the sample. In SPOS however, the measurement is performed as dilute sample passes under flow in front of a laser beam, therefore it does not rely on Brownian motion.

Secondly, if the particles are indeed air-filled, they would be expected to float which is incompatible with the reliance of DLS on Brownian motion. Another advantage of the SPOS technique is that the concentration of the particles can be calculated. A weakness of the SPOS Accusizer instrument is that the lower size limit is 0.51 μm, so particles smaller than this were not measured. Furthermore, particle aggregates cannot be distinguished from larger particles, as is the case in microscopy. Average particle size of PLA particles was smaller than expected (0.78 μm) based on the fact that homogenisation was used for the second emulsification step. Homogenisation generally gives rise to microparticles, while to form sub-micron particles two sonication steps would be employed.

SEM is an indispensable technique for the morphological characterisation of particles in the μm size range. SEM revealed an aggregate, rather than individual particles, with hollow round structures (**Figure 43C**). It was unclear whether these structures were generated during the imaging session because of the high vacuum conditions of the SEM chamber or that was the original state of the sample. The presence of a matrix on which the particles are embedded, was confirmed by SEM. To address the question of whether the particles are destroyed during imaging, the low vacuum and environmental SEM options were investigated. Similar SEM conditions have been used by others for imaging this type of particle[10,14,53]. For the LMW PLA particles, the image produced under low vacuum conditions was similar to that of conventional SEM, and so this technique failed to confirm the presence of particles even after these adjustments (**Figure 43D**). Hence, several characterisation techniques were in accordance in suggesting this LMW formulation was not worth pursuing and alternative polymers were explored.

Two directions were identified: first, opting for a higher molecular weight PLA or second, opting for a higher molecular weight PLGA. Given that the MW was to be increased, PLGA was preferred because of its faster degradation and higher flexibility compared to PLA. PLGA of various lactide-to-glycolide ratios is commercially available but 50:50 lactide-to-glycolide is the

ratio characterised by the highest degradation rate. For comparison purposes, a PLGA of much higher MW was also employed. The same preparation steps were followed for all three formulations (LMW PLA, IMW PLGA and HMW PLGA). Both PLGA polymers produced spherical particles, as seen in the bright field images (**Figure 44B and F**). Notably, the particles produced demonstrated buoyancy, confirmed by the fact that they were in focus above the level of the haemocytometer grid. As seen in the images (**Figure 44**), the PLGA particles varied in size with an average diameter of 1.01 and 1.47 μm for IMW and HMW PLGA respectively. This size distribution was not unexpected for particles developed by emulsification techniques. Importantly, no particles above 4-5 μm were detected by any of the techniques employed (optical and electron microscopy, SPOS). High vacuum EM was not attempted as low vacuum EM is in principle more in line with air-filled particles. Indeed, low vacuum EM revealed the presence of spherical particles. HMW PLGA particles had a smooth surface, in accordance with results from others[14] and were more easily dispersible in aqueous buffers. The surface of IMW PLGA were rougher, and in several cases one or more dimples were seen on the particles. This is a favourable feature for cavitation nucleation, as air can be entrapped in these surface irregularities, similarly to aspherical echogenic particles recently reported by Kwan's group[10]. Also, Wheatley's group investigated the effect of PVA, a commonly used emulsifier, in the morphology of MBs. They found that lower MW PVA (6 kDa) resulted in rough surface particles with large dents, although they used high MW PLGA[50]. The PVA used in this study was 8-10 kDa and the cavities observed are much smaller. A feature that is worth of further investigation is whether the particles have a single hollow core (capsule-like) or rather if they have pores or superficial dimples. The current images suggest that the latter case is more likely. Indeed, while this work was in progress, Kwan et al.[10] reported the development of PLGA UCAs which, unlike Wheatley group's design, air entrapment is superficial rather than in the core. This is an important development in support of the approach adopted in this project. Since polymeric structures are less capable of matching the expansion and contraction of

entrapped air bubbles, polymer capsule design is expected to be less responsive than a lipid capsule. However, if air is contained in open cavities, the bubble can freely oscillate while the better stability of the polymer, compared to the lipid bubble, is likely to retain the advantages of both approaches. In line with this, submicron polymeric cups were shown to be longer-lived than lipid MBs *in vitro* and *in vivo* and in fact provided more sustained cavitation. These cups, however, are fabricated from biocompatible but non-biodegradable polymer and are better suited for co-administration with a therapeutic rather than as drug carriers[4,49].

Both PLGA particle formulations were included in initial acoustic characterisation aimed at showing contrast and fragmentation in response to ultrasound (**Figure 44**). Two generic types of study can be done using the ultrasound setup employed in this chapter – particle characterisation and extravasation. Although the setup and process are similar in both cases, the main differences lie in sample concentration and the preparation of the phantom. For extravasation experiments, for which this setup is most frequently used, a softer phantom is prepared with lower agarose concentration (1-1.25%) and usually low melting point agarose gel is preferred. The phantom composition has been designed so that it closely matches the relevant properties (porosity, hardness, acoustic response) of animal tissue and the low melting point ensures that embedded cells, whenever used, can be harvested with minimal cell death[28,54,55]. The concentration of particles used in such experiments is typically determined based on the expected concentration range that might be achieved in further *in vitro* or *in vivo* experiments. In contrast, when characterising the particles, as is the case here, lower particle concentration is used as it minimises the shielding which can be created by a bubble cloud in the near focus which depletes the signal created and detected in the far region of the US focus. Therefore, the range of concentrations (0.1, 0.01 and 0.001 mg/mL) used here is significantly lower than the concentrations used for the degradation study that followed.

Overall, the particles showed good contrast in B-mode US (**Figure 44**) and, importantly for this work, were fragmented after ultrasound treatment. Quantification of contrast enhancement could be performed in future work. No positive control was used (e.g. SonoVue) because direct comparison between different formulations is difficult: volume of entrapped gas per mL formulation varies and resonance frequencies are also different among formulations depending on the particle size and shell composition. Of note, in this experiment the PLGA fragments were not separated for different US parameters. Rather, high amplitude ultrasound bursts from the B-mode transducer were used to break all particles in the sample. Therefore, fragmentation patterns cannot be correlated to ultrasound parameters. These high amplitude bursts can be applied *in vivo* as well[29], with no tissue damage so the information is still relevant. The collected fragments were lyophilised and imaged by low vacuum SEM. Resolution is lower when the SEM chamber is not evacuated so images of the fragments are not as clear as the ones of the intact particles. However, individual particles can still be distinguished. After manual measurement of particles on ImageJ, it was concluded that on average particles of both PLGA formulations reduced in size (1.00 ± 0.43 μm to 0.48 ± 0.18 μm for HMW PLGA and 0.68 ± 0.21 μm to 0.55 ± 0.14 μm before and after treatment respectively). This is a step beyond the results presented by Eisenbrey *et al*[14] because here it is shown that fragmentation can be achieved with conditions that are applicable *in vivo*. It would be interesting to harvest the particles after individual treatments and image them.

Only IMW PLGA particles were considered for detailed study of acoustic response and breakdown as their morphology and known polymer properties suggested that they were more likely to be more responsive to ultrasound and achieve faster degradation (**Figure 45**). Acoustic characterisation of these particles showed that at low acoustic pressures (0.18 MPa) non-inertial cavitation was evident. Ultrasound response was examined under flow conditions (0.5 mL/min) and without flow. Flow conditions are more representative of the *in vivo* settings, in which destroyed UCAs are replenished thanks to blood flow, so the ultrasound beam, usually a few mm

in focus, is constantly presented with fresh UCAs. However, 'No flow' conditions give an indication of how long cavitation of individual particles can be sustained for. At low pressure, cavitation was sustained for the duration of treatment (20 s). Higher pressure (0.77 MPa) resulted in inertial cavitation both under flow and in 'no flow' conditions. Importantly, 0.77 MPa pressure falls well within the range of ultrasound used *in vivo*, with certain UCAs requiring substantially higher pressures (e.g. droplets and cups)[55].

For degradation studies, higher MB concentration was used (2.5 mg/mL). Since there was no previous experience with this type of study, this high concentration was used to ensure that even minimal lactate release could be detected. For assessing polymer degradation, a colorimetric lactate dehydrogenase assay (LDH) assay was used. The most important limitation of this approach is that it underestimates polymer degradation, especially in the case of PLGA. The composition of the polymer used in this project is 50:50 lactide-to-glycolide. Lactide and glycolide refers to the cyclic dimers of lactic and glycolic acid respectively, which is the actual 'monomer' used in polymer synthesis via 'ring-opening polymerisation' reaction. This means that at least half of the released monomers are glycolic acid, which is not detected by the LDH assay. Further, glycolic residues might correspond to more than half of the released monomers since the less sterically hindered and more hydrophilic nature of the glycolic residues makes them more prone to hydrolysis. On top of this, LDH is selective towards L-lactate. The PLGA used in this work was not composed solely of L-lactate, but rather of a racemic (50:50) mixture of isomers. This was desirable because such polymers degrade faster, but this also results in further underestimation of polymer degradation. Lastly, hydrolysis does not necessarily happen at the terminal residues of the polymer chain. Therefore, water soluble (approximately up to 10 residues) oligomers can also be found and are not accounted for. With regards to uptake by the MCT1, oligomers are not directly relevant, since they are not expected to be transported. More detailed assessment of the water-soluble

components of PLGA degradation could be achieved with LC-MS, while the polymer chain distribution in the solid residue could be assessed with MALDI-TOF MS[56].

As a positive control, the MB suspension was treated with a probe sonication using conditions aggressive enough to ensure breakdown. Hence, this control represented conditions that would certainly destroy the bubbles, providing a good comparison to the two low but realistic ultrasound pressures that were tested (0.2 and 0.5 MPa) and control sample that was not exposed to US. For the first degradation study, treatment time was selected to match that used in chapter 4 (20 s) which is a duration roughly corresponding to *in vivo* settings. Unfortunately, no significant difference was seen compared to non-US control (**Figure 46C**). However, the samples treated with the probe sonication degraded faster (0.75 ± 0.039 vs 0.039 ± 0.020 μM lactate by day 2) suggesting that in principle, ultrasound treatment can accelerate degradation. The effect of ultrasound used for the preparation of PLGA particles has been shown by Reich[57], who fabribated PLGA microspheres using probe sonication operating from 20 to 60 W intensity and from 10 to 90 s duration, and showed that polymer MW is decreased. Kost and colleagues studied the degradation of a range of polymers including poly-lactides and poly-glycolides in response to ultrasound. The authors found an ultrasound intensity-dependent increase in degradation rate of these polymers formulated in films[58]. This is in accordance, in principle, with the results presented in this chapter however, to the best of the author's knowledge, ultrasound-induced degradation has not been investigated before in MB formulations under clinically-relevant conditions.

To elucidate whether clinically relevant pressures can achieve similar effects, 0.5 MPa was selected for the second study (**Figure 47**), and the duration of treatment was extended for as long as the cavitation signal persisted (8 min). The release was not as pronounced as achieved using the probe sonicator, but there was statistically significant difference between the 0.5 MPa sonicated sample and the non-US control. Also, it was shown that cavitation without flow could be

maintained for at least 8 min. This is certainly associated with the concentration of the particles, but it is an encouraging result worthy of further investigation.

The final objective of this work was to eventually replace some of the lactate residues with a derivative of therapeutic and /or imaging potential, such as ^{123}I-HPLA. Time limitations did not allow this objective to be realised but the first steps in this direction were taken. Two main prerequisites were identified in order to prove the feasibility of this idea and ultrasound-responsive particles which decreased in size to sub-micron scale following sonication were formulated. Furthermore, sonication increased the rate of monomer release. This chapter therefore provides proof-of-concept that these prerequisites can be met.

6.7 Concluding remarks & future directions

In this chapter, gas-entrapping microparticles were fabricated using biodegradable and biocompatible, lactic acid-based polymers. Three polymers were evaluated for particle formation: PLA 10-18 kDa, PLGA 25-38 kDa and PLGA 38-54 kDa. PLA did not form particles of appropriate properties with the double emulsion-solvent evaporation method employed. Both PLGA polymers formed spherical particles, but with different surface morphologies. Lower MW PLGA particles had rougher surfaces with cavities, while higher MW PLGA produced smooth spheres, which can impact the gas-entrapping capacity of the particles. Lower MW PLGA particles were indeed shown to cavitate non-inertially at low acoustic pressures (0.18 MPa) and inertially at higher pressures (0.77 MPa). Further, the particles showed fragmentation into particles of a few hundred nm and higher rate of monomer release in response to ultrasound, providing proof-of-concept that such particles, if optimised, could serve for the release of a modified, therapeutic monomer.

6.8 References

1. Chereddy, K. K., Vandermeulen, G. & Préat, V. PLGA based drug delivery systems: Promising carriers for wound healing activity. *Wound Repair Regen.* **24**, 223–236 (2016).
2. Azevedo-Silva, J. *et al.* The anticancer agent 3-bromopyruvate: a simple but powerful molecule taken from the lab to the bedside. *J. Bioenerg. Biomembr.* **48**, 349–362 (2016).
3. Pan, Q. *et al.* Hepatotoxicity and nephrotoxicity of 3-bromopyruvate in mice. *Acta Cir. Bras.* **31**, 724–729 (2016).
4. Kwan, J. J. *et al.* Ultrasound-Propelled Nanocups for Drug Delivery. *Small* **11**, 5305–14 (2015).
5. Eisenbrey, J. R., Huang, P., Hsu, J. & Wheatley, M. A. Ultrasound triggered cell death in vitro with doxorubicin loaded poly lactic-acid contrast agents. *Ultrasonics* **49**, 628–633 (2009).
6. Lasprilla, A. J. R., Martinez, G. A. R., Lunelli, B. H., Jardini, A. L. & Filho, R. M. Poly-lactic acid synthesis for application in biomedical devices - A review. *Biotechnol. Adv.* **30**, 321–328 (2012).
7. Swider, E. *et al.* Customizing poly(lactic-co-glycolic acid) particles for biomedical applications. *Acta Biomater.* **73**, 38–51 (2018).
8. Senapati, S., Mahanta, A. K., Kumar, S. & Maiti, P. Controlled drug delivery vehicles for cancer treatment and their performance. *Signal Transduction and Targeted Therapy* vol. 3 (2018).
9. Li, C. *et al.* Design of biodegradable, implantable devices towards clinical translation. *Nature Reviews Materials* (2019) doi:10.1038/s41578-019-0150-z.
10. Su, X., Thomas, R. G., Bharatula, L. D. & Kwan, J. J. Remote targeted implantation of sound-sensitive biodegradable multi-cavity microparticles with focused ultrasound. *Sci. Rep.* **9**, 9612 (2019).
11. Xu, Y., Kim, C.-S., Saylor, D. M. & Koo, D. Polymer degradation and drug delivery in

PLGA-based drug–polymer applications: A review of experiments and theories. *J. Biomed. Mater. Res. Mater. Res.* (2016).

12. Chereddy, K. K. *et al.* PLGA nanoparticles loaded with host defense peptide LL37 promote wound healing. *J. Control. Release* **194**, 138–147 (2014).

13. Chereddy, K. K. *et al.* Combined effect of PLGA and curcumin on wound healing activity. *J. Control. Release* **171**, 208–215 (2013).

14. Cochran, M. C., Eisenbrey, J., Ouma, R. O., Soulen, M. & Wheatley, M. A. Doxorubicin and paclitaxel loaded microbubbles for ultrasound triggered drug delivery. *Int. J. Pharm.* **414**, 161–170 (2011).

15. Danhier, F. *et al.* Paclitaxel-loaded PEGylated PLGA-based nanoparticles: In vitro and in vivo evaluation. *J. Control. Release* **133**, 11–17 (2009).

16. Arora, G. *et al.* PLGA Nanoparticles for Peptide Receptor Radionuclide Therapy of Neuroendocrine Tumors: A Novel Approach towards Reduction of Renal Radiation Dose. *PLoS One* **7**, (2012).

17. Bret, U. D., Lakshmi, N. S. & Laurencin, C. T. Biomedical Applications of Biodegradable Polymers. *J. Polym. Sci. Part B Polym. Phys.* **3**, 832–864 (2011).

18. Alexis, F. Factors affecting the degradation and drug-release mechanism of poly(lactic acid) and poly[(lactic acid)-co-(glycolic acid)]. *Polym. Int.* **54**, 36–46 (2005).

19. Zweers, M. L. T., Engbers, G. H. M., Grijpma, D. W. & Feijen, J. In vitro degradation of nanoparticles prepared from polymers based on DL-lactide, glycolide and poly(ethylene oxide). *J. Control. Release* **100**, 347–356 (2004).

20. Liu, R. *et al.* Effects of the molecular weight of PLGA on degradation and drug release in vitro from an mPEG-PLGA nanocarrier. *Chem. Res. Chinese Univ.* **32**, 848–853 (2016).

21. Proikakis, C. S., Mamouzelos, N. J., Tarantili, P. A. & Andreopoulos, A. G. Swelling and hydrolytic degradation of poly(d,l-lactic acid) in aqueous solutions. *Polym. Degrad. Stab.* **91**,

614–619 (2006).

22. Panyam, J. *et al.* Polymer degradation and in vitro release of a model protein from poly(d,l-lactide-co-glycolide) nano- and microparticles. *J. Control. Release* **92**, 173–187 (2003).

23. Viswanathan, N. B. *et al.* Morphological changes in degrading PLGA and P(DL)LA microspheres: implications for the design of controlled release systems. *J Microencapsul* **18**, 783–800 (2001).

24. Grizzi, I., Garreau, H., Li, S. & Vert, M. Hydrolytic degradation of devices based on poly (DL-lactic acid) size-dependence. *Biomaterials* **16**, 305–311 (1995).

25. Keles, H., Naylor, A., Clegg, F. & Sammon, C. Investigation of factors influencing the hydrolytic degradation of single PLGA microparticles. *Polym. Degrad. Stab.* **119**, 228–241 (2015).

26. Lajoinie, G. *et al.* In vitro methods to study bubble-cell interactions: Fundamentals and therapeutic applications. *Biomicrofluidics* **10**, 011501 (2016).

27. Kwan, J. J. & Borden, M. A. Lipid monolayer collapse and microbubble stability. *Adv. Colloid Interface Sci.* **183–184**, 82–99 (2012).

28. Mannaris, C. *et al.* MICROBUBBLES, NANODROPLETS AND GAS-STABILIZING SOLID PARTICLES FOR ULTRASOUND-MEDIATED EXTRAVASATION OF UNENCAPSULATED DRUGS: AN EXPOSURE PARAMETER OPTIMIZATION STUDY.

29. Thomas, E. *et al.* Ultrasound-mediated cavitation enhances the delivery of an EGFR-targeting liposomal formulation designed for chemo-radionuclide therapy. *Theranostics* **9**, 5595–5609 (2019).

30. Gorce, J. M., Arditi, M. & Schneider, M. Influence of bubble size distribution on the echogenicity of ultrasound contrast agents: A study of sonovue(TM). *Invest. Radiol.* **35**, 661–671 (2000).

31. Schneider, M. & Ph, D. Characteristics of SonoVueTM. **16**, 743–746 (1999).

32. Carlisle, R. & Coussios, C.-C. Mechanical approaches to oncological drug delivery. *Ther. Deliv.* **4**, 1213–5 (2013).

33. Minchinton, A. I. & Tannock, I. F. Drug penetration in solid tumours. *Nat. Rev. Cancer* **6**, 583–592 (2006).

34. Arvanitis, C. D., Bazan-Peregrino, M., Rifai, B., Seymour, L. W. & Coussios, C. C. Cavitation-Enhanced Extravasation for Drug Delivery. *Ultrasound Med. Biol.* **37**, 1838–1852 (2011).

35. Kwan, J. J. *et al.* Ultrasound-Propelled Nanocups for Drug Delivery. *Small* **11**, 5305–5314 (2015).

36. Stride, E. P. & Coussios, C. C. Cavitation and contrast: the use of bubbles in ultrasound imaging and therapy. *Proceedings of the Institution of Mechanical Engineers. Part H, Journal of engineering in medicine* vol. 224 171–191 (2010).

37. Sirsi, S. & Borden, M. Microbubble Compositions, Properties and Biomedical Applications. *Bubble Sci Eng Technol.* **1**, 3–17 (2010).

38. Sirsi, S. R. & Borden, M. A. State-of-the-art materials for ultrasound-triggered drug delivery. *Adv. Drug Deliv. Rev.* **72**, 3–14 (2014).

39. Lyon, P. C. *et al.* Safety and feasibility of ultrasound-triggered targeted drug delivery of doxorubicin from thermosensitive liposomes in liver tumours (TARDOX): a single-centre, open-label, phase 1 trial. *Lancet Oncol.* (2018) doi:10.1016/S1470-2045(18)30332-2.

40. Gray, M. D. *et al.* Focused Ultrasound Hyperthermia for Targeted Drug Release from Thermosensitive Liposomes: Results from a Phase I Trial. *Radiology* **291**, 232–238 (2019).

41. Ojha, T. *et al.* Pharmacological and physical vessel modulation strategies to improve EPR-mediated drug targeting to tumors ☆. (2017) doi:10.1016/j.addr.2017.07.007.

42. Bazan-Peregrino, M., Arvanitis, C. D., Rifai, B., Seymour, L. W. & Coussios, C. C.

Ultrasound-induced cavitation enhances the delivery and therapeutic efficacy of an oncolytic virus in an in vitro model. *J. Control. Release* **157**, 235–242 (2012).

43. Bazan-Peregrino, M. *et al.* Cavitation-enhanced delivery of a replicating oncolytic adenovirus to tumors using focused ultrasound. *J. Control. Release* **169**, 40–47 (2013).

44. Graham, S. M. *et al.* Inertial cavitation to non-invasively trigger and monitor intratumoral release of drug from intravenously delivered liposomes. *J. Control. Release* **178**, 101–107 (2014).

45. Yu, F. T. H., Chen, X., Wang, J., Qin, B. & Villanueva, F. S. Low Intensity Ultrasound Mediated Liposomal Doxorubicin Delivery Using Polymer Microbubbles. *Mol. Pharm.* **13**, 55–64 (2016).

46. PARK, S.-H. *et al.* Development of a novel microbubble-liposome complex conjugated with peptide ligands targeting IL4R on brain tumor cells. *Oncol. Rep.* **36**, 131–136 (2016).

47. Carugo, D. *et al.* Modulation of the molecular arrangement in artificial and biological membranes by phospholipid-shelled microbubbles. *Biomaterials* (2016) doi:10.1016/j.biomaterials.2016.10.034.

48. Zhao, X. *et al.* Preparation and in vivo evaluation of ligand-conjugated polymeric microbubbles as targeted ultrasound contrast agents. *Colloids Surfaces A Physicochem. Eng. Asp.* **452**, 59–64 (2014).

49. Myers, R. *et al.* Polymeric Cups for Cavitation-mediated Delivery of Oncolytic Vaccinia Virus. *Mol. Ther.* **24**, 1627–33 (2016).

50. El-Sherif, D. M. & Wheatley, M. A. Development of a novel method for synthesis of a polymeric ultrasound contrast agent. *J. Biomed. Mater. Res.* **66A**, 347–355 (2003).

51. Lathia, J. D., Leodore, L. & Wheatley, M. A. Polymeric contrast agent with targeting potential. *Ultrasonics* **42**, 763–768 (2004).

52. Eisenbrey, J. R. *et al.* Development of an ultrasound sensitive oxygen carrier for oxygen

delivery to hypoxic tissue. *Int. J. Pharm.* **478**, 361–367 (2015).

53. Jablonowski, L. J. *et al.* Balancing stealth and echogenic properties in an ultrasound contrast agent with drug delivery potential. *Biomaterials* **103**, 197–206 (2016).

54. Thomas, E. *et al.* Ultrasound-mediated cavitation enhances the delivery of an EGFR-targeting liposomal formulation designed for chemo-radionuclide therapy. *Theranostics* **9**, 19 (2019).

55. Paris, J. L. *et al.* Ultrasound-mediated cavitation-enhanced extravasation of mesoporous silica nanoparticles for controlled-release drug delivery. *Chem. Eng. J.* **340**, 2–8 (2018).

56. Montaudo, G., Samperi, F. & Montaudo, M. S. Characterization of synthetic polymers by MALDI-MS. *Prog. Polym. Sci.* **31**, 277–357 (2006).

57. Reich, G. Ultrasound-induced degradation of PLA and PLGA during microsphere processing: influence of formulation variables. *Eur. J. Pharm. Biopharm.* **45**, 165–171 (1998).

58. Kost, J., Leongt, K. & Langer, R. Ultrasound-enhanced polymer degradation and release of incorporated substances. *Appl. Biol. Sci.* **86**, 7663–7666 (1989).

7 General Discussion

The overarching theme of this thesis was to use a tumour-specific metabolic trait, the upregulation of the lactate transporter, MCT1, for the selective uptake of a therapeutic analogue of its natural substrate. Delivery challenges, but also advantages, of using small organic acids led to the simultaneous development of a delivery platform for this type of molecule.

7.1 Inhibition or 'Trojan horse'?

In targeting MCT1, inhibition of the transporter has received significant attention, and a comparison to the 'Trojan horse' approach is interesting. Research progress on 3BP has been discussed in **Chapter 3**.

Early reports of MCT1 inhibition showed a fall in the intracellular pH *in vitro*[1,2], cytotoxicity *in vitro*[2,3] and radiosensitisation[1,4]. Colen *et al*[4]., who reported radiosensitisation, worked with UB-87MG glioma cells *in vitro* and used CHC with the intention of inhibiting lactate efflux, without however characterising the cell line with respect to the expression of different MCT isoforms. Sonveaux *et al.*[1], worked with 'low oxidative rate' WiDr cells and 'high oxidative rate' SiHa cells. Blocking MCT1 either with CHC or siRNA-mediated silencing increased the glycolytic rate of SiHa cells. Although they did not find substantial toxicity of CHC *in vitro*, they observed tumour growth delay *in vivo*. The authors speculated growth delay was caused by the indirect starvation of the hypoxic core, due to the switch of oxygenated cells from a preferential lactate consumption to glucose consumption. In this pivotal work, they went on to propose their 'symbiotic' model.

However, later studies on the inhibition approach, either with small molecule inhibitors or siRNA, showed intriguing results. Morais-Santos *et al*[5]. evaluated CHC, quercetin and lonidamine in breast cancer cell lines. They found that inhibition of lactate transport reduced cell

aggressiveness. Higher sensitivity was observed in cells with the highest rate of lactate transport, rather than those with highest MCT1 expression. As such, BT20, one of the breast cancer cell lines with the highest MCT1 expression, was insensitive to all inhibitors. BT20 had the lowest rate of glucose consumption and lactate excretion out of the examined cell lines. In contrast, MDA-MB-231 and SkBr3 cells, which do not express MCT1, responded to treatment. Results from Zhao and co-workers, who examined the impact of MCT1 inhibition or shRNA-mediated silencing agree with those by Morais-Santos *et al.* This group used CHC and showed inhibition of clone formation and tumour growth in osteosarcoma cell lines. However, for assessing cell migration and invasion, they used shRNA-mediated silencing of the transporter and concluded that it has an inhibitory effect in these processes[6]. This raised the question of whether it is the expression of the transporter or its shuttling function that is important for migration and invasion.

A new class of highly selective MCT1/2 inhibitors, originally designed as immunomodulatory agents by AstraZeneca[7], have also been investigated for cancer therapy. The binding of AR-C155858, one of these compounds, has been resolved. AR-C155858 accesses the transporter from the intracellular side and its binding site is found in transmembrane helices (TMs) 7-10 of the C-terminal domain[8]. A later study by Nancolas and colleagues identified the amino acids aspartate-302, arginine-306, lysine-38, leucine-274, serine-278, phenylalanine-360 and serine-364 to be involved in the binding of the inhibitor[9]. Of those, aspartate-302, arginine-306 and lysine-38 are also required for lactate binding.

While this work was in progress, the effects of AR-C155858 were evaluated on cancer cells[10]. In their very interesting report, Guan and colleagues[10] treated murine triple-negative breast cancer cells, 4T1, with the inhibitor *in vitro* and *in vivo*. Inhibition of lactate transport was confirmed in both cases. However, the authors reported that inhibition of cell growth *in vitro* required much higher concentration (IC_{50}=20.2 nM) than that required for lactate transport inhibition (K_i=2.1 nM). Further, AR-C155858 did not inhibit cell invasion *in vitro* and it did not inhibit tumour growth

nor reduced tumour lactate levels *in vivo*[10]. Gray *et al.*[11] used MCT1-knockdown and inhibition to study the role of the transporter in the migration of TNBC (HCC1806) and prostate cancer cells (DU145). MCT1 knockdown did not alter cell growth or ATP production[11]. The authors also concluded that MCT1 function in promoting migration is independent of its transporter activity, which was in agreement with earlier findings by Payen *et al.* who showed that knockdown but not pharmacological inhibition of MCT1 reduces migration of superinvasive SiHa-F3 cells[12]. In contrast, Doherty et al.[13], who worked on MCF7 breast cancer cells (ER+, MCT1 and MCT4 expressing) reported that MCT1 pharmacological inhibition (in-house synthesised AR-C122982 and AR-C155858) or silencing resulted in reduction in ATP and glutathione production, accumulation of intracellular lactate and reduction in cell growth. Overexpressing MCT4 or CD147 (a chaperone protein for both MCT1 and 4) induced resistance to the effects of MCT1 inhibition[13].

Overall, there seems to be some overlap between the effects of pharmacological inhibition of MCT1 and treatment with 3BP. The rationale for the use of the AstraZeneca inhibitors for cancer treatment was to inhibit lactate efflux from glycolytic cells, and thus dampen secondary effects of lactate in the tumour microenvironment (low pH, angiogenesis, immunosuppression)[14,15], which is in common with how 3BP is frequently utilised[16,17]. However, whether inhibition of the transporter is cytotoxic as such remains unclear, and it could be context- and cell line-dependent. Resistance to treatment could arise from the upregulation of other MCT isoforms[15]. Although limited evidence is available to date, it seems that the transport-independent functions of MCT1 (e.g. in cell invasiveness) are not affected by pharmacological inhibition.

3BP, similarly, inhibits glycolysis and as such, it is expected to decrease lactate production – although lactate concentration was not measured directly in this work. Therefore, the benefits arising from lactate concentration reduction in the TME are in common for both strategies. Further, the present work and that of others have shown the pleiotropic actions of 3BP, which

expand further than glycolysis. Specifically, in **Chapter 3**, it was shown that PPP intermediates are markedly and selectively accumulating in MCT1-expressing cells (e.g. sedoheptulose phosphates) and nucleotide synthesis was decreased, which was presumably related to the effects on PPP. Thiol-containing compounds are important anti-oxidants with the main ones being GSH and NAC. 3BP was shown to cause depletion of these compounds. Therefore, it is likely that 3BP could also act as a radiosensitiser, although this effect has not been examined at present.

Critics of the potential of 3BP as an anti-cancer therapeutic argue that it is too 'crude' because of its multiple and context-dependent actions (e.g. baseline of glutathione concentration). In the author's opinion, the multiplicity of actions is not necessarily a disadvantage, as long as its actions can be limited to the tumour site, for which purpose, drug delivery strategies have been proposed in this work and the work of others. With a delivery strategy, multiple actions could actually be advantageous because development of resistance becomes less likely.

7.2 Need for companion diagnostics

For either of these approaches to be viable, determination of patient suitability and pre-selection would be valuable. Since MCT1 is the main pre-requisite for either of the treatments to be effective, MCT1 expression pre-assessment is a requirement. Unfortunately, the currently established ^{18}F-FDG PET scan would not be an accurate assessment for either treatment because upregulated glycolysis can be supported by MCT1, 2 or 4. With the currently used modalities, a biopsy would be required and, although invasive, it is commonly performed in cancer diagnosis. Imaging agents such as the recently synthesised ^{18}F-fluorolactate for PET scans[18] or hyperpolarilised ^{13}C-labelled lactate/pyruvate for MRI scans would be equally valuable for both approaches[19]. Temporary glutathione depletion can be simply achieved with various agents e.g. paracetamol, a widely used analgesic.

7.3 Potential delivery strategies

A multitude of very promising delivery platforms for different kinds of therapeutics has been developed, including those where an external stimulus is involved to trigger the release of the therapeutic or guide the carrier to the target site[20,21]. The delivery strategy needs to match the needs and strengths of the therapeutic, exploit the tropisms of the treated condition and shield the body from potential toxicities. For 3BP and ^{123}I-HPLA the primary concerns are their pharmacokinetics and potential toxicity to non-targeted tissues. Since they are small molecules targeted to a transporter expressed on the cell surface, and not intracellularly, there was no benefit in using a molecularly targeted, long-circulating carrier. Chemical functionalisation of the carrier adds complexity to the manufacturing process, which limits the applicability and scalability of the formulation[21]. Further, if this approach is to be used for the delivery of a radioactive compound, such as ^{123}I-HPLA, the active loading approach limits handling of radioactivity, which is a major practical advantage. Formulation process is fast (approximately 2 h) which makes it suitable for 3BP as well, given its short half-life in aqueous media[22]. It has been accepted by different researchers that 3BP needs a delivery system[23–25], if it is to be used for systemic treatment. Limited but promising efforts have been made in this direction. At the time of writing, a stimulus-responsive nano- or micro-carrier has not been reported before for 3BP.

Polymeric MBs have been reported in several publications[26–28]. The main contributions of the present work are related to assigning a new role to this type of particle. Here, it was shown that clinically used ultrasound conditions break the particles in 'nanoshards' that are of appropriate size (sub-micron) to extravasate through the tumour vasculature. It was also shown that ultrasound treatment using clinically relevant parameters can increase monomer release. Effect of ultrasound has been examined before but looking at the release of an entrapped therapeutic[26,27]. Hydrolytic degradation positively affects the release rate of encapsulated compounds but the latter is affected

by other parameters as well, e.g. the physicochemical properties of the therapeutic. Here, the interest is on the monomer release from the polymer.

The research area in which lactic acid based polymers have been investigated in this way is wound healing[29,30]. There are two interesting points arising from that area of research. First, PLGA is preferred over PLA even though a substantial percentage of the monomers are not useable (typically up to 50%). However, the faster degradation rate is seen as a major advantage[31]. Other factors that were also considered here were the carboxylic acid termini and polymer MW. The considerations of the present work are in agreement with what is regarded as suitable for wound healing applications[31]. The mechanism by which ultrasound (SAT2 device or probe sonicator) promotes polymer degradation was not examined in this thesis. It can be speculated, that ultrasound enhances degradation by reducing particle size, therefore increasing the surface-to-volume ratio, rather than by complex sonochemistry (breaking covalent bonds).

7.4 TRT for metabolic liabilities

Radioactive analogues of energy metabolism substrates have been synthesised for imaging purposes. The main compound in this category is ^{18}F-FDG, but other metabolites have been synthesised, of which ^{18}F-fluorolactate[18] and ^{18}F-(2S,4R)-4-fluoroglutamine[32] are of particular relevance. However, radio-labelled analogues of metabololites with theranostic potential are limited to radio-iodinated fatty acids[33]. At the time of writing, no other reports have been found regarding analogues of metabolites involved in energy metabolism labelled for imaging and therapy. Although further characterisation is required to unequivocally suggest that ^{123}I-HPLA is a substrate for MCT1, current results show selective uptake by an MCT1-expressing cell line (BT20). It is not expected that ^{123}I-HPLA will act similarly to 3BP, since it does not share its alkylating capacity. Downstream effects and subcellular localisation of the compound will be the focus of

future studies. Additionally, replacing ^{123}I with a therapeutic isotope (^{125}I or ^{131}I) could be attempted and evaluated.

7.5 Concluding remarks

In this thesis, the metabolic impact of a toxic MCT1 substrate, 3BP, was evaluated in terms of selectivity, intensity and target range. In agreement with previous reports, 3BP was found to be selectively toxic to cells expressing MCT1. The anti-glycolytic effect of the compound was also confirmed here. In contrast with most studies to date, metabolic effects were examined with no previous assumptions, using untargeted metabolomics. Selective metabolic effects outside glycolysis were found, with noteworthy examples being PPP (a redox regulator and provider of nucleotide precursors), nucleotide synthesis and depletion of thiol-based antioxidants. A distinguishing strength of this work was the use of multiple controls to establish the relevance of MCT1 (MCT1-positive and negative cells, siRNA-silencing of MCT1, transfection with scramble siRNA).

A viable delivery strategy was developed for 3BP *in vitro*, while its *in vivo* evaluation started. The main outcome of this part was that release of 3BP can be efficiently triggered with clinically-relevant ultrasound conditions.

The potential of MCT1 as a mediator of TRT was evaluated *in vitro*. A radio-iodinated lactate derivative (^{123}I-HPLA) was shown to be selectively taken up by MCT1-expressing cells. Although full evaluation remains to be performed, ^{123}I-HPLA could be the first radioactive analogue of lactate with therapeutic potential.

This work concluded with the preliminary evaluation of an alternative 'all-in-one' therapeutic, UCA and carrier approach. Echogenic PLGA MBs were shown to generate sub-micron fragments in response to ultrasound and subsequent lactate release was shown to be higher than non-sonicated control. Although release of encapsulated therapeutics has been examined, the

potential of therapeutic ultrasound to accelerate polymer degradation from a UCA has not been looked at previously.

Overall, this work added to a body of evidence suggesting that MCT1 can be targeted for cancer treatment not only by inhibitors, but also by synthetic analogues of natural substrates with therapeutic properties. Since MCT1 is widely expressed throughout the body, delivery strategies are needed in order to enhance the accumulation of the therapeutic at the tumour area and limit its effects at other sites.

7.6 References

1. Sonveaux, P. *et al.* Targeting lactate-fueled respiration selectively kills hypoxic tumor cells in mice. *J. Clin. Invest.* (2008) doi:10.1172/JCI36843.however.
2. Fang, J. *et al.* The H+-Linked Monocarboxylate Transporter (MCT1 / SLC16A1): A Potential Therapeutic Target for High-Risk Neuroblastoma. **70**, 2108–2115 (2006).
3. Mathupala, S. P., Parajuli, P. & Sloan, A. E. Silencing of monocarboxylate transporters via small interfering ribonucleic acid inhibits glycolysis and induces cell death in malignant glioma: An in vitro study. *Neurosurgery* **55**, 1410–1419 (2004).
4. Colen, C. B. *et al.* Metabolic remodeling of malignant gliomas for enhanced sensitization during radiotherapy: an in vitro study. *Neurosurgery* **59**, 1313–23; discussion 1323-4 (2006).
5. Morais-Santos, F. *et al.* Differential sensitivities to lactate transport inhibitors of breast cancer cell lines. *Endocr. Relat. Cancer* **21**, 27–38 (2014).
6. Zhao, Z. *et al.* Downregulation of MCT1 inhibits tumor growth, metastasis and enhances chemotherapeutic efficacy in osteosarcoma through regulation of the NF-jB pathway. (2014) doi:10.1016/j.canlet.2013.08.042.
7. Guile, S. D. *et al.* Potent blockers of the monocarboxylate transporter MCT1: Novel immunomodulatory compounds. *Bioorganic Med. Chem. Lett.* **16**, 2260–2265 (2006).

8. Ovens, M. J., Davies, A. J., Wilson, M. C., Murray, C. M. & Halestrap, A. P. AR-C155858 is a potent inhibitor of monocarboxylate transporters MCT1 and MCT2 that binds to an intracellular site involving transmembrane helices 7-10. *Biochem. J.* **425**, 523–30 (2010).

9. Nancolas, B., Sessions, R. B. & Halestrap, A. P. Identification of key binding site residues of MCT1 for AR-C155858 reveals the molecular basis of its isoform selectivity. *Biochem. J.* **466**, 177–188 (2015).

10. Guan, X., Bryniarski, M. A. & Morris, M. E. In Vitro and In Vivo Efficacy of the Monocarboxylate Transporter 1 Inhibitor AR-C155858 in the Murine 4T1 Breast Cancer Tumor Model. *AAPS J.* **21**, 3 (2019).

11. Gray, A. L., Coleman, D. T., Shi, R. & Cardelli, J. A. Monocarboxylate transporter 1 contributes to growth factor-induced tumor cell migration independent of transporter activity. *Oncotarget* **7**, (2016).

12. Payen, V. L. *et al.* Monocarboxylate Transporter MCT1 Promotes Tumor Metastasis Independently of Its Activity as a Lactate Transporter. *Cancer Res.* **77**, 5591–5601 (2017).

13. Doherty, J. R. *et al.* Blocking lactate export by inhibiting the Myc target MCT1 Disables glycolysis and glutathione synthesis. *Cancer Res.* **74**, 908–20 (2014).

14. Ždralević, M. *et al.* Disrupting the 'Warburg effect' re-routes cancer cells to OXPHOS offering a vulnerability point via 'ferroptosis'-induced cell death. (2017) doi:10.1016/j.jbior.2017.12.002.

15. Curtis, N. J. *et al.* Pre-clinical pharmacology of AZD3965, a selective inhibitor of MCT1: DLBCL, NHL and Burkitt's lymphoma anti-tumor activity. *Oncotarget* **8**, 69219–69236 (2017).

16. Hanafy, N. A., Dini, L., Citti, C., Cannazza, G. & Leporatti, S. Inihibition of Glycolysis by Using a Micro/Nano-Lipid Bromopyruvic Chitosan Carrier as a Promising Tool to Improve Treatment of Hepatocellular Carcinoma. *Nanomater. (Basel, Switzerland)* **8**, (2018).

17. Ganapathy-Kanniappan, S. *et al.* Glyceraldehyde-3-phosphate dehydrogenase is pyruvylated during 3-bromopyruvate mediated cancer cell death. *Anticancer Res.* **29**, 4909–4918 (2009).

18. Van Hée, V. F. *et al.* Radiosynthesis and validation of [18F]-3-fluoro-2-hydroxypropionate ([18F]-FLac) as a PET tracer of lactate to monitor MCT1-dependent lactate uptake in tumors. *Oncotarget* (2017) doi:10.18632/oncotarget.14705.

19. Kurhanewicz, J. *et al.* Hyperpolarized 13C MRI: Path to Clinical Translation in Oncology. *Neoplasia* **21**, 1–16 (2019).

20. Torchilin, V. P. Multifunctional, stimuli-sensitive nanoparticulate systems for drug delivery. *Nat. Rev. Drug Discov.* **13**, 813–827 (2014).

21. Rosenblum, D., Joshi, N., Tao, W., Karp, J. M. & Peer, D. Progress and challenges towards targeted delivery of cancer therapeutics. *Nat. Commun.* **9**, 1410 (2018).

22. Glick, M., Biddle, P., Jantzi, J., Weaver, S. & Schirch, D. The antitumor agent 3-bromopyruvate has a short half-life at physiological conditions. *Biochem. Biophys. Res. Commun.* **452**, 170–173 (2014).

23. Zhang, Q. *et al.* Hexokinase II inhibitor, 3-BrPA induced autophagy by stimulating ROS formation in human breast cancer cells. *Genes Cancer* **5**, 100–12 (2014).

24. El Sayed, S. M. Enhancing anticancer effects, decreasing risks and solving practical problems facing 3-bromopyruvate in clinical oncology: 10 years of research experience. *Int. J. Nanomedicine* **13**, 4699–4709 (2018).

25. Chapiro, J. *et al.* Systemic Delivery of Microencapsulated 3-Bromopyruvate for the Therapy of Pancreatic Cancer. *Clin Cancer Res. Clin Cancer Res* **20**, 6406–6417 (2014).

26. Cochran, M. C., Eisenbrey, J., Ouma, R. O., Soulen, M. & Wheatley, M. A. Doxorubicin and paclitaxel loaded microbubbles for ultrasound triggered drug delivery. *Int. J. Pharm.* **414**, 161–170 (2011).

27. Myers, R. *et al.* Polymeric Cups for Cavitation-mediated Delivery of Oncolytic Vaccinia

Virus. *Mol. Ther.* **24**, 1627–33 (2016).

28. Zhao, X. *et al.* Preparation and in vivo evaluation of ligand-conjugated polymeric microbubbles as targeted ultrasound contrast agents. *Colloids Surfaces A Physicochem. Eng. Asp.* **452**, 59–64 (2014).

29. Chereddy, K. K. *et al.* Combined effect of PLGA and curcumin on wound healing activity. *J. Control. Release* **171**, 208–215 (2013).

30. Chereddy, K. K. *et al.* PLGA nanoparticles loaded with host defense peptide LL37 promote wound healing. *J. Control. Release* **194**, 138–147 (2014).

31. Chereddy, K. K., Vandermeulen, G. & Préat, V. PLGA based drug delivery systems: Promising carriers for wound healing activity. *Wound Repair Regen.* **24**, 223–236 (2016).

32. Dunphy, M. P. S. *et al.* In Vivo PET Assay of Tumor Glutamine Flux and Metabolism: In-Human Trial of 18F-(2S,4R)-4-Fluoroglutamine. *Radiology* **287**, 667–675 (2018).

33. Eisenhut, M. *et al.* Trapping and metabolism of radioiodinated PHIPA 3-10 in the rat myocardium. *J. Nucl. Med.* **38**, 1864–1869 (1997).

8 Appendix

8.1 Standard curve for 3BP

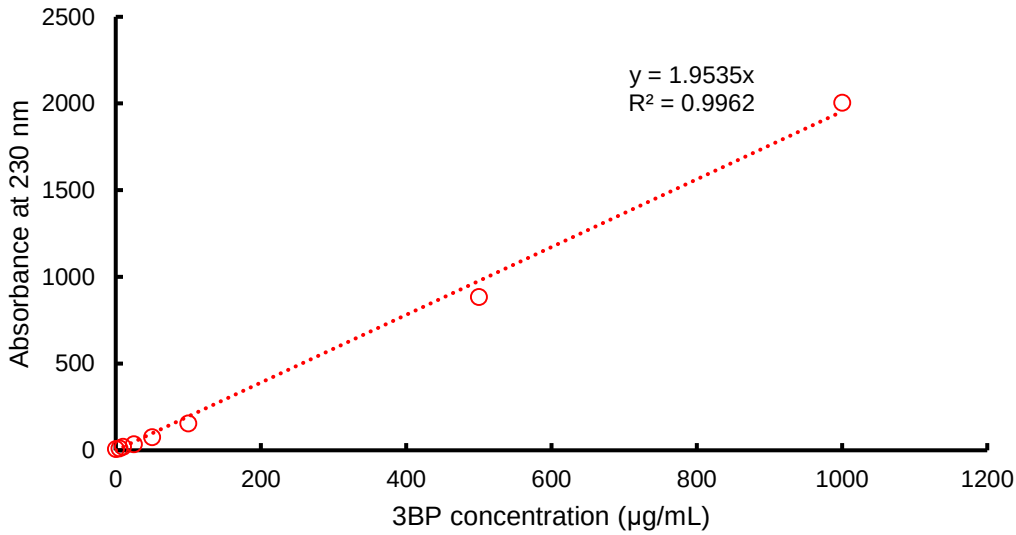

Figure A 1 Calibration curve of 3-bromopyruvate (3BP). 3BP concentration, separated from an emulsion of empty ('blank') liposomes, was measured by reversed phase high performance liquid chromatography (RP-HPLC). The area under the curve (AUC) of the 3BP peak was plotted. For full details, please refer to methods. Microsoft Excel (Microsoft Corporation, Washington, USA) was used to plot this graph.

8.2 Cell viability after 2 h treatment with 3BP

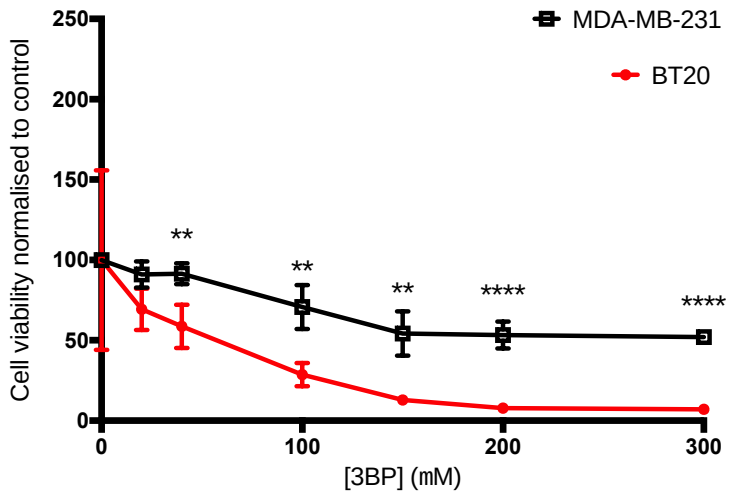

Figure A 2 Cell viability in response to 3BP treatment for 2 h. MDA-MB-231 and BT20 cells, representing MCT1 'low' and 'high' expression, were treated with a series of 3BP concentrations (0-300 µM) for 2 h. Cell viability was then measured with an MTT assay. N=4, SD shown, *P<0.05, **P<0.001, ***P<0.001, ****P<0.0001. Data were analysed on Prism 7 (GraphPad, CA, USA).

8.3 BT20 tumour growth and vascularity study

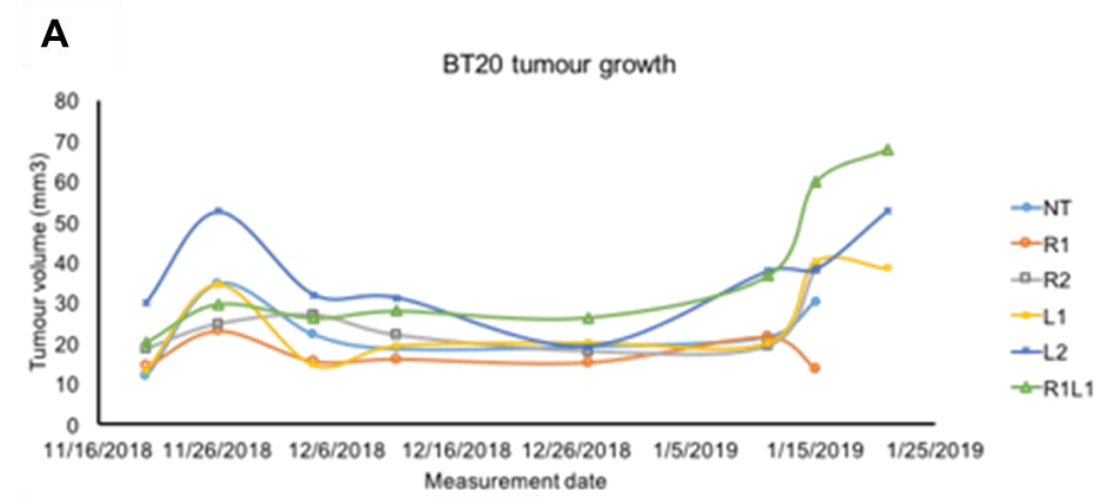

B

Mouse tail tag	Tumour volume (mm^3)	Vevo (fold increase)
NT	19.24	3x
R1	15.36	2x
R2	18.04	1.2x
L1	20.24	2x
L2	19.20	1.5x
R1L1	26.40	6x

C

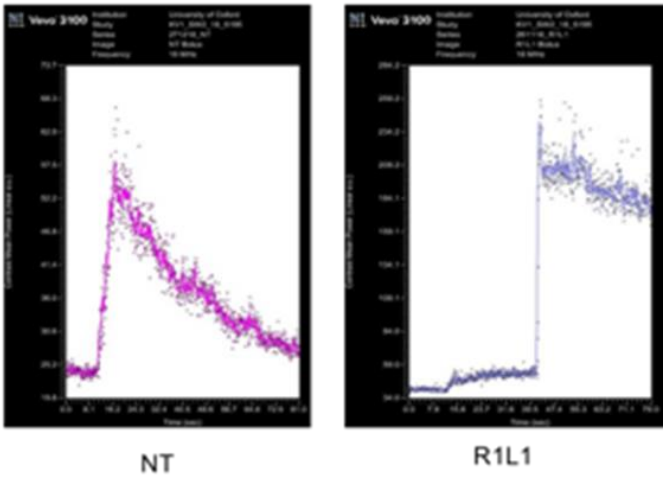

Figure A 3 BT20 tumour growth and perfusion. (A) BT20 cells (4 x 10^6 cells in 200 µL growth medium-matrigel 1:1) were inoculated in the right flank of female nude mice. Tumour growth was measured using callipers. (B)Tumour perfusion was assessed at the end of the 6th week of tumour growth by ultrasound contrast enhancement using a Vevo3100 scanner (FUJIFILM Visualsonics, Netherlands) with a MX250 probe (Centre Transmit Frequency: 20 MHz, Axial Resolution: 75 µm). SonoVue (SV) microbubbles (MBs) (0.25 mg/mL, 50 µL) were injected intravenously to anaesthesised mice and imaging was performed using non-linear contrast mode. (C) Best responses were acquired for 'NT' and 'R1L1' mice.